MULTIPHASE MULTISCALE PARTICLE-NANOFIBER INTERACTIONS IN COMPOSITES

by
FARZIN ASGHARI ARPATAPPEH

Submitted to the Graduate School of Engineering and Natural Science
in partial fulfillment of
the requirements for the degree of Doctor of Philosophy

Sabancı University
December 2022

Approval Page

FARZIN ASGHARI ARPATAPPEH 2023 ©
All Rights Reserved

DEDICATION

To

Ay, *Ulduz*, and *Gün*

To

Mom & Dad

ABSTRACT

MULTIPHASE MULTISCALE PARTICLE-NANOFIBER INTERACTIONS IN COMPOSITES

Materials Science and Engineering Ph.D. Dissertation

Supervisor: Mehmet Ali Gülgün, Co-advisor: Melih Papila

Keywords: Fiber composites, Nanocomposites, Plastic composites, Polymer composites, Laminated composite plates, Nanofiber, Nano particles, Mechanical properties, Fracture toughness, Electron microscope

Composite nanofibers have been of growing interest in various areas of science and engineering. They are intriguing due to tailorable properties by composition and/or the processing methods. Composite nanofibers can be produced from polymer solutions and suspensions with non-polymeric phases for multi-functionality. Material/processing development and materials characterisation aspects of this class of materials have great potential for novelty as also sought in this dissertation.

Among the various manufacturing methods, electrospinning is a versatile and established technique as also intensively used in this dissertation. Properties of the electrospun composite nanofibers can be modified by manipulation of the polymer chemistry and hybridization of multiple phases to polymer solutions. In this research, composites nanofibers were mostly used to interleave epoxy matrix carbon and aramid fiber reinforced composites. Aramid fiber woven fabric with phenolic binder layers was also utilized to host the nanofibrous interlayers. They were used as toughening agents of the interlaminar region of these composites.

Characterization of electrospun nanofiber composites is a major challenge in materials science and engineering. The present dissertation focuses on the hybridization of several types of polymers and non-polymeric phases which are produced by electrospinning technique. Also, it proposes special characterization methods using scanning electron microscopy. Several nanofiber composites were obtained from polystyrene, copolymerized poly[styrene-co-(glycidyl methacrylate)], polyacrylonitrile, and copolymerized poly[acrylonitrile-co-(glycidyl methacrylate)]. Several multiphase composites were produced through the hybridization of polymers and particles including

milled carbon fibers and zirconia polymorphs. Composite nanofibers were produced through single and dual electrospinning method, facilitating tailorable properties in the vicinity of particles. Several characterization methods were implemented, including thermogravimetric analysis, dynamic scanning calorimetry, x-ray diffraction analysis, Fourier transform infrared spectroscopy, Raman spectroscopy, optical microscopy, scanning electron microscopy, universal testing machine, and micro-indentation. Computer programming was utilized for image processing, statistical analysis, and data visualization through coding in MATLAB and Python. Overall, multiphase composite nanofibers were able to improve the mechanical performance of composites, standing out as an effective method in the future of the composite design and engineering.

This study includes the following novelties in the material development and processing: 1) synthesis of a new polymer by copolymerization of acrylonitrile monomer and glycidyl methacrylate, poly[acrylonitrile-co-(glycidyl methacrylate)], 2) synthesis of new multiphase interlayer with milled carbon fiber, 3) introduction of interface tailoring through dual electrospinning. This study includes a new method of characterization based on the secondary electron signal of polymorphs.

ÖZET

Kompozitlerde Çok-Fazlı ve Çok-Boyutlu Parçacık Nano-Elyaf Etkileşimi

Malzeme Bilimi ve Mühendisliği Doktora Tezi

Mehmet Ali Gülgün

Anahtar kelimeler: Lifli kompozitler, Nanokompozitler, Plastik kompozitler, Polimer kompozitler, Tabakalı kompozit levhalar, Nanoelyaf , Nano parçacık, Mekanik özellikler, Kırılma tokluğu, Elektron mikroskobu

Kompozit nanofiberler çeşitli bilim ve mühendislik alanlarında kullanılması artmaktadır. Karışımlarının değiştirilmesiyle ve/veya üretim süreçlerinin değişmesiyle özeliklerinin ayarlanabilir olmaları kompozitlerin ilginç olma sebeplerindendir. Kompozit nanofiberler polimer malzemeler polimer çözeltileri ve parçacık-çözelti karışımlarından elde edilebilir. Bu malzeme kategorisinin malzeme/süreç geliştirme ve malzemelerin tanımlama yenilikleri için yüksek potansiyeli olan bir konu olarak bu tezde aranmıştır.
Çeşitli üretim metotları arasından elektro-eğirme çok yönlü ve denenmiş bir teknik olarak bu tezde geniş bir şekilde kullanılmıştır. Elektro-eğirme kompozit nano elyaf polimer kimyası ve birden çok fazın karıştırma yöntemleriyle değişebilmektedir. Bu araştırmada kompozit nanofiberler genellikle epoksi matrisli karbon fiber-takviyeli ve aramid-fiber takviyeli polimerlerin kompozitlerde ara katman olarak kullanılmıştır. Aramid dokulu kumaşlar fenolik yapıştırıcı katmanlar da nano elyafı içlerine almak için kullanılmıştır. Bunlar kompozitlerin ara katmanlarının kırılma tokluğunu arttırmak amacıyla kullanılmıştır. Elektro-eğirme nano elyaf kompozitlerinin tanımlaması malzeme bilimi ve mühendisliğinde önemli bir problemdir. Bu tez çeşitli polimer ve polimer olmayan fazlarının karıştırılmasını odaklanmaktadır. Bu kompozit nanofiberler elektro-eğirme tekniğiyle üretilmektedir. Ayrıca bu tez taramalı elektron mikroskobu vasıtasıyla yeni bir metodu da sunmaktadır. Çeşitleri nano elyaf kompozitler polistiren, poli[stiren-ko-(glisidil metakrilat)], poliakrilonitril, ve poli[akrilonitril-ko-(glisidil metakrilat)] basında polimerlerden üretildi. Çeşitli çok fazlı kompozitler polimerler ve parçacıkların karışımından üretildi. Bu parçacıklar silikon karbür, öğütülmüş karbon fiber ve zirkonya polimorflarından ibarettir. Kompozit nanofiberler tek ve çift elektro-eğirme yöntemiyle üretildi. Bu üretim metotları parçacıkların etrafında ayarlanabilir özellikleri mümkün kıldı. Çeşitli tanımlama metotları kullanıldı. Termogravimetrik analiz, dinamik taramalı kalorimetri, x-ışını kırınım analizi, Fourier dönüşümlü kızılötesi spektroskopisi, evrensel

test makinesi ve mikro çentik metodu bu tezde kullanılmıştır. Bilgisayar programı görüntü analizi, istatistik analiz ve veri görselleştirme için kullanılırken MATLAB ve Python'da kodlama yapılmıştır. Genel olarak çok fazlı kompozitler nano elyaf fiber-takviyeli kompozitlerin mekanik özelliklerini iyileştirmeyi başardılar ve bir etkili metot olarak gelecekte kompozit tasarımı ve mühendisliğinde kendilerini örnek olarak ortaya koydular.

Bu araştırma malzeme ve süreç geliştirme alanında şu yenilikleri içermektedir: 1) bir yeni malzeme olarak poli[akrilonitril-ko-(glisidil metakrilat)] polimerinin sentezi. 2) öğütülmüş karbon fiber içeren çok fazlı yeni bir ara katmanın üretimi, 3) ara yüzeylerin ayarlamasının elektro-eğirme yöntemiyle değiştirme metodunun öne sürülmesi. Ayrıca, bu araştırma ikincil elektron sinyalini yeni bir polimorf tanımlama metodu olarak ortaya koymaktadır.

ACKNOWLEDGEMENT

I would like to express my gratitude to my supervisor Prof. Dr. Mehmet Ali Gülgün and my co-supervisor Prof. Dr. Melih Papila for their incredible leadership and patience during my studies, only with whom this dissertation was made possible. I would also like to thank the jury members Assoc. Prof. Dr. Güllü Kızıltaş-Şendur, Prof. Dr. Cleva Ow-Yang, Assoc. Prof. Dr. Elif Özden Yenigün, and Assist. Prof. Dr. Kaan Bilge.

I would like to thank Roketsan A.Ş. for funding of the project discussed in Chapter 2, Mr. Adem Şen from Department of Materials Science and Engineering of Gebze Technical University for his help in carrying out the micro-indentation test in Chapter 9, Dr. Marek Dosbaba from TESCAN ORSAY HOLDING and the assistance in obtaining correlative Raman and scanning electron microscopy (SEM) with secondary electron imaging microscopy in a fully integrated Raman Imaging and Scanning Electron Microscope (RISE; WiTec+Tescan TIMA) in Chapter 9. Also, I would like to thank Mr. Çağdaş Akalın from Sabancı University Integrated Manufacturing Technologies Research and Application Center for his help in machining of samples in Chapter 6.

I would like to thank my colleagues, Dr. Cem Ünsal for his mentorship through the project and Mr. Farzin Javanshour for his collaborations in the project which formed Chapter 2, Ms. Emel Manga and Mr. Berk Emre Aydemir for their collaborations in the synthesis of the materials mentioned in Chapter 3 and Chapter 4, Ms. Ecenaz Türkoğlu and Ms. Rukiye-Ayshe Egeli for their collaboration in preparing the samples described in Chapter 6. I also would like to thank Dr. Sorour Semsari Parapari, Dr. Gülcan Çorapçıoğlu, and Dr. Ali Ansari Hamedani for helping me with obtaining SEM images as well as training me to become an SEM user. I would like to acknowledge Dr. Bengisu Yılmaz, Mr. Hasan Emre Baysal, and Ms. Eylül Mina Aydın for their help in the laboratory work.

Also, I would like to thank Assist. Prof. Dr. Kaan Bilge, Prof. Dr. Cleva Ow-Yang, Prof. Dr. Raynald Gauvin from McMaster University, Mr. Ian Cotton from Hitachi High-Tech in Canada, and Mr. Vern Robertson from JEOL USA, Inc. for the fruitful discussions we had throughout the studies.

TABLE OF CONTENTS

DEDICATION iv
ABSTRACT v
ÖZET vii
ACKNOWLEDGEMENT ix
Chapter 1 General introduction 1
Chapter 2 Multiscale enhancement to aramid fabric-reinforced composites: electrospun P(An-co-GMA) nanofibrous interlayers 19
Chapter 3 Multiscale Reinforcing Interlayers of Selfsame P(St-*co*-GMA) Nanofibers Loaded with MCF for Polymer Composites and Nanocomposites 34
Chapter 4 Morphology evolution of self-same nanocomposites hybridized with jumbo-sized particles 51
Chapter 5 Design of experiment for nanocomposites of electrospun P(St-co-GMA) nanofibers loaded with zirconia nanoparticles 71
Chapter 6 Drilled Carbon Fiber Composites with Local Nanofiber-Nanoparticle Toughening Interlayer 91
Chapter 7 General Conclusion 128
Chapter 8 Quantification of Contrast Difference Between Monoclinic and Tetragonal Zirconia in Low-kV SEM 131
Chapter 9 Phase Differentiation of Zirconia Polymorphs with Low Voltage Secondary Electrons 136

LIST OF FIGURES

Figure 1: particle type and particle size used in the literature to produce composite nanofibers 8
Figure 2: map of research field and structures designed in this dissertation..... 16
Figure 3: structure and polymerization of poly(*para*-phenylene diamine terephthalamide). 21
Figure 4: ATR FTIR spectrum for P(An-*co*-GMA). 28
Figure 5: SEM micrographs and fiber diameter distribution of P(An-*co*-GMA) (upper row) and PAN (lower row). 29
Figure 6: Mechanical performance of AFRC in tensile test. 30
Figure 7: Epoxy composites reinforced with aramid or aramid/nanofibers. 31
Figure 8: Phenolic composites reinforced with aramid or aramid/nanofibers. 32
Figure 9: Uniaxial tensile test results for aramid fabric (left), epoxy-matrix composites (middle), and phenolic-matrix (right) composites. 33
Figure 10: ATR FT-IR spectra of monomers and the copolymer. 38
Figure 11: TG curve (left) and exo up DSC curve (right) from P(St-*co*-GMA). 38
Figure 12: Nanofibers of neat polymer and the mix of polymer with PA before and after heat-treatment. 39
Figure 13: combined nanofibrous structure of melting P(St-*co*-GMA) and the mix of P(St-*co*-GMA) with PA before (up) and after (down) heat-treatment. 40
Figure 14: Morphology changes of nanofibrous structures with MCF before (up) and after (down) left treatment. 41
Figure 15: Morphology changes in the combined melting polymer nanofibers and crosslinking mix of polymer and PA plus MCF before (up) and after (down) heat-treatment. 42
Figure 16: Morphology changes in the combined melting polymer nanofibers and crosslinking mix of polymer and PA plus MCF before (up) and after (down) heat-treatment. 43
Figure 17: Morphology changes in the combined melting polymer nanofibers and the crosslinking mix of polymer and PA plus MCF before (up) and after (down) heat-treatment 44
Figure 18: TG under nitrogen medium for P(St-*co*-GMA), P(St-*co*-GMA)-MCF, and their hybrid. 45

Figure 19: tensile test results for nanocomposites reinforced with the selfsame nanofibers containing MCF (left) and only selfsame nanofibers (right). 46
Figure 20: Tensile test results and failed specimens of neat CFRP (left) and CFRP interlayered with the selfsame P(St-*co*-GMA) nanofibers impregnated with MCF (right). 47
Figure 21: SEM micrographs of the fracture surfaces of failed specimens of CFRP interlayered with the selfsame P(St-*co*-GMA) nanofibers. 49
Figure 22: Flow chart of the process (a), preparation of precursors (b), dual electrospinning setup (c), heat-treatment program in a box oven along with the morphology analyses stages (d), schematic of laminated composite plate lay-up (e), composite plate and coupon sample geometry (f) 56
Figure 23: SEM micrograph of as-received MCF@m-phase nanofibers in different setup parameters (scalebar consistent within micrographs) 60
Figure 24: SEM micrograph of as- received MCF@m-phase (a,b), and as-received MCF@x-phase (c,d). (Scalebars consistent within micrographs of the same columns) 61
Figure 25: Examples of timing strategy of two syringes in dual electrospinning of 25/75 composition (a) and 50/50 composition (b) 63
Figure 26: SEM micrographs for heat treated hybrid system of MCF@m-phase/x-phase. dual-electrospun nanofibrous mats at various fractions of the polymer suspension/solution. (Scalebar is consistent in each column) 63
Figure 27: SEM micrographs heat treated hybrid system of m-phase/MCF@x-phase dual-electrospun nanofibrous mats at various fractions of the polymer suspension/solution. (Scalebar is consistent in each column) 65
Figure 28: Tensile test results and failed specimens of neat CFRC (a) and CFRC interlayered with the selfsame P(St-*co*-GMA) nanofibers impregnated with MCFs (b). 69
Figure 29: experimental space (left) and standardized experimental space (right). 75
Figure 30: Morphology of fibers regarding the data points of the revised experimental space 76
Figure 31: fiber diameter of P(St-*co*-GMA)-ZrO_2 nanofibers in the finalized experimental space (PL##: polymer wt.% and PR##: particle wt.%) 77
Figure 32: contact angle of epoxy with nanofiber mat surfaces after long time 78
Figure 33: fitted surfaces (left), fit properties (right) for response of fiber diameter..... 83

Figure 34: fitted surfaces (left), fit properties (right) for response of particle content .. 85
Figure 35: fitted surfaces (left), fit properties (right) for response of contact angle 87
Figure 36: TGA of segmented samples from a P(St-*co*-GMA)-ZrO_2 membrane with polymer concentration of 25 wt.% and nominal particle concentration of 20 wt.% (medium: synthetic dry air) 88
Figure 37: (a) Segmented samples from a P(St-*co*-GMA)-ZrO2 membrane with polymer concentration of 25 wt.% and nominal particle concentration of 20 wt.%, (b) actual particle content of segmented samples 90
Figure 38: Composite lay-ups (a) reference, (b) locally interleaved/toughened. 95
Figure 39: Processing and preparation of drilled samples (a) cure cycle, (b) vacuum-assisted compression molding, (c) waterjet cutting scheme for open-hole tension test samples. 96
Figure 40: Tensile test setup (a) and extensometer configuration (b) for mechanical testing 97
Figure 41: typical particle clusters before breaking into nanoparticles. 98
Figure 42: Morphology of the toughening nanofiber-nanoparticle interlayer. 98
Figure 43: Elemental characterization of t-nanoparticle-impregnated PAN nanofibers. 99
Figure 44: Drilled hole of reference sample with no toughening interlayer, sample N-1 to N-3 enter and exit. 100
Figure 45: Drilled hole of reference sample with no toughening interlayer, sample N-4 to N-6 enter and exit. 101
Figure 46: Drilled hole of toughened samples with PAN-c-ZrO_2 interlayer, sample CZ-1 to CZ-3 enter and exit. 102
Figure 47: Drilled hole of toughened samples with PAN-c-ZrO_2 interlayer, sample CZ-4 to CZ-6 enter and exit. 103
Figure 48: Drilled hole of toughened samples with PAN-t-ZrO_2 interlayer, sample TZ-1 to TZ-3 enter and exit. 104
Figure 49: Drilled hole of toughened samples with PAN-t-ZrO_2 interlayer, sample TZ-4 to TZ-6 enter and exit. 105
Figure 50: Optic microscope photos of left and right edges of composite coupons around the drilled hole. 106

Figure 51: Optic microscope photos of left and right edges of composite coupons around the drilled hole. 107
Figure 52: Optic microscope photos of left and right edges of composite coupons around the drilled hole. 108
Figure 53: representative micrograph of the angle of wall in the drilled hole for a neat composite and composites with the local interlayers of PAN-c-ZrO_2 and PAN-c-ZrO_2 108
Figure 54: Uniaxial tensile test for drilled-hole neat composites 109
Figure 55: Uniaxial tensile test for drilled-hole composites locally toughened by the interlayers of PAN nanofibers with cubic zirconia 110
Figure 56: Uniaxial tensile test for drilled-hole composites locally toughened by the interlayers of PAN nanofibers with tetragonal zirconia 110
Figure 57: images of composites after uniaxial tensile test for drilled-hole composites: neat (N-#), locally toughened by the interlayers of PAN nanofibers with cubic zirconia (CZ-#), locally toughened by the interlayers of PAN nanofibers with tetragonal zirconia (TZ-#) 112
Figure 58: images of representative drilled-hole composites after uniaxial tensile test: top half of the N-5 neat sample (N5T), bottom half of N-5 neat sample (N5B), top half of CZ-5 sample locally toughened by the interlayers of PAN nanofibers with cubic zirconia (CZ5T), bottom half of CZ-5 sample locally toughened by the interlayers of PAN nanofibers with cubic zirconia (CZ5B), top half of TZ-4 sample locally toughened by the interlayers of PAN nanofibers with cubic zirconia (TZ4T), bottom half of TZ-4 sample locally toughened by the interlayers of PAN nanofibers with cubic zirconia (TZ4B), inward vector $\otimes$ showing the drilling direction 113
Figure 59: fracture surface map of N5 sample (Neat-5) after failure around the drilled-hole from top half (T) and bottom half (B) generated from compilation of several SEM images of sites (S##), d showing the drilling vector 114
Figure 60: fracture surface map of CZ5 sample (CZ-5) after failure around the drilled-hole from top half (T) and bottom half (B) generated from compilation of several SEM images of sites (S##), d showing the drilling vector 115
Figure 61: fracture surface map of TZ4 sample (TZ-4) after failure around the drilled-hole from top half (T) and bottom half (B) generated from compilation of several SEM images of sites (S##), d showing the drilling vector 116

Figure 62: fracture of the epoxy inside the drilled hole (arrow showing the drilling direction) 117
Figure 63: fracture of the sample outside the drilled hole (arrow showing the drilling direction) 117
Figure 64: Diameter of drilled holes in composites with and without local toughening 120
Figure 65: properties of drilled hole composites average thickness, average weight, difference in diameter of enter and exit sides, and the hole wall angle..... 123
Figure 66: process of drilling a hole in composites..... 124
Figure 67: strain at break for drilled-hole composites 125
Figure 68: strength of the drilled-hole composites..... 125
Figure 69: areas on the cross section of failed drilled-hole composite 126
Figure 70: Manual segmentation of t-phase and m-phase from electron micrograph captured at 0.5 kV with an in-lens detector. 134
Figure 71: Histogram of grayscale levels for t-phase, m-phase and complete SEM micrograph captured with an in-lens detector at 0.5 kV. 134
Figure 72: Standardized difference between the AGSL (right) for t-phase and m-phase in SEM micrographs captured with an in-lens detector in a range of acceleration voltages (5 - 0.4 kV). 135
Figure 73: different signals generated when primary electrons impinge a specimen adapted from [204] with permission 137
Figure 74: XRD pattern analysis of prepared ZrO_2 powder..... 146
Figure 75: XRD pattern of 3Y-PSZ powder comprised mainly from tetragonal and monoclinic phases 147
Figure 76: Raman shift spectrum of prepared monoclinic ZrO_2. Identifying characteristic peaks indicated with asterisk (∗) 148
Figure 77: Raman shift spectrum of tetragonal 3Y-PSZ with peaks from monoclinic phase indicated with (+) 149
Figure 78: Micrograph of uncoated m-phase and t-phase captured on the Everhart-Thornley detector (SE2) 150
Figure 79: Micrograph of uncoated m-phase and t-phase captured on the in-lens detector (SE1)..... 151

Figure 80: BSE electron micrographs of monoclinic (rod) and tetragonal (sphere) zirconia particles (Brightness 50%, Contrast 45%). 152
Figure 81: SE2 micrographs of monoclinic (rod) and tetragonal (sphere) zirconia particles under different accelerating voltages, collected using a conventional Everhart-Thornley detector (Brightness 50%, Contrast 50%). 153
Figure 82: SE1 micrographs revealing contrasting signal intensity behavior between monoclinic (rod) and tetragonal (sphere) zirconia particles under different accelerating voltages, using a TTL detector (Brightness 50%, Contrast 32%). 155
Figure 83: SE1 micrographs revealing the effect of the working distance in the intensity difference between monoclinic (rod) and tetragonal (sphere) zirconia particles under different accelerating voltages, using a TTL detector (Brightness 42.5%, Contrast 35.0%). 157
Figure 84: SE2 micrographs revealing the effect of the working distance in the intensity difference between monoclinic (rod) and tetragonal (sphere) zirconia particles under different accelerating voltages, using an ET detector (Brightness 50.0%, Contrast 50.0%). 159
Figure 85: Identification of stress-induced phase-transformation regions in pellet sintered from partially stabilized zirconia; SEM micrograph of the micro-indented pellet (a), overlaid micrograph and Raman map (b), Raman map near a crack (c), overlaid micrograph and Raman map near crack; tetragonal matrix (green), monoclinic transformed phase (blue), carbon contaminations (red). 161
Figure 86: Contrast level difference near a crack initiated by a micro-indention on a pellet of partially stabilized zirconia; SE2 micrograph of indentation (a), schematic of indent and cracks along the corners (b), and TTL image of one of the cracks (c). 162
Figure 87: SEM micrograph (BSE, brightness 50%, contrast 45%). 164
Figure 88: Cropped area of the carbon tape support from SEM micrograph (BSE, brightness 50%, contrast 45%). The intensity of the area outside the phase was set to zero. 165
Figure 89: Cropped area of the m-phase from SEM micrograph (BSE, brightness 50%, contrast 45%). The intensity of all pixels subtracted by one. Then, the intensity of the area outside the phase was set to 255. 166

Figure 90: Cropped area of the t-phase from SEM micrograph (BSE, brightness 50%, contrast 45%). The intensity of all pixels raised by one. Then, the intensity of the area outside the phase was set to zero. 167
Figure 91: histogram of carbon tape support from segmented BSE image before exclusion of zero intensities (fixed brightness 50% and contrast 45%). 168
Figure 92: histogram of carbon tape support from segmented BSE image after exclusion of zero intensities (fixed brightness 50% and contrast 45%). 169
Figure 93: histogram of m-phase from segmented BSE image before the exclusion of pixels with the intensity values equal to 255 (fixed brightness 50% and contrast 45%). 170
Figure 94: histogram of m-phase from segmented BSE image after the exclusion of pixels with the intensity equal to 255 and addition of 1 to all pixel intensities (fixed brightness 50% and contrast 45%)..... 171
Figure 95: histogram of t-phase from segmented BSE image before the exclusion of pixels with the intensity values equal to zero (fixed brightness 50% and contrast 45%). 172
Figure 96: histogram of t-phase from segmented BSE image after the exclusion of pixels with the intensity equal to zero and subtraction of 1 from all pixel intensities (fixed brightness 50% and contrast 45%). 173
Figure 97: micrograph of carbon tape support from segmented BSE electron images (fixed brightness 50% and contrast 45%)..... 174
Figure 98: histogram of carbon tape support from segmented BSE electron images (fixed brightness 50% and contrast 45%). 175
Figure 99: micrograph of m-phase from segmented BSE electron images (fixed brightness 50% and contrast 45%)..... 175
Figure 100: histogram of m-phase from segmented BSE electron images (fixed brightness 50% and contrast 45%)..... 176
Figure 101: micrograph of t-phase from segmented BSE electron images (fixed brightness 50% and contrast 45%)..... 177
Figure 102: histogram of t-phase from segmented BSE electron images (fixed brightness 50% and contrast 45%)..... 178
Figure 103: micrograph of carbon tape support from segmented SE2 electron images (fixed brightness 50% and contrast 50%)..... 179

Figure 104: histogram of carbon tape support from segmented SE2 electron images (fixed brightness 50% and contrast 50%). 180
Figure 105: micrograph of m-phase from segmented SE2 electron images (fixed brightness 50% and contrast 50%). 182
Figure 106: histogram of m-phase from segmented SE2 electron images (fixed brightness 50% and contrast 50%)..... 182
Figure 107: micrograph of t-phase from segmented BSE electron images (fixed brightness 50% and contrast 50%)..... 184
Figure 108: histogram of t-phase from segmented SE2 electron images (fixed brightness 50% and contrast 50%)..... 184
Figure 109: micrograph of carbon tape support from segmented SE1 electron images (fixed brightness 50% and contrast 32%)..... 186
Figure 110: histogram of carbon tape support from segmented SE1 electron images (fixed brightness 50% and contrast 32%). 187
Figure 111: micrograph of m-phase from segmented SE1 electron images (fixed brightness 50% and contrast 32%). 189
Figure 112: histogram of m-phase from segmented SE1 electron images (fixed brightness 50% and contrast 32%)..... 189
Figure 113: micrograph of t-phase from segmented SE1 electron images (fixed brightness 50% and contrast 32%)..... 190
Figure 114: histogram of t-phase from segmented SE1 electron images (fixed brightness 50% and contrast 32%)..... 191
Figure 115: average intensity for carbon tape support, m-ZrO_2, and t-ZrO_2 from SEM micrographs captured by BSE detector 193
Figure 116: relative average intensity for carbon tape support, m-ZrO_2, and t-ZrO_2 from SEM micrographs captured by BSE detector..... 194
Figure 117: average intensity for carbon tape support, m-ZrO2, and t-ZrO2 from SEM micrographs captured by Everhart-Thornley detector..... 195
Figure 118: relative average intensity for carbon tape support, m-ZrO2, and t-ZrO2 from SEM micrographs captured by Everhart-Thornley detector 196
Figure 119: average intensity for carbon tape support, m-ZrO_2, and t-ZrO_2 from SEM micrographs captured by TTL detector 197

Figure 120: relative average intensity for carbon tape support, m-ZrO_2, and t-ZrO_2 from SEM micrographs captured by TTL detector 198
Figure 121: Stopping power of monoclinic (m-ZrO_2) and tetragonal (t-ZrO_2) phases 199
Figure 122: escape probability of electrons for m-phase and t-phase 200
Figure 123: calculated secondary electron yield of m-phase and t-phase 201
Figure 124: micrograph of carbon tape support from segmented SE1 electron images at EHT = 1 kV (fixed brightness 42.5% and contrast 35.0%). 203
Figure 125: histogram of carbon tape support from segmented SE1 electron images at EHT = 1 kV (fixed brightness 42.5% and contrast 35.0%). 204
Figure 126: micrograph of m-phase from segmented SE1 electron images at EHT = 1 kV (fixed brightness 42.5% and contrast 35.0%) 206
Figure 127: histogram of m-phase from segmented SE1 electron images at EHT = 1 kV (fixed brightness 42.5% and contrast 35.0%) 207
Figure 128: micrograph of t-phase from segmented SE1 electron images at EHT = 1 kV (fixed brightness 42.5% and contrast 35.0%) 209
Figure 129: histogram of t-phase from segmented SE1 electron images at EHT = 1 kV (fixed brightness 42.5% and contrast 35.0%) 210
Figure 130: average intensity in different working distances for carbon tape support, m-ZrO_2, and t-ZrO_2 from SEM micrographs captured by TTL detector. 212
Figure 131: relative average intensity in different working distances for carbon tape support, m-ZrO_2, and t-ZrO_2 from SEM micrographs captured by TTL detector. 213
Figure 132: effect working distances for on SEM micrographs captured by TTL detector. 214
Figure 133: micrograph of carbon tape support from segmented SE2 electron images at EHT = 1 kV (fixed brightness 50.0% and contrast 50.0%). 215
Figure 134: histogram of carbon tape support from segmented SE2 electron images at EHT = 1 kV (fixed brightness 50.0% and contrast 50.0%). 216
Figure 135: micrograph of m-phase from segmented SE2 electron images at EHT = 1 kV (fixed brightness 50.0% and contrast 50.0%) 218
Figure 136: histogram of m-phase from segmented SE2 electron images at EHT = 1 kV (fixed brightness 50.0% and contrast 50.0%) 219
Figure 137: micrograph of t-phase from segmented SE2 electron images at EHT = 1 kV (fixed brightness 50.0% and contrast 50.0%) 221

Figure 138: histogram of t-phase from segmented SE2 electron images at EHT = 1 kV (fixed brightness 50.0% and contrast 50.0%)..... 222
Figure 139: average intensity in different working distances for carbon tape support, m-ZrO_2, and t-ZrO_2 from SEM micrographs captured by E-T detector. 224
Figure 140: relative average intensity in different working distances for carbon tape support, m-ZrO_2, and t-ZrO_2 from SEM micrographs captured by E-T detector. 225
Figure 141: effect of working distances for on SEM micrographs captured by E-T detector. 226
Figure 142: selected transformed region along the crack (TTL image after brightness-contrast manipulated) 227

LIST OF TABLES

Table 1: Particle type and particle size used in the literature to produce composite nanofibers 6
Table 2: construction of various ingredients of the sample classes examined in the dissertation..... 17
Table 3: Mechanical test results for reinforced epoxy composites. 29
Table 4: Mechanical test results for the reinforced phenolic-matrix composites..... 31
Table 5: Mechanical properties of nanocomposites reinforced by nanofibers of selfsame properties and selfsame plus MCF. 45
Table 6: Mechanical properties of neat CFRP and CFRP with the interlayers of selfsame P(St-*co*-GMA) plus MCF. 46
Table 7: Fraction combinations for the two polymer variants and associated suspensions 62
Table 8: Effects of 50/50 m-phase/MCF@x-phase hybrid nanofibrous interlayers on the mechanical behavior of cross-ply carbon epoxy laminates under tensile loading 68
Table 9: The experimental points and the responses..... 79
Table 10: particles content various points of a P(St-*co*-GMA)-ZrO2 membrane (polymer concentration 25 wt.% and particle concentration 20 wt.%)..... 89
Table 11: tensile properties of neat composite samples 111
Table 12: tensile properties of composite with local toughening interlayer of PAN-c-ZrO_2 111
Table 13: tensile properties of composite with local toughening interlayer of PAN-t-ZrO_2 111
Table 14: Diameter of drilled holes in neat composite samples..... 118
Table 15: Diameter of drilled holes in composite samples with local toughening of electrospinning nanofibers loaded with cubic zirconia (PAN-c-ZrO_2). 118
Table 16: Diameter of drilled holes in composite samples with local toughening of electrospinning nanofibers loaded with tetragonal zirconia..... 119
Table 17: properties of composite samples with no local toughening (neat)..... 120
Table 18: properties of composite samples with local toughening of PAN-c-ZrO_2 121
Table 19: properties of composite samples with local toughening PAN-t-ZrO_2 121
Table 20: Average intensity for carbon tape support, m-ZrO_2, and t-ZrO_2 from SEM micrographs captured by BSE..... 178

Table 21: average intensity for carbon tape support, m-ZrO_2, and t-ZrO_2 from SEM micrographs captured by SE2..... 185
Table 22: average intensity for carbon tape support, m-ZrO_2, and t-ZrO_2 from SEM micrographs captured by SE1..... 192
Table 23: average intensity for carbon tape support, m-ZrO_2, and t-ZrO_2 from SEM micrographs captured by SE1 in EHT = 1 kV (fixed brightness 42.5% and contrast 35.0%) 211
Table 24: average intensity for carbon tape support, m-ZrO_2, and t-ZrO_2 from SEM micrographs captured by SE2 in EHT = 1 kV (fixed brightness 50.0% and contrast 50.0%) 223

LIST OF SYMBOLS, ACRONYMS AND ABBREVIATIONS

St	Styrene
GMA	Glycidyl methacrylate
PA	Phthalic anhydride
EDA	Ethylenediamine
TBA	Tributylamine
PS	Polystyrene
P(St-*co*-GMA)	Poly[styrene-*co*-(glycidyl methacrylate)]
DMF	*N,N*-dimethylformamide
m-phase	Soften-able P(St-*co*-GMA)
x-phase	Cross-linkable P(St-*co*-GMA) = P(St-*co*-GMA)/PA-TBA
MCF	Milled Carbon Fiber
MCF@m-phase	MCF-loaded P(St-*co*-GMA)
MCF@x-phase	MCF-loaded P(St-*co*-GMA)/PA-TBA
MCF@m-phase/x-phase	MCF-loaded P(St-*co*-GMA) + P(St-*co*-GMA)/PA-TBA
m-phase/MCF@x-phase	P(St-*co*-GMA) + MCF-loaded P(St-*co*-GMA)/PA-TBA
UD	Unidirectional
PW	Plain weave
CFRC	Carbon Fiber-Reinforced Composite
AFRC	Aramid Fiber-Reinforced Composite
T_g	Glass transition temperature
E	Elastic Young's modulus
ϵ	Strain
σ	Stress
σ_u	Ultimate tensile strength
K	Stress intensity factor
G	Strain energy release rate
TGA	Thermogravimetric analysis
DSC	Dynamic Scanning Calorimetry
UTM	Universal Testing Machine
SEM	Scanning electron microscopy

RSM	Response Surface Methodology

CHAPTER 1
GENERAL INTRODUCTION

1.1 Overview

1.1.1 Electrospinning nanofibers

Electrospinning is an over-a-century old, proven as a powerful and facile technique to fabricate nanofibers [1]–[3]. In its simplest lab-scale form, the process includes a polymer solution that is electrically charged and pumped through a micron-sized nozzle so that the solution drop is exposed to an electrostatic field between the nozzle tip and a grounded collector. The acceleration of electrically charged polymer chains in the electrostatic field reduces the diameter of the polymer thread from micrometers on the tip of the nozzle down to nanometers on the collector – nanofibers [4].

Thanks to its history and developing knowledge, electrospinning produces nonwoven mats which can be used in a variety of modern applications ranging from delicate medical uses to structural materials. They were used as environmental filters for water and air purifications [5], medical filters for virus removal [6], [7], scaffolds for tissue regeneration [8] , and toughening interlayers for laminated composites [9]–[18].

One specific application of electrospinning nanofibers is their use as toughening interlayers for laminated composites. In this method, the resin rich regions of laminated composites are reinforced using electrospinning nanofibers. When composites undergo stress, micro cracks are initiated in this region. Stress cause cracks to propagate and coalescence. Finally, the structure is disintegrated. Nanofibers resist the process of crack initiation and propagation by several mechanisms including 1) Fiber breakage, 2) Fiber pull-out, 3) Fiber peel-off, 4) Matrix spalling, 5) Snubbing, and 6) Fiber-matrix de-bounding. Collaboration of these mechanisms increases the toughness of composites.

Mechanical properties of nanofibers and the strength of the fiber/matrix interface are important two factors in the performance of toughened composites. Bisphenol A diglycidyl ether is common matrix polymer in the composite industry. It is known as epoxy resin because of the two epoxy rings on its polymer chain. While processing of the composites, these chains are opened. A crosslinking molecule (hardener) creates links between these opened rings of different epoxy chains. This mechanism causes the liquid resins to solidify [12].

Same epoxy rings were used to develop a new polymer with a stronger interface to epoxy resins. A new polymer based on polystyrene (PS) was synthesized copolymerizing St monomers with GMA in a free-radical polymerization. Electrospinning nanofibers of pristine PS and P(St-*co*-GMA) was produced. Further strength to the interface was introduced by spraying ethylenediamine on the nanofibers of P(St-*co*-GMA). Nanocomposites of epoxy resin with embedded nanofiber of PS, P(St-*co*-GMA), and P(St-*co*-GMA)/EDA were produced. Samples of the nanocomposites were analyzed by dynamic mechanical analysis. PS nanofibers improved the real part of the complex elastic modulus from 1187 ± 50 MPa at 30°C to 3939 ± 50 MPa at 30°C. P(St-*co*-GMA) nanofibers showed similar performance by an elastic modulus of 3825 ± 100 MPa at 30°C. Meanwhile, P(St-*co*-GMA)/EDA nanofibers showed an outstanding elastic modulus of 10083 ± 100 MPa at 30°C. When temperature increased to 80°C, the elastic modulus of the neat epoxy dropped to 130 ± 3 MPa. High-temperature modulus of nanocomposites with PS nanofibers showed the exact modulus of 130 ± 3 MPa at 80°C. Nanocomposites with P(St-*co*-GMA) nanofibers showed a higher elastic modulus equal to 415 ± 15 MPa at 80°C. The higher elastic modulus for P(St-*co*-GMA) at 80°C was associated with the crosslinking between opened epoxy rings on the P(St-*co*-GMA) and those on the epoxy matrix chains. Meanwhile, nanocomposites with P(St-*co*-GMA)/EDA showed the highest elastic modulus of 1570 ± 15 at 80°C. This increase was also associated with the populated crosslinks between epoxy rings on the nanofibers and those on the matrix chain. Stronger fiber/matrix interface caused a higher elastic modulus in elevated temperatures [12].

Analysis of the damping in the nanocomposites supported the role of crosslinking in the stiffness of the composites. Damping ratio ($\tan\delta$) of neat epoxy was measured as 0.679. PS nanofibers improved the damping ratio 0.471. Nanocomposites with P(St-*co*-GMA) nanofibers improved the damping ratio even more to 0.397. Meanwhile, nanocomposites

with embedded P(St-*co*-GMA)/EDA nanofibers showed the best damping ratio equal to 0.372. Furthermore, measured T_g values showed an increase from 60.1°C for neat epoxy to 67.0°C in the nanocomposites with embedded PS nanofibers. T_g of nanocomposites embedded with P(St-*co*-GMA) was measured as 64.8°C. T_g of nanocomposites embedded with P(St-*co*-GMA)/EDA was measured as 65.6°C. T_g for nanocomposites with embedded P(St-*co*-GMA) and P(St-*co*-GMA)/EDA nanofibers were all higher than that of neat epoxy. Fractographic analysis reaffirmed the transition of mirror-like fracture in brittle epoxy to a ductile fracture in toughened nanocomposites [12].

1.1.2 Nanocomposites

Toughening with additive particles is another toughening method used in the composite industry. When a crack front propagates in a composite, a particle can inhibit its propagation with several mechanisms such as 1) Crack pinning, 2) Crack branching, 3) Bridging, 4) Deflection leading [19]. Elastic particles have been used widely to improve the toughness of the resin-rich region of laminated composites. Effect of rubber filling on the toughness of epoxy was tested in single-edge-notch bending (SENB). Effect of filling on the stiffness of epoxy was tested in standard tensile test setup. Critical stress intensity factor (K_{IC}), critical strain energy release rate (G_{IC}) was measured for the toughness of the specimen. Elastic Young's modulus (E) and ultimate tensile strength (σ_u) were identified for the changes in the tensile properties of nanocomposites. For unfilled epoxy E = 2.86 ± 0.08 GPa, σ_u = 42.1 ± 2.6 MPa, K_{IC} = 0.951 ± 0.029 MPa $m^{1/2}$, and G_{IC} = 0.277 ± 0.025 kJ m^{-2}. Addition of 2, 4, 6, 8, 10, 12, 15 wt.% increased K_{IC} and G_{IC} monotonically. Epoxy filled with 15 wt.% rubber showed K_{IC} = 2.77 ± 0.06 MPa $m^{1/2}$ and G_{IC} = 3.10 ± 0.19 kJ m^{-2}. On the other hand, addition of 2, 4, 6, 8, 10, 12, 15 wt.% reduced E and σ_u monotonically. Epoxy filled with 15 wt.% of rubber showed E = 2.18 ± 0.04 GPa and σ_u = 32.2 ± 0.3 MPa [20].

To avoid the deterioration of the tensile properties while improving the toughness, toughening with hard particles was suggested. Fracture toughness of unfilled epoxy was improved after filling with silica particles. Filling of epoxy with 2, 4, 6, 8, 10, 12, 20 wt.% of silica increased the K_{IC} and G_{IC} of nanocomposites monotonically. Epoxy filled with 20 wt.% of silica showed K_{IC} = 2.11 ± 0.01 MPa $m^{1/2}$ and G_{IC} = 1.12 ± 0.05 kJ m^{-2}. Unlike rubber particles, epoxy filled with 20 wt.% of silica showed E = 3.48 ± 0.14 GPa

and σ_u = 54.2 ± 4.3 MPa. Both E and σ_u was improved compared to those of pristine epoxy [20]

1.1.3 Structure of nanocomposites

Two key factors limit taking the full advantage of the additives. One major factor is the homogeneity of the dispersion of particles in the matrix. Non-homogeneous dispersion leads the nanoparticles to agglomerate in the matrix. Formed aggregates create stress concentration points which are detrimental to the mechanical properties of nanocomposites. For instance, CNT is a type of particle with exceptional mechanical properties [21]–[23]. They can be produced as single-wall CNTs (SWCNT) and multi-wall CNTs (MWCNT). Tensile Young's modulus of SWCNTs were measured around 1 TPa [24]. Tensile strength of CNTs were found to be 10-100 times higher than that of the strongest steel. They show these enhanced properties only in a fraction of weight compared to common fillers [25], [26].

Addition of CNTs improved the mechanical properties of epoxy resins significantly [27]. CNTs were added to epoxy resin in 1 wt.%. Specimens for DMA were prepared in standard geometry. It was found that even 1 wt.% of CNTs increased the storage modulus of resin from 1.90 GPa to 2.12 GPa at -60°C, from 1.65 GPa to 1.90 GPa at -20°C, and from 1.43 GPa to 1.60 GPa at 20°C. It also increased the glass transition temperature of the resin from 63°C to 72°C when the temperature of the maximum damping factor $\tan\delta$ was considered. When the onset of the loss modulus was considered, 1 wt.% of CNTs increased the glass transition temperature 50°C to 53°C. The increase in the storage modulus was assumed as the indicator of an increase in the elastic modulus. The increase was associated with the outstanding mechanical properties of CNTs. Increase in the glass transition temperature was associated with the improved interface between the CNTs and the epoxy resin [27].

CNTs improved the mechanical properties of PS. Only 1 wt.% of CNT improved the elastic modulus of the PS films by 36%-42% and its ultimate strength by ~25%. Addition of 1 wt.% CNT increased the elastic modulus of PS from 1190 ± 130 MPa to 1620 ± 130 MPa. The same amount of CNT increased the ultimate strength of PS from 12.8 ± 1 MPa to 16 ± 0.2 MPa. Increasing the amount of CNT improved the mechanical properties even more. Addition of 2 wt.% CNT increased the elastic modulus of PS- nanocomposites to 1690 ± 130 MPa and the ultimate strength to 16 ± 2 MPa. Fractographic studies of the failed samples showed that cracks are initiated in the areas that CNTs are less crowded.

Crack front moves toward the areas CNTs are more. CNTs resist to crack propagation by peeling, pull-out, and bridging the crack faces [28].

Second major factor is the good interfacial bounding between the particle and the matrix. Strong interfacial bounding causes an effective load transfer from the matrix to the particles. The interface between CNTs and the epoxy resin was modified by adding a non-ionic surfactant to the mixture of CNTs and resins [27]. Nanocomposite samples were tested in DMA. Addition of MCFs along with surfactant (polyoxyethylene 8 lauryl) caused improved the storage modulus of nanocomposites when compared to those CNT-epoxy composites without surfactants. Interface improvement caused the storage modulus of nanocomposites to increase from 2.12 GPa to 2.54 GPa at -60°C. The storage modulus was increased from 1.90 GPa to 2.18 GPa at -20°C. Storage modulus improved from 1.60 GPa to 1.80 GPa at 20°C. Glass transition temperature increased from 72°C to 88°C when the temperature of the peak damping ($\tan \delta$) was considered. Glass transition temperature increased from 53°C to 64°C when the onset of the loss modulus was considered. The improvement in the storage modulus and the increase in the glass transition temperature was associated with the presence of the surfactant. It was believed that the surfactant created a steric repulsive force around the CNTs which overcame the van der Waals attractive forces between the carbon surfaces. Separation of CNTs caused a better dispersion in the resin [27].

1.1.4 Composite nanofibers

The common strategy in electrospinning of multiphase nanofibers is to produce composite nanofibers in a single step and directly from a colloid of particles along with a single polymer. Numerous composite nanofiber examples produced using this strategy were reported in the literature [8], [29]–[31]. Along with the typical electrospinning parameters, the size of the particles is a decisive factor for the successful process optimization and resultant morphology or structure. Table 1 summarizes the particle types and particle sizes used in the literature to produce composite nanofibers for different applications. Figure 1 presents an overview on the types of particles and their size ranging from 4 nm to 30 μm. When the particles have a non-spherical shape, the largest dimension was considered. For example, carbon nanotubes (CNT) had a diameter of ca. 20 nm and the length between 10-30 μm. For these CNTs, the length of the tubes was noted, not the diameter. Most of the particles are in the 10 to 500 nm.

Table 1: Particle type and particle size used in the literature to produce composite nanofibers

Particle name	**Size [nm]**	**Citation**
GO NPL	2000	Kim et al [32]
TiO_2@IP	250	Ding et al [33]
Ag NP	100	Yang et al [34]
TiO_2 NR	5000	Deniz et al [35]
Fe_3O_4 NP	13	Zhang et al [36]
$CoFe_2O_4$ NP	5	Chen et al [37], [38]
Fe_3O_4 NP	25	Chiscan et al [38]
SnO_2	10	Kong et al [39]
$Sn(CH_3COO)_2$ NP	390	Kong et al [40]
$SnCl_2 \cdot 2H_2O$	284	Kong et al [40]
$SnSO_4$	340	Kong et al [40]
SnS	327	Kong et al [40]
TiO_2	100	Cho et al [41]
TiO_3	250	Cho et al [41]
TiO_4	500	Cho et al [41]
rGO NSH	300	Guo et al [42]
ZnO	48	Lee et al [43]
TiO_2	21	Lee et al [44]
$FeCl_3 \cdot 6H_2O$	30	Fan et al [45]
$FeCl_2 \cdot 4H_2O$	30	Fan et al [45]
Au NR	78	Zhang et al [46]
Ag NP	12	Maity et al [47]
Au NP	29	Maity et al [47]
Au NP	80	Maity et al [47]
Au NP	100	Maity et al [47]
Au NP	15	Chang et al [48]
Au NP	4	Kim et al [49]
Ag NP	26	He et al [50]
Ag NP	5	Behler [51]
SiO_2 NP	50	Ji et al [52]
SiO_2@PS$	500	Ding et al [53]
SiO_2 NP	143	Jin et al [54]
SiO_2 NP	20	Hsu et al [55]
SiO_2 NP	23	Ding et al [56]
TiO_2 NP	20	Choi et al [57]
Fe_3O_4 NP	20	Huang et al [58]
PS NS	90	Friedemann et al [59]

Particle name	Size [nm]	Citation
SiO_2 NP	25	Hou et al [60]
CdTe NP	5	Cho et al [61]
Au Aerogel	7.5	Piperno et al [62]
Ag Aerogel	27	Piperno et al [62]
SiO_2 NP	100	Lim et al [63]
SiO_2 NP	300	Lim et al [63]
SiO_2 NP	450	Lim et al [63]
SiO_2 NP	700	Lim et al [63]
SiO_2 NP	1000	Lim et al [63]
PS NP	130	Stoiljkovic et al [64]
PMMA NP	300	Lee et al [65]
PU	80	Buruaga et al [66]
PLGA	151	Beck-Broichsitter et al [67]
PVA/EGF-AF488 NP	200	Dong et al [68]
PVA/BSA-TR NP	200	Dong et al [68]
PLGA	375	Yoshimatsu et al [69]
Au NR	49	Roskov et al [70]
Au NR	101	Wang et al [71]
Ag NW	35	Zhang et al ,[72]
Cellulose NWS	220	Lee et al [73]
Halloysite NT	445	Qi et al [74]
SWCNT	1500	Matrenichev et al [75]
SWCNT	30000	Obradović et al [76]
MWCNT	1000	Bazbouz et al [77]
MWCNT	15000	Gong et al [78]
MWCNT	10000	Wang et al [79]
MWCNT	30000	Merati et al [80]
MWCNT	20	Ahmad et al [81]

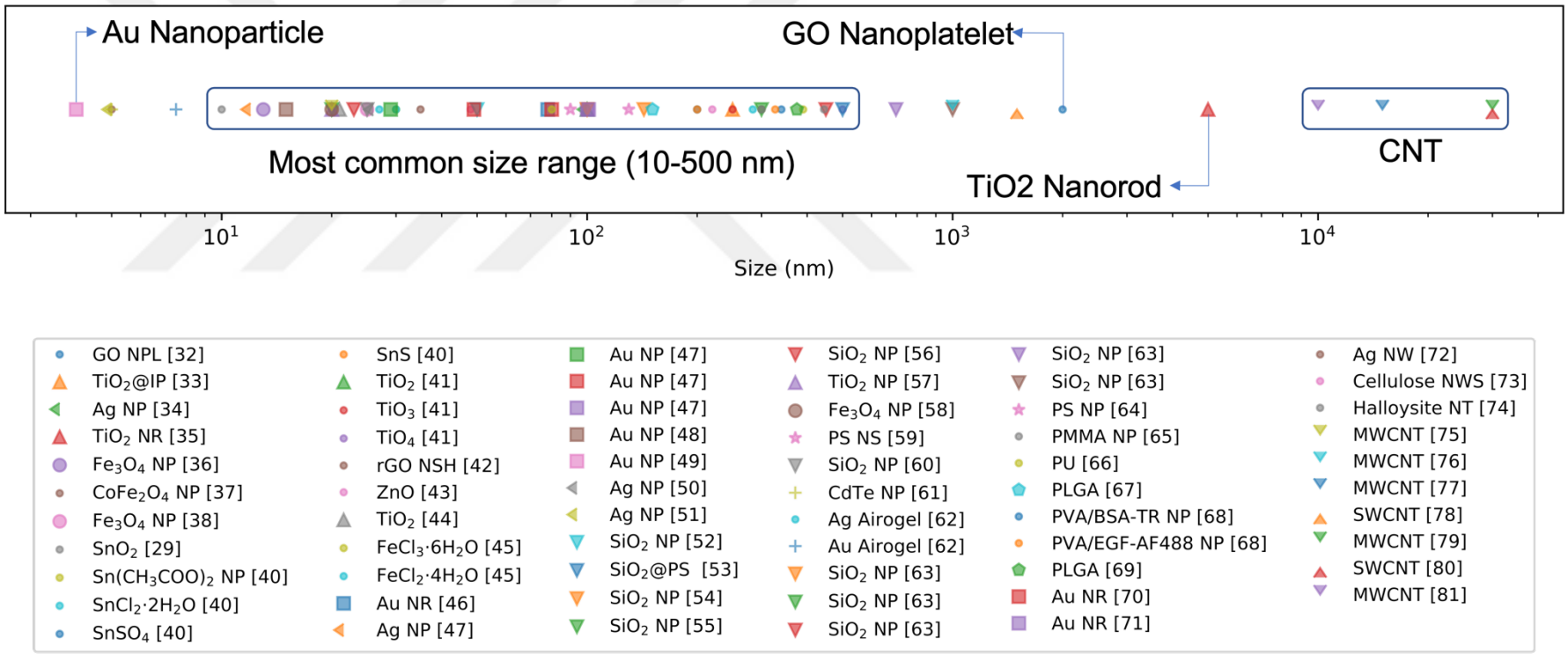


Figure 1: particle type and particle size used in the literature to produce composite nanofibers

1.1.5 Composite nanofibers in nanocomposites

Composite nanofibers were used to improve the mechanical properties of nanocomposites. Nanofibers of P(St-*co*-GMA) were impregnated by MWCNTs [82]. Composite nanofibers were produced using electrospinning technique of a slurries. The slurries were prepared from dissolving of 30 wt.% P(St-*co*-GMA) in DMF with 1, 1.5, and 2 wt.% of CNTs. Nanofibers were homogeneous and their diameters were between 630 nm and 460 nm. Composite nanofibers were embedded in epoxy resin as reinforcement. DMA were used to characterize the mechanical response of the nanocomposites. Addition of a single layer of composite nanofibers increased the storage modulus of nanocomposites. By addition of 1, 1.5, and 2 wt.% of CNTs, the room temperature storage modulus of the nanocomposites increased to 32, 46, 39%, respectively. 20% at 30°C. By addition of 1, 1.5, and 2 wt.% of CNTs, the storage modulus of nanocomposites at 150°C increased by 27, 29, 37%, respectively. Same nanocomposites were tested in flexural test configuration. Addition of 1, 1.5, and 2 wt.% of CNTs in nanofibers increased the flexural modulus by 22, 23, and 25%, respectively. Addition of 1, 1.5, and 2 wt.% of CNTs in nanofibers increased the flexural strength by 15, 16, and 18%, respectively. The enhancement was attributed to the combined effect of CNTs and nanofibers with epoxide rings which created crosslinks between the nanofibers and the epoxide rings of the resin [82].

1.1.6 Composite nanofiber interlayers

Composite nanofibers of P(St-*co*-GMA) with embedded CNTs were used as toughening interlayers for epoxy-matrix carbon fiber reinforced composites [10]. Nanofibers of P(St-*co*-GMA) copolymer were produced by electrospinning from solutions and slurries. Polymer was dissolved in DMF by 30 wt.%, and CNTs were added in 1 wt.%. Electrospun nanofibers were directly deposited on the prepreg layers [10].

Flexural strength and stiffness of (0/0/0) composites increased by addition of the interlayers. Interlayers of P(St-*co*-GMA) increased the flexural strength of composites from 875 ± 16 MPa to 965 ± 17 MPa. Interlayers of composite nanofibers from P(St-*co*-GMA) with 1 wt.% of CNTs increased the flexural strength of the composites to 1002 ± 14 MPa. Similarly, Interlayers of P(St-*co*-GMA) increased the flexural modulus of composites from 45.7 ± 0.8 GPa to 53.5 ± 0.9 GPa. Interlayers of composite nanofibers from P(St-*co*-GMA) with 1 wt.% of CNTs increased the flexural modulus of the composites even more to 57.3 ± 0.4 GPa [10]. Post-failure fractographic analyses were

performed on the cross section of composites. Two distinct failure mechanisms were found active namely. Transverse matrix cracking and delamination. Presence of both mechanisms were attributed to the inability of flexural test in generating a pure shear stress [10].

Flexural strength and stiffness of (90/0/90) composites increased by addition of the interlayers as well. Interlayers of P(St-*co*-GMA) increased the flexural strength of composites from 243 ± 6 MPa to 282 ± 9 MPa. Interlayers of composite nanofibers from P(St-*co*-GMA) with 1 wt.% of CNTs increased the flexural strength of the composites to 296 ± 6 MPa. Similarly, Interlayers of P(St-*co*-GMA) increased the flexural modulus of composites from 4.8 ± 0.2 GPa to 6 ± 0.1 GPa. Interlayers of composite nanofibers from P(St-*co*-GMA) with 1 wt.% of CNTs increased the flexural modulus of the composites even more to 6.4 ± 0.1 GPa [10]. Post-failure fractographic analyses were performed on the cross section of composites. Fracture mechanism was dominated by 90° plies at outer surface. Interlaminar stresses at 90/0 interface arose under bending load because of the stiffness mismatch between to laminae [10].

Interleaved campsites were tested in end-notched flexural test configuration. Composites with (0/0/0/0) layup were tested with and without interlayers at their midplane. Presence of pristine polymer nanofiber interlayers improved the Mode-II energy release rate (G_{IIc}) of composites from 0.95 ± 0.03 kJ m^{-2} to 1.47 ± 0.04 kJ m^{-2}. Composites with interlayers of composite nanofibers with CNTs increased G_{IIc} even more to 1.60 ± 0.10 kJ m^{-2} [10]. Post-failure fractographic analyses were showed common hackle patterns in non-toughened composites. The hackles were typical of the micro-crack coalescence along the crack pathway. The hackles were more complex or enlarged in the case of composites with interlayers [10].

Composites were tested in Charpy-impact test configurations. Impact energy absorbance increased by up to 20%. Composites with (0/0/0/0) geometry with and without interlayers were tested. Presence of pristine polymer interlayers increased the absorbed energy from 1.72 ± 0.05 kJ to 1.86 ± 0.1 kJ. Composites with composite nanofiber interlayers with embedded CNTs increased the absorbed energy even more to 2.13 ± 0.20 kJ [10].

Composites were tested in transverse tensile test configuration. The transverse tensile strength was increased by 27%. Presence of pristine polymer interlayers increased the ultimate strength of composites from 26.5 ± 0.7 MPa to 31.2 ± 0.6 MPa. Composites interleaved with composite nanofibers with embedded CNTs increased the ultimate

strength even more to 33.6 ± 0.7 MPa. Post-failure fractographic analyses showed a difference damage marks. In composites with no interlayer the damage marks came from the resin fracture in the plies and between plies. In composites with nanofiber interlayers, the reins morphology between the plies and inside the plies transformed [10].

1.1.7 In situ crosslinking

Polymer nanofibers are susceptible to the heat of processing. Processing heats are usually higher than the T_g of most polymers. Polymer nanofibers lose their fibrous structure throughout the processing whether used in nanocomposites or as interlayer for laminated composites. Heat-stimulated in situ crosslinking mechanism was designed to thermally stabilize the fibrous morphology of P(St-*co*-GMA) [83]. Solution of P(St-*co*-GMA) were prepared in DMF with several concentrations. Phthalic Anhydride (PA) was added to the solution as the main part of the cross-links between chains of P(St-*co*-GMA). PA molecules was supposed to link the open epoxide rings of GMA sites on P(St-*co*-GMA). Tributylamine (TBA) was added to the solution as the initiator and the minor part of the cross-links. TBA was supposed to be activated around 90°C (much below than the T_g of PS at 100°C) and link the epoxide rings to PA. Electrospinning nanofibers of P(St-*co*-GMA)/PA-TBA was produced with different molar ratios (R) of TBA to PA namely 1, 2, 5, and 10. Optimization of the solution and electrospinning setup revealed that 30 wt.% concentration of P(St-*co*-GMA) with PA-TBA of $R = 5$ produced the most homogenous nanofibers [83]. Applying this strategy, increased the T_g of the nanofibers from 98°C to 128°C. SEM analysis showed that the nanofiber morphology remained stable at 150°C [83].

Mechanical performance of nanocomposites was improved by electrospinning nanofibers of P(St-*co*-GMA)/PA-TBA [84]. Matrix material for nanocomposites was epoxy resin films. Stacks of epoxy/epoxy/nanofiber/epoxy/epoxy was prepared and heated up to 90°C to activate the in-situ cross-linking mechanism. After a long isothermal at this temperature, the stack was taken to the cure temperature of epoxy. Specimens with 200 mm × 15 mm geometry were tested in uniaxial tensile test configuration. Presence of nanofibers in the structure increased E from 3381 ± 187 MPa to 3675 ± 251 MPa. In addition, they increased σ_u of epoxy from 24.8 ± 3.2 MPa to 32. 1 ± 6.5 MPa. Post-failure fractographic analysis of cross-section revealed ridges and river lines in the fracture surface of unmodified epoxy. Fracture surface of nanocomposites showed several marks

belonging to the resistance of nanofibers to crack propagation. De-bounding and fiber fracture were the most dominant micro mechanisms that nanofibers showed against the fracture [84].

Nanofiber interlayers of P(St-*co*-GMA)/PA-TBA enhanced the flexural properties of CFRC [84]. Nanofiber interlayers produced using direct depositing of nanofibers on UD carbon prepregs. Standard ENF test samples were prepared by 48 layers of interleaved plies and about 50 mm of pre-crack at the midplane. Test results showed that nanofiber interleaves increased G_{IIc} of CFRC from 2.5 ± 0.6 kJ m^{-1} to 4.8 ± 0.8 kJ m^{-1} [84]. Post-failure fractographic analysis of the delaminated surfaces reconfirmed the transition of failure marks toward a tough failure. Fracture surface of non-interleaved CFRC showed typical hackles in the surface which are characteristic marks of Mode-II failure epoxy. Fracture surfaces of interleaved CFRC showed two main formations. Mode-II crack propagation happened at the interface of interlayer/prepreg. Large hackles within intact resin blocks were left behind, showing marks of contact nanofibers, de-bonded nanofibers, and fractured nanofibers. Mode-II crack propagation happened through the interlayer region. Carbon fibers were not visible and large hackles remained. Sophisticated fracture marks were found in the areas that interlayers were present, suggesting a stronger resistance against the crack propagation [84].

1.1.8 Self-same nanocomposites

Hybrid nanofiber structures from two different types of P(St-*co*-GMA) were prepared using dual electrospinning [83]. One nanofiber was produced from a solution of pristine P(St-*co*-GMA) that could lose its fibrous morphology during the processing. Second nanofiber was produced from a P(St-*co*-GMA) with the designed heat stimuli in situ crosslinking mechanism. The former could retain its nanofiber morphology even at elevated temperature beyond the T_g of the polymer. Hybrid nanofibrous structure from these nanofibers called “self-same”. SEM analysis showed that upon heating of the selfsame structure the soften-able part lost its morphology and formed a film around the cross-linkable fiber [83]. This was believed to offer a mechanism for engineering the interface of nanofibers. Tailorable morphology and interface with the surrounding matrix were thought to come in handy when these structures are used as the main reinforcement in nanocomposites or as the toughening interlayers for laminated composites.

1.2 Problem definition

There is an extensive literature in the production of electrospinning nanofibrous interlayers for the interlaminar toughening of laminated composites. Also, several types of composite nanofibers have been produced and employed toward this purpose. However, studies are very limited on micromorphology of nanofiber interlayers. The studies are even sparser in the case of the structure with multi-phase and/or multi-scale compositions. Application of hybrid nanofiber interlayers and their impact on the mechanical performance of composites has not been investigated yet.

1.3 Purpose of the study

Present dissertation investigates thoroughly the interaction of selected multiphase and multiscale composite nanofibers. It focuses on the synthesis and characterization of composite nanofibers especially the micromorphology. New materials, manufacture, and characterization methods are examined. The dissertation hypothesizes that the mechanical performance of the laminated composites can be improved by using multiscale multiphase composite nanofibers as toughening interlayers. Therefore, it introduces designs different types of interlayers for this purpose. In line with this aim, the dissertation suggests new materials and characterization methods. This need arose from the lack of proper method for characterization of polymorphic phases.

1.4 Thesis structure

In this dissertation, fiber-reinforced composites were produced with epoxy or phenolic matrices and fibers of aramid and carbon. Carbon fibers reinforcements were either unidirectional (UD) or plain weave (PW) fabrics. To improve the mechanical properties of these composites, interlayers of nanofibers were added to the structures. Production of nanofiber were performed using electrospinning. Particles of MCFs and zirconia were added to the nanofibers to benefit multiphase structures. Challenges were overcome in the production of nanofibers, characterization of the properties of the interlayers, and characterization of mechanical properties of the laminated composites. In the remainder of Chapter 1 shows the structure of following chapters.

Chapter 2 establishes the concept of multiscale enhancement of composites. It includes the production of aramid fabric reinforced composites with epoxy and phenolic matrices. The composite structure was modified by nanofibrous interlayers of a commercially available polyacrylonitrile (PAN) and a lab-synthesized copolymer of PAN and glycidyl

methacrylate (GMA). It would lead to an enhanced mechanical performance both in brittle epoxy-matrix composites and phenolic-matrix composites.

Chapter 2 and Chapter 3 introduce a new type multiphase reinforcement for composites, which contains MCFs as the particulate. These particles were chosen because of their extremely large size when compared to that of the electrospinning nanofibers. A new polymer was synthesized based on PS copolymerized with GMA. The chapter shows that the electrospinning of nanofibers with entailed enormous-sized particles is feasible.

Chapter 4 elaborates on the morphology of nanofiber interlayers obtained in Chapter 3. The local morphology of polymer interlayers was altered using dual electrospinning setup. Two grades of the same polymer were used, one soften-able and one crosslink-able. Particles were added to the precursor of one of these polymer grades. The morphology around the particles were engineered by changing the ratio of polymer grades. Tailorable interface was achieved in multi-phase polymeric interlayers, facilitating the interface between the interlayers and the matrix.

Chapter 5 examines the possibility of a adding multifunctional particles to the nanofibers of interlayers. This chapter introduces nanofiber interlayers of the same polymer studied in Chapter 4 and Chapter 3. However, as a multifunctional interlayer it adapts zirconia. This chapter contains the laying up of an optimized electrospinning setup following the RSM. Morphology of the fibrous interlayers were examined in terms of homogenous fiber diameter and composition of the interlayer. The resin/fiber compatibility was also analyzed.

Chapter 6 discusses the effect of interlayers in the drilling of carbon fabric-reinforced composite. Interlayers with two different zirconia phases were prepared. One of the phases were capable of phase transformation and the other was not. It was hypothesized that the presence of the phase-transforming particle in the area around the drilled region would improve the quality of the hole as they would absorbs some of the energy of the drilling process.

Chapter 7 collects the concluding remarks of the whole dissertation and suggests several possible future research opportunities that might be promising following this dissertation.

Chapter 8 starts the analysis of the multifunctional zirconia particles. The multifunctionally of these particles comes from their phase transformation response when underwent stress. The chapter introduces a new characterization method for analysis of the mechanism which lead to the multifunctionality in zirconia particles. It also lays the

foundation for the image analysis methodology for the quantification of the results. Chapter 9 develops the theory behind the characterization method. It treats the results in accordance with the available theories of electron-matter interaction. Also, it shows and analyzes the various conditions to discover the effect of the microscope geometry on the analysis.

Figure 2 shows the map of the research filed which this dissertation falls in. Some multi-phase composite nanofibers were already investigated in the literature. They have been cited in this Figure 2. Some new designs and nanofibers are suggested in this dissertation. Relevant cross-references were given in Figure 2 to the corresponding chapters. Highlights of each chapter in the dissertation were given in Table 2. Along with demonstrating the construction of the content, the table mentions the most important achievements of the following chapters.

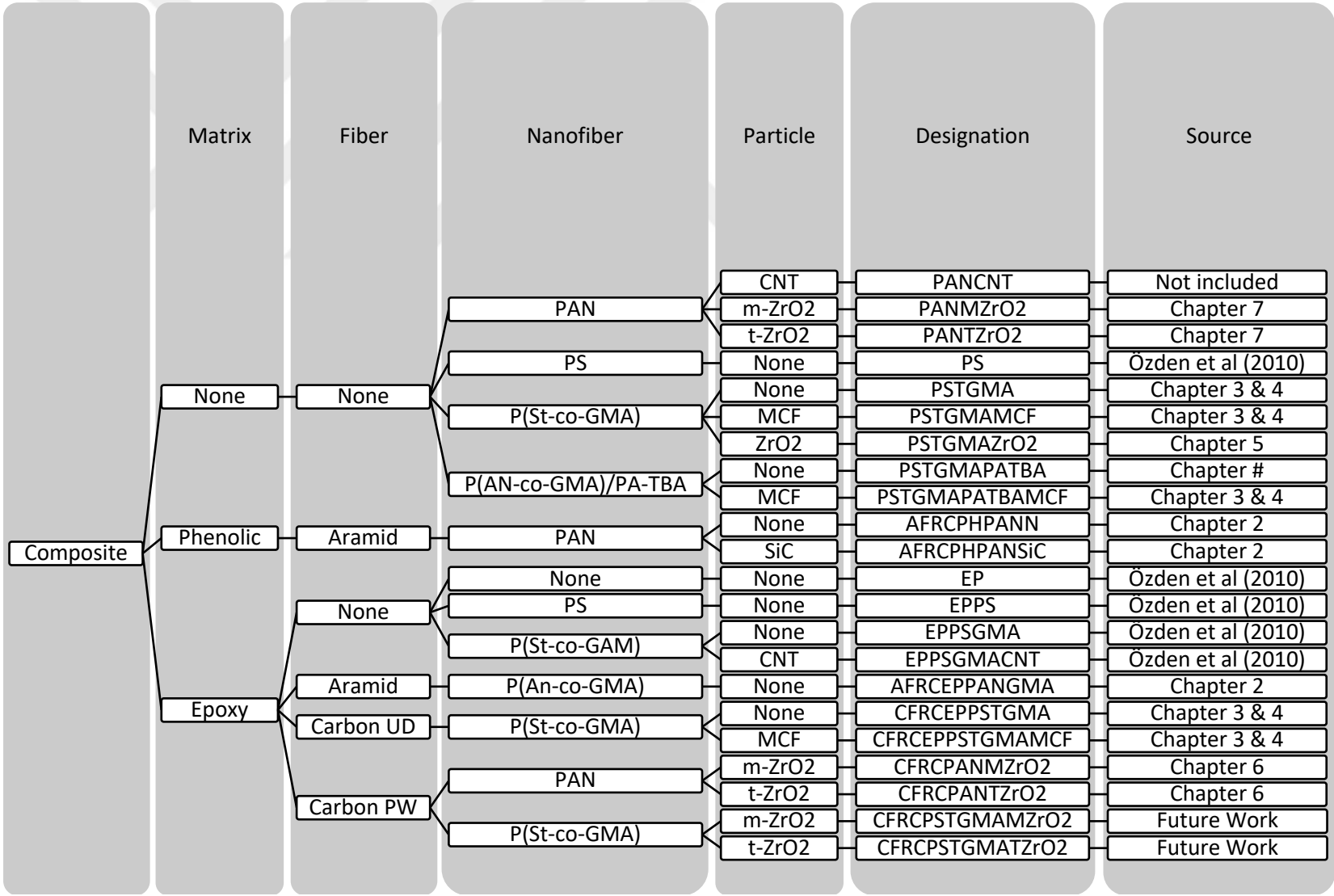


Figure 2: map of research field and structures designed in this dissertation

Table 2: construction of various ingredients of the sample classes examined in the dissertation

Section	Motivation	Nanofiber polymer	Particle	Matrix polymer	Reinforcing Fiber	Achievement
Chapter 2	Interlaminar toughening	P(An-*co*-GMA) or PAN	None	Epoxy or Phenolic	Aramid PW	Successfully synthesized thermally stable copolymer based on PAN Processed laminated composites with multi-phase multi-scale interlayers Characterized the tensile properties of laminated composites Improved the tensile stiffness and strain at break of composites
Chapter 3	Interlaminar toughening	P(St-*co*-GMA)	MCF	Epoxy	Carbon UD	Synthesized electrospinning hybrid nanofibers with self-same morphology Synthesized electrospinning with large particles Improved tensile strength of composites
Chapter 4	Interlaminar toughening	P(St-*co*-GMA)	MCF	Epoxy	Carbon UD	Synthesized ultra-hybrid multiphase interlayers in a single step Tailored the local morphology of polymer interlayers around particles using dual electrospinning
Chapter 5	Optimization of interlayer composition	P(St-*co*-GMA)	ZrO2	N/A	N/A	Synthesized homogenous composite nanofiber Optimized the electrospinning setup for maximum particle loading Characterized interface of nanofibers composites with liquid epoxy
Chapter 6	Interlaminar toughening	PAN	c-ZrO2 or t-ZrO2	Epoxy	Carbon PW	Synthesized electrospinning composite nanofibers Processed and machined laminated composites Analyzed quality of drilled holes and examined their fracture surfaces Characterized mechanical properties of laminated composites with different interlayers Analyzed fracture surfaces of failed composites

Section	Motivation	Nanofiber polymer	Particle	Matrix polymer	Reinforcing Fiber	Achievement
Chapter 8	characterization of phase transformation	N/A	t-ZrO2 and m-ZrO2	N/A	N/A	Demonstrated t-ZrO2 and m-ZrO2 in different brightness in SEM despite no BSE yield difference Quantified brightness differences in various EHT, adopting image analysis techniques
Chapter 9	characterization of phase transformation	N/A	t-ZrO2 and m-ZrO2	N/A	N/A	Developed theoretical background for the proposed characterization strategy in zirconia polymorphs Demonstrated the relation between the brightness difference and detection geometry

CHAPTER 2
MULTISCALE ENHANCEMENT TO ARAMID FABRIC-REINFORCED COMPOSITES: ELECTROSPUN P(AN-CO-GMA) NANOFIBROUS INTERLAYERS[*†]

Summary

This study reports the effect of electrospinning nanofiber interlayers of epoxy-compatible poly[acrylonitrile-*co*-(glycidyl methacrylate)], hereafter P(An-*co*-GMA), in the tensile properties of plain-weave aramid fabric-reinforced composites. Laminates of composites were interleaved by nanofiber mats of commercially available PAN and the copolymerized acrylonitrile with GMA; a molecule containing an epoxide. This ring was supposed to break by the heat of provided in the composite processing and make bonds to the same broken groups on epoxy matrix. Free-radical polymerization was run in solution environment and the success of the polymerization was verified with FT-IR. Nanofibers mats were collected electrospinning of both PAN and P(An-*co*-GMA) and analyzed morphologically using FE-SEM. Laminates were prepared using vacuum bag-assisted hot-press molding and cut into desired geometry using waterjet. The samples were tested according to the standard tensile tests. The results revealed that the interlayers of P(An-*co*-GMA) in epoxy-matrix increased the stiffness, E, by 34%, the strength, σ_u, by 8%, and reduced the ductility, ϵ_b, by 2.5% when compared to virgin laminates. PAN also improved the mechanical properties; increased E by 26%, reduced σ_u by 13%, and reduced the ϵ_b by 2.4%. Comparing the effect of these two interlayers, presence of

[*] Published: Arpatappeh, F. A., Ünsal, C., Bilge, K., Javanshour, F., Güngör, S., & Papila, M. (2022). Aramid fabric-reinforced composites by electrospun P(An-*co*-GMA) nanofibrous interlayers. *33rd Canadian Materials Science Conference*, 51.

[†] Published: Arpatappeh, F. A., Ünsal, C., Bilge, K., Javanshour, F., Güngör, S., & Papila, M. (2022). Multiscale enhancement to aramid fabric-reinforced composites: electrospun P(An-*co*-GMA) nanofibrous interlayers. *23rd Annual Conference YUKOMAT 2022*, 54.

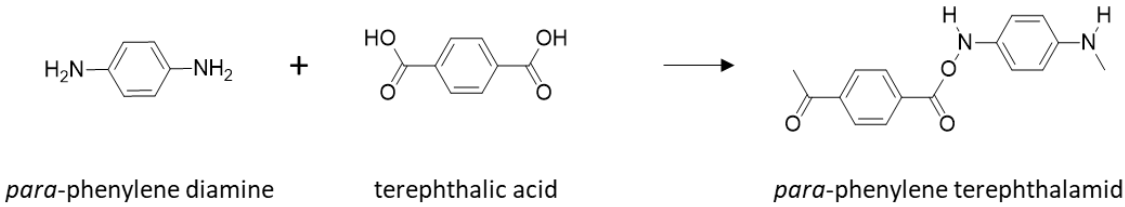
epoxide rings caused 8% excess increase in E, 5% extra decrease in σ_u, and almost no change in ϵ_b. When nanofibers interlayers of epoxy-compatible polymer laminated with phenolic matrix, the reinforcement mechanism changed from the improvement in elastic modulus to an improvement in σ_u by 18%. In conclusion, epoxy compatible polymers showed promising results in improving the mechanical properties of composites both with their morphological advantages, and covalent bonding they created with the epoxy matrix. The approach can be applied for tailoring the properties of aramid fiber-reinforced composites in automotive and aerospace structures.

2.1 Introduction

"Aramids are synthetic polymers in which more than 85% of links are directly attached to aromatic rings", defines U.S. Federal Trade Commission [85]. Aramids usually are synthesized from condensation polymerization of aromatic diamines and aromatic diacids or their halogenated derivatives[86], [87]. The aromatic rings give these polymers extraordinary mechanical and thermal properties. Aramids, therefore, are used when high mechanical and/or thermal performances are needed.

2.1.1 Aramid fibers

An important group of aramids are synthesized by copolymerization of para oriented phenylene diamine and terephthalamide - poly(*para*-phenylene diamine terephthalamide) abbreviated PPTA (Figure 3). Fibers of PPTA polymers are produced using dry-jet wet spinning method [88]. They consist of highly crystalline chains of benzene rings attached with amide joints [89], [90]. The chains are highly oriented almost along the fiber axis with covenant bonds. The chains are hold together with hydrogen bonds between the electron-dense oxygen atoms of amide links on one molecular chain and the electro-deficient hydrogen atoms of the amide links on the adjacent chains. This chemical structure along with the dry-jet wet spinning and subsequent heat treatments create fibers with enhanced physical and mechanical properties. Specific gravity of polyamide fibers is 1.4 g cm^{-3} [91]. PPTA is commercially traded under Technora®, Twaron®, and Kevlar®.



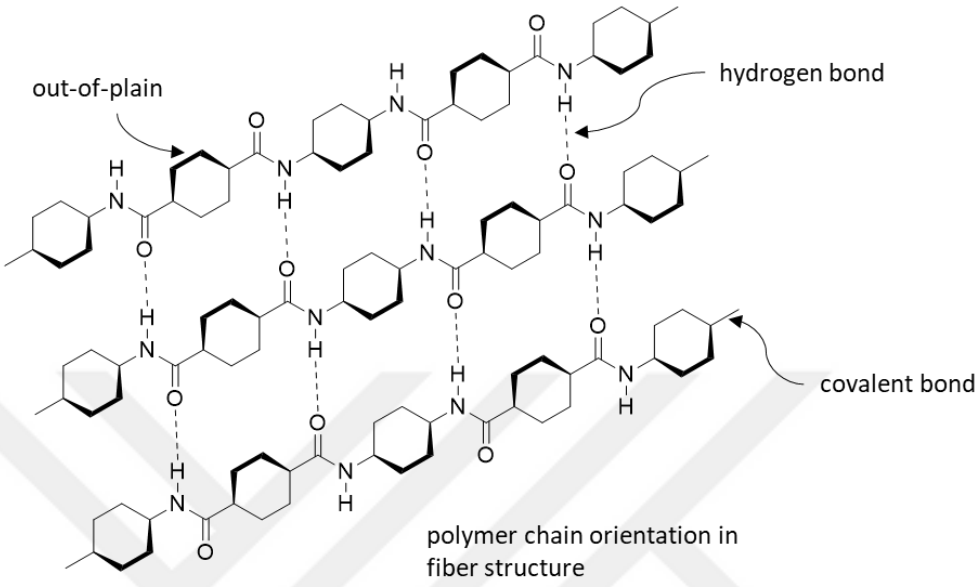


Figure 3: structure and polymerization of poly(*para*-phenylene diamine terephthalamide).

Kevlar-49 is a certain type of PPTA fibers optimized for composites reinforcement. Fibers were studied for their tensile, creep, and tension-tension fatigue behavior [92]. Their elastic properties were measured as follow: elastic modulus, E, equal to 144 GPa, ultimate tensile strength, σ_u, equal to 3.06 GPa, and breaking strain, ϵ_b, equal to 2.3%. Kevlar-49 fibers were found to outperform other common reinforcement fibers at the time, including high-modulus carbon (E = 400 GPa, σ_u = 1.9 GPa, ϵ_b = 0.5%), high-strength carbon (E = 200 GPa, σ_u = 2.6 GPa, ϵ_b = 1%), and E-glass (E = 70 GPa, σ_u = 1.8 GPa, ϵ_b = 3%). Main failure mechanism in Kevlar was found to be fiber splitting which was attributed to the poor transverse strength of fibers depending only on the hydrogen bonds between adjacent polymer chains. Aramid fibers are applied in tire cords, ropes, and armor fabrics.

2.1.2 Aramid fiber-reinforced composites

Extremely attractive mechanical properties of aramid fibers candidates them as a desired reinforcement for composites. Kevlar fibers were used as the reinforcement of epoxy-matrix composites in the form of strands, rings, and filament-wound vessels [93]. The

composites were tested for UD tensile properties. Kevlar composites were evaluated to perform better than glass and carbon fibers in tensile although the shear performance remained questionable.

Aramid fiber-reinforced composites are recognized for their weak fiber-matrix interface and interlaminar properties [94]–[96]. This weakness arises because the aramid fiber surface is typically very smooth and chemically inert that does not intend to make bonds to the matrix. Strengthening of the interphase region is, therefore, the way in which these composites can be enhanced.

Interfacial shear strength and frictional shear strength of aramid fibers were enhanced by surface treatments [97]. Kevlar-49 fibers were either sized or boiled in water to create different surface properties in the interface region with several thermoplastic resins. Bare and surface-treated fibers were tested using single fiber pull-out test, and their interfacial surface strength as well as frictional shear strength were measured. Both measures were superior in the treated fibers in comparison to the bare fiber. Water-treatment increased both strengths by providing a rougher surface in compression to the untreated fibers. Sized fibers enhanced the strengths the most, providing an interface region of covalent bonds to the matrices.

Coating of aramid fibers was not able to make a significant improvement in the strength of the fiber/matrix interface with epoxy resin [98]. Kevlar fibers' surface energy was measured against various liquids. Fibers were coated with aromatic sulfonamide, aromatic polyamide, amidoamine, an azide complex, and an organic titanite to populate intermolecular hydrogen bonds, metal ion coordination, reactions with matrix, or dispersion (London) forces in the fiber/matrix interface. Silicon-coated fiber surface was selected as the reference. Interfacial shear strength of coated fiber/epoxy sample was measured using a single fiber pullout test. Composite samples of coated fibers were prepared in the form of tapes and the interlaminar shear strength of composites were measured using the short beam shear test. A formulation was established between the fiber surface energy and interfacial shear strength as well as the interlaminar shear strength. Even though surfaces of all sized fibers and the bare fiber were found to be stronger than that of silicon-coated one, none of the organic coatings improved the interfacial shear strength when compared to the bare Kevlar.

Fracture toughness of Kevlar-epoxy composites improved significantly with controlled interfacial bonding [99]. Kevlar fibers were intermittently coated with silicon vacuum

fluid and polyurethane varnish, to enhance the fiber/matrix interface. Laminated composite was prepared with UD fibers and tested for tensile properties. Fracture toughness specimen were prepared from notched laminates and tested in Charpy impact setup. Tensile properties of composites were found almost insensitive to the coatings whereas the fracture toughness was improved by 200 to 300%. The authors attributed the improvement to the increased fracture work and fiber pullout toughness.

Peel strength and apparent interlaminar shear strength of aramid fiber-reinforced composites were enhanced remarkedly with introduction of amine functional groups to the fiber surface [100]. The surface of Kevlar fibers was functionalized with two methods: 1) bromination followed by ammonolysis and 2) nitration followed by reduction. Tensile properties of fibers, peel strength of fibers with T-peel test, and interlaminar shear strength of laminates with short beam test method were measured. The authors attributed the improvement to the introduction of amino groups on fiber surface which can create covalent bonding and improve adhesion of aramid to epoxy composites.

Bonding mechanism of aramid fibers to epoxy matrix was analyzed for effective microstructural and macrostructural mechanisms which affect the composite properties [94]. Fiber-matrix interphase was found to significantly affect the mechanical and thermal properties of composites. Combination of aramid fiber chemical and physical properties as well as its morphology was found to be responsible for the relatively low aramid-epoxy adhesion. Mechanical interlocking, adsorption interaction, electrostatic attraction, and polymer interdiffusion to epoxy matrices were effective mechanism in the strength of interphase. Only weak secondary type interactions were found to act chemically in the aramid/epoxy adhesion. Aramid fibers were found to be formed in a skin-core morphology which led to weak cohesive boundary at the fiber-matrix interphase.

Mechanical stresses due to fiber-matrix thermal strains and Poisson's ratio mismatch, covalent chemical bonding, fiber-matrix wetting, and effects of physicochemical weak boundary layers were examined for high performance fibers [94]. Aramid and carbon fibers were investigated for their thermal stresses and interfacial shear strength of fibers were measured. Aramid fibers exhibited low interfacial shear strength than expected theoretical value. Authors attributed the poor interfacial adhesion to the fibrillar separation within the fiber surface.

Tensile properties of UD Kevlar/epoxy composites were studied with different volume fraction ranging between 0.26 and 0.73 [101]. Kevlar-49 fibers and epoxy matrix were

used to prepare composite samples using fiber winding and impregnation technique. Composite samples were tested in parallel to fiber direction in a tensile test setup to measure the tensile strength and observe the damage evolution. It was found that the tensile strength of composites deviate from that is predicted with Rule of Mixture due to geometrical deficiencies such as volumetric non-homogenous fiber spread, lack of matrix between fibers and fiber squeezing. Initial parts of loading led to fiber straightening in misaligned fibers which was accompanied by fiber/matrix debonding and matrix damaging. The authors attributed the premature failure to these matrix cracks which are generated in the initial stages of loading and evolve until cause a catastrophic failure in composites.

Plasma surface modification was used to enhance the fiber surface in aramid FRCs [102]. Kevlar-49 fibers were treated with gaseous discharge of ammonia/nitrogen and were impregnated in DGEBA epoxy to prepare composite samples. Four-point shear test, three-point bending, and double cantilever beam tests were conducted. Interlaminar shear strength, flexural modulus, and flexural strength as well as mode-I interlaminar fracture energy were measured. Electron microscopical fractography revealed clean whereas fibrillation and matrix fractures in composites with surfaced-treated fibers. The authors attributed the marked increase in the interlaminar shear and flexural strength to the reduced compressive fiber buckling which is the result of the introduction of amine groups to the surface of fibers.

Optimized plasma polymerization was used to improve the interfacial adhesion of aramid FRCs [103]. Kevlar fibers were treated first with argon plasma and then with allylamine plasma to create a polymerization of these groups on the fiber surface. Fiber tensile strength and single fiber pull-out test were conducted to measure the difference in tensile properties of fiber and the interlaminar shear strength of composite samples. It was found that the interfacial adhesion was improved by five folds after surface treatment. Increase in the treatment time was found to cause the increase in the improvement. Authors attributed this improvement to the allylamine groups introduced to the surface of the fibers.

Chemical treatment of aramid fiber with organic solvents improved the interfacial strength of aramid FRCs by 60% [104]. Kevlar fibers were treated acetic anhydride and then washed in three different solvents: 1) distilled water, 2) methanol for 3 minutes, and 3) methanol for 10 minutes. Bare and surface treated fibers were impregnated with epoxy

resin for a single fiber pullout test. The results showed that anhydride treatment followed by 3-minutes methanol caused the interfacial strength to rise from 39 MPa to 63 MPa. Authors attributed the improvement to the presence of an oxygen rich fibers surface because of anhydride treatment which led to a stronger interface between fiber and matrix. Coating of aramid fibers with matrix-compatible polymers enhanced the interfacial adhesion in aramid FRCs [105]. As-spun high-modulus Twaron fibers (HM), with standard finished (HMF), and with epoxy-based adhesion-activating finish (HMA) was prepared and embedded in epoxy resin. Pull-out test and stress-induced Raman band shift was conducted. Interfacial shear stress and interfacial shear strength were measured from pullout test and the profile of fiber stress was extracted form band shifts. It was found that HM fibers had an interfacial shears strength about 40 MPa and an interfacial friction stress about 10 MPa. HMA fibers were improved in interfacial shear strength to 38 MPa and in interfacial friction stress to 22 MPa. HMF showed 38 MPa of interfacial shear strength and a double-level frictional shear stress at 10 MPa and 25 MPa. Fractographic reveled that HM fibers failed due to deboned propagation along fiber/matrix interface, HMA fibers did not extract from the resin and failed due to deskinning of fibers. HMF fibers failed with a complex manner caused by separation of the fiber skin at fiber/finish interface. Authors attributed the improvement to the introduction of epoxy-compatible coating on fibers.

2.1.3 Electrospinning

Fibers are produced with diameters as small as a few micrometers and even in the range of nanometers [2], [3]. With decreasing the diameter of fibers, the number of inherent defects reduces, and the mechanical properties are enhanced [106]. With this small diameter, they acquire extreme surface-to-volume ratios which unleash another aspect of nanofibers: extraordinary activity [107], [108]. Nanofibers are collected to in the form of nonwoven mats. These mats are used in a variety of applications including filtration, wound healing, tissue engineering, skin healing, and reinforcing agent in composites [9].

2.1.4 Electrospinning nanofiber interlayer

Mechanical behavior of composites can be enhanced with the fillers of electrospun polymeric nanofibers: nanofibrous interlayers [109]–[111]. In contrast to microfibers, nanofibers can make more bonds to the resin matrices due to their high surface-to-volume ratio. They offer stronger interphases with resins, thus stronger composites.

Some reinforcements were performed using polymers which make chemical bonds to the matrix materials: matrix-compatible polymers. For instance, , epoxy resin was reinforced with nanofibrous interlayers of styrene (St) copolymerized with GMA [12]. The latter is an epoxide which its ring break down with the curing heat, and cross-links with similar sites on the epoxy matrix. The extra bonds, thus, enhances the reinforcement in the nanocomposites.

Some research expanded this concept further to fiber-reinforced composites. Nanofibrous interlayers of electrospun P(St-*co*-GMA) was used globally and locally to improve the epoxy-composites reinforced with UD and PW carbon fibers [13]. The ultimate tensile strength of UD laminates increased by 12% while the tensile strength of the woven fabric composites increased by 18%. Authors attributed the improvement to the presence of nanofiber interlayers effect which toughened the matrix and created a reinforced interphase region making bonds to the epoxy matrix.

Electrospun nanofibers of thermoplastic polymers improved the tensile strength of glass fiber-reinforced composites by approximately 30% and the interlaminar fracture toughness by 30-45%. Polyamide-6, polyamdide-69, and polycaprolactone nanofiber veils were interleaved in UD glass fiber-reinforced composites [112]. Laminates were prepared for central cut-ply and end-notch flexural tests. The authors attributed the improvement to the development of nanofiber bridging zones at interlaminar crossings.

To the open literature, multiscale reinforcement, however, have not been implemented in other advanced composites such as those reinforced with aramid fibers. This research presents an investigation of the aramid fabric-reinforced composites which are filled with the nanofibrous interlayers of an epoxy-compatible copolymer.

2.2 Experimental

2.2.1 Polymer synthesis

Poly[acrylonitrile-*co*-(glycidyl methacrylate)], P(An-*co*-GMA), was synthesized by the molar ratio of 90% acrylonitrile (An, Sigma-Aldrich) to 10% GMA (Sigma-Aldrich), both in the analytical grade. Without further purification, in a medium of DMF (Sigma-Aldrich, anhydrous 99.8%), a free radical polymerization initiated by 2.2'-Azobis(2-methyl-propoionitrile) between An and GMA. The process continued for 120 hours to yield higher than 90%. The final viscous solution, then, precipitated into a vortex of methanol (technical grade). The precipitated copolymer particles were washed for a few times in ethanol (technical grade) to remove the residual monomers and solvent. Further

removal continued by conditioning in a vacuum oven (168 hours, room temperature) which resulted in solid copolymer particles.

2.2.2 Polymer characterization

For the material in the solid state, ATR technique was adapted in FT-IR (ThermoFisher Scientific, Nicolet IS10) to examine the presence of the epoxy groups of GMA. The group's characteristic peak is assumed as the evidence of a successful polymerization.

2.2.3 Reference polymer

To test the effect of epoxy-compatibility, PAN (M_w = 150000 g/mol, Sigma-Aldrich) was also used as the reference. Both polymers, PAN, and P(An-*co*-GMA), were dissolved with different concentrations in DMF on a magnetic stirrer and the homogenous polymer solutions were obtained overnight.

2.2.4 Nanofiber synthesis

The solutions, immediately, were electrospun in different processing configurations. The fibers were collected sparsely on aluminum foils for morphological analysis. These samples were sputter-coated with an Au-Pd target (Cressington 108) under 0.2 mbar pressure and 40 mA for 40 s, and their structure were analyzed in a field-emission scanning electron microscope (FE-SEM, Zeiss, Leo Supra VP 35). The electron micrographs were inspected in an image processing software (ImageJ) and based on 50 diameter measurements per each micrograph, the smallest average fiber diameter was sought. The correlated optimum configuration was found to be 17 wt.% solution concentration, 4 mL/h feeding rate, 23 kV applied potential, and 21 cm tip-to-collector distance.

2.2.5 Laminate preparation

In the selected optimum configuration, 13 mL of copolymer solution was electrospun on one side of a 30×30 cm^2 plain-weave aramid fabric (aerial weight 750 GSM, Twaron®-750, Teijin Aramid B.V.) while the other side was covered by either an epoxy or a phenolic film. Three sheets of the Resin/Aramid/NF were manually laid up and a final protector resin film was placed on the top. Every layered structure was cured in a hot press after being covered by a vacuum bag. To cure, epoxy-matrix composites initially heated 2°C/min from the room temperature to 135°C, then stayed there for 60 minutes under 0.4 MPa, and finally conditioned to cool down to the room temperature. In the other hand, phenolic-matrix composites initially heated 2°C/min from the room temperature to

150°C, then stayed at this temperature for 120 minutes under 2 MPa pressure, and finally conditioned to cool down to the room temperature.

Using a water jet, five coupons were cut and tested according to ASTM 3039 in a universal tensile machine (Zwick/ Roell, Z100 Proline) operated with 100 kN loadcell and at an extension rate of 2 mm/min. To compare the mechanical performance of the composites against their building materials, the tensile test was conducted on the pristine epoxy and phenolic resins according to the same standard as well as on the aramid fabric according to ASTM 5035.

2.3 Results and discussion

Nanofibrous interlayers have been explored increasingly due to their significant potential as reinforcing and toughening agents for composites [111]. Epoxy matrix composites with the nanofibers of electrospun epoxy-compatible polymers have been of interest to us [12], [13]. The present study seeks the benefits of this approach when incorporated into the aramid fabric-reinforced composites.

2.3.1 Polymer synthesis

The characteristic peak of the epoxy group at 853 cm^{-1} (Figure 4) shows that GMA exists in the copolymer. In addition, polymer barely absorbs at 1626 cm^{-1} which belongs to the C=C groups, collectively suggesting appreciable conversion of monomers to polymers. The peaks at 2241 cm^{-1} and 1452 cm^{-1} belong to the stretch of -CN and the bending of -CH groups respectively, both coming from the acrylonitrile monomer. The peak at 1727 cm^{-1} comes from the stretch of C=O groups and the peak at 1125 cm^{-1} belongs to the stretch of the C-O groups, both from GMA part.

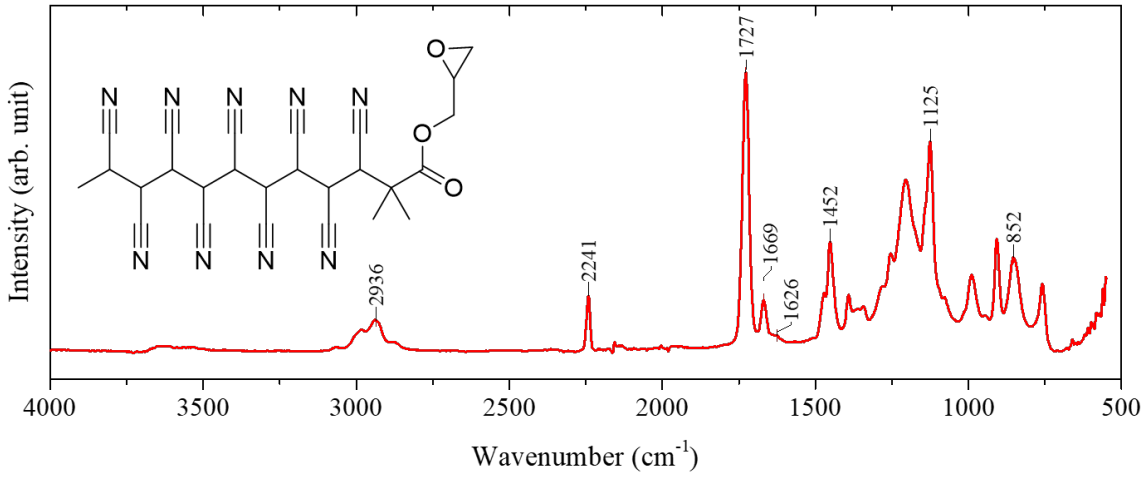


Figure 4: ATR FTIR spectrum for P(An-*co*-GMA).

2.3.2 Nanofiber morphology

Electrospun fibers of P(An-*co*-GMA) and PAN were morphologically analyzed by SEM (Figure 5). Fiber morphology was found to be mostly homogenous with very few beads. Average diameter of fibers was measured equal to 667±48 nm for PAN and 613±64 nm for P(An-*co*-GMA).

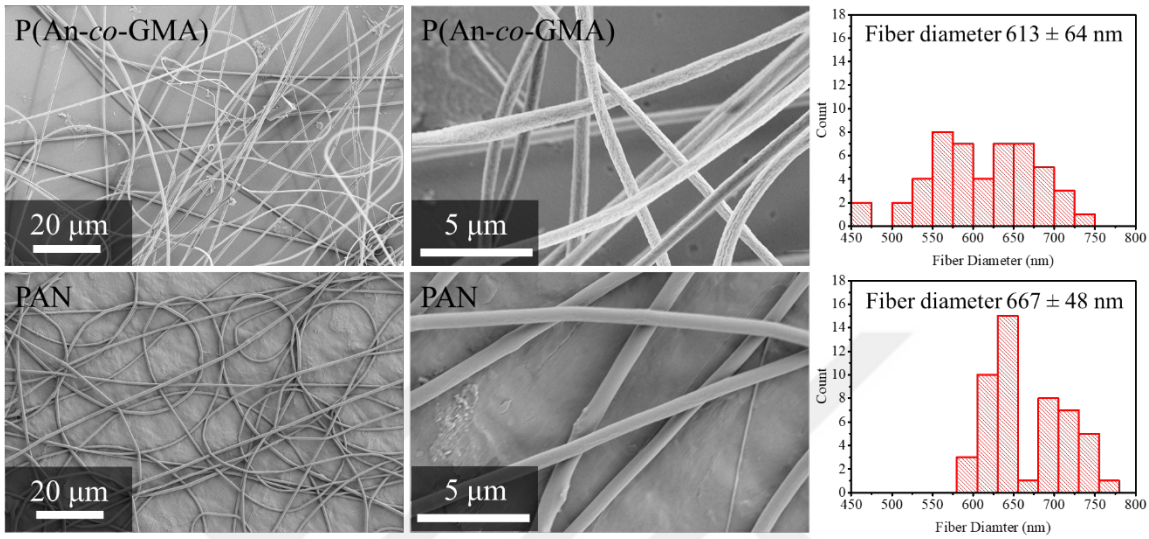


Figure 5: SEM micrographs and fiber diameter distribution of P(An-*co*-GMA) (upper row) and PAN (lower row).

As it is evident from the histograms, the commercial PAN polymer produced more homogenous fibers although thicker, probably because of the uniform polymer chain length which led to more stable and uniform rheological properties of the solution. Lab-synthesized P(An-*co*-GMA), however, produced finer fibers but with wider distribution in the fiber diameter. In the scope of this research, the possible effect of the difference in the fiber diameters of these polymers was assumed insignificant.

2.3.3 Tensile properties of epoxy-matrix composites

Nanofibrous interlayers of P(An-*co*-GMA) has improved the tensile properties of epoxy-matrix composites which were reinforced with aramid fabric (Table 1). They have enhanced because (1) they crosslinked to the matrix and (2) they made secondary bonds to the other system elements.

Table 3: Mechanical test results for reinforced epoxy composites.

Composition	Elastic Modulus (MPa)	Ultimate Tensile Stress (MPa)	Breakage strain (%)
Ep/Ar	97.5±4.4	359±23	4.08±0.12

Ep/Ar/PAN	122.6±3.4	407±11.9	3.55±0.10
Ep/Ar/P(An-*co*-GMA)	134.5±3.6	388±27	3.45±0.06

Averagely, P(An-*co*-GMA) has increased the elastic modulus of the composites by 34%. To distinguish the share of the crosslinking, aramid composites were produced with a similar polymer structure, but without GMA; that is, PAN. The elastic modulus for the PAN-reinforced composites were increased by 26% as well. The excess 8%, therefore, were concluded to be the effect of GMA.

P(An-*co*-GMA) has strengthened the composites by 8%. In this case, the epoxy compatibility and the secondary bonds played in different directions. While PAN has increased the strength 13%, the copolymer has alleviated the increase by 5%. Therefore, crosslinking has degraded the enhancing effect of the interlayers.

Both P(An-*co*-GMA) and PAN has decreased the ultimate strain of the composites. The decrease is more severe in the case of copolymer because it crosslinks to the matrix resulting in a more brittle composite.

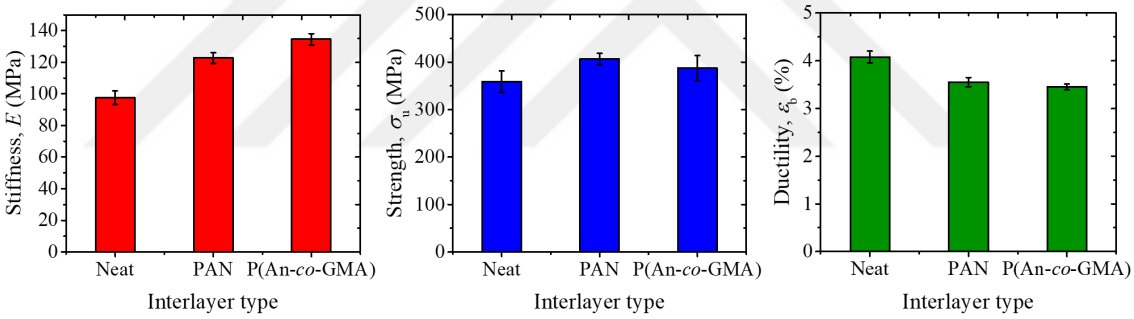


Figure 6: Mechanical performance of AFRC in tensile test.

The tensile behavior of the composites is controlled by the epoxy matrix until 2.5% of strain (Figure 7). When the specimen is elongated further, the matrix fails, and the aramid fabric dominates the composite behavior (linear elongation) until the final failure point.

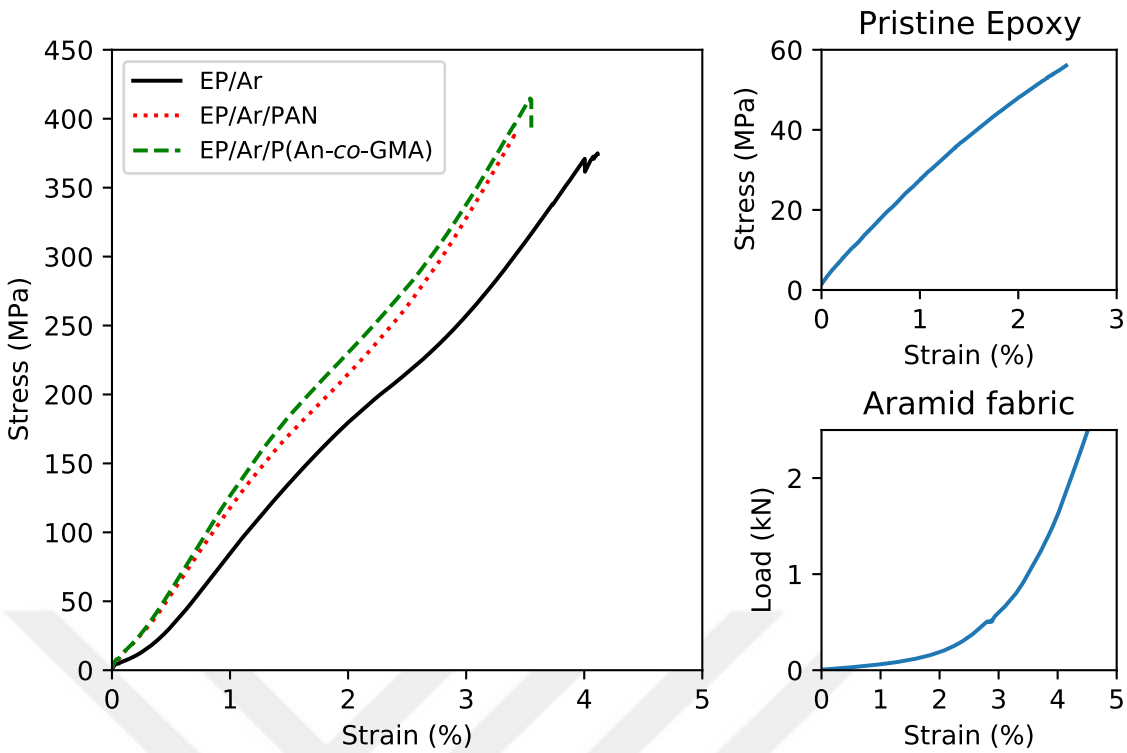


Figure 7: Epoxy composites reinforced with aramid or aramid/nanofibers.

2.3.4 Tensile properties of phenolic-matrix composites

To nullify the matrix-compatibility of P(An-*co*-GMA), its interlayers were implemented to aramid composites of phenolic matrix. The results show that the interlayer has a relatively less significant effect in the stiffness of the material. This fact suggests that the elastic modulus is more related to the crosslinks that the filler makes. On the other hand, the interlayer has still increased the strength of the composite by 18%. The strength, therefore, is mostly associated with the nature of the nanofibers.

Table 4: Mechanical test results for the reinforced phenolic-matrix composites.

Composition	Elastic Modulus (MPa)	Ultimate Tensile Stress (MPa)	Breakage strain (%)
Ph/Ar	66±8	453±13	4.28±0.18
Ph/Ar/ P(An-*co*-GMA)	69.1	537±15	4.54±0.08

The tensile behavior of the composite is not dominated by the resin in any noticeable range of extension. That is the aramid fabric which controls the behavior of the composite at all the way through the failure. It can be observed when the stress-strain curves of the composites are compared with the load-strain curve of the aramid fabric (Figure 7).

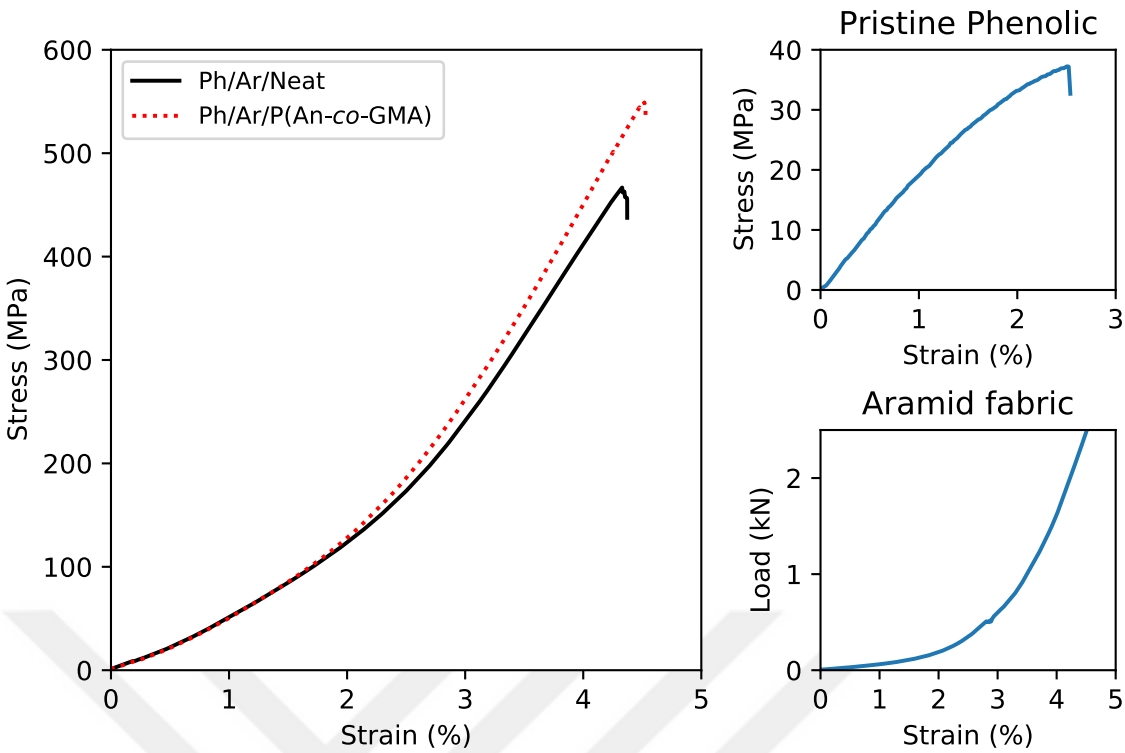


Figure 8: Phenolic composites reinforced with aramid or aramid/nanofibers.

The nanofibrous reinforcement has increased the toughness of the composite with the combination of increases in the strength and the ductility of the composite.

2.3.5 Comparison between the epoxy- and phenolic-matrix composites

The epoxy-matrix composites demonstrated a higher tensile modulus when compared to that of the phenolic-matrix composites because the epoxy resin is stiffer than phenolic. The strength of the epoxy-matrix composites was surpassed by the phenolic-matrix composites which were sort of surprising because the latter is renown by being a less strong resin when it compared to the first. When the behavior of the composites considered in the high strain values, the higher strength of the phenolic-matrix composite is due to its aramid-dominated behavior rather than the resin (Figure 9).

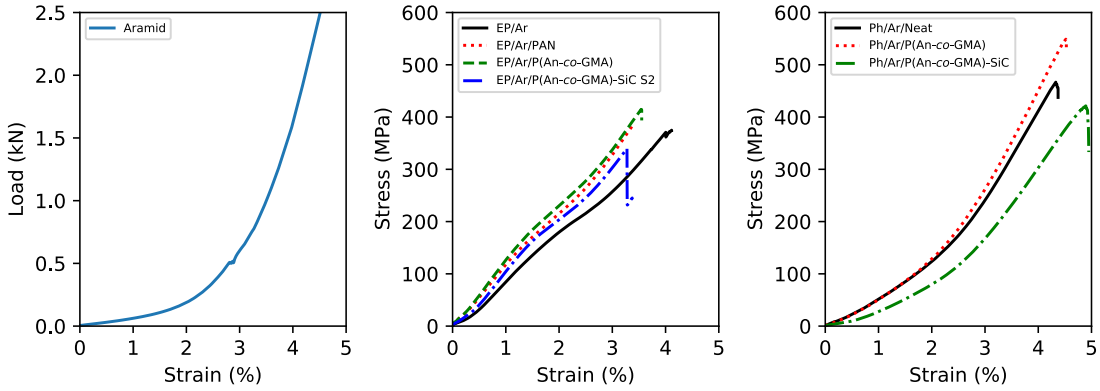


Figure 9: Uniaxial tensile test results for aramid fabric (left), epoxy-matrix composites (middle), and phenolic-matrix (right) composites.

2.4 Conclusion

Electrospun nanofibrous interlayers of P(An-*co*-GMA) suggests a significant potential to play as an additional candidate filler in the aramid-fabric reinforced composites. They enhance the mechanical properties of both epoxy- and phenolic-matrix composites. Because of this potential, they are proposed as an opportunity to modify the mechanical properties of advanced structural composites.

CHAPTER 3

MULTISCALE REINFORCING INTERLAYERS OF SELFSAME P(ST-*CO*-GMA) NANOFIBERS LOADED WITH MCF FOR POLYMER COMPOSITES AND NANOCOMPOSITES[‡]

Summary

Strong particles are hindered to represent their reinforcing potential in composites because they cannot create strong particle-matrix interfaces. This problem is stressed when the particles agglomerate before they are implemented to the matrix. Homogenous distribution of reinforcing particles is possible using a carrier medium of polymer nanofibers. However, the fibers lose their fibrous shape during the composite curing. Hence, they cannot contribute effectively to the mechanical strength of the composite. This condition is suppressed partially by implementing a selfsame strategy. In this research, two classes of P(St-*co*-GMA) nanofibers are combined to reinforce composites and nanocomposite. One class of fibrous reinforcement is produced with nanofibers of neat P(St-*co*-GMA) while the other contains crosslinking agent of PA. During heating, the neat copolymer melts and covers the particles to create a better interface to the matrix, while the other copolymer crosslinks and preserves its fibrous structure. The multiscale interlayer will contribute to the mechanical properties of the composite and nanocomposite both in the form of the compatible particle-matrix interface and in the form of a fibrous structure. So far, the copolymer has been synthesized and analyzed compositionally using FT-IR. The polymer was analyzed thermally using TG and DSC. The suitable thermal treatment strategy was designed accordingly. The polymer solutions and polymer-MCF suspensions were prepared and dually electrospun. The nanofibrous

[‡] Published: Arpatappeh, F. A., Papila, M., & Aydemir, B. E. (2019, January 7). Multiscale Reinforcing Interlayers of Self-same P(St-co-GMA) Nanofibers Loaded with MCF for Polymer Composites and Nanocomposites. *AIAA Scitech 2019 Forum*. https://doi.org/10.2514/6.2019-1762

structures were analyzed morphologically before and after heat treatment. Homogenous distribution of particles in the fibrous structures, melting of the neat copolymer, crosslinking of the polymer mix, and selfsame fibrous structure was determined. It is aimed to embed the reinforcing structure into epoxy composite and carbon-fiber epoxy composites to investigate their mechanical enhancement.

3.1 Introduction

Mechanically strong particulates are suppressed by agglomeration and poor particle/matrix interface area [109], [111], [113]. To strengthen this area, there are several strategies such as using the matrix-compatible polymers and thermal postprocessing of reinforcements [114].

The first technique can be adapted through the modification of common polymers with matrix-compatible groups. For example, if epoxy is aimed to be used as the matrix of a composite, those monomers can be used which contain breakable chemical groups such as an epoxy group. The epoxy rings on the modified polymer breaks by heat as those of the epoxy resin. Then, the hardener binds these dangling groups - crosslinking. The covalent nature of the new bonds strengthens the interface area much better in comparison to the usual secondary bonds. The bond strength in the fiber/matrix interface was improved for an epoxy resin through the modification of PS with an epoxy -compatible monomer - GMA [10], [11]. The copolymer reinforcement, P(St-*co*-GMA), folds the elastic modulus of the composite 10 times in three-point bending when compared to that of PS [12]. Presence of GMA in the nanofibers of P(St-*co*-GMA) resulted in a 18% improvement in the tensile strength of carbon fiber/epoxy composites [13], [115].

The second technique is applied to P(St-*co*-GMA) nanofibers [83]. Two classes of nanofibers were produced, one containing the neat polymer and the other a mix of the polymer with PA - a crosslinking agent. The melting temperature of the P(St-*co*-GMA) increases by increasing the ration of PA into the mix. When the combination of these two nanofibers is heat-treated, the nanofibers from the neat polymer melts while the nanofibers from the mix of polymer and PA crosslinks. Furthermore, the molten polymer covers the crosslinked fibers - selfsame strategy.

Carbon-based reinforcements are one of the best classes of reinforcing agents for polymeric composite both in the form of fibers and in the form of particles. MCF is a candidate to reinforce polymer resins too. These particles are suppressed to represent their

reinforcing potential in the composites because generally they are hindered by poor interface and agglomeration.

Agglomeration of particles is aimed to be reduced in this research using the electrospinning technique. This way, MCF particles are planned to be homogenously transformed to a reinforcing interlayer. The selfsame interlayers are planned to adapt built upon the nanofibers of neat P(St-*co*-GMA) and the nanofibers of the mix of P(St-*co*-GMA) with PA as the carrier media. The melting part of the interlayer is expected to melt and cover the particulates, hence create a better particle-matrix interface while the crosslinking part is expected to contribute to the strength of the composite as a fibrous structure.

3.2 Experimental

P(St-*co*-GMA) were prepared in accord with another work of this research group [12]. Monomer of St was procured from Merck, Germany, and GMA was purchased from Sigma-Aldrich, Germany. The polymer composition was analyzed in ThermoFisher Scientific Nicolet iS10, Germany. The thermal properties of the polymer were investigated by thermogravimetric analysis (TG) (Shimadzu DTG-60H) and dynamic thermal calorimetry (DSC) (TA Q2000).

Two classes of polymer solutions were prepared in DMF: 1. neat polymer (30 wt.%) and 2. polymer (20 wt.%) with the crosslinking agent of PA, initiator of TBA [83]. Milled carbon fibers (MCF) (EasyComposites, MFG100) were added to the second mix in the cases which the MCF-loaded nanofibers were aimed to produce from the suspension. All solutions and suspensions were stirred overnight to be homogenous.

The solution and suspension were electrospun in ~0.4 mL/h feeding rate, 12 kV applied potential, and 10 cm tip-to-collector distance. The solution/suspension was fed by a syringe pump (NewEra NE-100) through a needle with an inner diameter of 300 μm while the electrostatic field were created by a high-voltage bias potential (Gamma High Voltage ES 30P-20W) in between the needle and an aluminum collector.

The nanofibers were analyzed morphologically first using visual light microscopy (Nikon SMZ 1500 and Nikon Eclipse ME600). Then, after sputter-coating by Au/Pd (Cressington 108), they were analyzed in a scanning electron microscope (FE-SEM, Zeiss, Leo Supra VP 35). The nanofibers were heated at 10°C/min from room temperature up to 250°C and kept there for 1 hour in a box oven (Protherm PLF 130/6). Then, the samples took out of

the oven and left to cool down to the room temperature. The heat-treated specimens were analyzed morphologically as mentioned above.

The polymer and polymer-particle solutions were used as the reinforcement of nanocomposites and the interlayers of Carbon Fiber-Reinforced Composites (CFRP). The nanocomposites were prepared from two layers of electrospinning mats (10 cm × 10 cm) which were subsequently sandwiched with three epoxy adhesive films. In one of the nanocomposites, the only reinforcement was the nanofibrous layer, and in the other one, the reinforcement was the MCF-loaded nanofiber layer.

Composites were prepared by staking of the four sheets of 30 cm × 30cm prepregs (CM-Preg T-C- 150/600 CP004). In the case of neat CFRP, the prepregs were cut and used as received. However, in the case of nanofiber interlayered CFRP 30cm×30cm plies were mounted on a collector of the same size, and the polymer solutions were electrospun onto them beforehand. After covering three prepregs, they were stacked with a neat front ply. Both nanocomposites and composites first sealed in a vacuum bag, then underwent a cure cycle as follows: 1. heating from 30 °C by 2 °C/min up to 90°C, 2. isothermal process at 90°C for 1h for wetting of interlayers, 3. heating from 90°C by 2°C /min, to 145°C, curing temperature of carbon prepreg, 4. isothermal process in 145°C for 2h. Nanocomposites cured in a box oven, and CFRP's cured in hot-press under 5bar.

After curing, nanocomposite samples were cut to a dog-bone shape with a 14cm length and 1cm width. The specimen thickness measured around 0.5mm, and the specimens weighted about 1.08g. The composite specimens were cut out from the large sample in a rectangular shape of 2.5cm×25cm with a waterjet.

All nanocomposites and composites underwent a UD tension test in a Zwick/ Roell, Z100 Proline universal testing machine (UTM) with a 100 kN load cell, extension rate of 2 mm/min. The gauge length for nanocomposites was 10cm and for composites were 15 cm according to ASTM 3039-D3039M-14.

3.3 Results and Discussion

3.3.1 Compositional analysis

GMA were successfully copolymerized with St. The copolymer is believed to be compatible with epoxy resin because both the GMA and epoxy contain epoxy rings which can create crosslinks. In the IR spectrum of the copolymer (Figure 10), the epoxy group is identified with a peak around 800 cm^{-1}. In addition, C=O bond at 1750 cm^{-1} comes from GMA which is another evidence of successful polymerization.

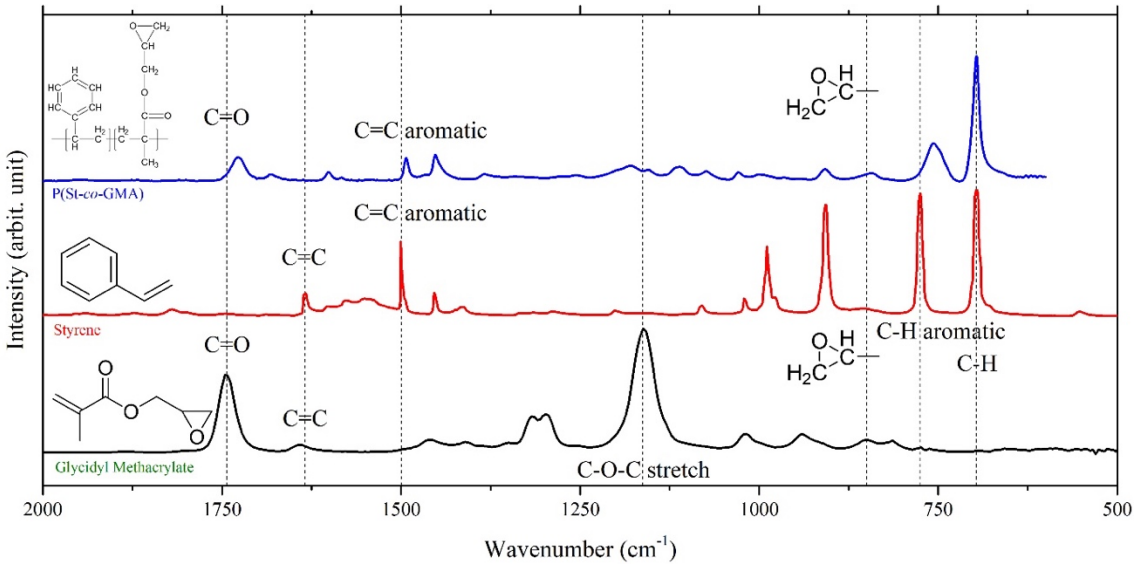


Figure 10: ATR FT-IR spectra of monomers and the copolymer.

The peak at 1500 cm^{-1} belongs to the aromatic C=C which comes from St. Both monomers show a C=C peak around 1650 which is lacking at the copolymer spectrum. Lack of this peak shows that the C=C double bonds in the monomers have broken and created single bonds along the copolymer backbone, i.e.: polymerization.

3.3.2 Thermal analysis

The TG curve of the copolymer shows that the mass loss is negligible up to 250°C (Figure 11 left). It means that the polymer does not degrade until this temperature. Thus, it can be heated while being sure that no structural changes will happen to the polymer.

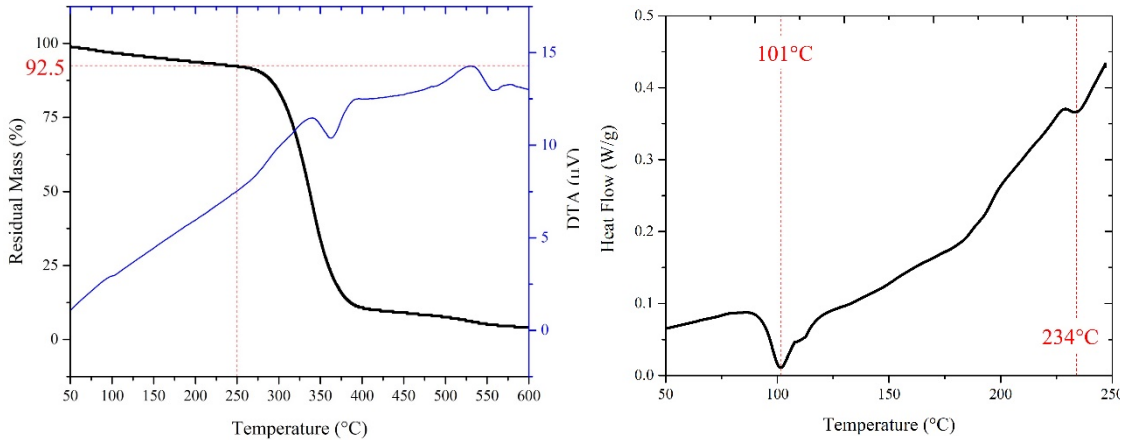


Figure 11: TG curve (left) and exo up DSC curve (right) from P(St-*co*-GMA).

The only changes which are expected to be observed in this region are the transformation from rubbery to glassy state at glass transition temperature (T_g) and complete melting (T_m) which are detected in the DSC curve (Figure 11 right). T_g is about 100°C and melting

completes around 234°C. Therefore, the latter temperature was chosen to heat-treat the nanofibers.

3.3.3 Morphological analysis

The prepared nanofibers of the melting neat polymer and the crosslinking mix of the polymer and PA were investigated morphologically under SEM (Figure 12) before and after heat-treatment. The upper images show the successful production of bead-free nanofibers. The diameter of the fibers is different in each specimen due to the jet instabilities at the head of the tip. The lower images show the morphological changes to the nanofibers after heating up to 250°C. The neat polymer melted completely while the nanofibers of the crosslinking melts sustained with almost no morphology change.

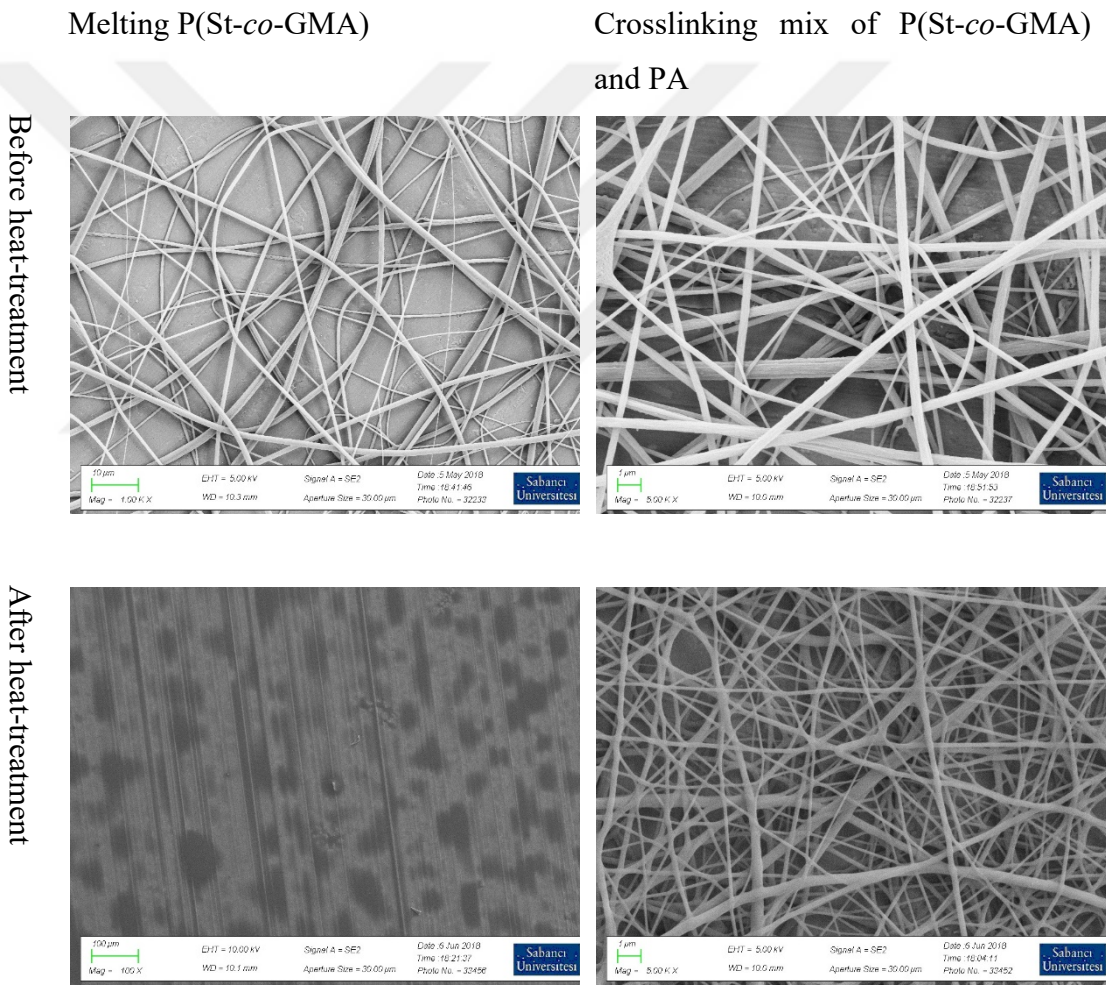


Figure 12: Nanofibers of neat polymer and the mix of polymer with PA before and after heat-treatment.

The different behavior of these classes of specimens is expected to lead to interesting structures if they both are present at a certain structure. This was performed using a dual electrospinning technique, and the samples were heat-treated accordingly (Figure 13).

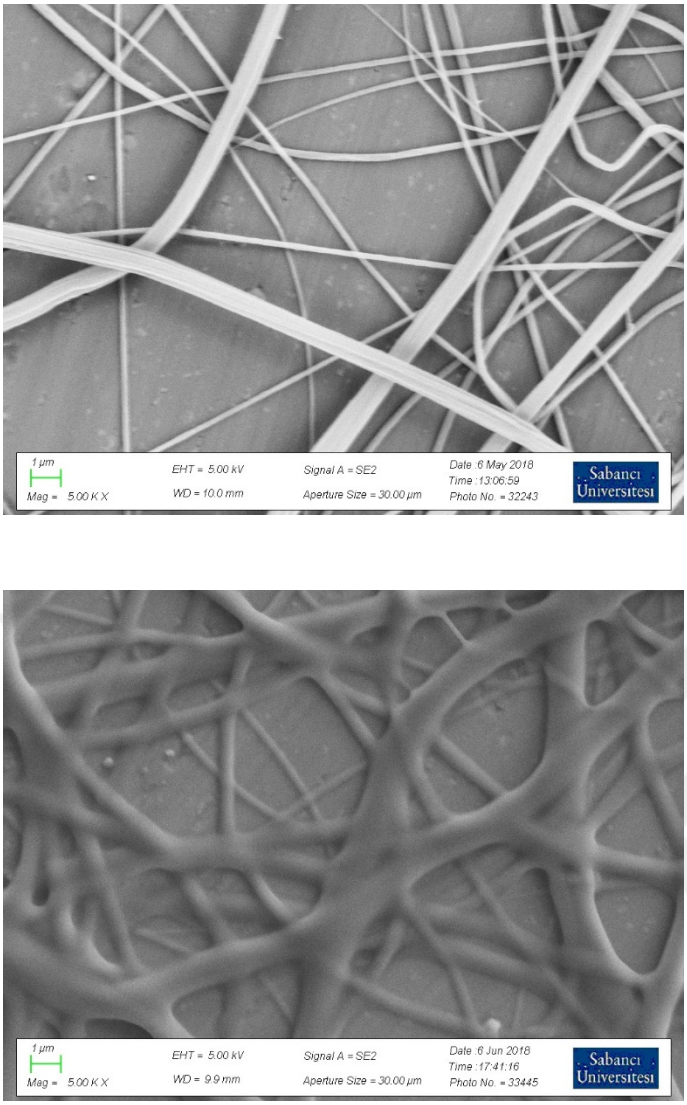


Figure 13: combined nanofibrous structure of melting P(St-*co*-GMA) and the mix of P(St-*co*-GMA) with PA before (up) and after (down) heat-treatment.

As it is observed, while heat-treating the melting nanofibers melt and cover the crosslinking fibers. Thus, the diameter of the fibers increase. The strategy has worked well here. While some part of the reinforcement melted to create a better interface with the matrix, the other part preserved the fibrous structure. Therefore, a potential composite structure which is reinforced with this nanofibrous layer would be expected to be enhanced both due to a more compatible interface provided by the melting agent and, simultaneously, the fibrous structure provided by the crosslinking agent.

The tests were repeated by adding MCF to the crosslinking mix too (Figure 14). In the upper left images, the MCF particles are seen to be distributed well throughout the examined region. By heating the sample, polymer nanofibers melt and the MCF's from different layers are observed in the lower left image. The melting polymer promises a

gentle and homogenous interface between the reinforcement and the matrix. The upper and lower right micrographs show that the heat treatment did not change the structure of the nanofibers. Accordingly, no morphological changes happen in the MCF's contained in the crosslinking copolymer which will help obtain their maximum of the strength.

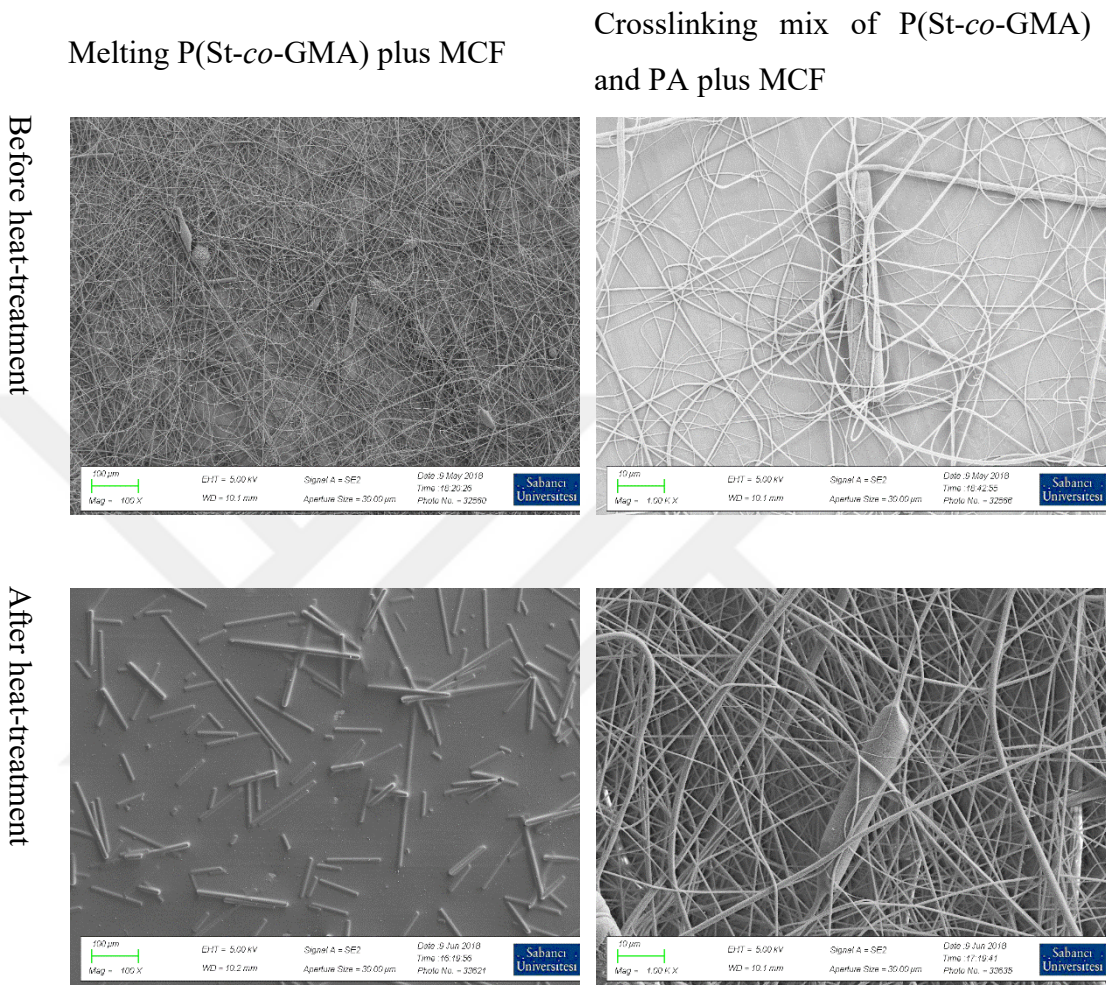


Figure 14: Morphology changes of nanofibrous structures with MCF before (up) and after (down) left treatment.

To investigate the morphology changes in the case of the combination, samples of neat polymer and the mix of polymer, PA, and MCF were prepared by dual electrospinning. The samples were heat-treated accordingly and analyzed morphologically (Figure 15). The images show that the fibrous structures stayed unchanged after the heat-treatment. It shows that it would be hard to show the specimen correctly using this method. Thus, other methods of identifying the location of the particles should be tested.

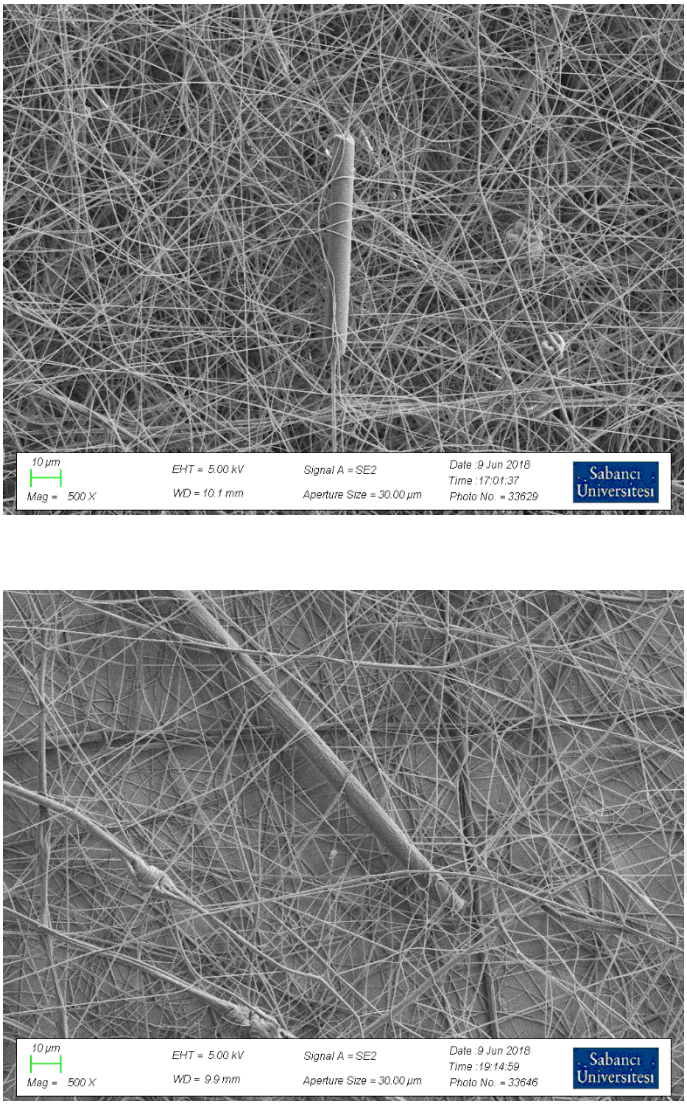


Figure 15: Morphology changes in the combined melting polymer nanofibers and crosslinking mix of polymer and PA plus MCF before (up) and after (down) heat-treatment.

In SEM images, only the surface is observable. Thus, only the MCF's which are close to the surface can be seen in electron micrographs. To detect the depth of the layer, VLM photomicrographs were taken and examined (Figure 16). The MCF particles were distributed homogenously throughout the mat. When the fibers were heated, the melting polymer loses its fibrous structure while the crosslinking sample keeps the morphology.

Melting P(St-*co*-GMA) plus MCF

Crosslinking mix of P(St-*co*-GMA) and PA plus MCF

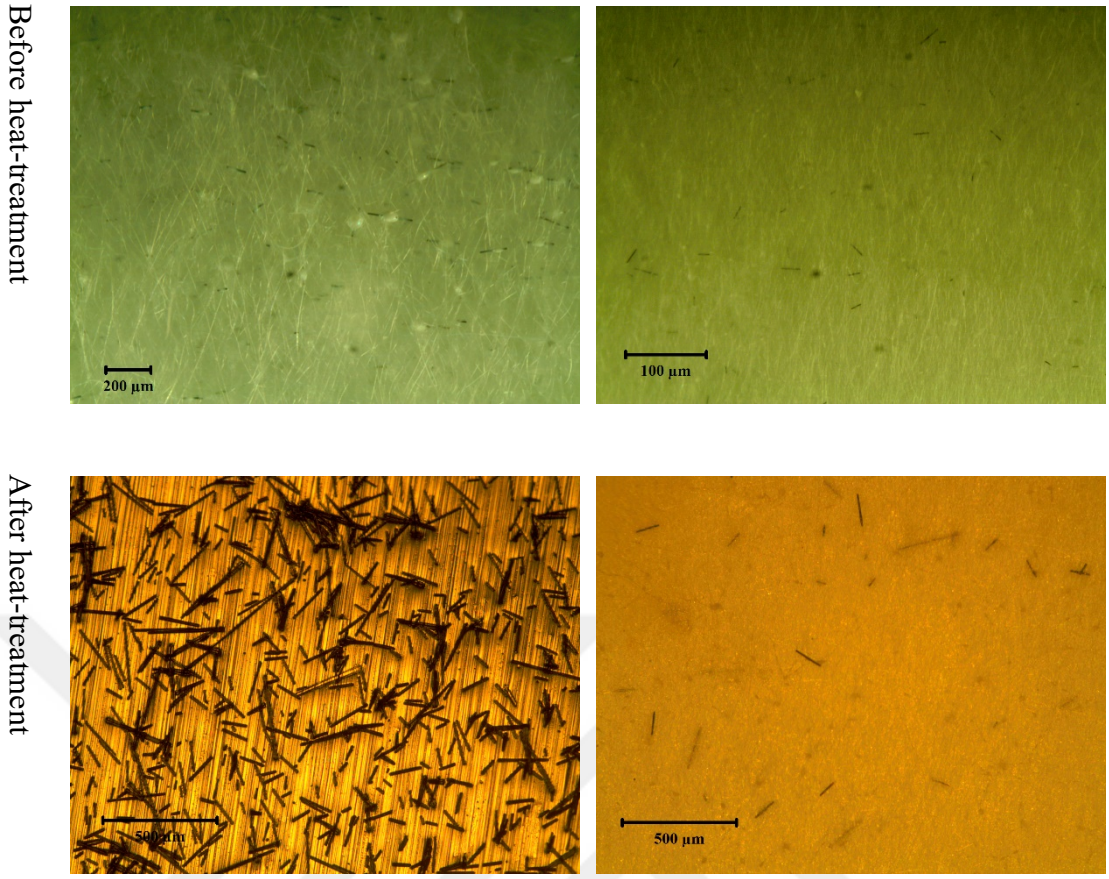
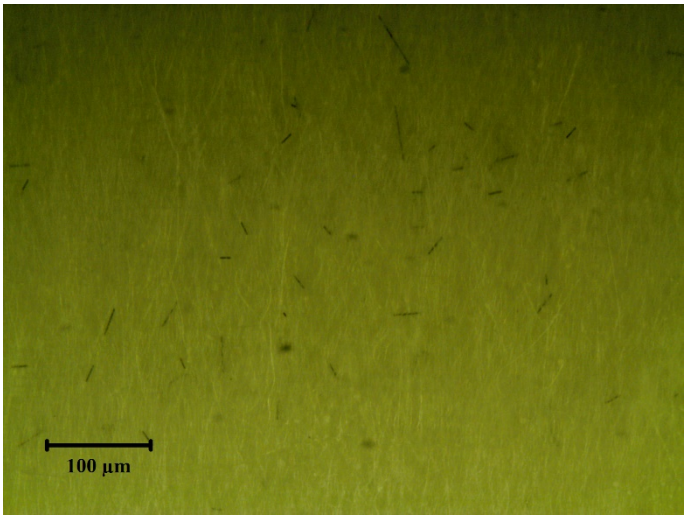


Figure 16: Morphology changes in the combined melting polymer nanofibers and crosslinking mix of polymer and PA plus MCF before (up) and after (down) heat-treatment.

The combined sample was investigated too (Figure 17). The fibrous structure of the nanofibers stays almost unchanged after the heat-treatment. Clearly, there are MCF particles which are beneath the surface. It is not possible to detect them under SEM.



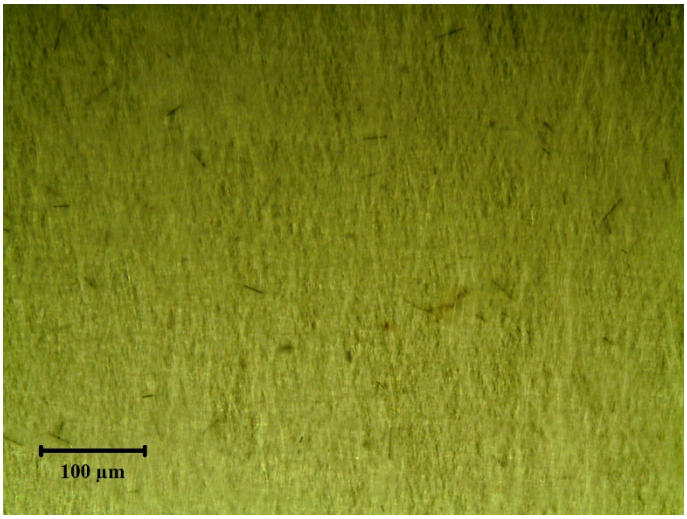


Figure 17: Morphology changes in the combined melting polymer nanofibers and the crosslinking mix of polymer and PA plus MCF before (up) and after (down) heat-treatment

3.3.4 MCF content determination

Only 1.5 wt.% transfer rate was measured (Figure 18) for MCF (out of the primary 10 wt.%) in the hybrid nanofiber mat. The transfer rate was measured to be 3 wt.% in the case of crosslinking polymer.

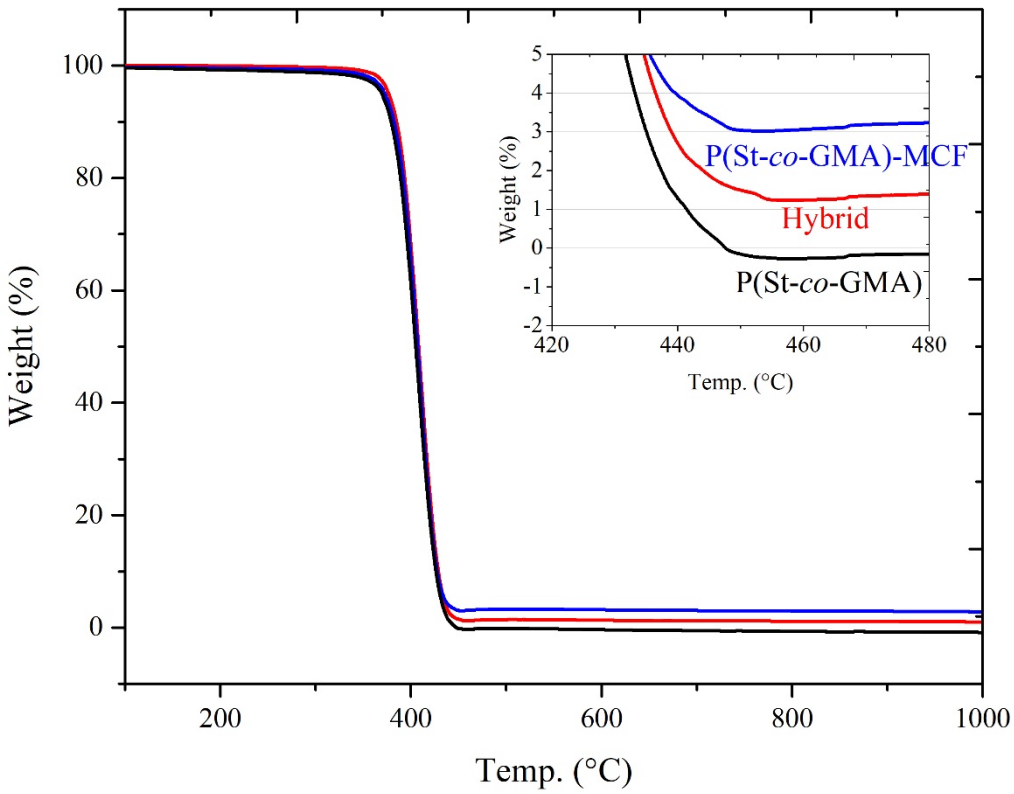


Figure 18: TG under nitrogen medium for P(St-*co*-GMA), P(St-*co*-GMA)-MCF, and their hybrid.

3.3.5 Mechanical analysis

MCF increased the elastic modulus of nanocomposites produced with hybrid interlayers of melting and crosslinking P(St-co-GMA) by 8.79 (Table 1). This indicates the enhancement was accomplished successfully and a stronger matrix-reinforcement interface was created. A similar effect was expected in the case of ultimate tensile strength, but the data diverge vastly (Figure 19), which makes any justification doubtful.

Table 5: Mechanical properties of nanocomposites reinforced by nanofibers of selfsame properties and selfsame plus MCF.

Specimen reinforcement	Elastic Modulus (MPa)	Change (%)
Selfsame	523±30	Not applicable
Selfsame-MCF	569±29	8.79

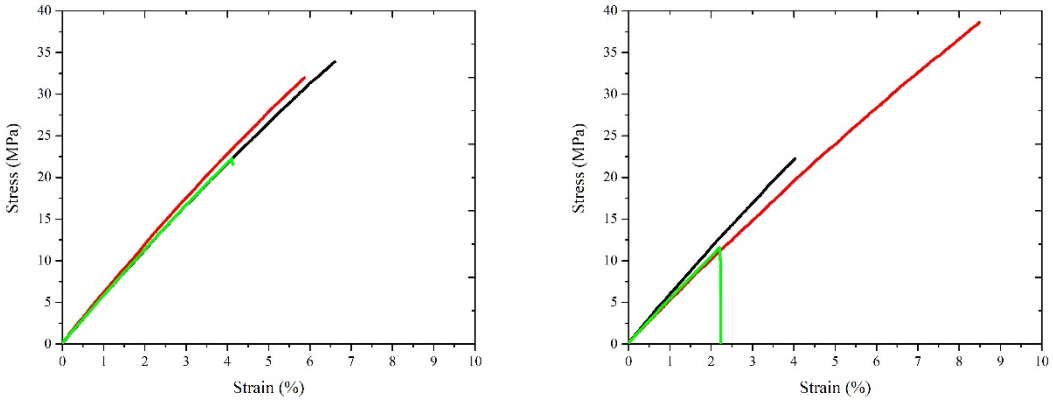


Figure 19: tensile test results for nanocomposites reinforced with the selfsame nanofibers containing MCF (left) and only selfsame nanofibers (right).

Selfsame nanofibers contained MCF increased the ultimate tensile strength by 8.85%, where they were implemented as the interlayer for carbon-fiber reinforced composites. The composites also barely improved the elastic modulus (Table 2).

Table 6: Mechanical properties of neat CFRP and CFRP with the interlayers of selfsame P(St-*co*-GMA) plus MCF.

Sample class	Elastic Modulus (GPa) (Change %)	Ultimate strength (MPa) (Change %)
Neat	58.5±6.51 (N/A)	723±48.4 (N/A)
Selfsame-MCF	60.8±4.50 (+3.91%)	787±54 (+8.85%)

The interlayered composites resisted more against the loading. The final features in the stress-strain curves (Figure 20) indicated this extra resistance, which also affected the failure modes of composites (the insets of Figure 20).

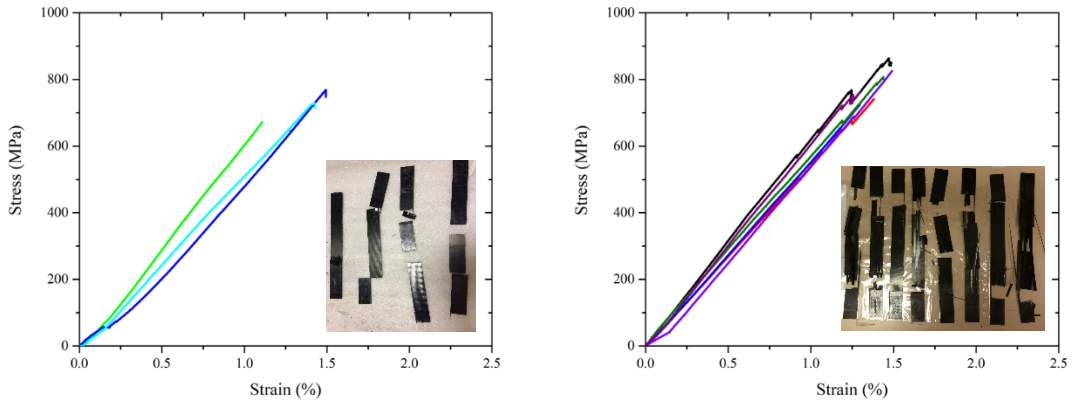


Figure 20: Tensile test results and failed specimens of neat CFRP (left) and CFRP interlayered with the selfsame P(St-*co*-GMA) nanofibers impregnated with MCF (right).

3.3.6 Fracture Surface analysis and toughening mechanism

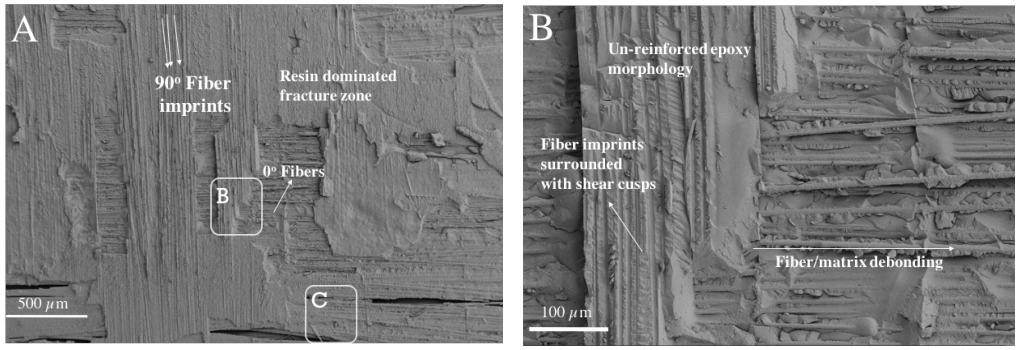
The toughening mechanism for self-same interlayers consisted of two major mechanisms in constituent level(micro) and laminate level (macro) [Figure 21]. As depicted in the fractured specimen micrographs (Figure 21) the ultimate failure of un-reinforced laminates was due to fiber failure occurring at the middle of the test specimens whereas for nanofiber/MCF integrated specimens the failure was rather complex with apparent marks of 90^0 block failure, ply splitting and delaminated 0^0/90 ply interfaces. Failure of a cross ply laminate typically initiates with transverse cracking due to weakness of 90^0 plies [111]. These microcracks typically are multiplied at the random locations in the gauge region and subsequently causes major failure modes like delamination and ply-splitting depending on the crack propagation mechanisms. To understand the role of nanofibrous interlayers two fracture surfaces corresponding to top part of a failed 90º block (in contact with the bottom of the subsequent 0º ply) and the bottom of a delaminated 0º ply (delaminated from the surface of first specimen) are investigated. Figure 21(a) and Figure 21(c) exemplifies two major failure modes such as interlaminar failure and ply-splitting. As depicted in Figure 21a, the fracture surface consisted of large resin blocks with fiber imprints and local appearance of 0º fibers underneath which suggests that an interlaminar crack locally deflected towards 0º plies has caused the final failure. 90º fiber imprints on the resin surfaces Figure 21(b) suggests that the delamination due to mode I crack propagation has occurred. These fiber imprints were more distinguishable when appeared on un-reinforced resin failure surfaces [Figure 21(b)] and fuzzy when appeared on P(St-*co*-GMA)(melt)/epoxy complex [Figure 21 (d)]. No signs

of crosslinked P(St-*co*-GMA)/TBA-PA fibers were captured in 0º ply surfaces. This observation suggests the fact that a part of melt P(St-*co*-GMA) has interacted with epoxy resin while separating itself from dual -electrospun nanofiber mix and plays a significant role on the specimen fracture [113]. The matrix structure in Figure 21(d) shows that this interaction gives a more plasticized resin microstructure that can be more effective against crack propagation. The progressive failure of interlayered specimens is more apparent when 90º ply surfaces are investigated. Figure 21(e) is an informative micrograph where intralaminar and interlaminar crack formation can be seen as well as the altered resin morphology when self-same nanofibers were integrated [Figure 21 (g)]. Similar to Figure 21(a), Figure 21(e) also contain resin block formation with fiber imprints on their surfaces however the localized appearance of 0º fibers in ply surfaces has been replaced by self-same nanofiber/epoxy complex who is partly able to crosslink [109] with epoxy resin and to modify the surrounding resin morphology [114] [Figure 21(g)]. Crack deflection mechanism associated with self-same/nanofibers is shown in [Figure 21(f)]. where interlaminar failure is locally deflected towards 90^0 plies causing resin fracture.

When two fracture surfaces are compared following conclusions can be made:

- Self-same nanofibrous interlayers not only acts as an "interlayer" but also as a resin modifier at multiple scales [Figure 21(d) and Figure 21(g)]
- Self-same nanofibrous interlayers plays an effective role in the transverse cracking of 90^0 plies and forms an obstacle for them to grow and multiplicate. More severe fracture modes such as ply splitting and delamination. Local load-drops in stress-strain curves before ultimate failure also supports that interaction.
- Presence of self-same nanofibers produces a rather complicated fracture surfaces with apparent crack deflection regions that might contribute to the strength of laminates.

----------0º ply surfaces----------



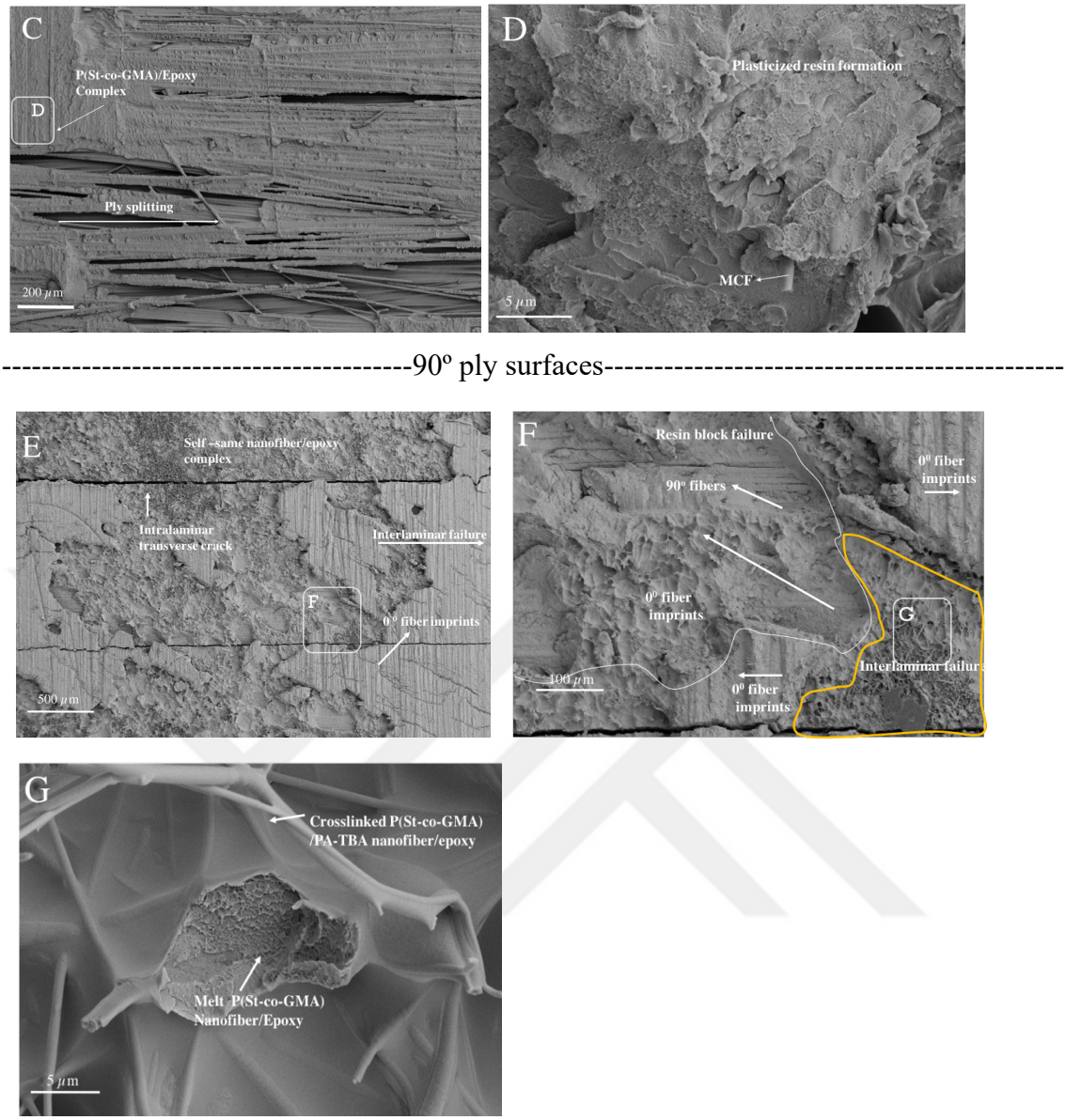


Figure 21: SEM micrographs of the fracture surfaces of failed specimens of CFRP interlayered with the selfsame P(St-*co*-GMA) nanofibers.

3.4 Conclusion

Introduction of extra covalent bonds is reported to strengthen the matrix-reinforcement interface in composites, called matrix compatible reinforcement. An epoxy-compatible polymer was produced by the modification of PS with additional functional sites - P(St-*co*-GMA) [10]–[12]. In this polymer, a potential disadvantage was detected as a change in the fiber morphology during the composite cure, and it was tackled by implementing a selfsame strategy [83]. Moreover, MCF particles were added to the reinforcement system to further enhance the properties of the nanocomposites and composites.

Morphological analysis revealed that the crosslinking nanofibers preserved their structure up to 250°C. The selfsame approach was detected successfully as the melting of a neat P(St-*co*-GMA) class and covering of the crosslinking P(St-*co*-GMA).

MCF was loaded into the mix of P(St-*co*-GMA) and PA, then was transferred in the carrying medium of electrospinning fiber homogenously. The loaded MCF content was measured to be 3wt.% for P(St-*co*-GMA) and 1.5wt.% for selfsame nanofiber mat.

Nanocomposites were successfully impregnated with selfsame nanofiber reinforcement. The presence of MCF in this structure led to an 8.79% increase in the elastic modulus.

CFRP's were enhanced using the selfsame nanofiber interlayers impregnated with MCF. The implementation of this interlayer resulted in 8.85% increase in the ultimate tensile strength while preserving the elastic modulus of the composite.

The research demonstrated the potential of MCF and nanofiber reinforcement as an effective reinforcement for nanocomposites and useful interlayer for fiber -reinforced composite. The results call for further research in fiber-particle combinations as well as systems optimizations.

CHAPTER 4

MORPHOLOGY EVOLUTION OF SELF-SAME NANOCOMPOSITES HYBRIDIZED WITH JUMBO-SIZED PARTICLES[§,**]

Summary

This paper reports the production, morphological analyses, and application of electrospun self-same nanocomposites with MCFs. The new hybridized structure was also incorporated into conventional fiber reinforced epoxy composites with improved properties. The MCF-hybridized polymeric nonwoven mats were formed with the simultaneous dual electrospinning of a soften-able (*m*-phase) and a crosslink-able (*x*-phase) variants of P(St-*co*-GMA). The morphology of the hybrid material was investigated using SEM The results showed that electrospinning can successfully deposit reinforcing particles of giant size (MCFs are 7 μm in diameter, 50 μm to 3 mm in length) compared to the diameter of the carrier nanofibers (nanometers). The new hybrid structure preserved the fibrous morphology of the polymer phases up to 250 °C. The overall morphology of the hybrid composite was tunable by changing the fractions of the two polymeric phases. The particle-polymer hybrid structures created morphologies that might find applications in various areas such as the interlayer toughening of laminated composites. It was shown that m-phase/MCF@x-phase nonwoven integrated into epoxy matrix composite laminates as interlayer, increased the strain at failure and ultimate strength under tensile loading by 11% and 9%, respectively.

[§] Published: Asghari Arpatappeh, F., Manga, E., Bilge, K., Aydemir, B. E., Gülgün, M. A., & Papila, M. (2022). Morphology evolution of self-same nanocomposites hybridized with jumbo-sized particles. *Journal of Applied Polymer Science*. https://doi.org/10.1002/app.53073

[**] Published as cover image: Asghari Arpatappeh, F., Manga, E., Bilge, K., Aydemir, B. E., Gülgün, M. A., & Papila, M. (2022). Cover Image, Volume 139, Issue 48. *Journal of Applied Polymer Science*, *139*(48). https://doi.org/10.1002/app.51160

4.1 Introduction

Electrospinning is an over-a-century old, powerful, and facile technique to fabricate nanofibers [1]–[3]. Mats of electrospinning nanofibers have found applications in many engineering fields stretching from environmental filters for water and air purifications [116] to medical filters for virus removal [6], [7], from scaffolds for tissue regeneration [110] to toughening interlayers for laminated composites [9], [11]–[14], [16], [18], [84], [111], [117]–[120].

In its simplest form, the process operates by pumping a polymer solution through a micron-sized nozzle while exposing the solution stream to an electrostatic field. The electrostatic field is created between the charged nozzle tip and a grounded collector. Sufficiently high electrostatic field leads to the formation of a jet of the polymeric solution. This reduces the diameter of the polymer thread from micrometers at the tip of the nozzle down to nanometers at the collector [4]. Mastery of electrospinning has allowed synthesis of multi-material/multi-phasic nanofibers. The phases can all be polymeric materials or their combinations with non-polymeric materials, such as metallic, ceramic, or carbon-based particles.

One common strategy in the electrospinning of multi-phase nanofibers is to produce composite nanofibers directly from a colloid of particles in a single polymeric phase. Numerous combinations of materials systems in composite nanofibers by this strategy were reported in the literature [8], [29]–[31]. Along with the typical electrospinning parameters, size of the filler or reinforcing particles is a decisive factor for optimizing the process and resultant morphology or structure. An overview on the types of particles and their size was included in the supplementary data. Figure S1 and Table S1 in the supplement shows the size of the particles ranged from 4 nm to 30 μm. Gold nanoparticles as small as 4 nm in diameter were added into a solution of poly(ethylene oxide) and then the colloid was electrospun. Electrically conductive composite nanofibers were produced (diameter ranged between 400-650 nm) [49]. Another study reported electrospinning of nano-to-submicron SiO_2 particles (100, 300, 450, 700 nm, and 1 μm in diameter) in solutions of different polymers such as polyacrylamide, poly(ethylene oxide), and PAN. It was shown that the particles were arranged in a necklace alike morphology as they were swallowed by the polymeric fibers. These composite fibers were used for immobilization of proteins [63].

At the other end of the size scale, graphene oxide (GO) aggregates with the diameter of about 2 μm were dispersed in a solution of PAN. Composite nanofibers were produced through electrospinning of the mixture for super-capacitor electrode applications [32]. The average fiber diameter in this hybrid composite ranged between 225 nm - 415 nm as a function of the concentration of GO aggregates. These nanofibers were carrying almost ten times larger particles than their own average diameter [32], [49], [63].

There is a variety of setups for the electrospinning. Among them, coaxial electrospinning and dual electrospinning are noted as the choices for producing multi-material/multi-phase nanofiber synthesis. The former setup is known to yield core/shell fiber formation. The latter is a typical setup in which two different polymeric solutions can be electrospun on a shared collector. This setup forms a hybrid intermingled fibrous nonwoven mat[121]. Synthesis of such a nonwoven mat made up was reported earlier by this group[83]. A soften-able (m-phase) and a cross-linkable (x-phase) form P(St-*co*-GMA), were electrospun through this method. The new hybrid nonwoven nanofiber mat was shown to be effective in the formation of toughening interlayers for laminated epoxy matrix composites [84], [114]. Under a heat-treatment the hybrid nonwoven showed a combination of the morphologies coming from m-phase and x-phase. The m-phase appeared to form a cover around the x-phase. The improvement in the interlayer toughening was associated with the formation of this cover. The nonwoven interlayer of the similar polymers was named as the self-same nanofibers [83].

One of the most intriguing areas of hybridization is arguably in structural composites. Recent review article [122] focused on and summarized the efforts on epoxy matrix fiber reinforced composites hybridized by nano-fillers. It showed that the appeal of nanoscale materials in composites is well recognized and studied for. Nevertheless, efforts for hybridizing with larger size fillers have also continued as there are several practical advantages. They are typically easier to incorporate into processes and much less hazardous to human health while handling [49]. They do not tend to agglomerate at high loading ratios [32]. Moreover, large fillers such as milled fibers can be obtained as the by-products of recycling processes as well [63]. Therefore, they are in general cost-efficient additives for mass production rates. Recycled milled glass fibers were used to modify epoxy matrix before impregnating continuous glass fiber reinforcements [123]. The results suggested that the addition of 5 wt.% milled glass fibers increased the mode-

I and mode-II fracture toughness by 102% and 175%, respectively. They also emphasized the importance of interfacial interactions of the milled glass fibers with the epoxy matrix. Most of the research on particle/filler hybridized structural composites have been based on liquid resin processes where fillers can be directly incorporated into the resin. There is still a lack of hybridization in the case of high-performance composites. It is because they are typically made of commercial continuous fiber-reinforced carbon prepreg materials which may not possess fillers/particles as they are. One strategy to incorporate multi-scale hybridization is the use of interlayers [9]–[14], [16], [18], [84], [111], [117]–[120]; An earlier work of this group [10] for instance, demonstrated interlayer applications of electrospun polymeric nanofibers hybridized with MWCNT.

Two research hypotheses in this study are the following:

- Relatively giant MCFs can be effectively incorporated within a polymeric nanofiber network using dual-electrospinning process.
- Morphology of an electrospun mat hybridized with MCFs and their surface coating can be tuned by heat stimulation of the two distinct phases of P(St-*co*-GMA) based polymer. Such a tuning ability is instrumental to achieve effective adhesion characteristics of interlayers that can enhance the mechanical performance of epoxy-matrix laminated composites.

The present work reports an extension of the self-same strategy[83] for testing the ability of dual electrospinning technique in incorporating relatively "giant" particles. Micrometer sized MCF (typically about 6-7 μm in diameter and 50 μm to 3 mm in length [124]–[126]) were used in manufacturing of "self-same" nanocomposites [127]–[134]. Two variants of the same polymer and MCFs were incorporated. Additionally, the new hybrid composite was studied for its unexpected thermal response. Overall, the novelty of this work comes from the self-same strategy [83] extended here for its unique interfacial tuning ability for highly hybridized composites.

4.2 Experimental

4.2.1 Materials and precursors

The polymeric material for electrospinning was PS copolymerized with GMA, [P(St-*co*-GMA)]. Detailed information about the in-house polymer synthesis was previously reported elsewhere [83]. Steps that follow the synthesis of polymer were depicted by the flowchart in Figure 22(a). The polymer solutions and suspensions were prepared by dissolving P(St-*co*-GMA) in DMF (Aldrich Chemical Co, United States). For the soften-

able variant the polymer was dissolved without any additives in the solution. For the cross-linkable variant, PA (Aldrich Chemical Co, United States) was added to the solution. It was shown earlier that PA triggers crosslinking at around 50 °C [135]. This temperature is well below the glass transition temperature of P(St-*co*-GMA) which is at about 100 °C [83]. The polymer solutions of pristine, soften-able P(St-*co*-GMA) and cross-linkable P(St-*co*-GMA)/PA are referred as m-phase and x-phase, respectively [Figure 22(b)] [84].

Suspensions from these solutions were prepared by adding the MCFs. They were purchased from EasyComposites (FP-MCF-004). Dimensional characterisation of the MCFs can be found in the supplementary material (Figure S4). Briefly, they are 7.5 μm in diameter and 100 μm in length on average. This dimensional characteristic is about three orders of magnitude larger compared to the nominal diameter of the electrospun polymeric fibers. The concentration of MCFs in the suspensions was 10 wt.% [Figure 22(b)]. All the polymer solutions and suspensions were homogenized by mixing overnight at room temperature, using a magnetic stirrer (Velp Scientifica ®, Arex Hotplate Stirrer, Italy) at a speed of 600 rpm.

Electrospun nanofiber mats were used as an interlayer to illustrate a potential application. Laminated composites were prepared with UD carbon fiber prepregs. The epoxy matrix prepreg material was CM-Preg T-C- 150/600 CP004.

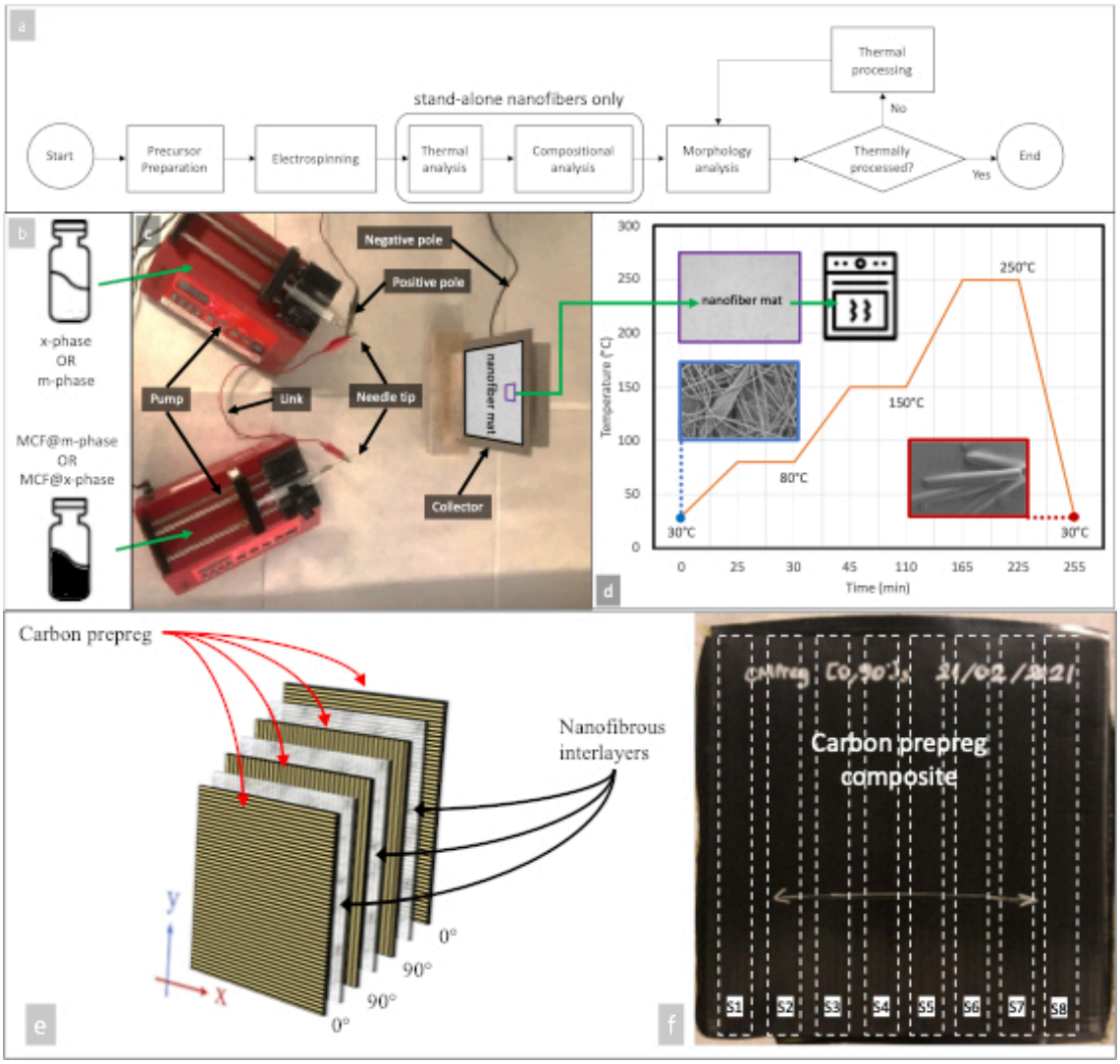


Figure 22: Flow chart of the process (a), preparation of precursors (b), dual electrospinning setup (c), heat-treatment program in a box oven along with the morphology analyses stages (d), schematic of laminated composite plate lay-up (e), composite plate and coupon sample geometry (f)

4.2.2 Electrospinning

The polymer solutions and their suspensions with the MCFs were electrospun using a dual electrospinning setup composed of two syringes. They were positioned at the same height and aligned with 60º angle to each other [Figure 22(c)]. The syringes of 1 mL (Set Inject®) were used with 18-gauge aluminum needles of 300 µm inner diameter as the reservoir tip. Electrospinning process parameters for the polymer-only solutions were adapted from a previous study [83]. Moreover, a full factorial design of two-factors at four levels was followed [136] to determine the process parameters for successful MCF-incorporated nanofiber collection. Optimized electrospinning setting was identified by

varying the polymer solution feeding rate and applied voltage at a constant tip-to-collector distance. The limits of each parameter were determined based on the previous studies from this group [83], [136]. The levels of each parameter were determined based on the capabilities of the pump and the volume of the syringe. The electrospinning was performed using the syringe pumps (NewEra Instruments, NE-100, United States), high voltage (Gamma High Voltage Research, Inc., ES 30P-20W, United States). The nanofibers were collected on an aluminum foil that covered the grounded aluminum plate collector. The flat square collector plate was 10 cm × 10 cm and positioned at 10 cm away from the needle tips. The whole setup was kept in a ventilated cabin so that the electrospinning process was carried out in a controlled environment at 23 °C temperature and about 40% relative humidity.

4.2.3 Heat treatment

One of the important applications of the nanofibers is their use in laminated composites. As the composite manufacturing typically requires processing at elevated temperatures, the effect of heat on the morphology of electrospun nanofiber mats were investigated. They were cut into samples and heated in a conventional box oven (Binder GmbH, Safety drying chamber, Germany) according to Figure 22(d). Note that the heat exposure strategy is consistent with the work reported earlier [83]. The typical high performance epoxy matrix composite materials are processed at a temperature ranging from 135 to 180 ºC. A higher temperature (250 ºC) was chosen as the maximum temperature for the heat treatment of polymer nanofibers. This temperature is well beyond the processing temperatures of nanofibrous nonwovens, but lower than the degradation temperature of the polymer [83], [135]. Throughout the heat treatment, samples were heated at a rate of 3 ºC/min and cooled down with the same nominal rate to 23 °C in 30 minutes. Despite this cooling rate, the cooling process was limited by the airflow cooling of the oven. Only after reaching the room temperature, morphology analysis was performed.

4.2.4 Scanning electron microscopy

To analyze the morphologies, samples of the polymeric nanofibers and MCF-nanofiber hybrid systems were all inspected by scanning electron microscope (SEM). The samples for the SEM analyses were cut and sputter-coated (Cressington 108, Ted Pella, Inc., United States) with Au-Pd alloy target under 0.04 mbar air pressure with 40 mA current and for 120 s. Then, they were analyzed by FE-SEM, Zeiss, Leo Supra VP 35 which can collect a mix signal of backscattered and secondary electrons on a lateral detector [Figure

22(d)]. Measurements of diameter of the nanofibers and length of the MCFs were performed on the SEM images using the ImageJ software tool. The average diameter values reported were the arithmetic means of more than 100 measurements.

4.2.5 Laminated composite specimens and testing

Epoxy matrix carbon fiber reinforced composites (CFRC) were prepared to demonstrate the interlayer effect of the hybrid polymer/MCF nanofibrous mats. The composites were prepared as cross-ply laminates with [0/90]s stacking of four pre-cut sheets of 30 cm × 30 cm prepreg (CM-Preg T-C- 150/600 CP004). In the case of neat CFRC, the UD prepreg plies were used as is. However, in the case of interleaved CFRC, the prepregs were cut in 30 cm × 30 cm geometry and mounted on an aluminum collector of the same size. Then, the prepreg was positioned on the collector of dual electrospinning setup and the polymer suspension was electrospun directly onto the prepreg surfaces. After coating three prepreg layers by electrospun nanofibers, the layers were stacked forming [0/I/90/I/90/I/0] where "I" stands for the nanofibrous interlayer. The laminates molded between two caul plates were vacuum bagged and cured in a conventional box oven (Binder GmbH, Safety drying chamber, Germany). Preparation of the interlayered laminates and their specimens are represented in Figure 22(e,f).

The cure cycle of CFRCs was as follows: 1. Heating from 30°C by 2 °C/min up to 90 °C, 2. Isothermal holding at 90 °C for 1 h, 3. Heating from 90°C by 2 °C /min, up to 145 °C, the curing temperature of carbon prepreg, 4. Isothermal heating in 145 °C for 2 h, 5. Cooling down to 30 °C.

It is important to note the isothermal step (step 2 of the cycle) is to stabilize the x-phase nanofiber morphology [83]. The cross-linking agent activated in this step due to the existence of PA. This step helped circumventing of the softening of the base polymer at around its T_g = 100 ºC.

Rectangular CFRC specimens were cut out from the panels in the size of 2.5 cm × 25 cm using a waterjet cutting machine. To avoid sliding of composite specimens in between the jaws of the grips, aluminum tabs (2.5 cm × 5 cm) were glued to both ends of the CFRC specimens. All composite specimens were tested under uniaxial tension using Zwick/ Roell, Z100 Proline UTM. The crosshead speed was set to 2 mm/min. The gauge length for the specimens was 15 cm according to ASTM D3039-D3039M-14.

4.3 Results and Discussion

Note that supplementary material presents the polymer-only electrospun nanofiber characteristics, namely soften-able (m-phase) and crosslink-able (x-phase) nanofibers also in line with the literature[83]. Their MCF-added hybridized variants along with a laminated composite application are reported here in detail.

4.3.1 Processing for the MCF particle/single-polymeric phase hybrid systems

Two sets of giant particle-incorporated polymeric nanofiber mats were electrospun. The first particle/single-polymer phase structure was prepared by adding the MCFs into the solution of m-phase polymer. The resultant suspension, labelled as MCF@m-phase, was electrospun using the dual electrospinning setup, with only one syringe operating (Figure 22). Sixteen different process settings were studied through a design of experiments methodology. Applied voltage and polymer solution feed rate (at four-levels each) were varied while the collector distance and polymer concentration were fixed. Figure 23 reports the sixteen settings and associated SEM images sampled from the regions away from the MCFs. The combinations that enabled homogeneous fiber collection from a stable jet were determined. The settings at which bead-free and homogenous nanofibers were fabricated are shown in Figure 23(e,i-k,m,n). Among these combinations, when the feed rate was set to 0.2 mL/h and applied high voltage to 16 kV [Figure 23(e)], a multi-jet formation [137] was observed [inset of Figure 23(e)]. In contrast, when the feed rate was set to 0.6 mL/h and applied voltage to 12 kV [Figure 23(k)], the suspension droplet [138] grew substantially on the nozzle tip after a few minutes [inset of Figure 23(k)]. The setting to produce a stable jet for the processing of a bead free and homogeneous nanofiber mat was with a feeding rate of 0.4 mL/h and applied voltage of 12 kV [Figure 23(j)] at needle-to-collector distance of 10 cm. Note that this setting was the same combination as in the literature [83] used for the electrospinning of polymer-only solutions without the MCFs.

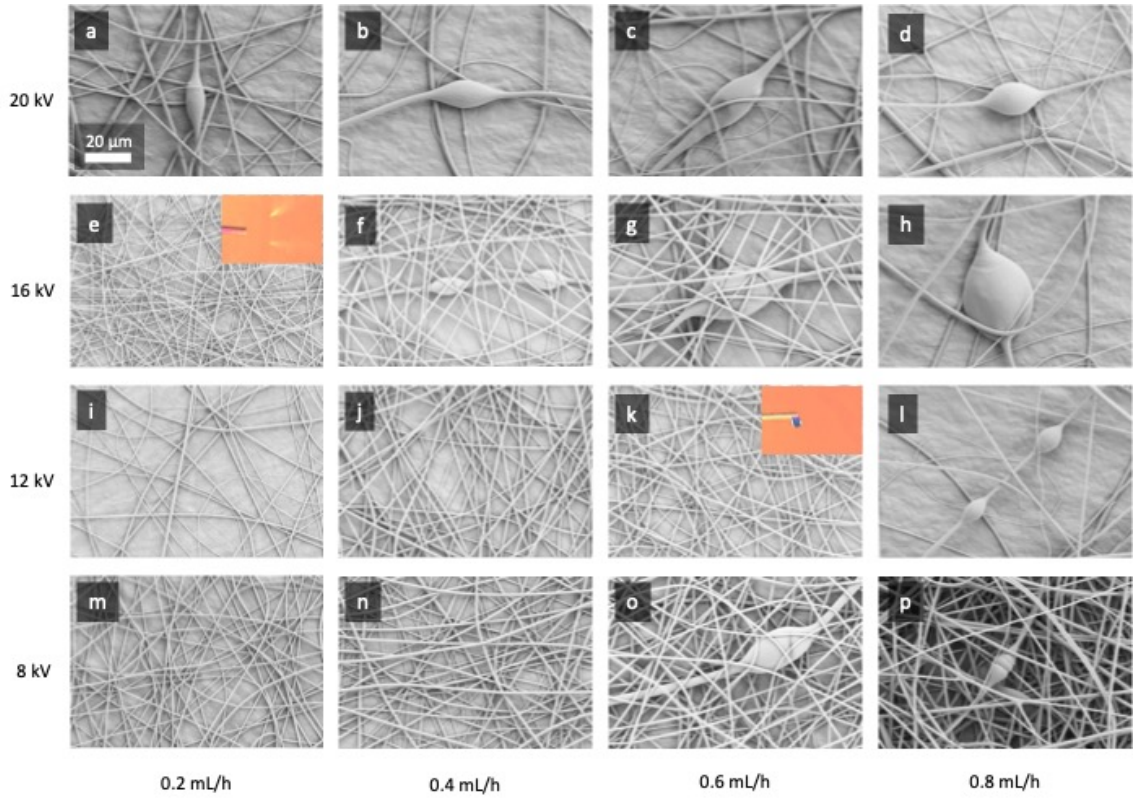


Figure 23: SEM micrograph of as-received MCF@m-phase nanofibers in different setup parameters (scalebar consistent within micrographs)

The second particle/single-polymer phase structure was prepared by adding the MCFs into the solution of x-phase polymer. Since the rheology of the x-phase and m-phase polymer solutions were similar [83], the suspension with MCF@x-phase was also electrospun at the same settings (0.4 mL/h in feeding rate, 12 kV in high voltage, 10 cm needle-to-collector distance).

4.3.2 Morphology of single-polymeric phase MCF incorporated mats

Two sets of electrospun nanofiber mats were fabricated. In the first set, MCFs were incorporated into the soften-able m-phase polymer. In the second set they were incorporated into the cross-linkable x-phase polymer. Figure 24 illustrates SEM images of the electrospun MCF/nanofiber samples, focusing at near MCFs regions. The observations confirmed that for both sets of nanofibers, the MCFs were successfully transferred from both suspensions to the respective nanofiber mats despite their orders of magnitude difference in their dimensional characteristics (Figure 24). The micrograph of single polymeric MCF@m-phase [Figure 24(a)] suggested that the polymer formed a cover layer on MCFs as well as nanofiber mats [83]. The polymeric cover layer on MCFs resulted in a non-uniform cross-sectional shape of the MCFs. For more detailed

observations, the close-up view of the covered area [solid rectangle in Figure 24(a)] was shown in Figure 24(b).

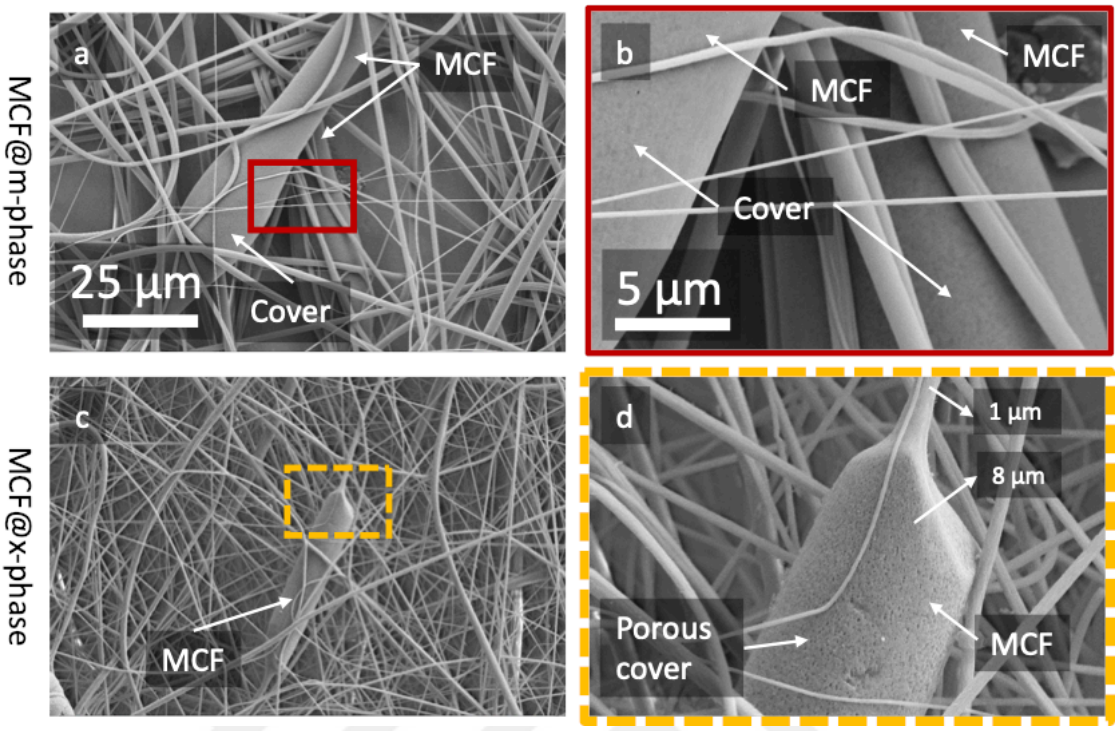


Figure 24: SEM micrograph of as- received MCF@m-phase (a,b), and as-received MCF@x-phase (c,d). (Scalebars consistent within micrographs of the same columns)

MCF@x-phase structure on the SEM image, Figure 24(c) shows that the MCF was again swallowed by the polymeric fiber despite the significant difference between the diameter of the MCF and that of the typical electrospun polymeric fiber. The continuation of the nanofiber is visible in the enlarged image in Figure 24(d). The yellow rectangle (of dashed-line boundary) in Figure 24(c) was zoomed for a detailed examination. Figure 24(d) revealed also that the surface of the polymeric cover was porous [139]. The pores could be attributed to the evaporation of the solvent [140], [141] during the electrospinning. The diameter of these pores was measured by ImageJ on the SEM image. Their diameter was about 50 nm [139].

Overall, the electrospun mats of single polymeric phases were bead-free [142] and the diameter of the fibers was homogenous. Observations suggested that adding MCFs directly to the polymer solutions of m-phase and x-phase worked well for producing integrated particle-nanofiber structures. Despite minor differences in the formation of polymeric cover around MCFs, both cases represent full integration between the particle and the polymer.

4.3.3 Morphology of particle-dual-polymeric hybrid systems

Again, two sets of MCF-incorporated hybrid nanofiber mats were fabricated. In line with the self-same strategy introduced in the literature [83]. Dual electrospinning of the m-phase and x-phase polymers was investigated when MCFs were introduced into one polymeric phase. In addition, the thermal behavior of the hybrid MCF-nanofiber mats in these two sets of samples were of concern. Therefore, the SEM images illustrating the morphology of the mats in this section were taken after the samples were heat treated at 250 °C.

In the hybrid MCF/nanofiber sample production, one of the syringes contained one polymer phase while the other syringe deposited the other polymer solution mixed with the MCFs. Volumetric proportions of the polymeric solution and suspension were varied according to Table 7 summarizing the hybrid systems studied for their morphological characteristics. For the syringe contents other than 50/50 (i.e., same amounts of polymeric solution), both syringes were pumped and electrically charged in sync at the beginning. The syringe associated with the lower amount was paused after half of its content was electrospun. It was then timed to resume so that both syringes were in sync again at the end of the deposition. This timing strategy, schematized in Figure 25, was utilized to make sure that both surfaces of the mats are balanced regarding the deposition from the solution and suspension (the solution with the MCFs).

Table 7: Fraction combinations for the two polymer variants and associated suspensions

Syringe 1 / Syringe 2 MCF@m-phase / x-phase	Syringe 1 / Syringe 2 m-phase / MCF@x-phase
100 / 0	
75 / 25	
50 / 50	
25 / 75	
0 / 100	

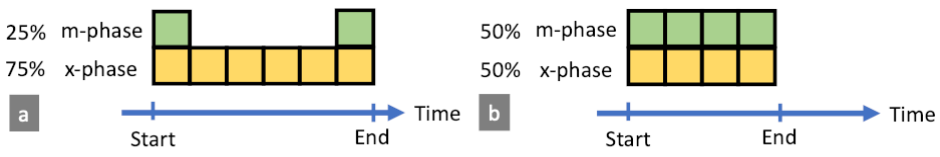


Figure 25: Examples of timing strategy of two syringes in dual electrospinning of 25/75 composition (a) and 50/50 composition (b)

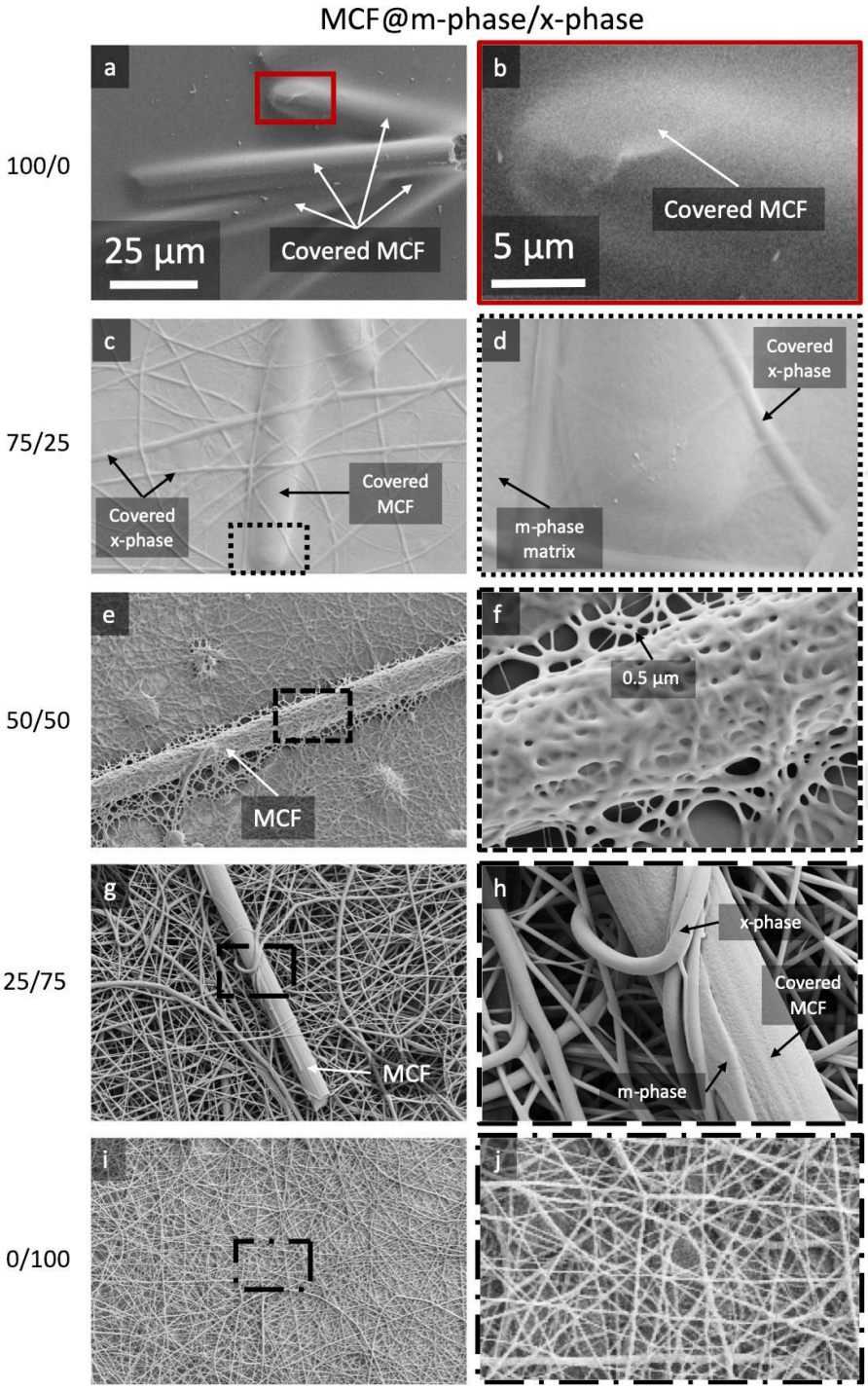


Figure 26: SEM micrographs for heat treated hybrid system of MCF@m-phase/x-phase. dual-electrospun nanofibrous mats at various fractions of the polymer suspension/solution. (Scalebar is consistent in each column)

Figure 26 and Figure 27 illustrate the SEM images of the two sets (i.e., MCF@m-phase/x-phase or m-phase/MCF@x-phase hybrid structures, respectively, at the fraction settings given in Table 7).

Figure 26(a, b) correspond to the heat treated soften-able polymeric phase consisting of the MCFs, i.e., MCF@m-phase (100/0). The SEM images show that the morphology changed completely due to the heat treatment. The polymeric part in the MCF@m-phase electrospun mat softened drastically and wetted/covered the MCFs like a matrix material [in contrast to pristine nanofibrous morphology in Figure 24(a, b) before the heat treatment]. When the inset red rectangle area of Figure 26(a) was zoomed in, it was evident that the MCFs were effectively impregnated by the softened m-phase polymer [Figure 26(b)], suggesting high compatibility of the MCF surface with the polymer [143], [144].

Introducing the x-phase polymer solution to the hybrid mat so that the fractions during the dual-electrospinning were 75/25. Figure 26(c,d) show that the morphology after the heat treatment was dominated by the matrix-like transformation of the m-phase. However, sparsely deposited x-phase nanofibers were also embedded in the softened m-phase [84].

Varying the fractions of MCF@m-phase/x-phase hybrid mats to 25/75, Figure 26(g,h) showed that the dominance was shifted in favor of the x-phase fibers while the m-phase softening polymer left marks on the MCF surface and caused an increase in the diameter of the cross-linked nanofibers.

Lastly, 0/100 MCF@m-phase/x-phase Figure 26(i,j) did not possess MCFs, but preserved the morphology of single-phase crosslinked x-phase nanofibers.

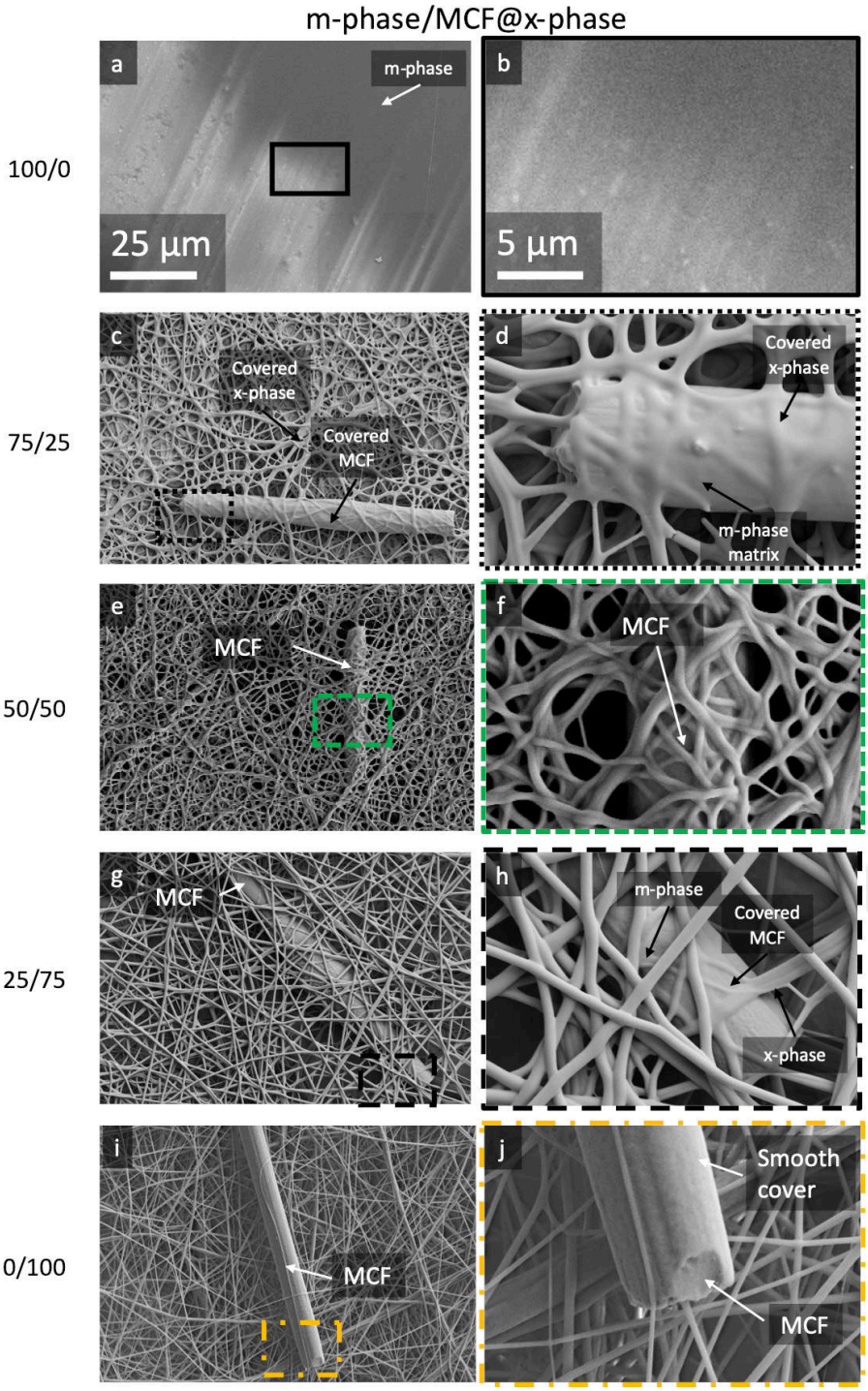


Figure 27: SEM micrographs heat treated hybrid system of m-phase/MCF@x-phase dual-electrospun nanofibrous mats at various fractions of the polymer suspension/solution. (Scalebar is consistent in each column)

Similar investigation was performed on the hybrid structures at varying fractions of m-phase/MCF@x-phase where this time MCFs were in the same syringe with the cross-linkable polymer solution. Results were collectively shown in Figure 27. Figure 27(a,b)

correspond to m-phase alone (100/0), therefore the heat treatment beyond the T_g of the m-phase resulted in a polymeric film with neither MCFs nor nanofibers. By tuning the fractions, m-phase to 75% and MCF@x-phase to 25%, MCFs were introduced along with the x-phase cross-linked nanofibers [Figure 27(c,d)]. The softening of m-phase created a coat on the surface of the MCFs and wetted the cross-linked x-phase nanofibers.

When the hybrid structure was produced with 25% of m-phase and 75% of MCF@x-phase [Figure 27(g,h)], the cross-linked fibrous morphology was dominant. Zoomed-in image [Figure 27(h)] revealed that the m-phase created a cover around the MCF and caused nanofibers of x-phase to stick to each other. Finally, SEM images of the electrospun MCF@x-phase nanofibers alone (0/100) revealed that the fibrous structure was preserved after heating up to 250 °C [Figure 27 (i,j)], because the cross-linking agent was already activated around 50 °C [84], [135]. After the heat treatment beyond 50 °C, the porous polymeric cover on the MCF observed at Figure 24(d) was also transformed into a smooth surface [139]. The smoothened surface upon heating [Figure 27(j)] was attributed to the conformation of polymer chains beyond the glass transition temperature [131], [145].

Special attention was given to the balanced fractions referred as 50/50. Although type of the nanofibers being m-phase or x-phase were not distinguishable in the SEM images of the pristine fibers (not shown here), the heat treatment resulted in different morphologies in the vicinity and on the surface of the MCFs [Figure 26(e,f) and Figure 27(e,f)]. The polymeric fibrous structure in this 50/50 hybrid was not disintegrated upon heat cycle [Figure 26(e,f)] as it was otherwise for dominant MCF@m-phase presence, 100/0 and 75/25 [Figure 26(a,b) and Figure 26(c,d), respectively]. The x-phase nanofibers were sufficiently present in this structure along with the fibers of MCF@m-phase. It appeared that the cross-linked x-phase was preserving the fibrous morphology [83]. Similarly, dual electrospinning resulted in effective hybridization of the m-phase/MCF@x-phase at 50/50 fractions. After the heat-treatment, again the fibrous morphology was preserved [Figure 27(e,f)]. However, a comparison between the hybrid forms of 50/50 and 0/100 m-phase/MCF@x-phase fractions solution, revealed that at the balanced presence of m-phase and MCF@x-phase the nanofibers [Figure 27(e,f)] seemed flattened and wider than that of MCF@x-phase alone [Figure 27(i,j)].

The sample of 50/50 MCF@m-phase/x-phase [Figure 26(e)] illustrates the representative morphology formation around the MCFs after the heat treatment. Careful inspections

revealed that the fibrous structure was preserved, and the thermal treatment created a mesh-like highly knotted/nodal networks of self-same finer fibers along the edges of the MCF [Figure 26(f)]. The diameter of the polymeric self-same fibers was measured by ImageJ on the SEM images, to be in the range of 50 nm to 500 nm. The presence of the nodes and the mesh of the fibers were the result of the simultaneous presence of the dual, chemically alike phases, and their unique interaction that was caused by the thermal treatment [11], [83].

Analysis of the alternative heat-treated structure, m-phase/MCF@x-phase, depicts the representative morphology formation around the MCFs [Figure 27(e)]. When the area in the dashed green rectangle on Figure 27(e) was magnified, interesting interminglements of nanofibers and the fusion to the MCFs were observed [Figure 27(f)].

Variations in the local composition can be advantageous for different goals[116]. Morphologies in which the m-phase is dominant [Figure 26(e,f)] suggest a more effective method to obtain a very thin non-conductive polymeric interphase around a conductive carbon fiber. Such a morphology may be advantageous for structural battery concepts [5], [146], [147]. From mechanics point of view, however, MCF@m-phase/x-phase hybrid structure in Figure 26(e,f) may not be favorable for an application requiring adhesion to another media [148]. Because their reduced free surface available within the nanofibrous network means decreased interfacial area at the MCF-present zones [99], [133], [149]–[152]. On the other hand, m-phase/MCF@x-phase hybrid [Figure 27(e,f)] with less amount of m-phase in the vicinity of the MCFs, provides larger free surface for adhesion [151], [152].

Earlier works showed that both the x- and m-phase polymers have effective interaction and chemical compatibility with an epoxy resin [13], [84]. In terms of their use in composite laminates, the m-phase/MCF@x-phase hybrid formation suggests more promises for structural performance applications [10], [13]. The available free volume of the hybrid morphology on and in the vicinity of the MCFs will be filled homogenously by epoxy resin[114]. Therefore, balanced m-phase/MCF@x-phase was chosen as toughening agent or interlayer for the next example of structural composites.

4.3.4 Effects of MCF-loaded self-same nanofibers in mechanical properties of composites

Interlaminar toughening of laminated structural composites is a common method to enhance their mechanical performance [125], [150], [153]. One approach in interlaminar

toughening is the addition of fibrous interlayers. This approach typically benefits from material designs through hybridizing different polymers and particles [131]. Majority of the efforts targeted improvement on out-of-plane mechanical behavior [109], [154], [155]. However, it has also been reported that such interlayer material solutions facilitated the increase in the performance of the composites when subjected to in-pane loading [10], [13], [14], [84], [135], [156]. Toughening was typically against pre-maturated failure modes such as transverse cracking and delamination [114]. Use of both m-phase and x-phase nanofibers for such applications was reported in the literature [10], [84]. A similar testing methodology was applied here to assess the performance of 50/50 m-phase/MCF@x-phase hybrid nanofibrous mats as interlayers.

Tensile tests were performed on the neat samples [Figure 28(a)] and the samples with hybrid m-phase/MCF@x-phase interlayers [Figure 28(b)]. The results suggested that the ultimate tensile strength and strain at failure of the cross-ply composite laminates increased by 9% and 11%, respectively (Table 8). This enhanced performance is mostly attributed to the engineered polymeric nanofiber architecture [10], [84]. Nevertheless, it is also vital to note that the addition of the large MCFs did not cause an adverse effect in the performance of composite laminates [127], [131], [134], [157], [158]. Improved interaction between the polymeric nanofibers and MCFs led by the self-same strategy arguably prevented the large MCF particles (~ 100 μm) to behave as impurities or source of stress-concentration within the laminate interlaminar regions (<100 μm).

Table 8: Effects of 50/50 m-phase/MCF@x-phase hybrid nanofibrous interlayers on the mechanical behavior of cross-ply carbon epoxy laminates under tensile loading

Laminated specimen layup	Strain to Failure (%)	Relative Change in Modulus	Ultimate strength (MPa)	Relative Change in Strength
$(0/90)_s$	1.23±0.1	-	723±48.4	-
(0/I/90/I/90/I/0) I: m-phase/MCF@x-phase	1.37±0.2	+11.38%	787±54	+8.85%

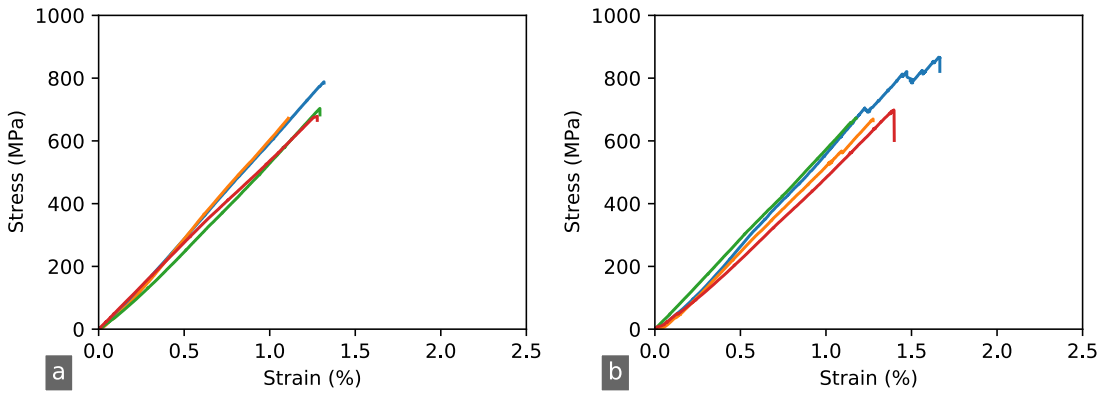


Figure 28: Tensile test results and failed specimens of neat CFRC (a) and CFRC interlayered with the selfsame P(St-*co*-GMA) nanofibers impregnated with MCFs (b).

4.4 Conclusion

Electrospun nanofibers and hybrid nanofiber-large particle structures were studied for their morphological transformations after thermal treatment. Based on the analyses it was found that:

- MCFs were successfully transferred from precursor solutions into nanofiber mats using the electrospinning technique. Order of magnitude difference between the diameter of the polymeric fibers and the characteristic dimensions of the MCFs did not prevent the transfer of the MCFs by electrospinning.
- Hybrid membrane-like structures were successfully prepared using dual electrospinning with one polymer solution carrying the MCF particles. They were found to be well integrated with the polymeric nanofibers and their self-same nanocomposites.
- Placing of the MCFs in the soften-able precursor or cross-linkable one resulted very similar morphologies prior to heat treatment. However, after the heat treatment the morphology on and around the MCFs revealed a different stability against the elevated temperatures (~250 °C).
- Depending on the choice of carrier polymer for the MCFs and fractions of the two polymeric phases, the local composition and morphology around the MCFs can be tuned for different applications in mind (e.g., membranes for structural batteries and toughening interleaves).
- Highly hybridized m-phase/MCFs@x-phase interlayers showed their promise for enhancing mechanical properties of laminated composites. The tensile strain at failure and ultimate strength of a cross ply CFRP laminate were increased by about 11% and 9%, respectively.

CHAPTER 5
DESIGN OF EXPERIMENT FOR NANOCOMPOSITES OF ELECTROSPUN P(ST-CO-GMA) NANOFIBERS LOADED WITH ZIRCONIA NANOPARTICLES

Summary

Multiphase composite nanofibers are structures which contain more than one phase. These phases might be both polymeric or a combination of polymeric and non-polymeric materials. This paper reports the synthesis of a novel polymer and a multi-phase composite nanofiber of the same polymer. The polymer was poly[styrene-co-(glycidyl methacrylate)] and the particle was ZrO_2. Nanofiber of this polymer and particle were produced using electrospinning technique following an RSM. Morphology analysis by SEM images, compositional analysis by thermogravimetry, and contact angle measurement was performed. ANOVA was used to statistically analyze the results. It was found that fiber diameter and the contact angle depend concurrently on both polymer and particle concentration of the suspension. Particle content of the nanofiber depends on those variables in a more linear way. Homogenous dispersion of fibers in the polymer nanofiber membranes was show cased down to 10 wt.% variance. The polymeric phase was shown to be an effective carrier medium. It ensured minimal agglomeration of particles and areal homogeneous distribution of the particles.

5.1 Introduction

Composite nanofibers are mixed fibrous structures that have multiple phases. They might include different types of polymers or different types of inorganics. One class of nanofibers are composed of a polymeric phase with an inorganic phase like metal or ceramic particles [4]. The significance of composite nanofibers is that their properties can be adjusted by changing the morphology and composition. Composite nanofibers have

found applications in a range of areas. They have been used as environmental filters for water and air purifications [5], medical filters for virus removal [6], [7], scaffolds for tissue regeneration [8] , and toughening interlayers for laminated composites [9]–[18].

Electrospinning is common method to produce composite nanofibers nanofibers [1]–[3]. It is an easy technique that can produce nanofibers from solutions and multi-phase suspensions. There are advantages to produce nanofibers with electrospinning. One, electrospinning can produce very thin nanofibers which can enhance the properties of the composite nanofibers. Second, the properties of the nanofibers are tailorable both with adjusting the suspension properties and those of the setup. Finally, membranes that are produced with electrospinning are homogeneous. All these advantages can be controlled with multiple precursor and processing factors.

Zirconia (ZrO_2) is well-known materials that has several applications in the industry. It was employed as refractory material due to the high thermal properties. It has been used as a dental material as it can provide high resistance to chemicals and excellent mechanical properties. It has also been used in the form of additive phase in multi-phase composite nanofibers. Sandwich Composite Membranes were produced using nanofiber for lithium-ion batteries. Nanofibers of poly(vinylidene fluoride-co-hexafluoropropylene) were electrospun and zirconia particles were integrated with them using an electrostatic spray. SCMs with these membranes showed improved electrolyte uptake as high as 2.06×10^{-3} S cm^{-1} at room temperature. In addition, they exhibited a high electrochemical stability potential of 5.4 V. They showed a high initial discharge capacity of 149.7 $mAhg^{-1}$ in with a $LiCoCO_2$ cathode [159]. Zirconia was integrated with poly(vinyl alcohol) in the form of fibers and radiopacity was introduced to the polymer fibers. Polymer and particle phases were electrospun co-axially and formed a skin-core morphology. The amount of zirconia in the structure was increased up to 9 wt.% with the penalty of losing the morphological uniformity. More uniform morphologies obtained with changing the integration geometry from skin-core to embedded particles [160]. Composite nanofibers were produced by electrospinning of polycaprolactone and zirconia as scaffolds. Particle content in the composite varied between 6 to 30 wt.%. It was found that the presence of particles enhanced the fibroblast proliferation and improved bioactivity of the scaffold [161]. Despite these promising results, very limited research touched upon the synthesis of composite nanofibers from other polymers loaded

with zirconia particles. There is no systematic study that reported the effect of the precursor and processing parameter on the morphology of the composite nanofibers.

Design of experiment (DOE) is a useful approach to assess the effect of multiple factors. It includes the response surface methodology (RSM) which has been applied for electrospinning of several solutions and suspension. This method was used for optimization of the precursor and process parameter in electrospinning of solution and suspensions. For instance, the effects of electrospinning parameters on PAN nanofiber diameter were performed by RSM. DOE approach was adapted with variables of solution concentration, voltage, and collector distance. Average diameter was considered, and the coefficient of variation were modeled by polynomial response surfaces. It was found that in high solution concentrations and high collector distances the effect of voltage was minor in the micron-scale. The effect of those parameters became statistically significant in nanoscale [136]

This research focus on the production of multi-phase composite nanofibers using electrospinning. The composite nanofibers are composed of P(St-co-GMA) and zirconia particles. RSM is used to optimize the experiment. ANOVA was used to analyze the data.

5.2 Experimental

P(St-*co*-GMA) was copolymerized using a free-radical polymerization based in a medium of DMF (Sigma-Aldrich, USA) [120], [162]. Solutions of this polymer with the DMF was prepared later for electrospinning. The concentration of the polymer varied between 10 wt.% and 30 wt.%. Zirconia particles (Zirconium(IV) oxide, Merck, USA) particles were added to the solutions. The solutions and suspensions were stirred using a magnetic stirrer. They were homogenized through overnight stirring.

Solutions and suspensions were electrospun using a conventional electrospinning setup. The solution and suspension were electrospun in ~1 mL/h feeding rate, 15 kV applied potential, and 20 cm tip-to-collector distance. The solution/suspension was fed by a syringe pump (NewEra NE-100) through a needle with an inner diameter of 300 μm while the electrostatic field were created by a high-voltage bias potential (Gamma High Voltage ES 30P-20W) in between the needle and an aluminum collector. The collector was covered by aluminum foil beforehand when samples were needed for morphology analysis. Stainless steel mesh was mounted on the collector so that the fibers were

collected on it. The mesh facilitated the later peeling of the fibers as a stand-alone membrane.

Samples on aluminum foil were sputter-coated by Au/Pd (Cressington 108). They were analyzed in a scanning electron microscope (FE-SEM, Zeiss, Leo Supra VP 35). Fiber morphology was analyzed from SEM images using ImageJ (National Institute of Health, USA).

Specimens from the stand-alone membrane were cut for the analysis of the compatibility with between composite fibers with liquid epoxy resin (RenLam® LY 113, Huntsman Advanced Materials, Switzerland). Fiber samples were laid on a standard glass microscope slide. A drop of 4 µl liquid resin was located on the fiber. The change in the shape of the drop was recorded using an optical tensiometer (Attension® Theta Lite, Nanoscience Instruments, USA). Contact angle change was measured from the recorded video.

Specimens from the stand-alone membrane were cut for TGA. TGA was used in two different configurations. Once, it was used to determine the composition of composite nanofibers with different polymer and particle concentrations. In this case, the specimens were heated under synthetic dry air from the room temperature by a rate of 10°C/min to 600°C. Second, TGA was used to determine the homogeneity of the particle content in representative nanofiber composite. In that case, the samples were heated under synthetic dry air from room temperature by a rate of 20°C/min up to 500°C.

RSM was used to statistically analyzed the measured attributes of the nanofibers, including the average diameter, particle content, and the average contact angle with the liquid epoxy. Polynomial surfaces were fit the data using MATLAB®.

5.3 Results and Discussion

5.3.1 Response surface methodology

To investigate the impregnation feasibility of epoxy-compatible polymers, P(An-*co*-GMA), with a particle zirconium dioxide was chosen. A design of experiment method (Figure 29) was built upon three levels of polymer concentration (20, 25, 30 wt.%) and three levels of particulate concentration (10, 20, 30 wt.%) as the most experimental parameters which affect the morphology of the nanofibers.

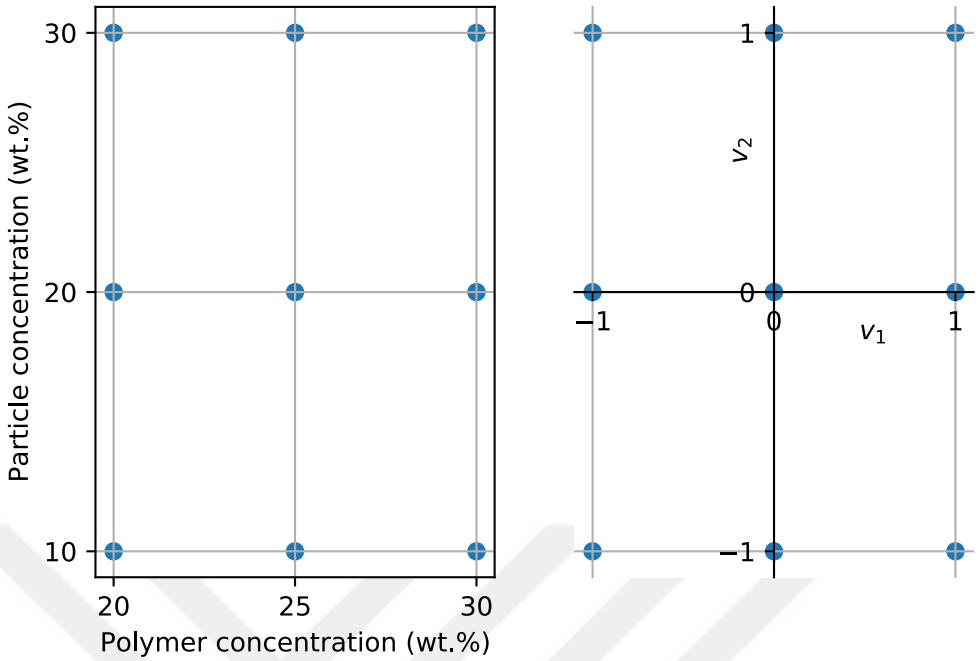


Figure 29: experimental space (left) and standardized experimental space (right).

5.3.2 Morphology analysis of fibers

Aside from the 10 wt.% polymer, the others were homogenous nanofibers with almost no beads. A slight change was made in the experimental space from **Error! Reference source not found.** to Figure 29 to entail all fibrous structures. The bright particles shown in the top right image are zirconia particulates. SEM images were taken for the data points corresponding to the revised experimental space .

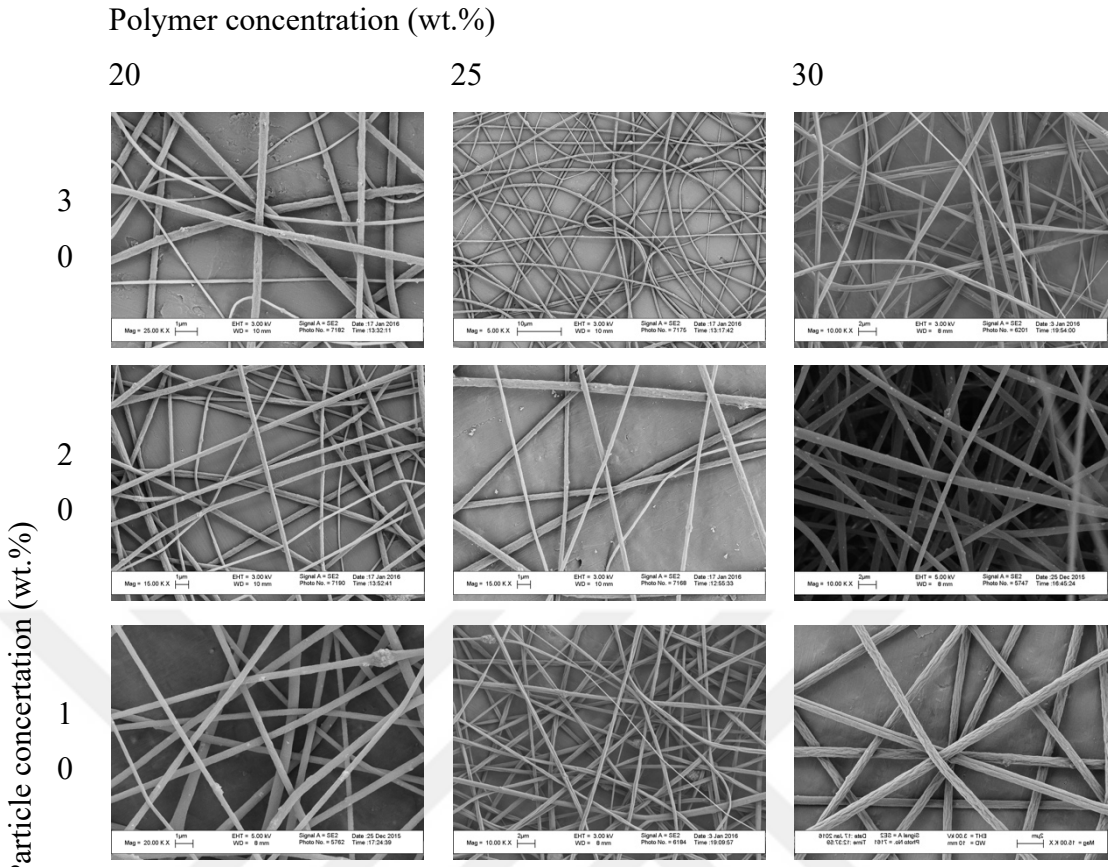


Figure 30: Morphology of fibers regarding the data points of the revised experimental space

The actual amount of particle was tested using a TGA in the air. The residual mass was assumed to be the particle mass in that nanofiber structure. It was selected as the response value for the optimization simulations. An RSM was adapted to the weight loss data to find the optimum configuration in which the maximum particle has been transferred (Table 9) or the efficiency of particle transfer is maximized. The results show that the method of loading particulates to fibers using electrospinning is quite successful.

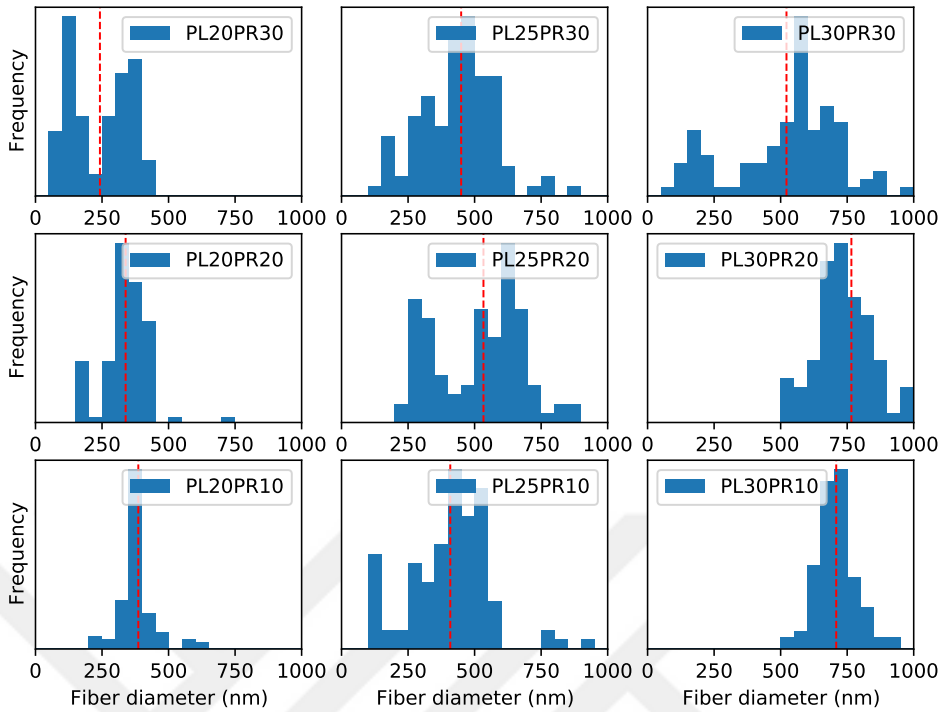


Figure 31: fiber diameter of P(St-*co*-GMA)-ZrO_2 nanofibers in the finalized experimental space (PL##: polymer wt.% and PR##: particle wt.%)

5.3.3 Contact angle measurement

Contact angle was shown for a liquid epoxy droplet on a membrane sample of composite after stabilization (Figure 32). All samples exhibited a good interface with the epoxy resin. This was mainly due to the nature of PS and the presence of the epoxy rings in GMA. The contact angle varied from 36° to 45° (Table 9).

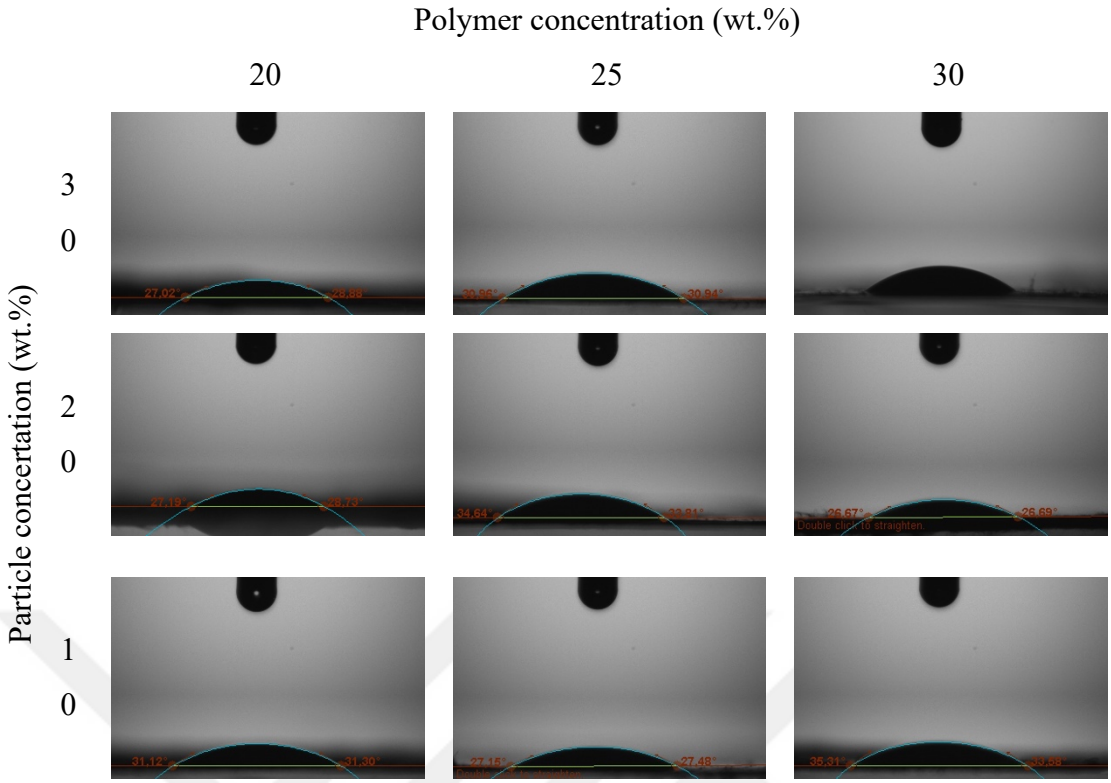


Figure 32: contact angle of epoxy with nanofiber mat surfaces after long time

Actual particle content was measured from the TGA results. The content changed between 8.21% to 21.77% (Table 9).

Table 9: The experimental points and the responses

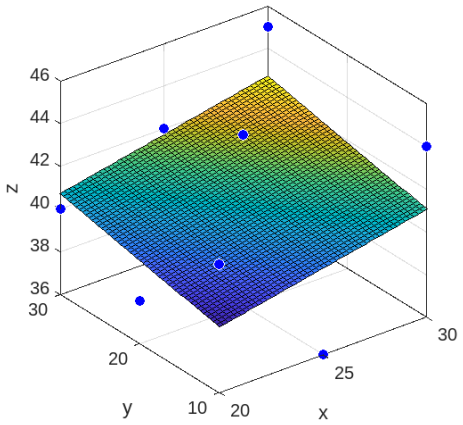
Variable, v_1 (polymer conc., wt.%)	Variable, v_2 (particle conc., wt.%)	Standardized variable, v_1	Standardized variable, v_2	Average fiber diameter (nm), z_1	Particle content (%), z_2	Average contact angle (º), z_3
20	10	-1	-1	386 ± 95	9.34	42
20	20	-1	0	533 ± 216	14.54	38
20	30	-1	1	242 ± 113	17.61	40
25	10	0	-1	409 ± 153	8.21	36
25	20	0	0	533 ± 216	13.73	44
25	30	0	1	449 ± 169	21.7	42
30	10	1	-1	709 ± 74	9.29	44
30	20	1	0	766 ± 145	15.59	37
30	30	1	1	522 ± 202	21.77	45

5.3.4 Analysis of variance

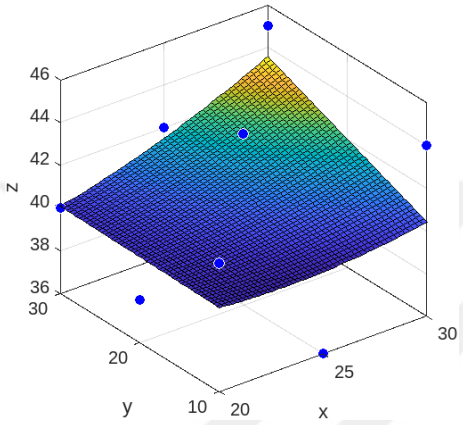
Data points for each repones in the experimental space was analyzed using the analysis of variance (ANOVA) in Figure 33, Figure 34, and ANOVA of the contact angle was shown in Figure 35. A fit of the first-order polynomial showed that the contact angle increased by increasing the polymer concentration or particle concentration. Although the contact angle changed only slightly. This had a rsquare of 0.1170 which was far from the acceptable region.

Next, the fit was increased to a second-order polynomial. When the parabolic behavior was assigned to the polymer concentration only, the dependence of the response lowered in lower (second row in Figure 35). This fit improved the rsquare to 0.2203, but it was yet far from acceptable. When the parabolic behavior switched the particle concentration, it was shown that the dependence of the contact angle to the particle content became more complex (second row in Figure 35). The rsquare value, however, was worsened to 0.1455. Finally, when parabolic behavior was assigned to both polymer and particle concentration, the complex dependence of the contact angle on the particle concentration stayed. Yet, the complex dependence of the contact angle on the polymer concentration was quite strait forward (third row in Figure 35).

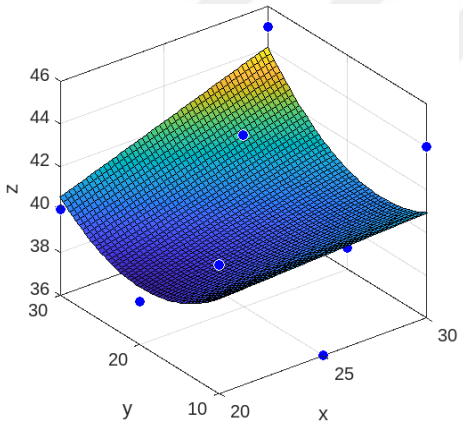
The dependence of the contact angle on the polymer concentration (third row in Figure 35) was like that of the fiber diameter (third row in Figure 33). In other words, increasing the polymer concentration increased the fiber diameter and the contact angle. This behavior might suggest that finer fibers provide the epoxy resin with higher surface that it can create an interface.



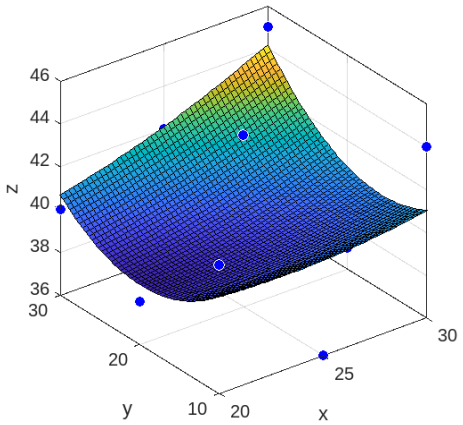
Linear model Poly11:
sf(x,y) = p00 + p10*x + p01*y
Coefficients (with 95% confidence bounds):
p00 = 34.22 (14.77, 53.68)
p10 = 0.2 (-0.5144, 0.9144)
p01 = 0.08333 (-0.2739, 0.4405)
sse: 76.7222
rsquare: 0.1170
dfe: 6
adjrsquare: -0.1773
rmse: 3.5759



Linear model Poly21:
sf(x,y) = p00 + p10*x + p01*y + p20*x^2 + p11*x*y
Coefficients (with 95% confidence bounds):
p00 = 49.83 (-166.1, 265.8)
p10 = -0.7667 (-17.88, 16.35)
p01 = -0.2917 (-3.322, 2.738)
p20 = 0.01333 (-0.325, 0.3517)
p11 = 0.015 (-0.1046, 0.1346)
sse: 67.7500
rsquare: 0.2203
dfe: 4
adjrsquare: -0.5595
rmse: 4.1155



Linear model Poly12:
sf(x,y) = p00 + p10*x + p01*y + p11*x*y + p02*y^2
Coefficients (with 95% confidence bounds):
p00 = 47.83 (-20.25, 115.9)
p10 = -0.1 (-2.568, 2.368)
p01 = -1.025 (-5.364, 3.314)
p11 = 0.015 (-0.09927, 0.1293)
p02 = 0.01833 (-0.06246, 0.09913)
sse: 74.2500
rsquare: 0.1455
dfe: 4
adjrsquare: -0.7091
rmse: 4.3084



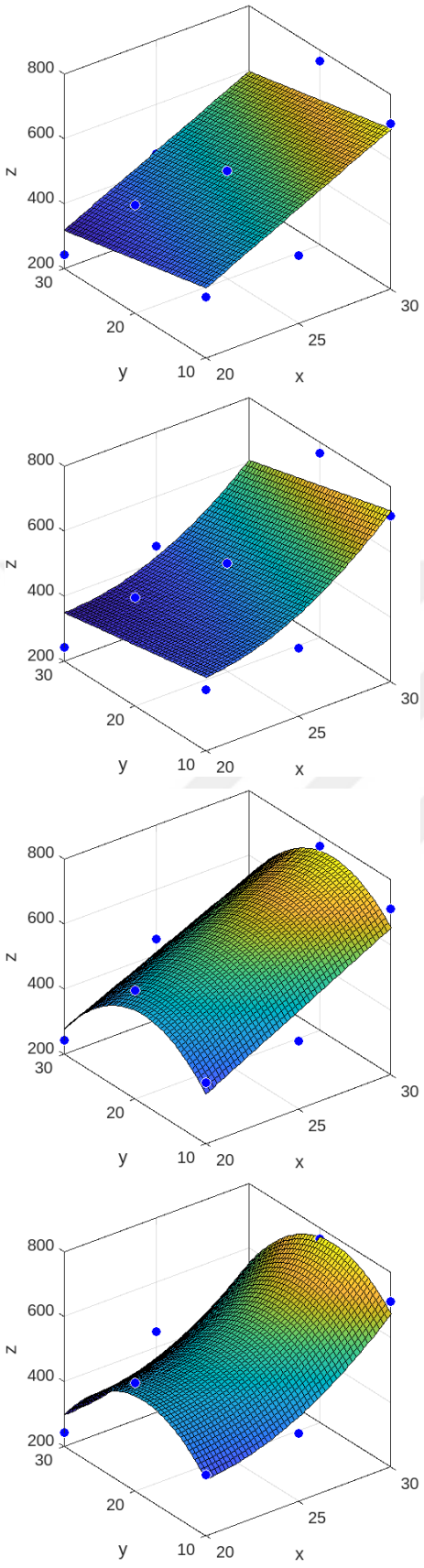
Linear model Poly22:
sf(x,y) = p00 + p10*x + p01*y + p20*x^2 + p11*x*y + p02*y^2
Coefficients (with 95% confidence bounds):
p00 = 55.94 (-219, 330.9)
p10 = -0.7667 (-22.37, 20.83)
p01 = -1.025 (-6.758, 4.708)
p20 = 0.01333 (-0.4137, 0.4404)
p11 = 0.015 (-0.136, 0.166)
p02 = 0.01833 (-0.08843, 0.1251)
sse: 67.5278
rsquare: 0.2228
dfe: 3
adjrsquare: -1.0725
rmse: 4.7444

Figure 35. In each row a polynomial surface was fitted the data points. The images of the fitted surface and the data points were given in the left column and the polynomial of the surface as well as the data of the Goodness of Fit (GoF). This data includes sum of squares due to error (sse), R-squared or the coefficient of determination (rsquare), degrees of freedom in the error (dfe), degree-of-freedom adjusted coefficient of determination (adjrsquare), root mean squared error or standard error (rmse).

The analysis for the fiber diameter response was shown in Figure 33. A polynomial of the first degree showed that the average diameter of the fibers increased by increasing the polymer concentration and decreased by increasing the particle concentration. However, the rsquare for this fit was 0.6702. Since it was less than 0.9 this fit was not regarded an acceptable surface. Therefore, a second-degree polynomial was fit the data (second raw in Figure 33). This parabolic behavior was assigned to the polymer concentration. The fit showed that improved the fiber diameter had a second-degree dependence on the polymer concentration. This dependence was especially evident in the case which the particle concentration was lower (10 wt.%).

Next, the parabolic behavior was assigned to the polymer concentration only. The analysis showed that by increasing the particle concentration in a certain polymer concentration, the fiber diameter increased first and then dropped (third row in Figure 33). This might suggest that there exists a certain optimum particle concentration that a solution can carry with a determined polymer concentration. If the particle concentration increased in fixed polymer concentration, the fiber saturated and stopped carrying more particles. The switch of the parabolic behavior from the polymer concentration to the particle concentration improved rsquare to 0.8727.

Finally, the parabolic behavior was assigned to both polymer and particle concentrations (last row in Figure 33). This fit combines second-order dependency of the concentrations. It increased the rsquare to 0.9106 which was acceptable variance. The analysis showed that the fiber diameter has an exponential relation with the polymer concentration. It also showed the saturation behavior with the variable of particle concentration.




```
     Linear model Poly11:
     sf(x,y) = p00 + p10*x + p01*y
     Coefficients (with 95% confidence
bounds):
       p00 =      -94.22  (-709.3, 520.9)
       p10 =       27.87  (5.281, 50.45)
       p01 =      -4.85  (-16.14, 6.443)
           sse: 7.6678e+04
       rsquare: 0.6301
           dfe: 6
    adjrsquare: 0.5068
          rmse: 113.0472
```

```
     Linear model Poly21:
     sf(x,y) = p00 + p10*x + p01*y +
p20*x^2 + p11*x*y
     Coefficients (with 95% confidence
bounds):
       p00 =        1323  (-5230, 7877)
       p10 =      -93.17  (-612.4, 426.1)
       p01 =       0.525  (-91.42, 92.47)
       p20 =       2.507  (-7.76, 12.77)
       p11 =      -0.215  (-3.845, 3.415)
           sse: 6.8362e+04
       rsquare: 0.6702
           dfe: 4
    adjrsquare: 0.3404
          rmse: 130.7302
```

```
     Linear model Poly12:
     sf(x,y) = p00 + p10*x + p01*y +
p11*x*y + p02*y^2
     Coefficients (with 95% confidence
bounds):
       p00 =      -727.8  (-2072, 615.9)
       p10 =       32.17  (-16.55, 80.89)
       p01 =       63.66  (-21.97, 149.3)
       p11 =      -0.215  (-2.47, 2.04)
       p02 =      -1.578  (-3.173, 0.0164)
           sse: 2.6393e+04
       rsquare: 0.8727
           dfe: 4
    adjrsquare: 0.7453
          rmse: 81.2297
```

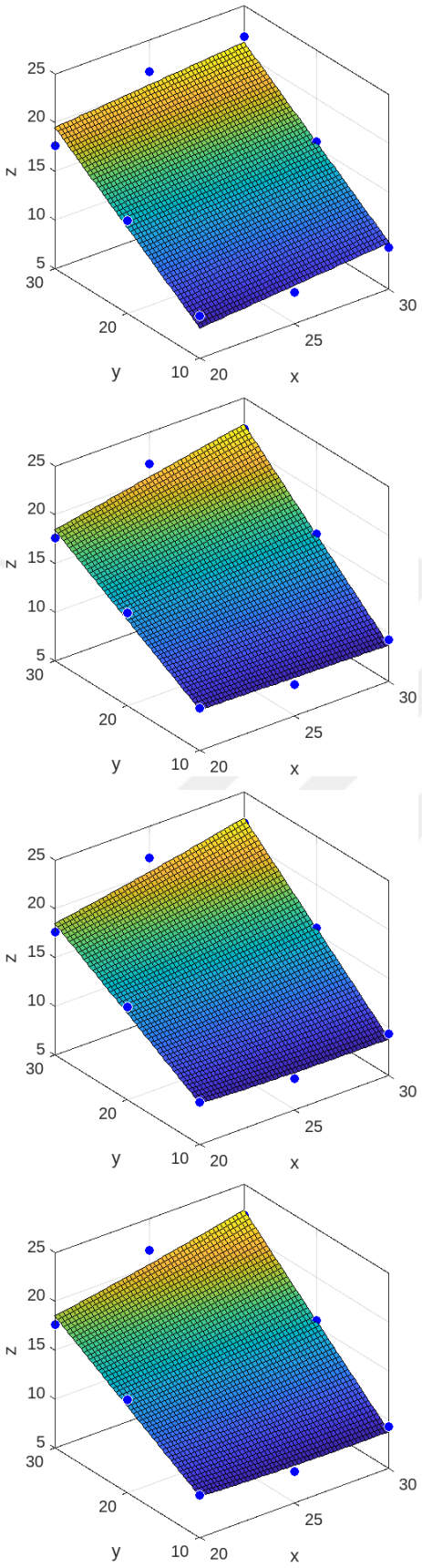
```
     Linear model Poly22:
     sf(x,y) = p00 + p10*x + p01*y +
p20*x^2 + p11*x*y + p02*y^2
     Coefficients (with 95% confidence
bounds):
       p00 =       797.1  (-3758, 5352)
       p10 =      -93.17  (-451.1, 264.7)
       p01 =       63.66  (-31.33, 158.6)
       p20 =       2.507  (-4.569, 9.583)
       p11 =      -0.215  (-2.717, 2.287)
       p02 =      -1.578  (-3.347, 0.1907)
           sse: 1.8539e+04
       rsquare: 0.9106
           dfe: 3
    adjrsquare: 0.7615
          rmse: 78.6106
```

Figure 33: fitted surfaces (left), fit properties (right) for response of fiber diameter

ANOVA for the particle content was shown in Figure 34 for different polynomials. A first-degree polynomial fit (first row in Figure 34) showed that the particle content increased by increasing the polymer concentration. Higher polymer concentrations provided higher polymer chains which facilitated the conversion of the particles to the nanofibers. The polymer content showed a stronger dependence with the particle concentration in the suspension. Quite intuitively, the more particle was added to the suspension, the higher the particle content was transferred. This fit provided a rsquare of 0.9548. Although it was in the acceptable range, second-order polynomial fits were tried as well.

When the parabolic behavior was assigned to the polymer concentration only, the rsquare was dropped 0.9760. When the parabolic behavior was assigned to the particle concentration only, the rsquare was increased slightly to 0.9761. When the parabolic behavior was assigned to both polymer concentration and the particle concentration, the rsquare was improved to 0.9762.

Therefore, it was revealed that as the polymer concentration or the particle concentration increased, the transferred particle content increased accordingly and almost linearly. This result was compared to the saturation phenomenon mentioned in the variation of the fiber diameter. I was concluded that the increase in the polymer concentration was accompanied by the increase in the fiber diameter. Increase in particle concentration at first was accompanied by an increase in the fiber diameter. However, they became independent of each other after certain particle concentrations.




```
     Linear model Poly11:
     sf(x,y) = p00 + p10*x + p01*y
     Coefficients (with 95% confidence
bounds):
       p00 =      -1.071  (-7.905, 5.763)
       p10 =       0.172  (-0.07894,
0.4229)
       p01 =      0.5707  (0.4452, 0.6961)
           sse: 9.4655
       rsquare: 0.9548
           dfe: 6
    adjrsquare: 0.9397
          rmse: 1.2560
```

```
     Linear model Poly12:
     sf(x,y) = p00 + p10*x + p01*y +
p11*x*y + p02*y^2
     Coefficients (with 95% confidence
bounds):
       p00 =       9.565  (-8.99, 28.12)
       p10 =      -0.249  (-0.9217, 0.4237)
       p01 =     0.03108  (-1.151, 1.214)
       p11 =     0.02105  (-0.01009,
0.05219)
       p02 =   0.0003333  (-0.02169,
0.02235)
           sse: 5.0322
       rsquare: 0.9760
           dfe: 4
    adjrsquare: 0.9519
          rmse: 1.1216
```

```
     Linear model Poly21:
     sf(x,y) = p00 + p10*x + p01*y +
p20*x^2 + p11*x*y
     Coefficients (with 95% confidence
bounds):
       p00 =       12.94  (-43.07, 68.95)
       p10 =     -0.5357  (-4.974, 3.902)
       p01 =     0.04442  (-0.7414, 0.8302)
       p20 =    0.005733  (-0.08201,
0.09347)
       p11 =     0.02105  (-0.009971,
0.05207)
           sse: 4.9934
       rsquare: 0.9761
           dfe: 4
    adjrsquare: 0.9523
          rmse: 1.1173
```

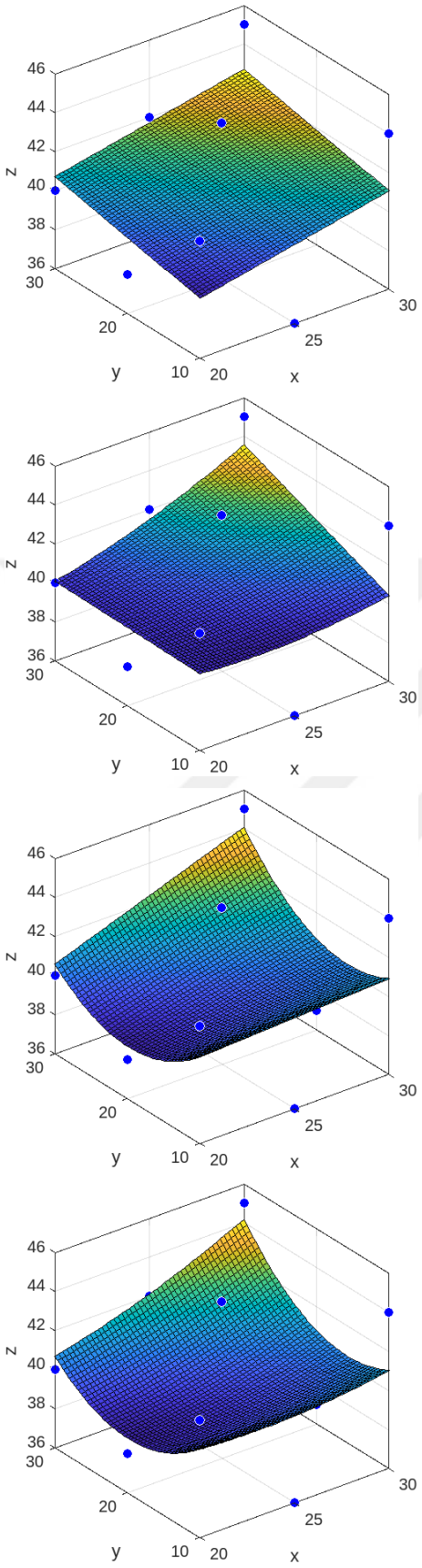
```
     Linear model Poly22:
     sf(x,y) = p00 + p10*x + p01*y +
p20*x^2 + p11*x*y + p02*y^2
     Coefficients (with 95% confidence
bounds):
       p00 =       13.05  (-61.69, 87.8)
       p10 =     -0.5357  (-6.408, 5.337)
       p01 =     0.03108  (-1.528, 1.59)
       p20 =    0.005733  (-0.1104, 0.1218)
       p11 =     0.02105  (-0.02, 0.0621)
       p02 =   0.0003333  (-0.02869,
0.02936)
           sse: 4.9912
       rsquare: 0.9762
           dfe: 3
    adjrsquare: 0.9364
          rmse: 1.2899
```

Figure 34: fitted surfaces (left), fit properties (right) for response of particle content

ANOVA of the contact angle was shown in Figure 35. A fit of the first-order polynomial showed that the contact angle increased by increasing the polymer concentration or particle concentration. Although the contact angle changed only slightly. This had a rsquare of 0.1170 which was far from the acceptable region.

Next, the fit was increased to a second-order polynomial. When the parabolic behavior was assigned to the polymer concentration only, the dependence of the response lowered in lower (second row in Figure 35). This fit improved the rsquare to 0.2203, but it was yet far from acceptable. When the parabolic behavior switched the particle concentration, it was shown that the dependence of the contact angle to the particle content became more complex (second row in Figure 35). The rsquare value, however, was worsened to 0.1455. Finally, when parabolic behavior was assigned to both polymer and particle concentration, the complex dependence of the contact angle on the particle concentration stayed. Yet, the complex dependence of the contact angle on the polymer concentration was quite strait forward (third row in Figure 35).

The dependence of the contact angle on the polymer concentration (third row in Figure 35) was like that of the fiber diameter (third row in Figure 33). In other words, increasing the polymer concentration increased the fiber diameter and the contact angle. This behavior might suggest that finer fibers provide the epoxy resin with higher surface that it can create an interface.




```
     Linear model Poly11:
     sf(x,y) = p00 + p10*x + p01*y
     Coefficients (with 95% confidence
bounds):
       p00 =       34.22  (14.77, 53.68)
       p10 =         0.2  (-0.5144, 0.9144)
       p01 =     0.08333  (-0.2739, 0.4405)
           sse: 76.7222
       rsquare: 0.1170
           dfe: 6
    adjrsquare: -0.1773
          rmse: 3.5759
```

```
     Linear model Poly21:
     sf(x,y) = p00 + p10*x + p01*y +
p20*x^2 + p11*x*y
     Coefficients (with 95% confidence
bounds):
       p00 =       49.83  (-166.1, 265.8)
       p10 =     -0.7667  (-17.88, 16.35)
       p01 =     -0.2917  (-3.322, 2.738)
       p20 =     0.01333  (-0.325, 0.3517)
       p11 =       0.015  (-0.1046, 0.1346)
           sse: 67.7500
       rsquare: 0.2203
           dfe: 4
    adjrsquare: -0.5595
          rmse: 4.1155
```

```
     Linear model Poly12:
     sf(x,y) = p00 + p10*x + p01*y +
p11*x*y + p02*y^2
     Coefficients (with 95% confidence
bounds):
       p00 =       47.83  (-20.25, 115.9)
       p10 =        -0.1  (-2.568, 2.368)
       p01 =      -1.025  (-5.364, 3.314)
       p11 =       0.015  (-0.09927,
0.1293)
       p02 =     0.01833  (-0.06246,
0.09913)
           sse: 74.2500
       rsquare: 0.1455
           dfe: 4
    adjrsquare: -0.7091
          rmse: 4.3084
```

```
     Linear model Poly22:
     sf(x,y) = p00 + p10*x + p01*y +
p20*x^2 + p11*x*y + p02*y^2
     Coefficients (with 95% confidence
bounds):
       p00 =       55.94  (-219, 330.9)
       p10 =     -0.7667  (-22.37, 20.83)
       p01 =      -1.025  (-6.758, 4.708)
       p20 =     0.01333  (-0.4137, 0.4404)
       p11 =       0.015  (-0.136, 0.166)
       p02 =     0.01833  (-0.08843,
0.1251)
           sse: 67.5278
       rsquare: 0.2228
           dfe: 3
    adjrsquare: -1.0725
          rmse: 4.7444
```

Figure 35: fitted surfaces (left), fit properties (right) for response of contact angle

5.3.5 Homogenous distribution of particles

Thermogravimetry analysis was shown for 9 segmented samples of a representative nanofiber composite . The polymer concentration of this composite was 25 wt.% and the nominal particle concentration of 20 wt.% (Figure 36). The onset temperature was determined for the degradation of the polymer as the temperature at which the residual mass was still equal to 95%. This situation corresponded to approximately 330°C. The end temperature for the degradation of polymer was determined based on the stabilized residual mass. It was assumed that after this temperature no further mass loss occurs. This caused the Residual mass curve to stay flat onwards. The end temperature for the polymer degradation was determined to be around 468°C. The residual mass was calculated between the onset and end temperatures of the polymer degradation. The residual mass after the end temperature of the polymer degradation was assumed to be identical to the initial particle content the segmented sample.

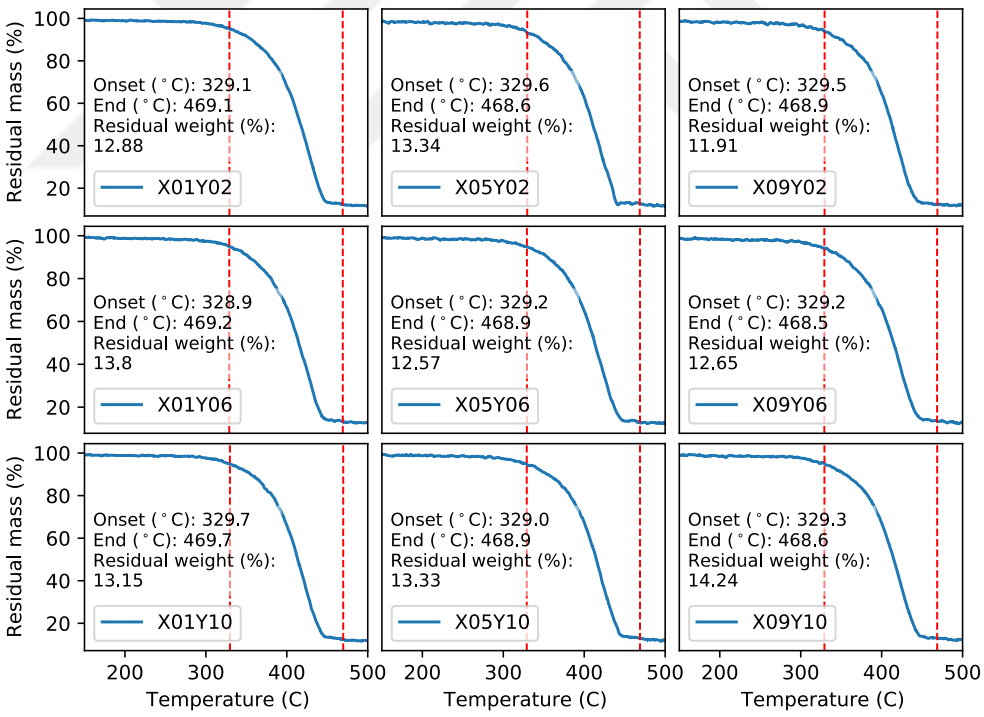


Figure 36: TGA of segmented samples from a P(St-*co*-GMA)-ZrO_2 membrane with polymer concentration of 25 wt.% and nominal particle concentration of 20 wt.% (medium: synthetic dry air)

Residual mass for all segmented samples were reported in Table 9. The maximum particle content was 13.7% and the minimum particle content was 12.0%. The difference between the maximum and the minimum particle content was 1.7%. The average particle content for the representative membrane was 12.5 ± 0.6. Overall, the areal dispersion of the particles could be considered as homogeneous in the sample.

Table 10: particles content various points of a P(St-*co*-GMA)-ZrO2 membrane (polymer concentration 25 wt.% and particle concentration 20 wt.%)

Sample ID	Coordinate X (cm)	Coordinate Y (cm)	Residual mass [%]
X01Y02	1	2	12.4
X01Y06	1	6	13.2
X01Y10	1	10	12.6
X05Y02	5	2	12.6
X05Y06	5	6	12.1
X05Y10	5	10	12.7
X09Y02	9	2	11.3
X09Y06	9	6	12.0
X09Y10	9	10	13.7
Average			12.5
Standard Deviation			0.6

Analysis of the segmented nanofiber membrane in Figure 31 showed that starting from the top left corner of the membrane (X00Y00 in Figure 31), the particle content tended to reduce toward the center of the membrane and again increase toward its opposite corner (X09Y10 in Figure 31). This might imply that in every electrospun nanofiber membrane the edges could attract slightly more of the particles due to the accumulation of charges. Also, there are two opposite corners which this phenomenon arises more strongly there, X01Y02 and X09Y10 in this case.

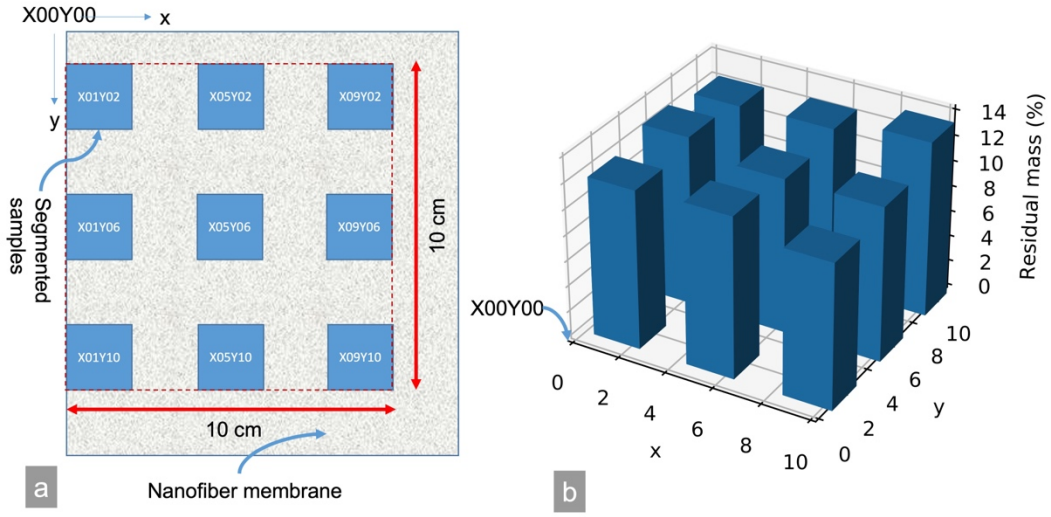


Figure 37: (a) Segmented samples from a P(St-*co*-GMA)-ZrO2 membrane with polymer concentration of 25 wt.% and nominal particle concentration of 20 wt.%, (b) actual particle content of segmented samples

5.4 Conclusion

Composite nanofibers of P(St-*co*-GMA) and zirconia particles was synthesized using electrospinning. Polymer and particle concentrations were varied systematically following a RSM with full factorial design. Three different responses were analyzed: fiber diameter, actual particle content, and contact angle with liquid epoxy resin. Fiber diameter was increased by polymer concentration but increased with particle concentration only to a certain degree, then it reduced. Particle content was increased by both polymer and particle concentrations. Contact angle was found to be correlated to the fiber diameter. The lower the fiber diameter, the lower the contact angle in general. Homogeneity of particle content in a membrane of composite fibers was analyzed. It was found that the particle content was homogenous withing 10% throughout the membrane.

CHAPTER 6
DRILLED CARBON FIBER COMPOSITES WITH LOCAL NANOFIBER-NANOPARTICLE TOUGHENING INTERLAYER[††]

Summary

Present study focuses on the improvement of the damage resistance of composites against the drilling. Local interlayer toughening agents were added to the interlaminar region to improve the fracture behavior of composites. Additives of cubic and tetragonal zirconia were used to benefit from the stress-induced phase transformation of the metastable tetragonal zirconia. Composites samples prepared from PW carbon-fabric prepregs with epoxy matrix. Interlayers were synthesized using electrospinning technique with a suspension of PAN nanofibers loaded with cubic or tetragonal zirconia particles. Samples were mechanically tested and machined to the standard geometry of open hole. Fracture surface were analyzed around the hole and far from the hole using optical microscopy and SEM. It was found that the presence of interlayers had only a minor effect on the mechanical properties of composites. The effect was associated with the polymeric phase in the composite nanofibers. Stress-induced phase transformation of tetragonal zirconia was not found to have a significant effect.

[††] Submitted abstract to the 23rd International Conference Composite Materials (ICCM 23), Belfast, Northern Ireland, 30 Jul – 04 Aug 2022

6.1 Introduction

6.1.1 Drilling damage

Drilling is often used as part of the mechanical joining for composites in aerospace and automotive industries. In the aircraft industry, about 60% of part rejections come from drilling-associated delamination [163]. Drilling-induce peel-off damages in the entrance of the hole and push-out damages at the exit of the hole lead composites to fail to satisfy the quality assurance and application endurance requirements.

Machining-induced damages include 1) edges cut with waterjet, 2) the entering and exit zone of drilled hole, 3) through the thickness of the hole. According to the literature [164], we anticipate observing damages like 1) pulled-out fibers and 2) indents at the interlaminar region along the edges and drilled hole. Several types of drill bit geometry were used to for machining of composites, including (a) standard twist drill, (b) step drill, (c) brad-spur (or candle stick) drill, (d) one shot (or dagger) drill, (e) multi-faced drill, (f) core (or trepanning) drill [165]. Furthermore, special types of drill bits also were designed for composites to minimize the damages.

Reason for most of the damages is the lack of toughness in the resin rich area of composites. Mode I (opening) and Mode III (tearing shear) are effective fracture modes and at the exit damage zone Mode I (opening) and Mode II (sliding shear) mechanisms are effective in disintegration of the laminated structure, which finally results in delamination [166]

Toughening of composites, at least in the vicinity of the hole, would be a promising approach to increase the drilling resistance of composite parts. There are several methods to increase the toughness of the composites among which implementation of toughening interlayer has been proven to be effective. Toughening materials were employed in forms of particles, polymer sheets, and fibrous interlayers. Additive particles such as glass beads [167], rubber [168], silica [52], [56], [169], silicon carbide [170]–[173], and CNT [174]–[179] have improved the toughness polymers extensively.

Nanofibrous toughening interlayers have been investigated deeply and found to be effective in the improvement of fracture toughness of composites in all three modes. Therefore, in the scope of this research, a toughening interlayer has been prepared and implemented in the area around the drilling hole. Various changes in drilling-induced damages are aimed to be determined using computed tomography. It is hypothesized that the nature of the drilling-induced damages will be different for toughened samples than

that of the references. For instance, nanofibrous interlayers of P(St-*co*-GMA) was used to improve the fracture toughness of UD carbon fibers composites with epoxy resin [13]. Composites were prepared for standard tensile samples and open-hole geometry. Single layer nanofiber reinforcement at the laminate mid-plane was also synthesized. G_{IIc} was measured in an end-notch fracture configuration [13].

Composite nanofibers are the application of these fibers as toughening interlayer [4], [29], [30]. The presence of these interlayers inhibits crack opening and propagation in the interlaminar region of laminated composites. This region is considered as the weakest point in the strength of composites. Inherent imperfections in this region start to create microcracks when the campsites undergo mechanical load. Improving the properties of this region suppresses the crack initiation or propagation. Finally, this change leads to an improved delamination resistance [180].

Zirconia is mechanically strong ceramic that has various application in ceramic industry [181], [182]. Zirconia has three polymorphs in monoclinic (m-ZrO_2), tetragonal (t-ZrO_2), and cubic (c-ZrO2) crystallographic orientations. Among them only m-ZrO_2 is stable at room temperature. Others emerge at elevated temperature. To stabilize them in room temperature, they should be dopped with other oxides such as yttria (Y_2O_3) [183]. The amount of this doping determines the crystallographic structure of the polymorph. If ZrO_2 is doped by 3 mol.%, the resulted structure is m-ZrO2. If ZrO_2 is doped by higher than 9 mol.%, the obtained ZrO2 is in the cubic structure. Once special feature about m-ZrO2 is that it is metastable. If t-ZrO2 undergoes enough stress, it can go through a phase transformation to m-ZrO2. Therefore, t-ZrO2 is called metastable or partially stabilized m-ZrO2. On the other hand, c-ZrO2 lacks this feature as it is fully stabilized [182], [184]. Metastable mZrO2 has been used to introduce pseudo ductility to ceramics. Transformation toughening of t-ZrO2 improved the fracture toughness of ceramics [185]. Metastable t-ZrO_2 particles were used as an additive to epoxy matrix. The aim was to benefit from the metastability of these particles in fracture tests. It was found that the addition of the particle up to 10 wt.% increased the fracture toughness from ~0.7 MPa√m to ~1.0 MPa√m. After this particle content, the fractur toughness of the composites started to be deteriorate. At 50 wt.% , the filled epoxy had the fracture toughness as low as the unmodified epoxy resin. The lack of significant contribution from the phase transformation of zirconia was associated with the high stress of transformation zirconia

($\sigma_T = 450$ MPa). The crack tip was not able to transfer that amount of stress to zirconia particles to trigger the phase transformation [186].

However, no open literature focused so far on the possibility of taking the advantage of stress-induced phase transformation to suppress drilling damage in laminated composites. This research hypothesized that 1) composite nanofibers of PAN loaded with particles of zirconia can improve the interlayer toughening of composites, and 2) presence of partially stabilized zirconia (t-ZrO_2) can absorb some of the energy and transform to m-ZrO_2, 3) same effect could not be obtained by fully stabilized zirconia (c-ZrO_2).

6.2 Experimental

6.2.1 Materials

Composite material for this study was provided by KORDSA. It is carbon fiber woven fabric epoxy prepreg with PW. Nanofibers were produced by electrospinning of polymer particle suspension. The polymer was PAN average Mw 150,000 (Sigma-Aldrich) which was dissolved in *N,N*-Dimethylformamide (DMF, Sigma-Aldrich). Two grades of particles were added to the polymer solution at the beginning. Cubic ZrO_2 (TZ-9Y-E, Tosoh, Japan) and tetragonal ZrO_2 (TZ-3Y-E, Tosoh, Japan). The mixtures were produced with 10 wt.% of polymer and 10 wt.% of the powders. The suspension was fed by a syringe pump (NewEra NE-100) through a needle with an inner diameter of 300 μm while the electrostatic field were created by a high-voltage bias potential (Gamma High Voltage ES 30P-20W) in between the needle and an aluminum collector. To collect nanofibers directly on the prepreg composite material, a modified collector was used which had a 50 mm wide aluminum plate at the center from side to side. Only this aluminum plate was connected to the potential. The electrostatic field was built between the tip of the needle and this aluminum plate.

6.2.2 Composite design

The main reinforcement was positioned and connected to this collector so that nanofibers were preferably collected on the region of interest. The rest of the ply was covered by support plastics to prevent randomly scattered fibres being collected on the regions outside of the interest. Neat samples were prepared as a stack of 10 plies (Figure 38a). Locally toughened samples were also produced as a stack of 10 prepreg plies, 9 of them being partially coated with nanofibers. Composite laminates were produced as 250 mm by 250 mm in size (Figure 38b). Two peel plies were added on the opposite sides of the stack. The stack was placed between two caul plates covered by Teflon sheets. The

composite plates was processed with a hot press using the curing cycle steps: 1. Heating from 25C° by 2 C°/min to 80°C, 2. Isothermal at 80°C for 10 min, 3. Heating from 80°C by 2 C°/min to 120°C, 4. Isothermal at 120°C for 60 min, 5. Cooling from 120°C by to room temperature (Figure 39a). Throughout the processing, the vacuum-bagged composite lay-up was under 0.5 MPa pressure and connected to a vacuum pump to facilitate extraction of volatiles (Figure 39b).

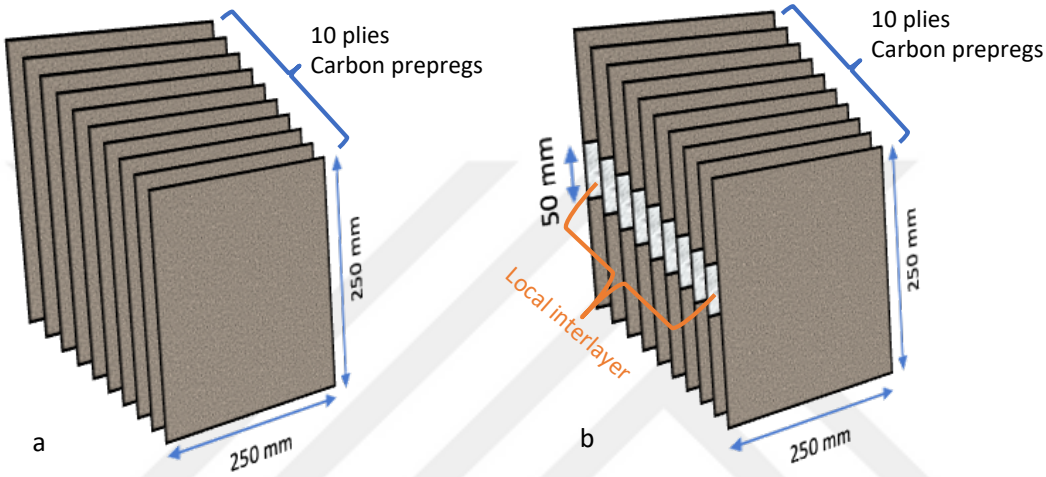


Figure 38: Composite lay-ups (a) reference, (b) locally interleaved/toughened.

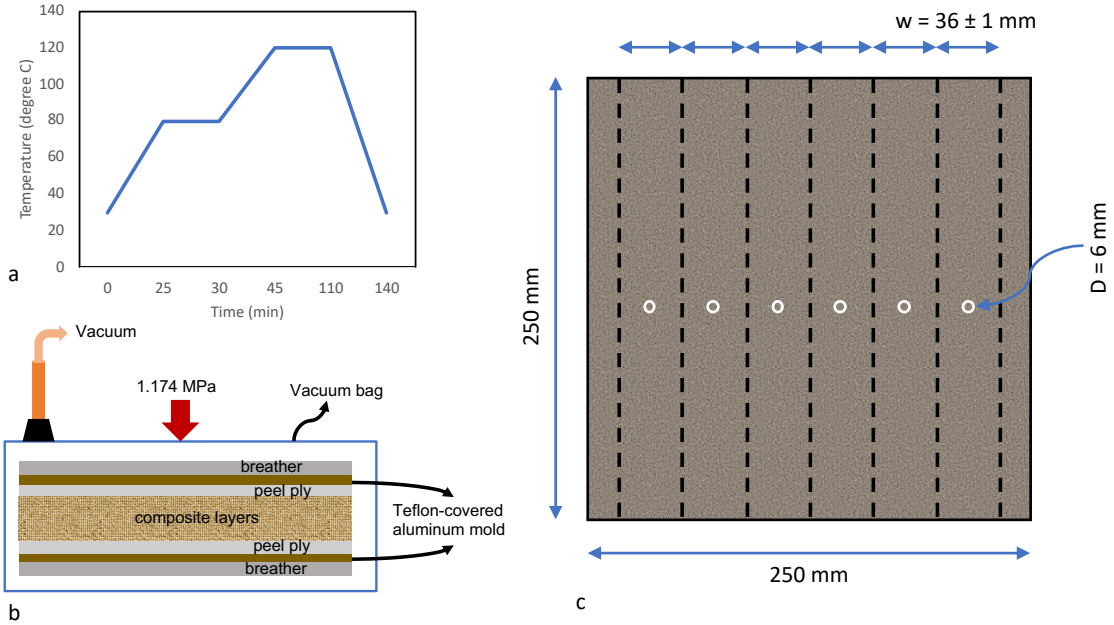


Figure 39: Processing and preparation of drilled samples (a) cure cycle, (b) vacuum-assisted compression molding, (c) waterjet cutting scheme for open-hole tension test samples.

6.2.3 Machining

Coupons were cut from the composite plates by KTM Neoline / 40i OEM Water Jet, 3800 bar with 10% Abrasive grit (Gurmet 80 mesh) and 250 mm/min feed-rate. Samples were cut to comply with ASTM D5766/D5766M (Figure 39c). The coupons were drilled by a Poysan 3-axis cutting router, Zünd R290 bit composite milling with 2.4 mm diameter, 6000 RPM, and 300 mm/min feed-rate and circular interpolation cutting .

6.2.4 Fracture analysis

All the samples with drilled holes were investigated using optical microscope (Nikon SMZ 1500) both at the sides and faces exposed to machining. Further analyses were performed by FE-SEM, Zeiss, Leo Supra VP 35. SEM analyses were performed around the hole before the mechanical testing and on the fracture surface after mechanical testing.

6.2.5 Mechanical testing

Composite specimens were tested under uniaxial tensile testing mode using a Zwick/ Roell, Z100 Proline machine operated with 100 kN loadcell and at an extension rate of 2 mm/min (according to ASTM D5766). The gap between the grips were set to 110 mm. The strain was measured using a contact extensometer with 50 mm gap. The hole was equally distanced with respect to the arms of the extensometer (Figure 40).

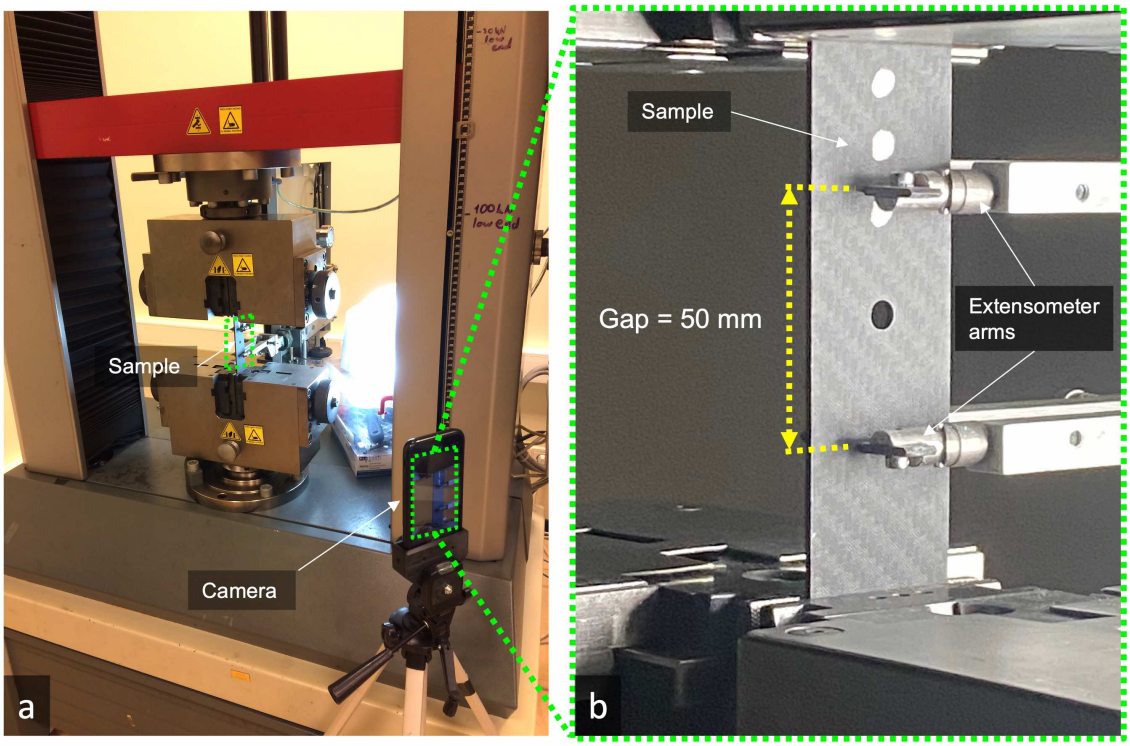


Figure 40: Tensile test setup (a) and extensometer configuration (b) for mechanical testing

6.3 Results

6.3.1 Morphology of particles

SEM image of the powders revealed the spherical clusters produced by spray drying method in both powders, i.e., c-ZrO2 and t-ZrO2 (Figure 41). Some of the spheres were kept their integrity while some of them were broken by the forces exerted in the sample preparation steps.

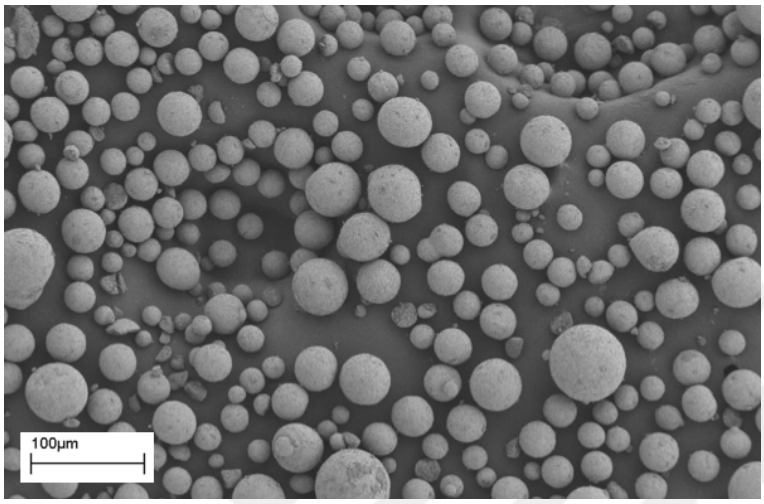


Figure 41: typical particle clusters before breaking into nanoparticles.

In the solution the clusters were broken down to nanoparticles with a diameter of around 100 nm (Figure 42). Embedded particles were determined in the polymer nanofibers using the higher backscattered electron yield of Zirconium atoms with comparison to that of carbon atoms in the backbone of the polymer (Figure 42).

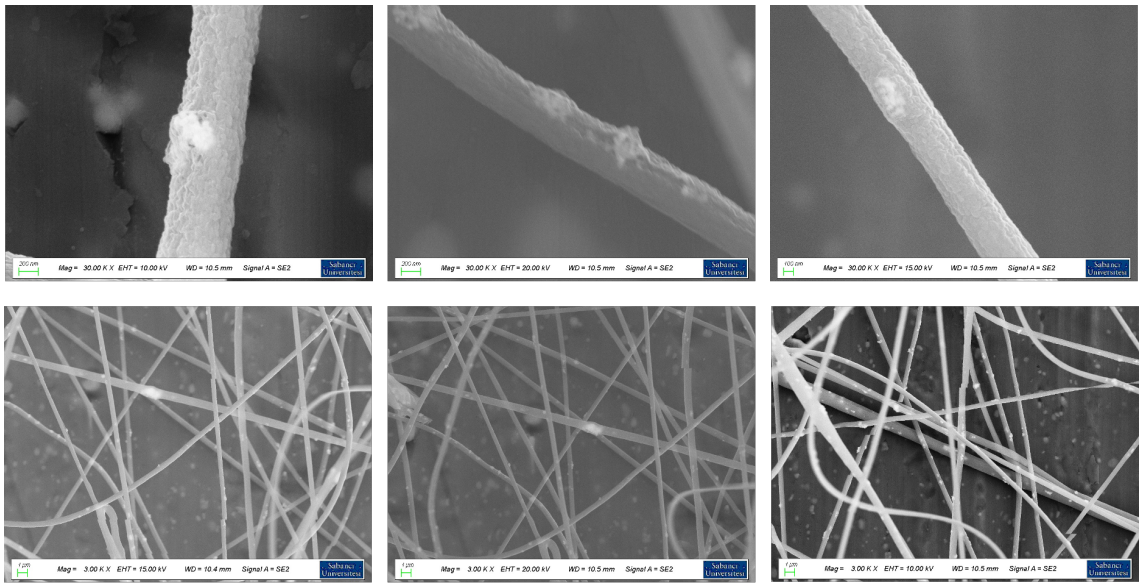


Figure 42: Morphology of the toughening nanofiber-nanoparticle interlayer.

EDS analysis of the PAN-c-ZrO2 and PAN-t-ZrO2 nanofibers showed the Zr Lα energy peak at one of the bright points in the composite nanofiber (Figure 43).

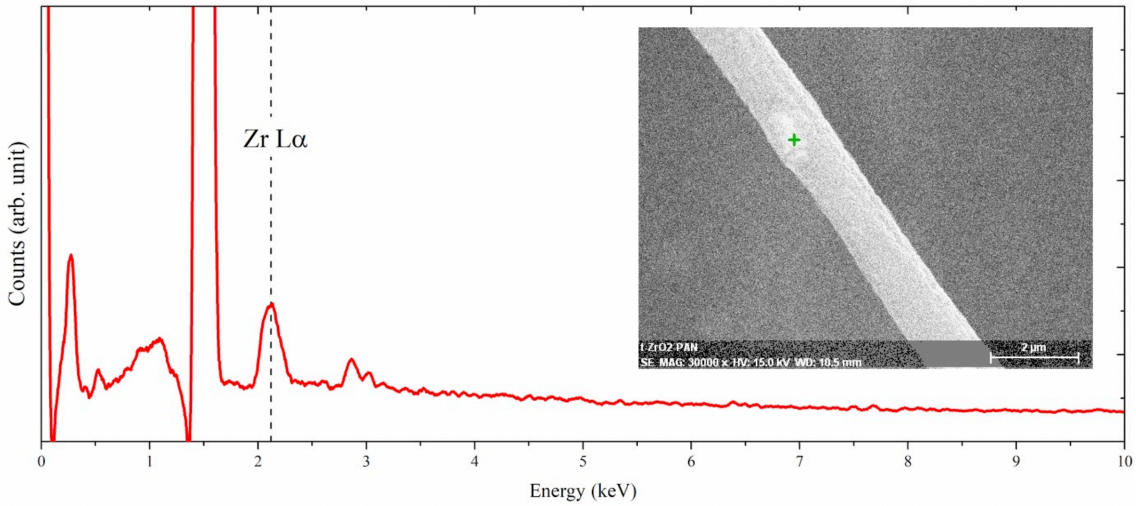


Figure 43: Elemental characterization of t-nanoparticle-impregnated PAN nanofibers.

6.3.2 Optical microscopy of drilled holes

Samples are prepared in 36 mm x 250 mm using a waterjet cut on the edges and a drilled hole at the center with 6 mm diameter. It is aimed that the quality of the cut at the edges near the hole and the periphery of the hole be investigated in terms of the quality of the cut and the possible effects of the toughening interlayers. Optic microscope images of the neat samples were given in Figure 44 and Figure 45. Optic microscope images of composites with the interlays of PAN-c-ZrO2 were given in Figure 46 and Figure 47. Optic microscope images of composites with the interlayers of PAN-t-ZrO2 were given in Figure 48 and Figure 49. Optic microscope image of the sideview of the selected neat sample was given in Figure 50. Optic microscope image of the sideview of the selected composite with PAN-c-ZrO2 was given in Figure 51. Optic microscope image of the sideview of the selected composite with PAN-t-ZrO2 was given in Figure 52.

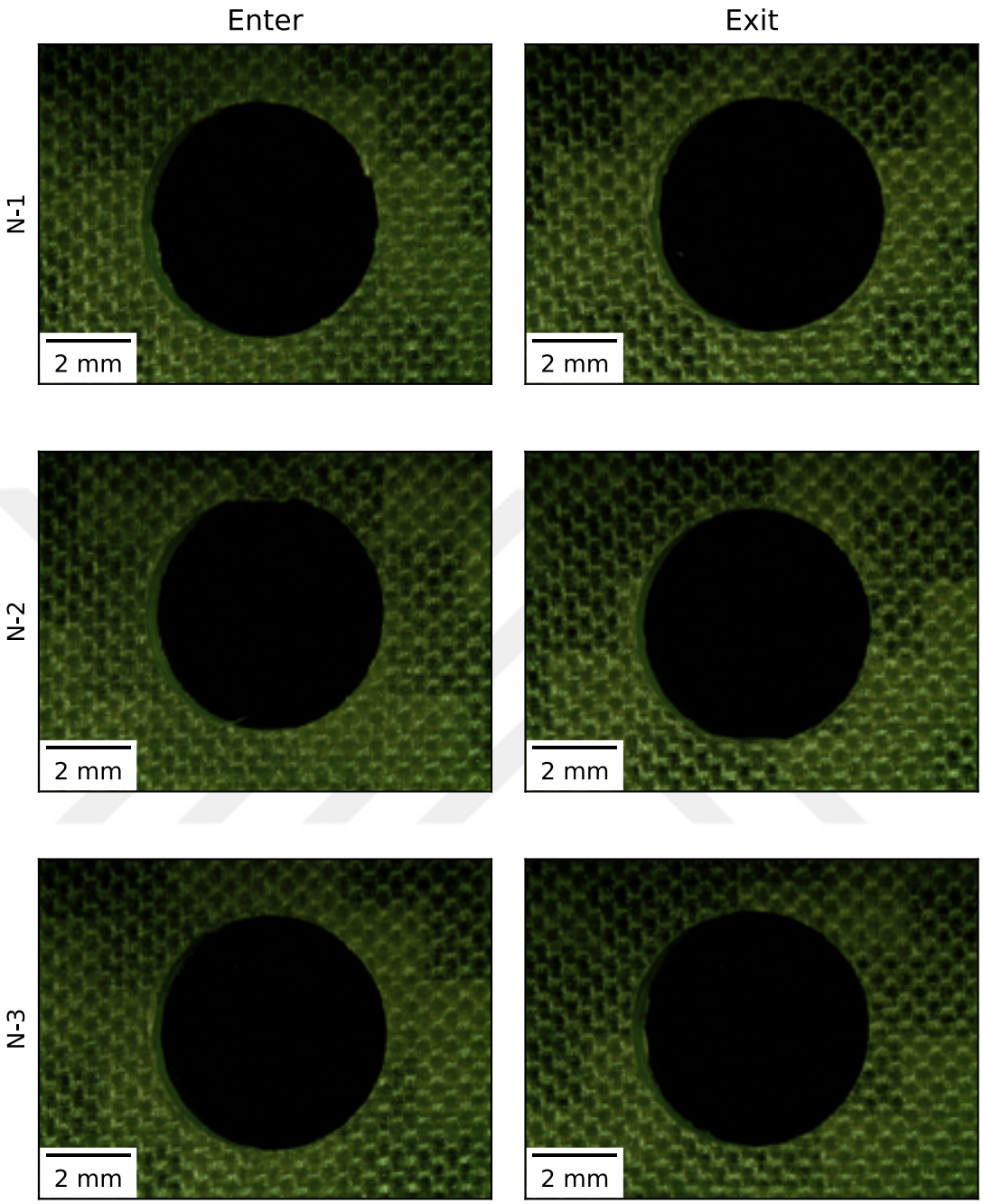


Figure 44: Drilled hole of reference sample with no toughening interlayer, sample N-1 to N-3 enter and exit.

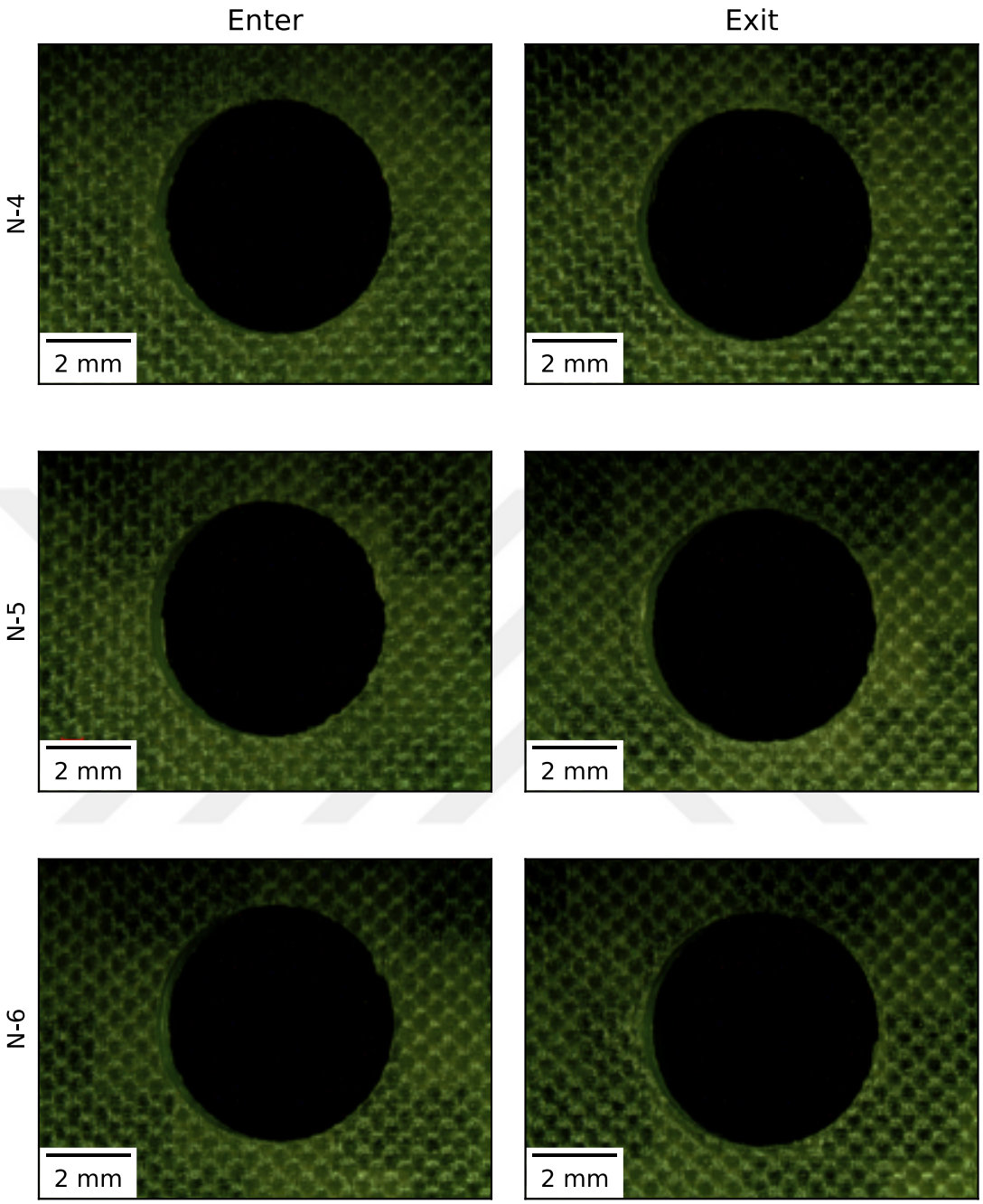


Figure 45: Drilled hole of reference sample with no toughening interlayer, sample N-4 to N-6 enter and exit.

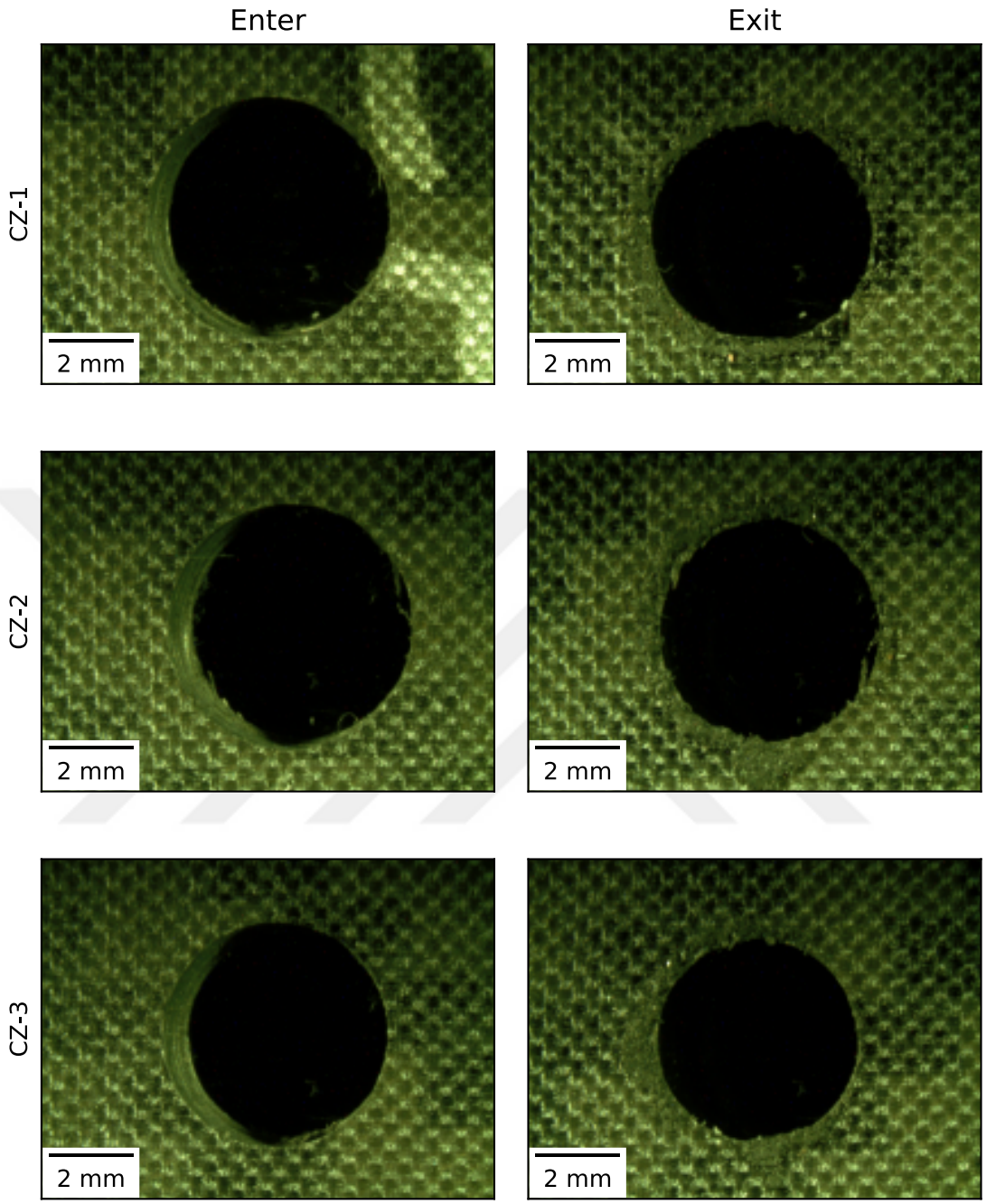


Figure 46: Drilled hole of toughened samples with PAN-c-ZrO_2 interlayer, sample CZ-1 to CZ-3 enter and exit.

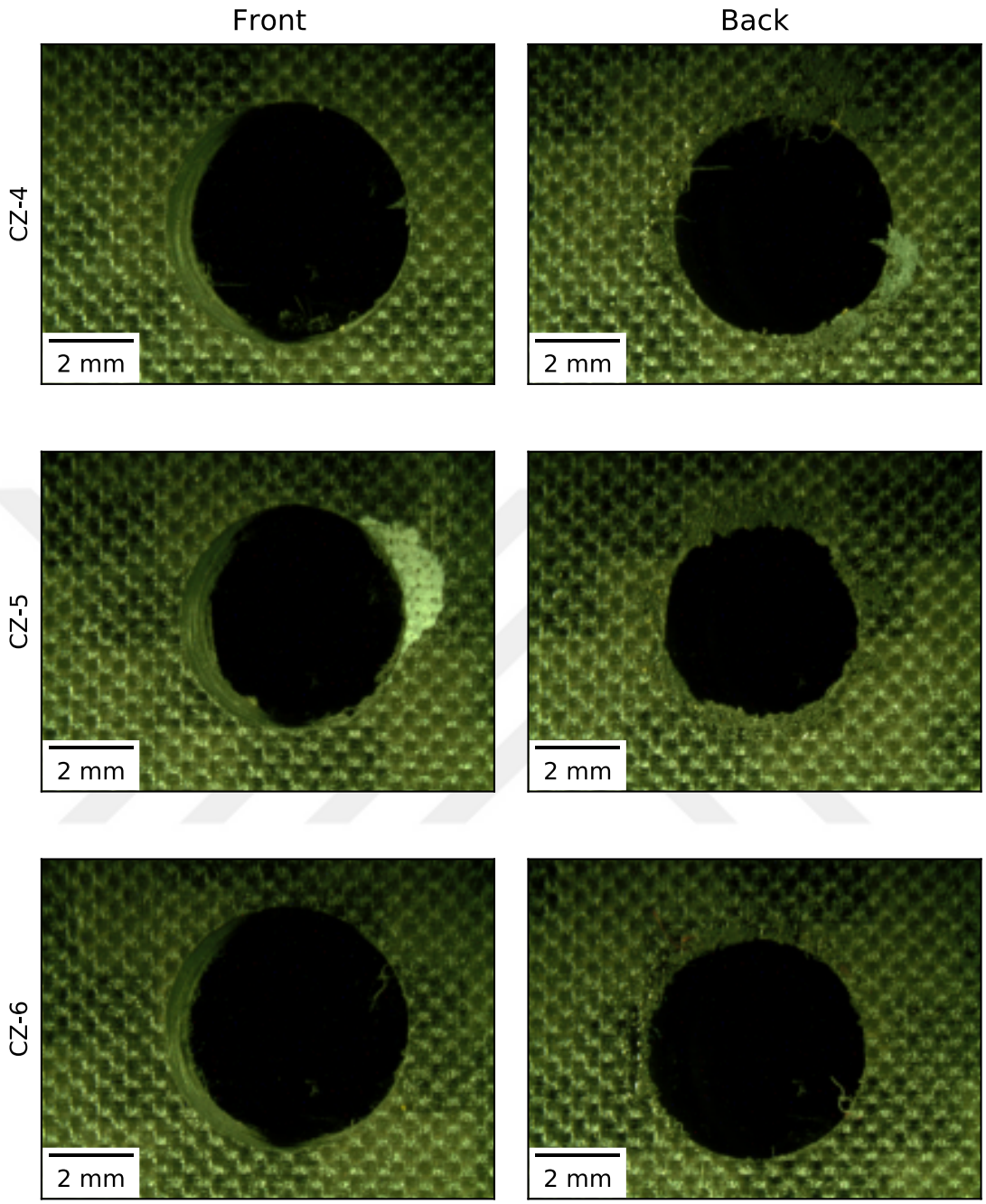


Figure 47: Drilled hole of toughened samples with PAN-c-ZrO_2 interlayer, sample CZ-4 to CZ-6 enter and exit.

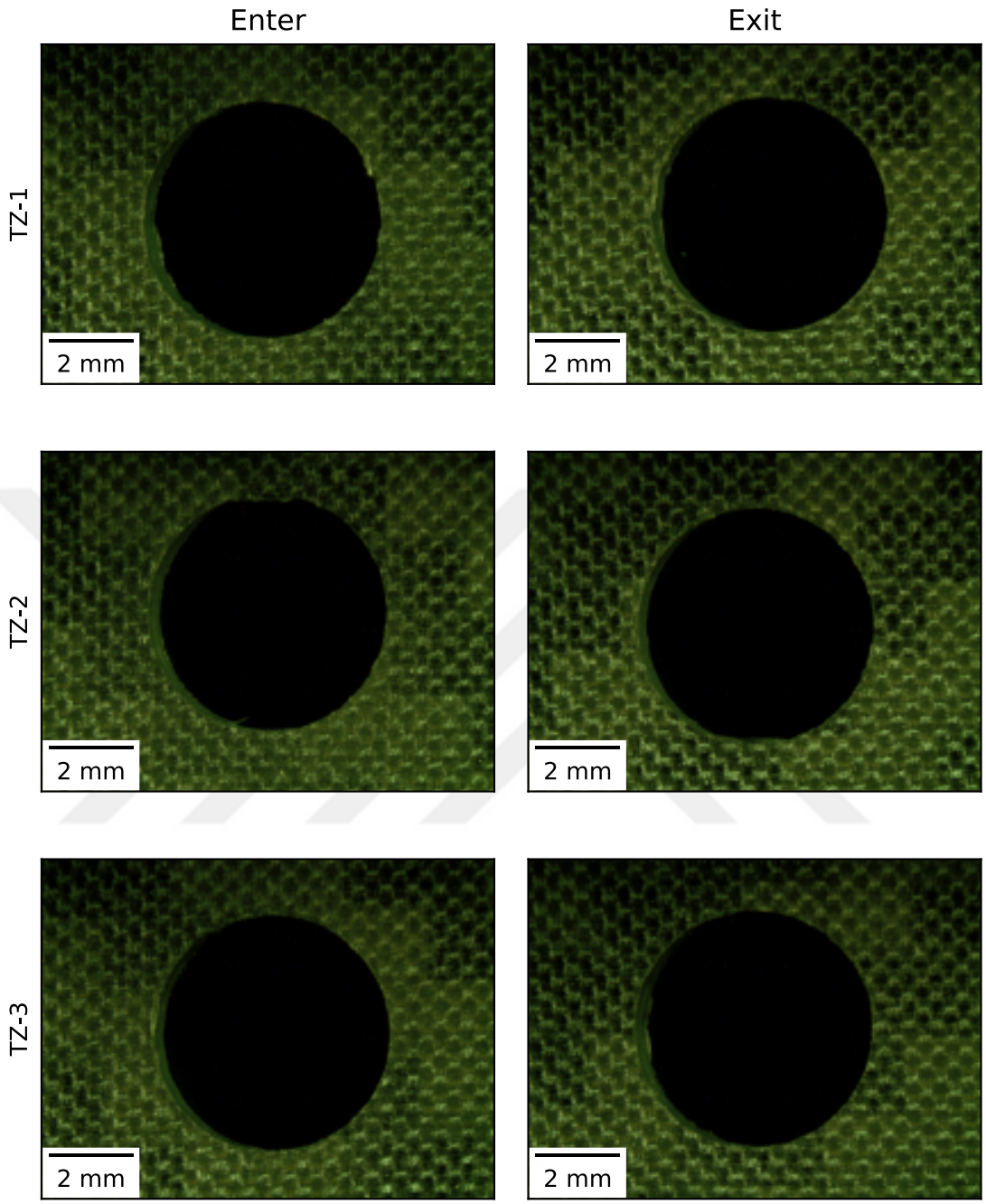


Figure 48: Drilled hole of toughened samples with PAN-t-ZrO_2 interlayer, sample TZ-1 to TZ-3 enter and exit.

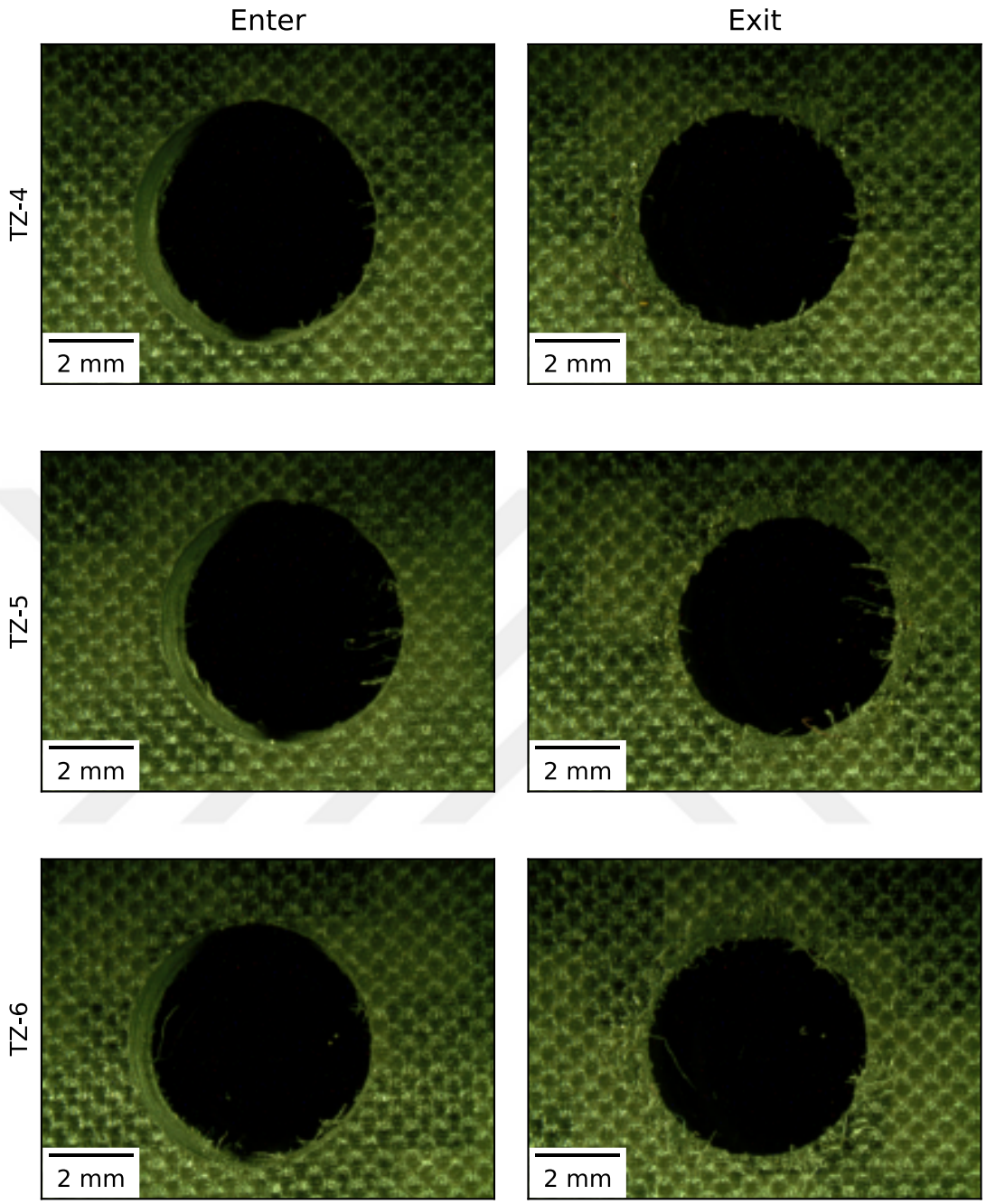


Figure 49: Drilled hole of toughened samples with PAN-t-ZrO_2 interlayer, sample TZ-4 to TZ-6 enter and exit.

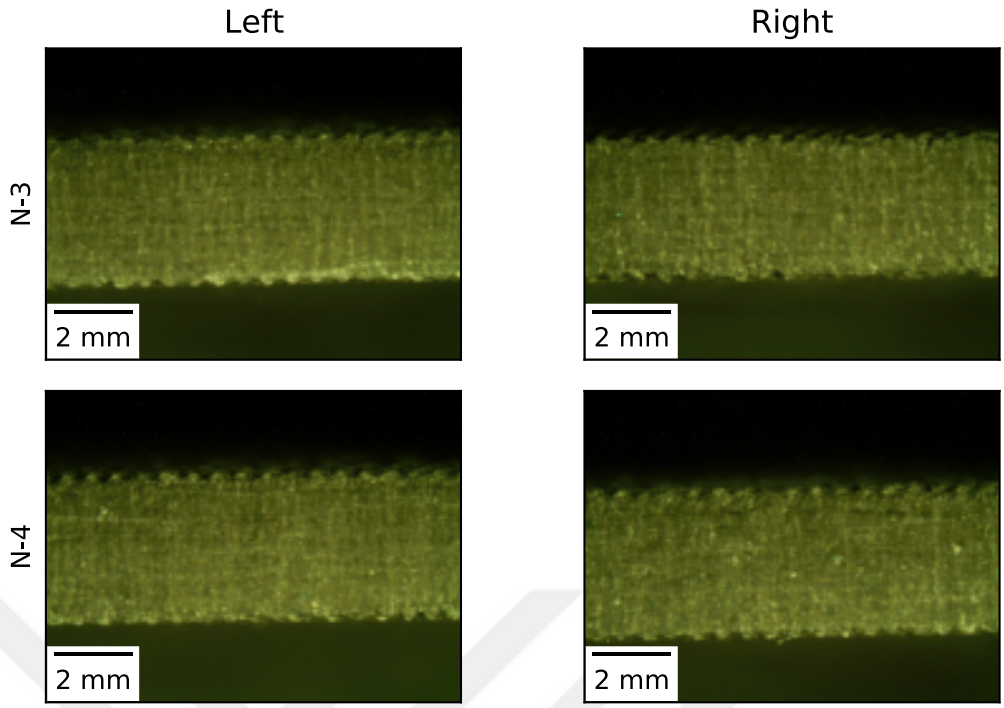


Figure 50: Optic microscope photos of left and right edges of composite coupons around the drilled hole.

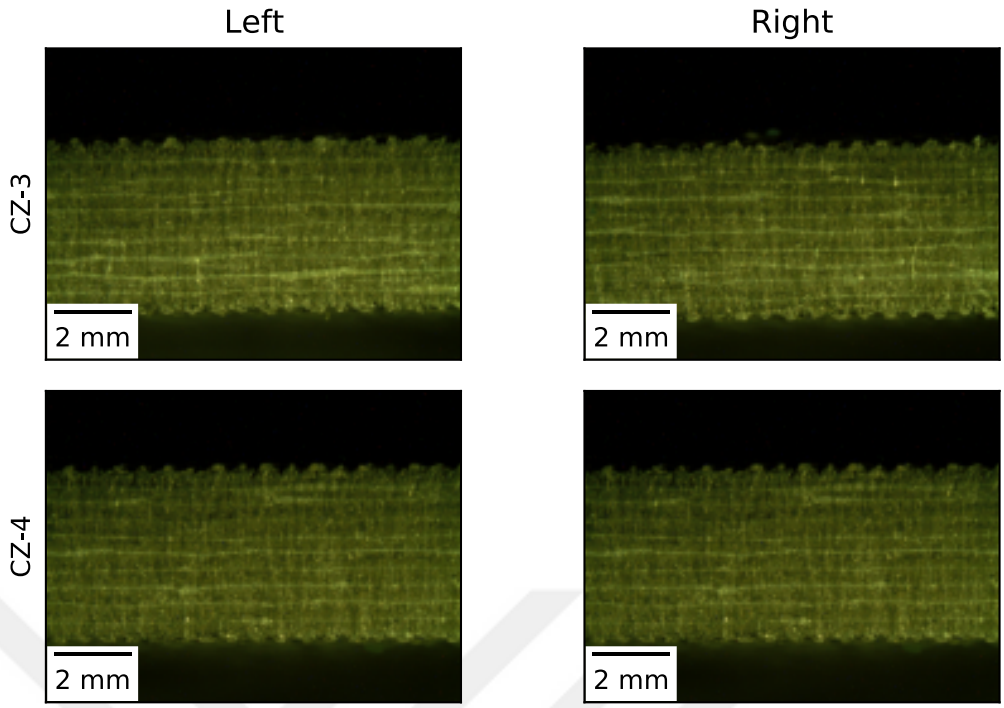


Figure 51: Optic microscope photos of left and right edges of composite coupons around the drilled hole.

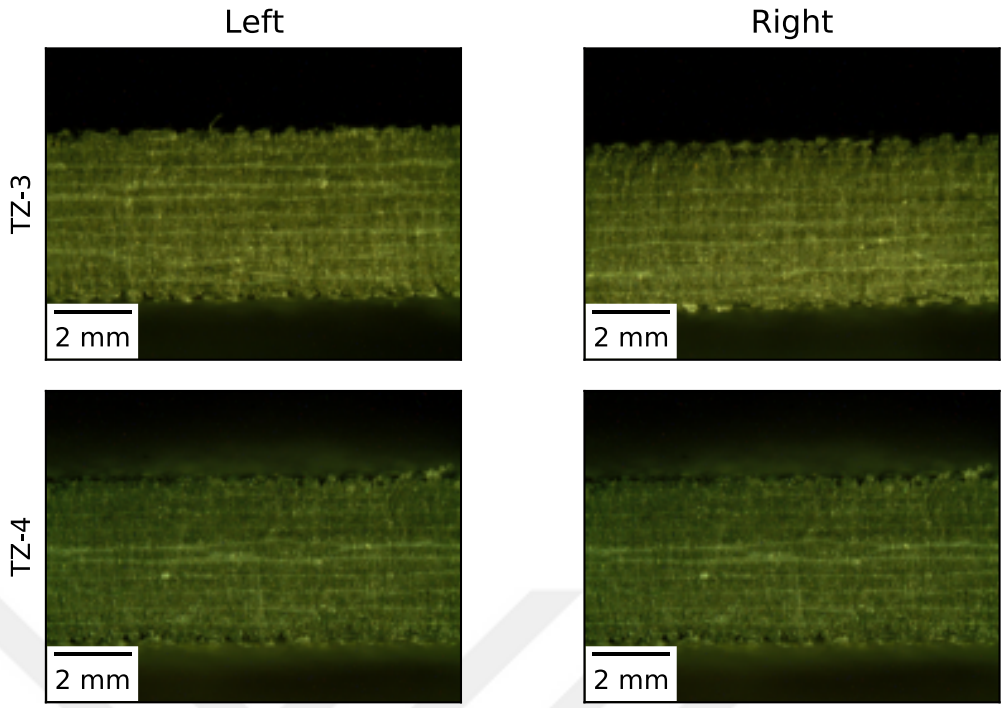


Figure 52: Optic microscope photos of left and right edges of composite coupons around the drilled hole.

6.3.3 SEM microscopy of drilled holes

Drilled holes of a neat composite sample, one composites with local toughening of PAN-c-ZrO_2, and one composite with local toughening of PAN-t-ZrO2 were analyzed in the microscope before any mechanical test (Figure 53). The drilling vector was shown by $\vec{d}$ on the micrographs. The wall angles for neat sample was 85°, for the composite sample with the local toughening interlayer of PAN-c-ZrO2 was 81°, and for the composite with the local toughening interlayer of PAN-t-ZrO_2 was 79°.

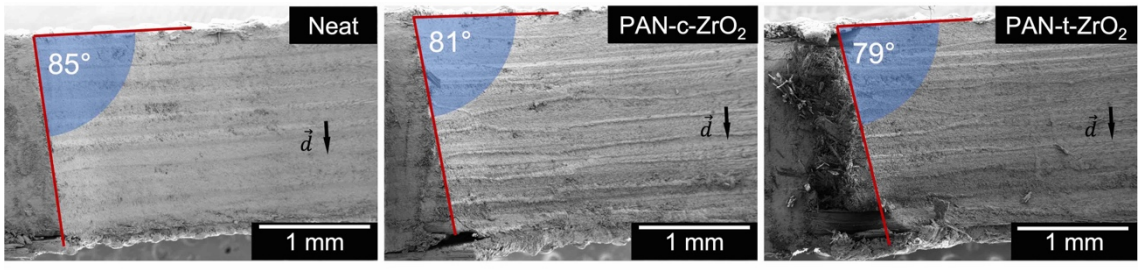


Figure 53: representative micrograph of the angle of wall in the drilled hole for a neat composite and composites with the local interlayers of PAN-c-ZrO_2 and PAN-c-ZrO_2

6.3.4 Mechanical testing

Drilled hole composites with no interlayers were tested under uniaxial tension (Figure 54 and Table 11). The composites showed a linear behavior in the lower strains and failed through the drilled hole. The tensile strength of the 316 ± 14 MPa. Although not affecting the mechanical strength, the maximum strain for these samples were quite scattered. The average maximum tensile strain was 0.95 ± 0.29 %. Tensile test results for composite samples with the interlayers of cubic zirconia particles were given in Figure 55 and Table 12. The average strength of the composites was 314 ± 34 MPa. The maximum strain at beak for these set of composites was 0.71 ± 0.12 %. Tensile test results for composites locally toughened with interlayers of PAN fibers with tetragonal zirconia are demonstrated in Figure 56 and Table 13. The average tensile strength for this class of composites were 281 ± 10 MPa and 0.6 ± 0.01 %, respectively.

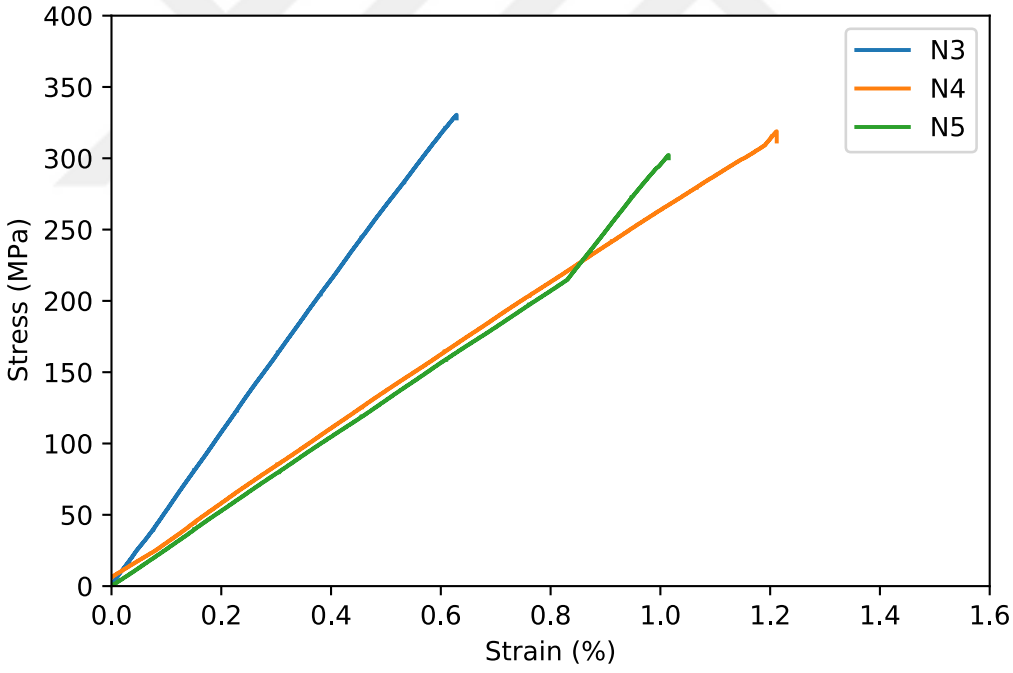


Figure 54: Uniaxial tensile test for drilled-hole neat composites

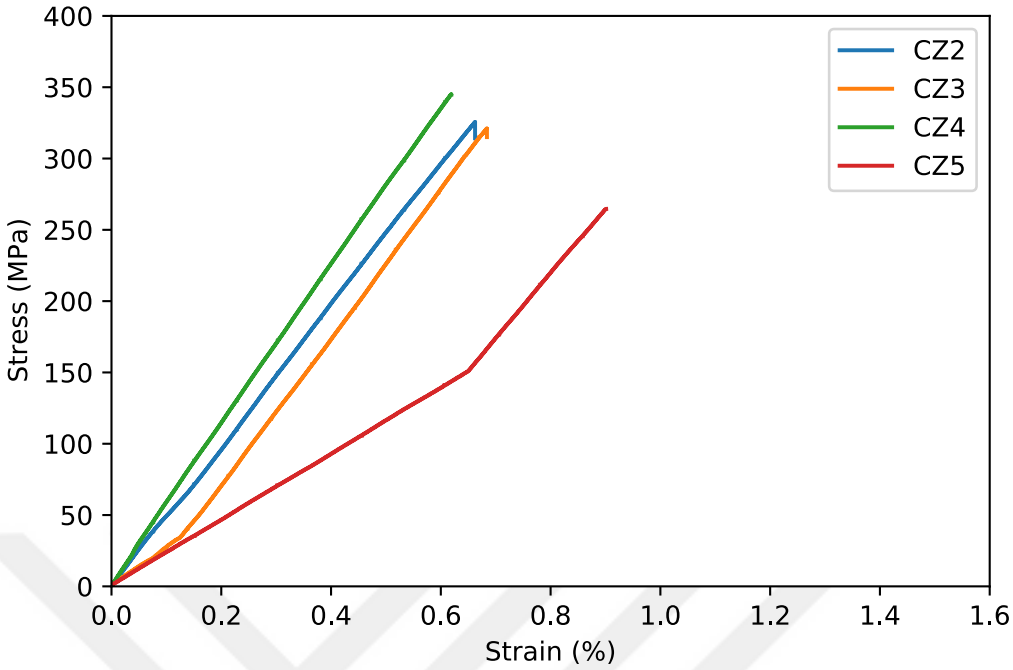


Figure 55: Uniaxial tensile test for drilled-hole composites locally toughened by the interlayers of PAN nanofibers with cubic zirconia

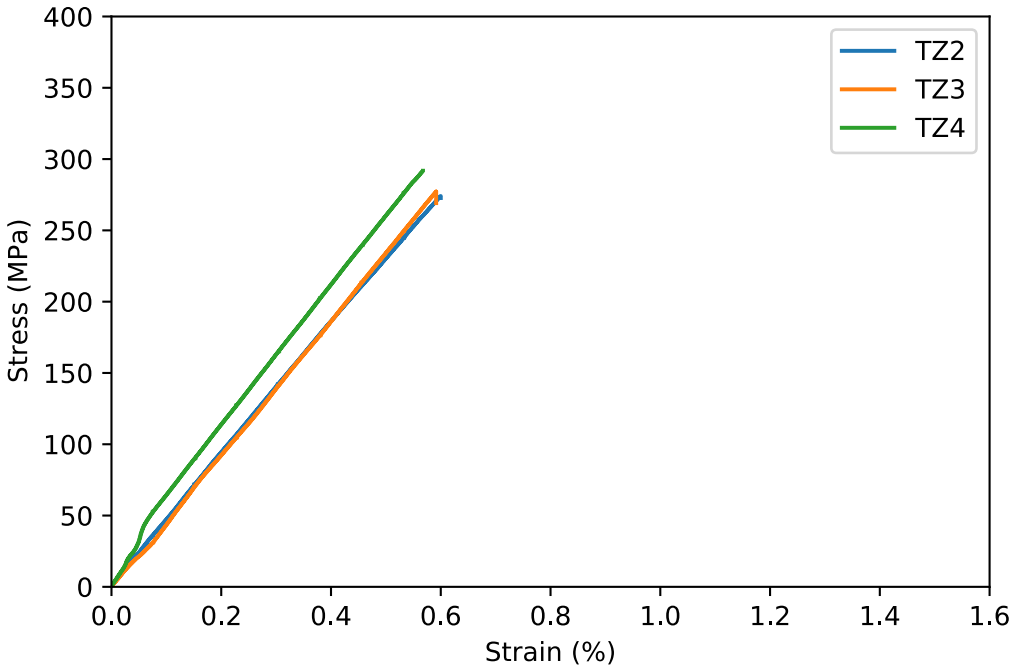


Figure 56: Uniaxial tensile test for drilled-hole composites locally toughened by the interlayers of PAN nanofibers with tetragonal zirconia

Table 11: tensile properties of neat composite samples

Composite class	Ultimate tensile stress, σ_u (MPa)	Strain at break, ϵ_b
N-1	N/A	N/A
N-2	N/A	N/A
N-3	330	0.63
N-4	318	1.21
N-5	302	1.02
Average	0.95	316
Standard deviation	0.30	14

Table 12: tensile properties of composite with local toughening interlayer of PAN-c-ZrO_2

Composite class	Ultimate tensile stress, (MPa)	Strain at break
CZ-1	N/A	N/A
CZ-2	326	0.66
CZ-3	321	0.68
CZ-4	345	0.62
CZ-5	265	0.9
Average	0.71	314
Standard deviation	0.13	34

Table 13: tensile properties of composite with local toughening interlayer of PAN-t-ZrO_2

Composite class	Ultimate tensile stress, (MPa)	Strain at break
TZ-1	N/A	N/A
TZ-2	274	0.6
TZ-3	277	0.59
TZ-4	292	0.57
TZ-5	N/A	N/A
Average	0.59	281
Standard deviation	0.01	10

6.3.5 Fracture modes

Failed composite samples were photographed after failure took place (Figure 57). All samples failed in the hole region which was the accepted failure by the standard. TZ-5 sample did not fail after multiple tries due to the slipping in the grip area.

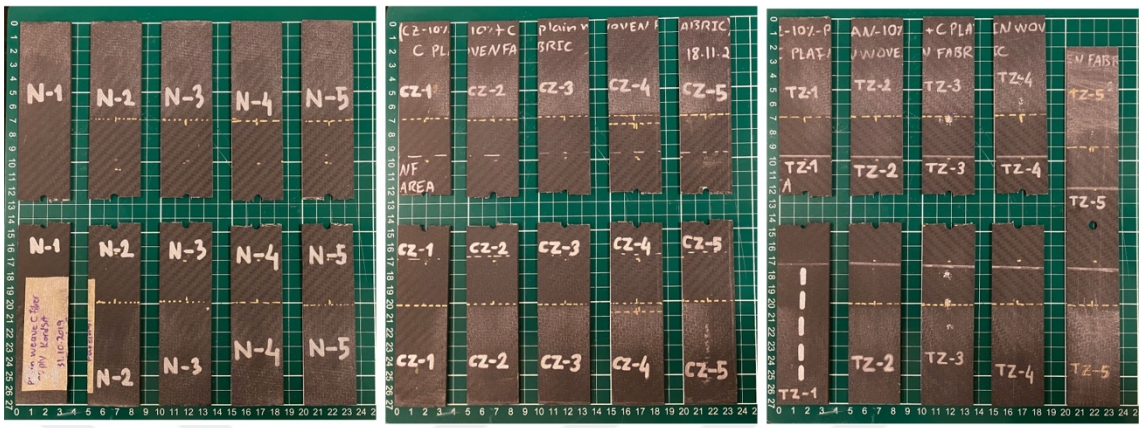


Figure 57: images of composites after uniaxial tensile test for drilled-hole composites: neat (N-#), locally toughened by the interlayers of PAN nanofibers with cubic zirconia (CZ-#), locally toughened by the interlayers of PAN nanofibers with tetragonal zirconia (TZ-#)

One sample per composite class was dissected for fractography with SEM (Figure 58). The inward arrow showed the drilling direction. Dissected samples were analyzed on the opposite sides of the fracture surface, namely top (T in the code) and bottom (B in the code).

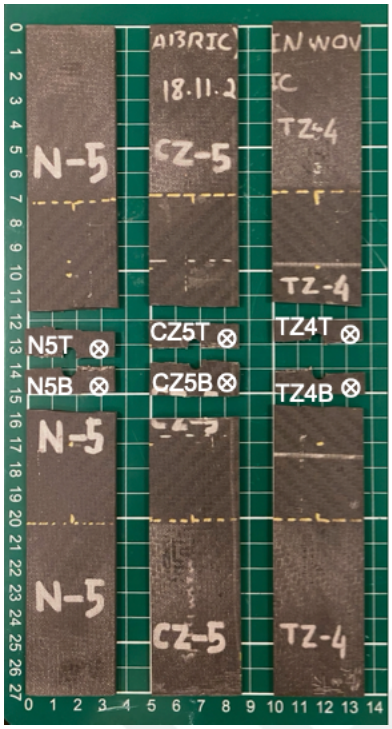


Figure 58: images of representative drilled-hole composites after uniaxial tensile test: top half of the N-5 neat sample (N5T), bottom half of N-5 neat sample (N5B), top half of CZ-5 sample locally toughened by the interlayers of PAN nanofibers with cubic zirconia (CZ5T), bottom half of CZ-5 sample locally toughened by the interlayers of PAN nanofibers with cubic zirconia (CZ5B), top half of TZ-4 sample locally toughened by the interlayers of PAN nanofibers with cubic zirconia (TZ4T), bottom half of TZ-4 sample locally toughened by the interlayers of PAN nanofibers with cubic zirconia (TZ4B), inward vector ⊗ showing the drilling direction

Fracture surface maps were generated for three composite classes by tiling low magnification SEM images of the fracture surfaces. Fracture surface map of neat composite was given in Figure 59. Fracture surface map of composites with PAN-c-ZrO_2 interlayers was given in Figure 60. Fracture surface map of composites with the interlayers of PAN-t-ZrO2 was given in Figure 61.

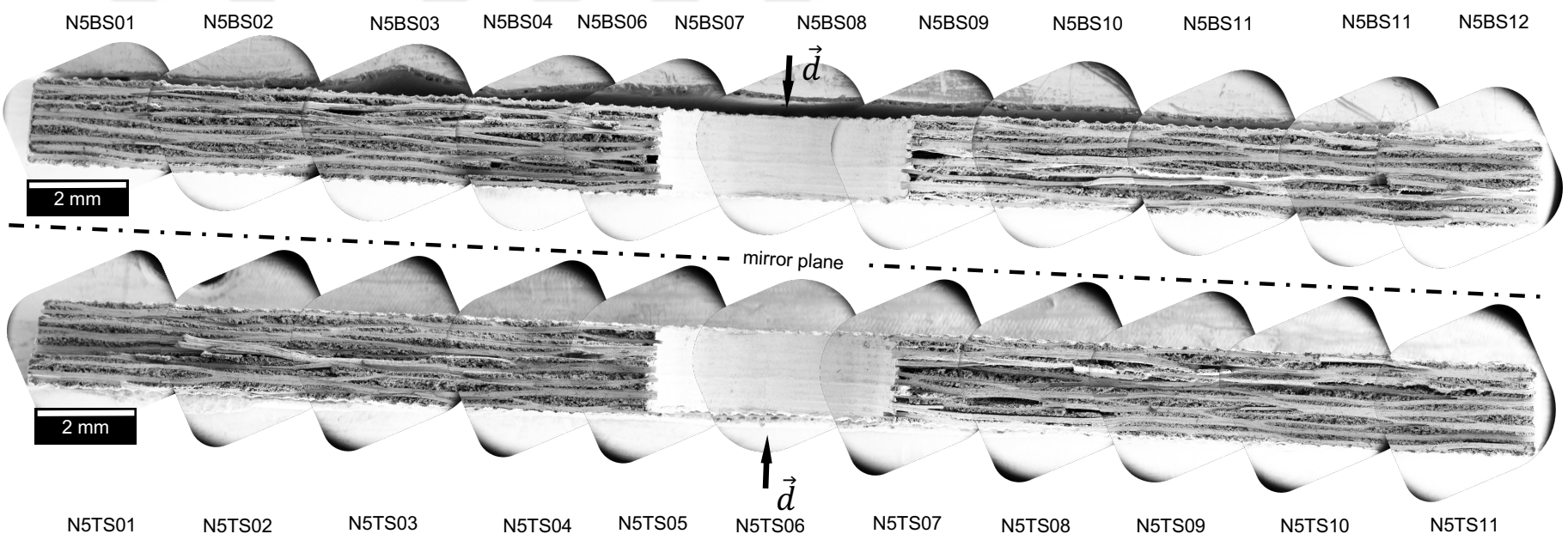


Figure 59: fracture surface map of N5 sample (Neat-5) after failure around the drilled-hole from top half (T) and bottom half (B) generated from compilation of several SEM images of sites (S##), $\vec{d}$ showing the drilling vector

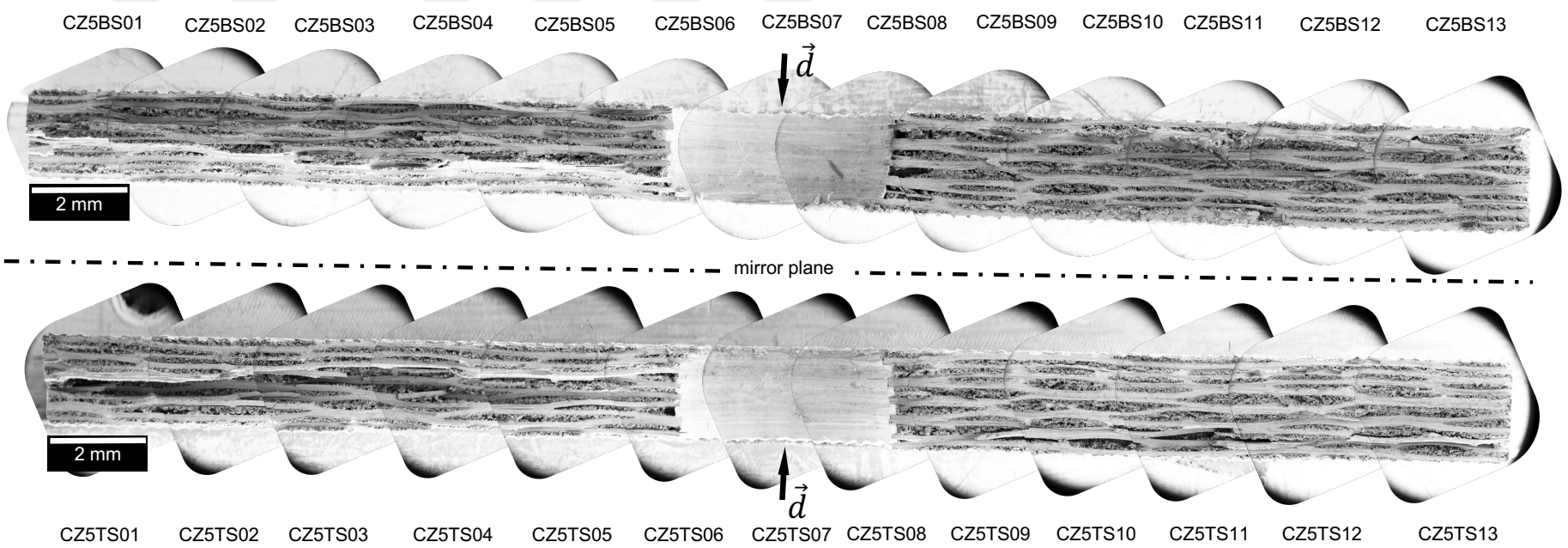


Figure 60: fracture surface map of CZ5 sample (CZ-5) after failure around the drilled-hole from top half (T) and bottom half (B) generated from compilation of several SEM images of sites (S##), $\vec{d}$ showing the drilling vector

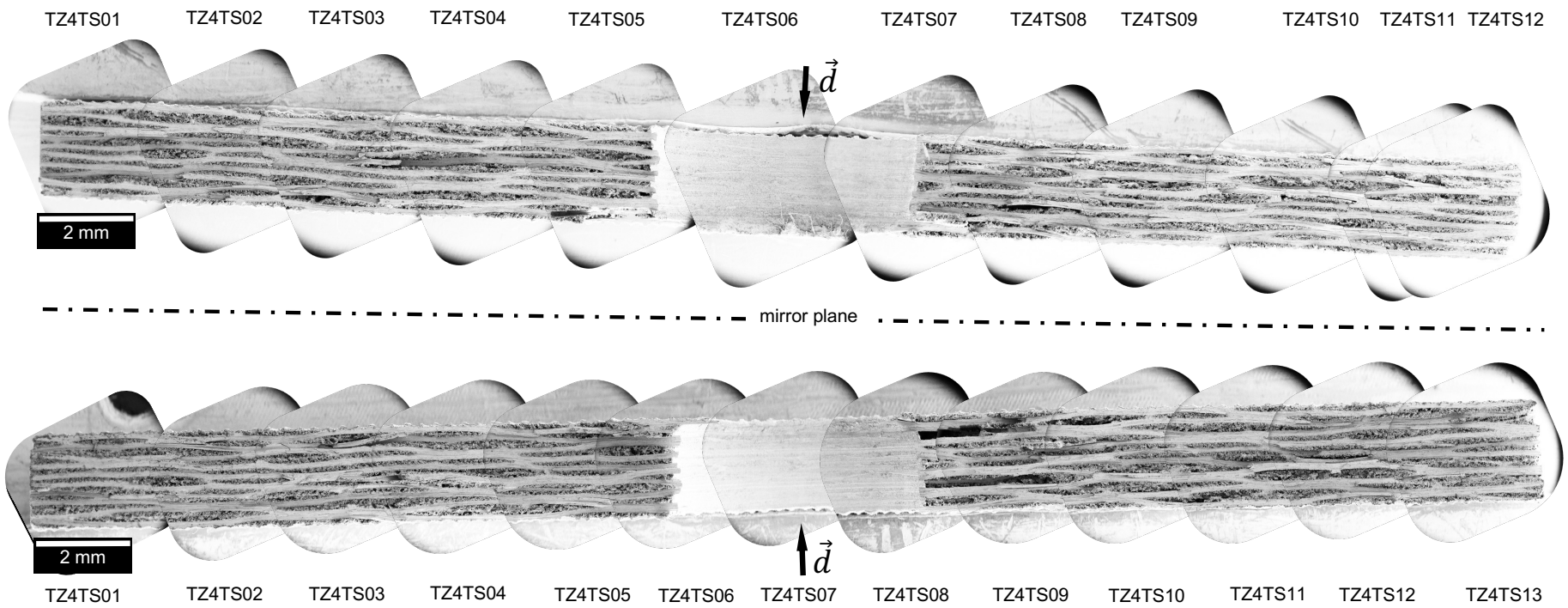


Figure 61: fracture surface map of TZ4 sample (TZ-4) after failure around the drilled-hole from top half (T) and bottom half (B) generated from compilation of several SEM images of sites (S##), $\vec{d}$ showing the drilling vector

6.3.6 Detailed fractographic analysis

6.3.6.1 Inside drilled hole

Behavior of the epoxy against the drilling damage was captured in Figure 64. In the sample with no interlayer (none), epoxy showed brittle fracture. In the sample with PAN-c-ZrO2 interlayer or PAN-t-ZrO2 interlayer, epoxy showed ductile fracture behavior.

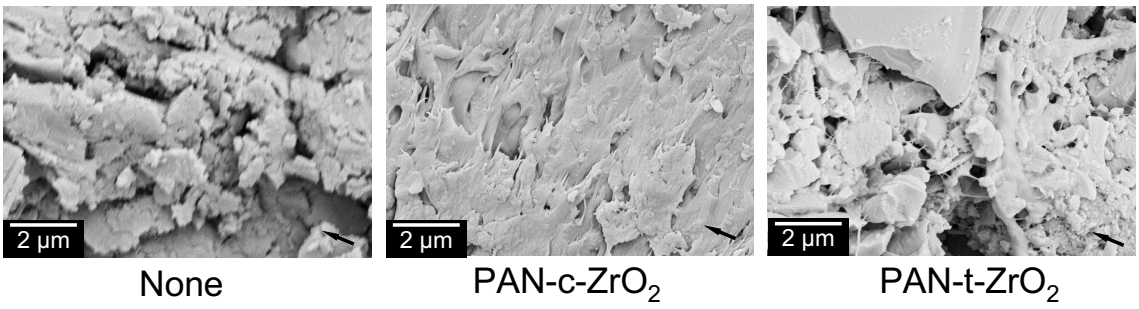


Figure 62: fracture of the epoxy inside the drilled hole (arrow showing the drilling direction)

6.3.6.2 Outside drilled hole

Nanofibers were captured outside the drilled hole in the interlayer zone (Figure 63).

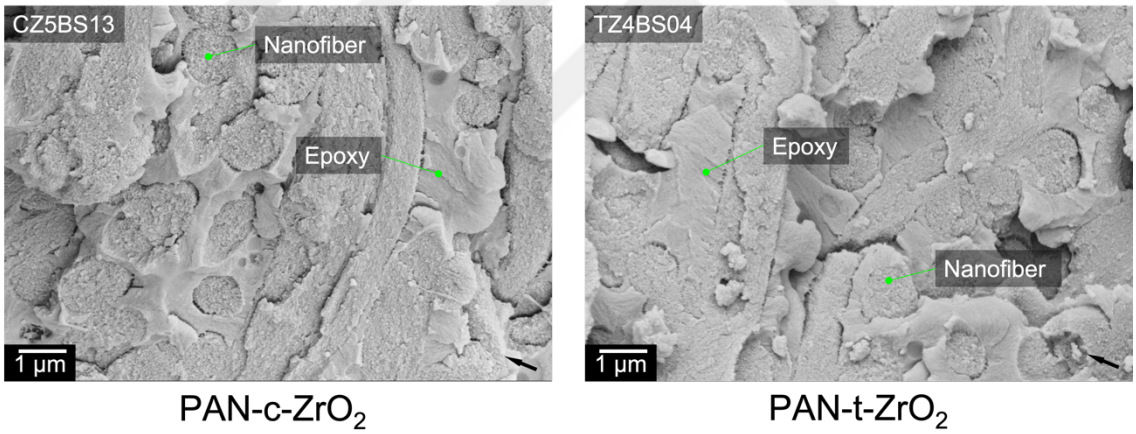


Figure 63: fracture of the sample outside the drilled hole (arrow showing the drilling direction)

6.4 Discussion

6.4.1 Quality of hole

6.4.1.1 Analysis of homogeneity in hole diameters

The drilling condition produced holes on neat composites and average diameter of 5.52 ± 0.05 mm the enter side and 5.52 ± 0.04 mm on the exit side of the hole (Table 14). Both diameters were smaller than the drill-bit diameter (6 mm). The diameter of the hole in both sides were quite similar. The standard deviations of the hole diameter were very

close on both sides. Therefore, the diameter was quite consistent throughout all neat samples.

Table 14: Diameter of drilled holes in neat composite samples

Sample	Enter (mm)	Exit (mm)
N-1	5.52	5.56
N-2	5.51	5.47
N-3	5.53	5.51
N-4	5.42	5.50
N-5	5.56	5.53
N-6	5.57	5.57
Average diameter (mm)	5.52	5.52
Standard deviation (mm)	0.05	0.04

The drilling condition produced holes on the composites interleaved by PAN-c-ZrO_2, with an average diameter of 5.53 ± 0.25 mm the enter side and 4.98 ± 0.26 mm on the exit side of the hole (Table 15). Both diameters were far from the desired diameter (6 mm). The diameter of the hole in the enter sides was always larger than that of the exit side. The standard deviation for the diameters of enter and exit sides were close. Therefore, despite the large scatter in the diameter of hole on each side, the variation of the diameter was almost identical for both sides.

Table 15: Diameter of drilled holes in composite samples with local toughening of electrospinning nanofibers loaded with cubic zirconia (PAN-c-ZrO_2).

Sample	Enter (mm)	Exit (mm)
C-1	5.56	5.19
C-2	5.71	5.12
C-3	5.23	4.69
C-4	5.71	5.13
C-5	5.21	4.61
C-6	5.74	5.14
Average diameter (mm)	5.53	4.98
Standard deviation (mm)	0.25	0.26

The drilling condition produced holes on the composites interleaved by PAN-t-ZrO_2, with an average diameter of 5.65 ± 0.03 mm the enter side and 5.13 ± 0.02 mm on the exit side of the hole (Table 16). Both diameters were far from the desired diameter (6 mm). The diameter of the hole on the enter side was always larger than that of the exit side. The standard deviation of the diameters of enter and exit sides were small. The standard deviation of the diameter on both sides were very similar. Therefore, the variation of the diameter was almost identical for both sides.

Table 16: Diameter of drilled holes in composite samples with local toughening of electrospinning nanofibers loaded with tetragonal zirconia

Sample	Enter (mm)	Exit (mm)
T-1	5.67	5.12
T-2	5.67	5.13
T-3	5.61	5.18
T-4	5.67	5.13
T-5	5.68	5.13
T-6	5.61	5.11
Average diameter (mm)	5.65	5.13
Standard deviation (mm)	0.03	0.02

Comparison of diameter for three classes of composites (Figure 64) showed that composites interleaved by PAN-t-ZrO_2 had the largest diameter on the enter side. Neat composites and the composites with PAN-c-ZrO_2 had smaller diameters on the enter side. It suggests that during the peel-off and chip formation neat composites and the composites with PAN-c-ZrO_2 behaved similarly. There is no possible phase transformation in c-ZrO_2. The effect of PAN fibers in peel-off is considered insignificant. Therefore, the composites with PAN-c-ZrO2 behaved almost the same as the neat samples in Mode-I. On the other hand, in the case of the composites with PAN-t-ZrO2, particles transform

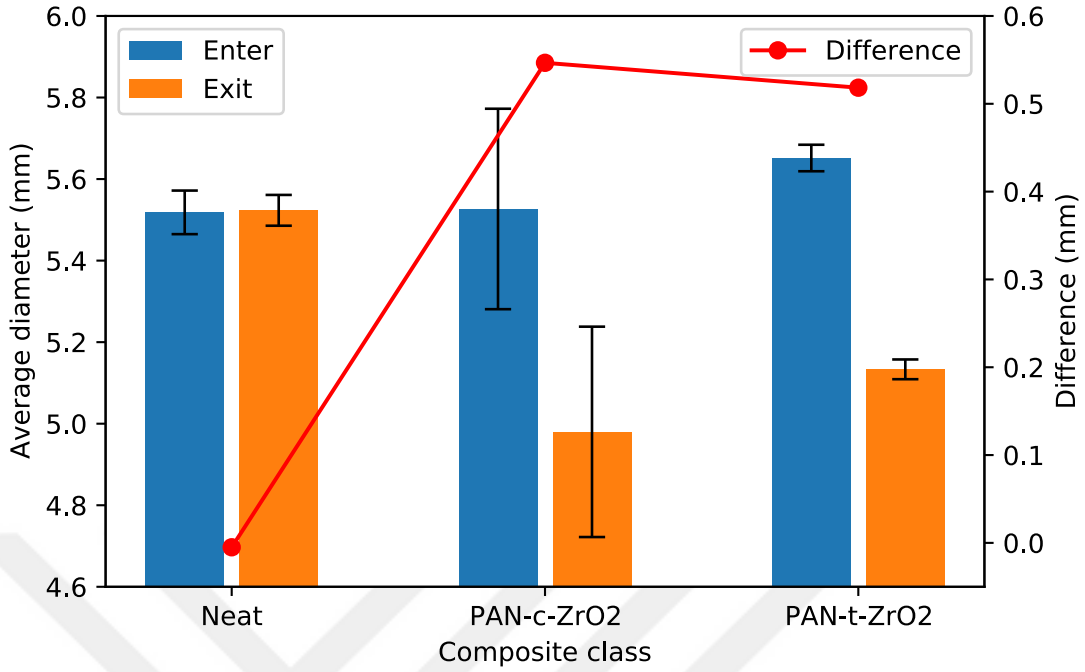


Figure 64: Diameter of drilled holes in composites with and without local toughening Thickness

6.4.1.2 Analysis of homogeneity in composite thickness

The average thickness of neat composites was measured to be 2.11 ± 0.06 mm (Table 17), the thickness of composites locally reinforced by PAN-c-ZrO2 was measured to be 2.39 ± 0.19 mm (Table 18), and the thickness of composites locally reinforced by PAN-t-ZrO2 was measured to be 2.37 ± 0.08 mm (Table 19). The average weight of the neat composite samples was measured to be 27.45 ± 0.62 g (Table 17). The average weight of composites with local toughening interlayer of PAN-c-ZrO2 was measured to be 28.93 ± 1.83 g (Table 18) and for composites with local toughing interlayer of PAN-t-ZrO2 was measured to be 29.03 ± 0.98 g , respectively (Table 19).

Table 17: properties of composite samples with no local toughening (neat)

Sample Codes	Coupon thickness top (mm)	Coupon thickness mid (mm)	Coupon thickness bottom (mm)	Coupon thickness average (mm)	Weight of the coupon (g)
N-1	2.05	2.07	2.05	2.06	26.85
N-2	2.03	2.04	2.06	2.04	26.70

N-3	2.15	2.15	2.15	2.15	27.83
N-4	2.14	2.16	2.18	2.16	27.99
N-5	2.17	2.15	2.16	2.16	27.87
Average				2.11	27.45
Standard Deviation				0.06	0.62

Table 18: properties of composite samples with local toughening of PAN-c-ZrO_2

Sample Codes	Coupon thickness top (mm)	Coupon thickness mid (mm)	Coupon thickness bottom (mm)	Coupon thickness average (mm)	Weight of the coupon (g)
CZ-1	2.03	2.1	2.06	2.06	25.84
CZ-2	2.51	2.53	2.41	2.48	29.81
CZ-3	2.53	2.54	2.45	2.51	30.08
CZ-4	2.49	2.55	2.42	2.49	30.24
CZ-5	2.41	2.46	2.33	2.40	28.71
Average				2.39	28.93
Standard Deviation				0.19	1.83

Table 19: properties of composite samples with local toughening PAN-t-ZrO_2

Sample Codes	Coupon thickness top (mm)	Coupon thickness mid (mm)	Coupon thickness bottom (mm)	Coupon thickness average (mm)	Weight of the coupon (g)
TZ-1	2.29	2.27	2.24	2.27	27.73
TZ-2	2.46	2.51	2.42	2.46	29.96
TZ-3	2.42	2.47	2.31	2.40	29.78
TZ-4	2.42	2.43	2.37	2.41	29.41
TZ-5	2.32	2.33	2.28	2.31	28.27
Average				2.37	29.03

Standard Deviation				0.08	0.98

Comparison of the thickness of the composites showed that addition of PAN-c-ZrO2 increases the thickness of the composite by 0.28 mm (280 µm, that is 31 µm per interlayer). Interleaving PAN-t-ZrO2 increases the thickness of the composites by 0.26 mm (260 µm, that is 28 µm per interlayer) (Figure 65). The thickness of composites with PAN-c-ZrO2 is higher than that of the composites with PAN-t-ZrO2 by 0.02 mm. This difference is statistically insignificant because it is smaller than the standard deviation of the thickness for composites with PAN-c-ZrO2 (0.19 mm). Therefore, the thickness of the composites with toughening interlayers are considered identical.

Comparison of the weight of the composites showed that the addition of PAN-c-ZrO2 increases the weight of the composite by 1.52 g (that is, 0.16 g per interlayer). Interleaving PAN-t-ZrO2 increases the thickness of the composites by 1.58 g (that is, 0.18 g per layer) (Figure 65). The weight of the composites with PAN-c-ZrO2 is less than that of the composites with PAN-t-ZrO2 by 0.1 g. This is not statistically meaningful as the standard deviation of the average thickness for composites with PAN-c-ZrO2 is higher than this difference. Therefore, the weight of the campsites with local interlayers are taken equal. Since the thickness and the weight of the composites with toughening interlayers are equal, their density is identical.

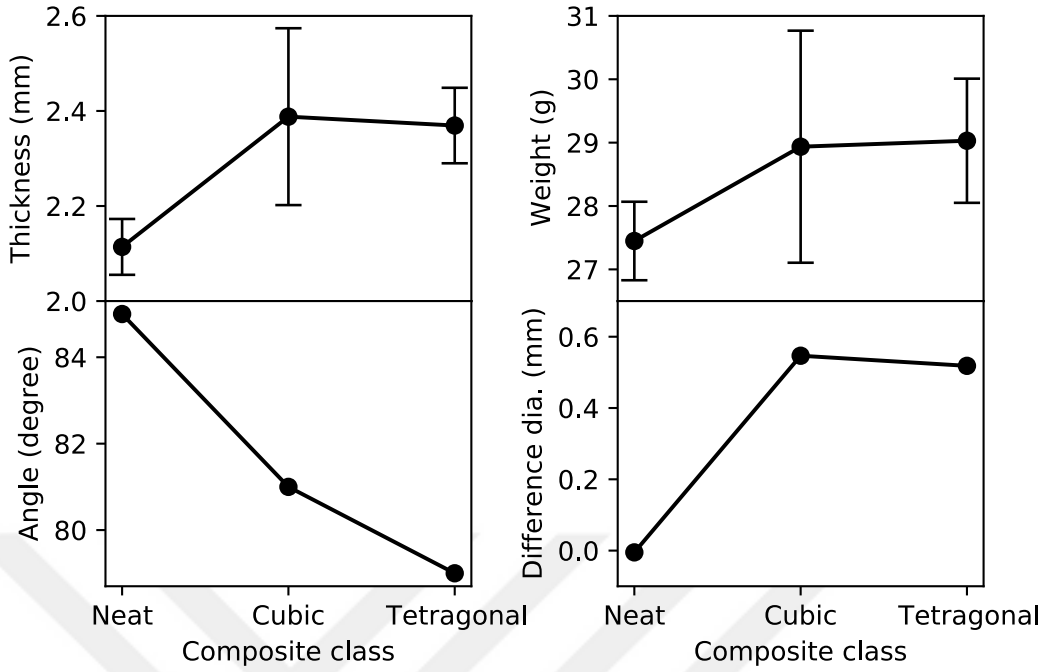


Figure 65: properties of drilled hole composites average thickness, average weight, difference in diameter of enter and exit sides, and the hole wall angle

The trends in the angle of wall between the enter and exit side did not follow the trends in the change of thickness. The angle of wall decreased parallel to by the increase in the thickness from neat composites to the composites with the local reinforcement of PAN-c-ZrO_2 (Figure 65). The angle continued to change from composites with PAN-c-ZrO_2 to composites with PAN-t-ZrO_2. Meanwhile, the thickness stayed the same from composites with PAN-c-ZrO_2 to composites with PAN-t-ZrO_2 (Figure 65). Therefore, the difference in diameter was independent of the thickness of the sample.

The trends in the difference of diameter in the enter side and exit side of composites followed the trends in the thickness. The difference in the diameter increased from the neat composites to that of the composites with PAN-c-ZrO_2 parallel to the increase in the thickness of the same composites. The difference in the diameter of the composites with local toughening interlayers remained marginal along with the thickness of the same composites (Figure 65). Therefore, the difference in the diameter of the composites depends on the thickness of the composites.

Drilling of composites was interpreted to have four steps as in Figure 66. Composite body is with a special design needed to be drilled in desired diameter. The drill bit was usually from a lower diameter (bit dia.). The hole first was made in the part as wide as the

diameter of the drill bit in the direction that was indicated by $\vec{d}$. This caused a minor delamination in the enter side and a major delamination in the exit side of the part. Interpolate drilling required widening of the hole in circular motions from bit diameter to the desired diameter. The programmed drilling should produce holes with the wall angle of 90°. However, the hole relaxed after the drill bit pressure was removed. Therefore, instead of right-angle hole wall, a tilted angle hole wall appeared with an actual diameter (Figure 53).

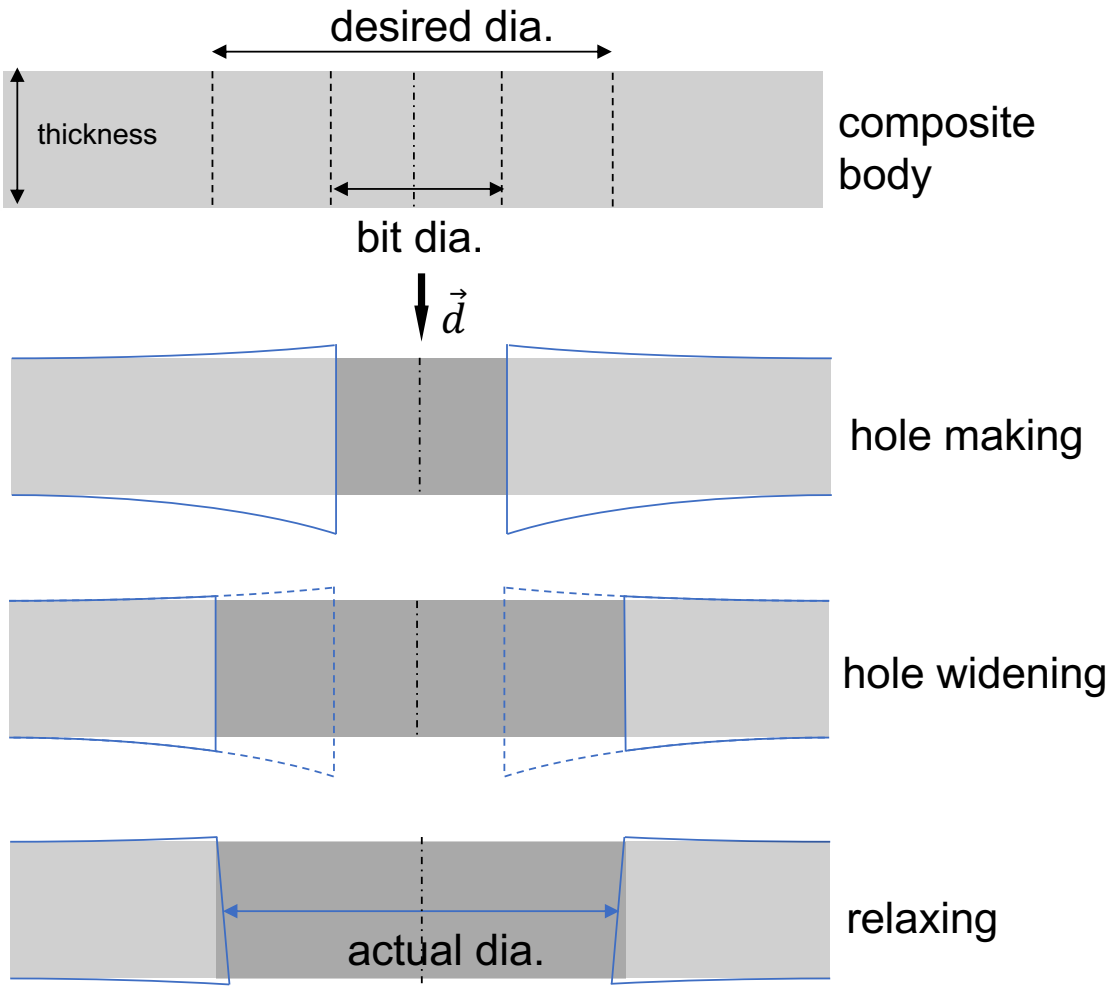


Figure 66: process of drilling a hole in composites

6.4.2 Mechanical properties

Analysis of the mechanical test results showed that there were only minor differences between the classes of composites. Failed composites samples showed similar maximum strain at break (Figure 67).

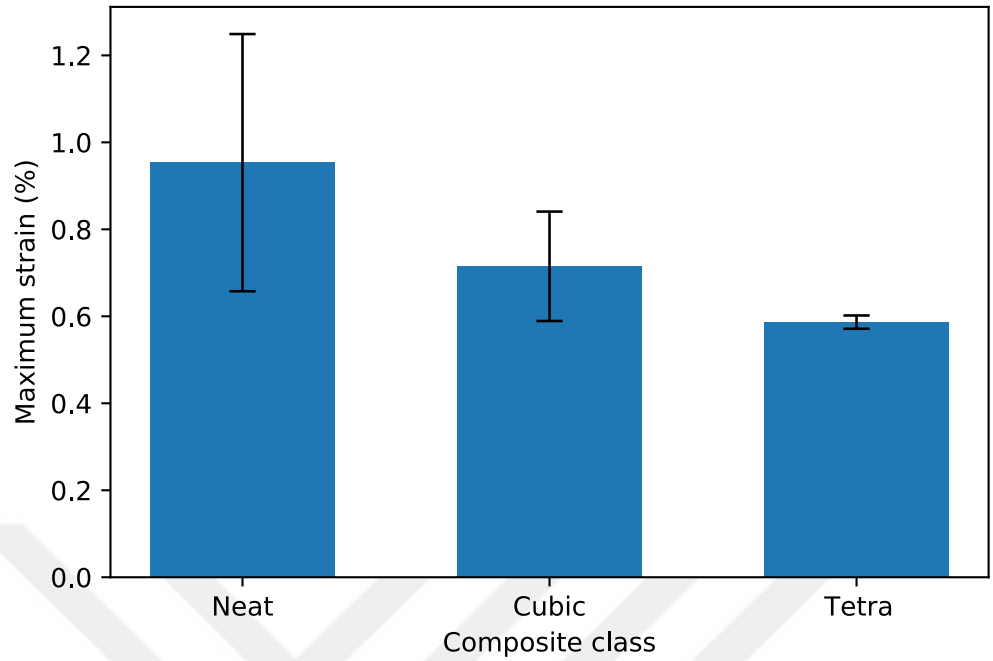


Figure 67: strain at break for drilled-hole composites

Tensile strength of the composite samples showed minor differences between the composite classes (Figure 68).

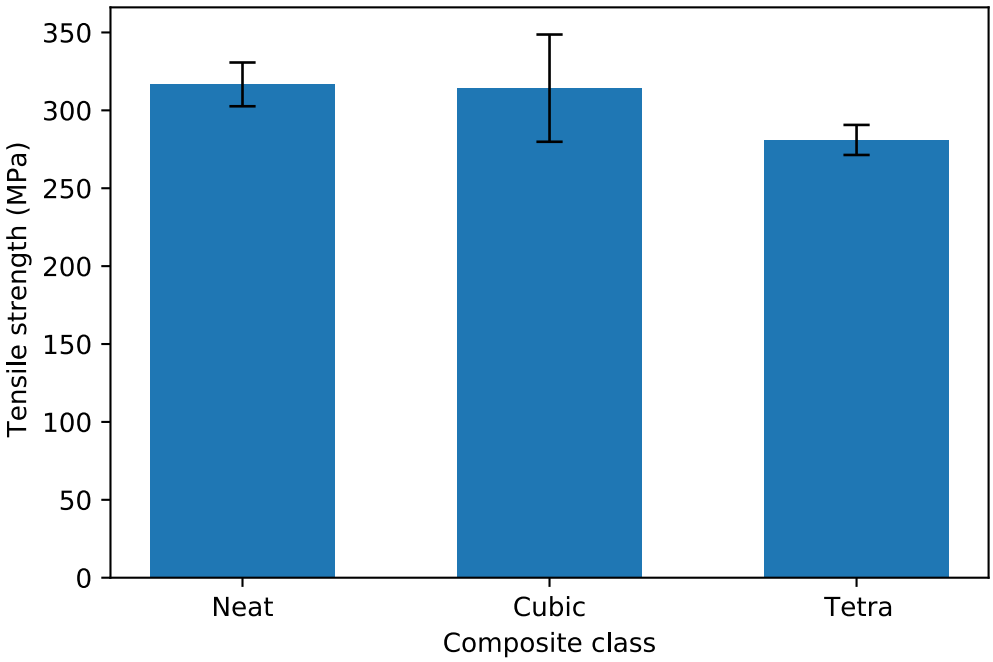


Figure 68: strength of the drilled-hole composites

6.4.3 Fractographic studies

Areas on the cross section of a failed composite with drilled hole consists of seven regions (Figure 69). Among them A1 and A2 were far from the hole, thus expected to include similar fractographic features (colored red in Figure 69). B1 and B2 were close regions to the hole and expected to show similar fractographic features (colored yellow in Figure 69). Region C was inside the hole and on the enter side of the drill. It had its specific features (colored green in Figure 69). Region D which was inside the hole and midway from the enter and exit side of the hole (colored white in Figure 69). Area E which was in the hole and close to the exit side of the drill (colored blue Figure 69).

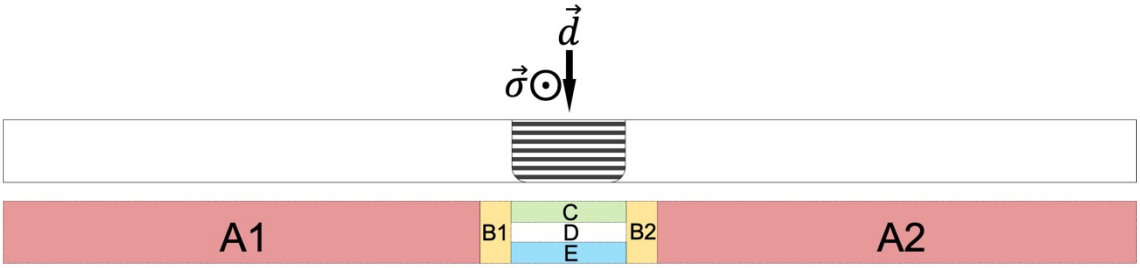


Figure 69: areas on the cross section of failed drilled-hole composite

Fracture analysis showed that the behavior of the behavior of epoxy changed in the hole region (C in Figure 69). In the neat sample without any interlayer, epoxy showed a brittle fracture (Figure 64). Meanwhile, it showed a ductile fracture surface in the interlayer zone. Both types of the interlayers PAN-c-ZrO2 (Figure 64) and PAN-t-ZrO2 (Figure 64) changed the fracture behavior of epoxy. This was associated with the toughening effect of nanofibers. No apparent difference was detected between the composites with PAN-c-ZrO_2 and PAN-t-ZrO_2. Further analysis showed that the interaction of the nanofibers with the epoxy is similar in both PAN-c-ZrO2 and PAN-t-ZrO2 (Figure 63). The resemblance in the interlayer zone can justify the minor differences in the mechanical properties of the composites with interleave (Figure 67 and Figure 68).

6.5 Conclusion

Composites with different types of interlayers were prepared from carbon fabric composites. Two types of interlayers were used based composite nanofibers of PAN with t-ZrO_2 and c-ZrO_2. Former particle was used due to its stress-induced phase transformation properties. It was hypothesized that during the drilling process, t-ZrO2 could go through phase transformation. This phase transformation could absorb some of

the damage energy. Meanwhile, the composite integrity would preserve. In this research, main findings are as follows:

- Production of the interlayers from PAN and ZrO_2 particles was feasible using electrospinning technique
- Characterization of the particles integrated to PAN nanofibers showed compatibility with the carrier polymer and the particle
- Presence of interlayers changed the microscale toughness of the composites against the damage of drilling
- Inside the hole composite nanofibers drawn by the force of drill bit and their diameter decreased
- Presence of nanofiber interlayers hindered the chip removal from the hole by holding the particles even after fracture
- Macroscale mechanical properties of composites remained almost the same after adding interlayers
- Presence of the metastable particles did not show any significant effect on the mechanical properties of composites

CHAPTER 7
GENERAL CONCLUSION

7.1 Overview

This dissertation aimed at the designing and engineering of multi-phase multi-scale particle-nanofiber interactions for composites materials. Multi-phase particle-nanofibers nanocomposites were produced using electrospinning technique. Another multi-phase approach was followed by hybridizing polymeric nanofibers with different response mechanisms to heat stimulus. Multi-scale approach was adapted by designing produced nanocomposites inside macroscale laminated composites. Also, the advantages of multi-scale mechanisms were also taken by producing nanofibers that carried microscale particles. Synergy of multi-scale approach and multi-phase designs was implemented.

During this dissertation the following achievements were made. New polymers based on commercial polymers were synthesized. Two commercial polymers, namely PAN and PS were selected as the base polymer. They were copolymerized by GMA using a free-radical polymerization. It was showed that the interface between the fibers and the surrounding material could be engineered using the GMA groups. They were formed into nanofibers using solution electrospinning. They were used as toughening interlayers for laminated epoxy-matrix composites. The interface between the fibers and the surrounding matrix was controlled by engineering the crosslinks between GMA groups on the polymers and those on the polymer chains of the epoxy matrix. Electrospinning nanofibers with engineered interrace were shown as a reliable candidate for toughening of the resin-rich region in laminated composites. The enhancement was achieved by only minimal mass addition and minimal geometry changes in the design. Thus, composite industry can benefit nanofiber interlayers as design ingredient.

Multi-phase composite nanofibers were produced using electrospinning. multi-scale structures were successfully designed and employed as interlayers for hierarchal reinforced composites. It was found that multi-phase multi-scale structures that contained MCF were successful in improving the toughness of laminated composites. Also, dual electrospinning was used to modify the local morphology around the MCFs. It suggests a promising method for tailoring the interaction of MCFs with the surrounding matrix. The hybrid nanofibrous structures around the particle were created with P(St-*co*-GMA). M-phase and t-phase nanofibers were prepared using crosslinking agents. This research showed that it is possible to engineer the interface of MCF using the multi-phase design. Furthermore, dual electrospinning was presented as a useful method in single-step manufacturing method for toughening interlayer. It was demonstrated as manufacturing process which reduced the complexity of the tailorable interlayer production in composite industry.

Composites nanofiber with multiphase structure were used with zirconia as inorganic particle and P(St-*co*-GMA) as the polymeric carrier. RSM was implemented. ANOVA was used to find the optimized electrospinning setup. The Novel polymers for better interface with matrix resins were synthesized based on PS and PAN and obtain thermally stable nanofibers. Correlation of fiber morphology and particle content with the contact angle against epoxy resin was investigated. This research suggested that the morphology of fiber and particles could be used to tailor the interface between surrounding materials and the composite nanofibers. This might suggest a useful method for the use of composite nanofibers in nanocomposites and laminated fiber-reinforced composites.

Multi-phase composite nanofibers of the inorganic zirconia particles and PAN polymeric carrier. They were used as local toughening interlayers for drilled hole carbon-fiber reinforced composites. Tetragonal zirconia particles with multi-functional capabilities were embedded in the composite nanofibers. Cubic zirconia particles with no multifunctionality were used as the reference. It was showed that the presence of composite nanofibers improved the toughness of the matrix in microscale. Fracture surfaces were found with characteristic features of ductile failure. Composite nanofibers were shown as useful candidate for local toughening of composites with mass addition and design changes. Local toughening with nanofibers could be used as an effective additive in aerospace industry where drilling is a must but also a major source of damage in structural composites.

Effective multifunctionally was not able to be detected in polymer composites with local toughening. Two existing methods were studied to identify the phase transformation of multifunctional zirconia particles. X-ray tomography failed to act as an effective method. The resolution of x-ray tomography was found to be much lower than the particle size. Raman spectroscopy failed to act as an effective method as well. Although it worked showed the phase transformation in ceramic samples, it did not work with polymer composites reinforced with ceramic particles. Polymeric parts of the sample fluoresce under the laser light. A new method was developed to SEM electron microscopy (supplement). It was found promising in identification of the phase transformation. Application of this method to polymer composites with local additives of zirconia is yet to be researched.

In summary, nanofibers and multi-scale, multi-phase composite nanofibers were found to be effective additives for toughening of laminated structural composite. There are several control mechanisms for these additives that could tailor the mechanism that are possible to be used as tailoring mechanisms. Dialing of the materials, processing, morphology, and properties of these interlayers could lead to efficient composite designs suitable for specific applications in the composite industry.

7.2 Future work

Every chapter of this dissertation has accomplished certain goals. Yet, they can be elaborated on or be extended in several directions. Study of multi-phase multi-scale reinforcement of polymer-nanofiber structures in toughness-specific test conditions would be a great route to be tracked. End-notch fracture and double-cantilever beam configuration could be useful methods to further clarify the enhancement in the mechanical properties.

One possible future study can focus on the enhancement of the mechanical properties of composites with different particle content of MCF. This dissertation exemplified the nominal 10 wt.% of MCF in polymers. The amount of the MCF can be altered in the future. Also, this dissertation investigated the mechanical enhancement composites where the ratio of m-phase to x-phase was of 50:50. Other ratios were shown to have different morphologies. Most probably, they will enhance the mechanical properties of composites up to different levels and in the different fracture modes.

Phase transformation in locally toughened composites can be investigated using Raman analysis with red lasers so that the polymeric parts do not fluoresce. This method could elucidate the phase transformation of multifunctional zirconia.

Investigation of martensitic phase transformation of zirconia in the drilled hole area using x-ray tomography of milled samples with Focused Ion Beam (FIB) could be another route. Samples that are milled with FIB could be taken from the parts of the campsites that have contain the particles. Thin samples could reduce the noise from the surrounding material so that the phase transformation in zirconia could be identified.

Phase transformation of multifunctional zirconia is hard to be triggered in conventional isostatic tests. This dissertation, therefore, focused on the possible transformations due to the aggressive damage of drilling. Other damage forms impact tests can be used to trigger the phase transformation. Increasing the amount of the zirconia content can facilitate the visualization of phase transformation in the fracture surface. Another approach to increase the amount of phase transformation can be improving the stress transfer from the surrounding material to the particles. This aim can be achieved by using P(St-*co*-GMA) as the carrier phase. The phase transformation can always be examined in the fracture surfaces by low-voltage SEM that was developed in the supplement of this dissertation.

Supplement

PHASE DIFFERENTIATION OF ZIRCONIA POLYMORPHS WITH LOW VOLTAGE SECONDARY ELECTRONS

by

FARZIN ASGHARI ARPATAPPEH

Submitted to the Graduate School of Engineering and Natural Science
in partial fulfillment of
the requirements for the degree of Doctor of Philosophy

Sabancı University
December 2022

CHAPTER 8

QUANTIFICATION OF CONTRAST DIFFERENCE BETWEEN MONOCLINIC AND TETRAGONAL ZIRCONIA IN LOW-KV SEM[*†‡]

To address the challenge in differentiating between two different allotropes when imaging with secondary electrons in the SEM, we present a study in which we quantitatively interpreted the contrast in secondary electron images collected using a through-the-lens detector. We demonstrated this new quantitative approach on a sample containing both tetragonal zirconia (t-ZrO_2) and monoclinic zirconia (m-ZrO_2) that was imaged over an accelerating voltage range of 0.4 - 1 keV. These results complement the existing capabilities offered by TEM, EBSD, micro-Raman, and correlative Raman-secondary electron imaging.

Previous studies have used image contrast levels to differentiate between semiconductors, metals, alloys, organic structures, and ceramics arising from their inherent differences in composition. For example, in semiconductors, this method was used to the direct visualization of dopant types [187]–[191], mapping of dopant levels [192]–[194] and even for capturing the four-dimensional images of the carrier interface dynamics in p-n junctions [57], [195]. In metals, fine grains of precipitates in a Cr-Mo steel were identified and visualized based on the difference in the secondary electron contrast [196]. In organic materials, compositional contrast of uncoated fungal spores and stained section-face was

---

[*] Published: Arpatappeh, F. A., Ow-Yang, C., Semsari-Parapari, S., Çorapçıoğlu, G., Gülgün, M. A., & Papila, M. (2022). Quantification of Contrast Difference Between Monoclinic and Tetragonal Zirconia in Low-kV SEM. *Microscopy and Microanalysis*, *28*(S1), 560–563. https://doi.org/10.1017/S1431927622002823

[†] Presented: Arpatappeh, F. A., Çorapçıoğlu, G., Semsari-Parpari, S., Papila, M., Gülgün, M. A., & Ow-Yang, C. (2017). Phase Differentiation of Zirconia Polymorphs in Low Voltage Scanning Electron Microscopy. *23. Ulusal Elektron Mikroskopi Kongresi*.

[‡] Published: Arpatappeh, F., Ow-Yang, C., Semsari-Parapari, S., Çorapçıoğlu, G., Gülgün, M. A., & Papila, M. (2022). Phase Differentiation of Zirconia Polymorphs in Low-Voltage Scanning Electron Microscopy. *33rd Canadian Materials Science Conference2*, 58.

also imaged by this method [197]. In the case of ceramics, the results of investigations on composites such as BN/TiB_2, $Si_3N_4/MoSi_2$, and $ZrO_2/Al_2O_3/Ti(C,N)$ using a low-voltage field-emission scanning electron microscope (FESEM) revealed a relationship between the phase contrast in the images and the local electrical conductivity, which made it possible to distinguish between grains that formed a three-dimensional conductive network from those grains which were isolated in the composite [198]. Percolated and non-percolated Ni phases were differentiated based on their difference in the SE yield in solid oxide fuel cells of Ni–yttria stabilized zirconia (ZrO_2) [199]. The contrast level differences were associated with physical properties, such as the variation in local conductivity, the difference in the secondary electron yield, and the difference of the bandgap width, due to the different electronic configurations. In this paper, we focus on the quantification and numerical analysis of the contrast difference originating in two distinct polymorphs of ZrO_2, i.e., of different crystal structures.

Partially stabilized tetragonal ZrO_2 doped with 3 mol% Y was obtained from TOSOH. Monoclinic zirconia was synthesized from zirconyl chloride octahydrate (Fluka™, Honeywell International Inc., USA) by calcination at 1000 ºC for 1 hour. Both powders were analyzed for their crystallographic structure using an XRD (D2 Phaser, Bruker Corporation, Germany).

The two ZrO_2 powders were investigated using a FE-SEM (Leo Supra 35 VP, Carl Zeiss AG, Germany) with an accelerating voltage tunable between 150 V and 30 kV, with a step resolution of 10 V. The samples were sputter-coated with an Au-Pd alloy of thickness *ca.* 4.38 nm. FE-SEM imaging was performed under a vacuum level of *ca.* 10^{-7} mbar and over accelerating voltages of 0.4 to 1 keV. The “in-lens” detector used preferentially collected Type I and Type II secondary electron signals (representative micrograph in Figure 70). This operation mode provided high resolution imaging with sensitivity to variations in the surface energy enabling correlation of electronic structure, work function, and crystal structure in materials with the observed contrast level in electron micrographs.

Images that included the two phases and the background were analyzed. Before processing, the images were prepared for analysis with an image editing software (GIMP). The two phases were singled out of the micrograph in the form of two separate phase images with the same size of the parent image, but all the areas except for the phases were set to be transparent (Figure 70). A Python® code was written to quantify

the contrast difference between the m-ZrO_2 (m-phase) and t-ZrO_2 (t-phase), as a function of accelerating voltage.

The parent image and the phase images were analyzed to extract histograms of their intensity (Figure 70) in the range of grayscale level (GSL) of 0 (black) to 256 (white). In the case of phase images, the program interpreted the transparent area as a GSL = 0. After removing these values from the image matrix, the average grayscale level (AGSL) of the remnant part (solely the phase) was calculated. The difference in AGSL, designated as Δ_{AGSL}, was calculated by subtracting the AGSL of t-phase from that of m-phase. The percentage difference in AGSL was also calculated by divided by AGSL of m-phase. The standardized Δ_{AGSL} plotted versus electron acceleration voltage Figure 71.

Figure 70 shows the representative micrograph of the secondary electron signals from both phases captured by the in-lens detector in 0.5 kV. There is a difference between the contrast levels in the electron micrograph so that m-phase appear brighter than the t-phase. When the same powders were captured in a range of acceleration voltages, it was revealed that the contrast difference increased as the acceleration voltage was decreased from 1 kV to 0.4 kV. The difference between the contrast levels of m-phase and t-phase is because of the difference in the SE yield of these phases.

Figure 70 also shows the processing steps of micrograph. The image shows two particles belonging to different phases and the way they were singled out in the form of m-phase and t-phase. The same parent electron micrograph and two sub-micrographs were analyzed using the computer code. Their histograms and processed images were presented in Figure 71. AGSL for the histograms of m-phase and t-phase are shown with a red dashed line.

Figure 71 shows the standardized Δ_{AGSL} between m-phase and t-phase against the acceleration voltage. It shows how the standardized Δ_{AGSL} monotonously increased as the acceleration voltage was reduced. The Δ_{AGSL} was about 2.81% when the acceleration voltage was 5 kV. Δ_{AGSL} starts to rise as the acceleration voltage was reduced. When the acceleration voltage was 0.4 kV, the standardized Δ_{AGSL} was to 69.2%.

This method appears to be a promising and feasible method for the differentiation of allotropes that would not be distinguishable in an SEM unless using complex equipment. This method can be further improved to distinguish even smaller grains of allotropes.

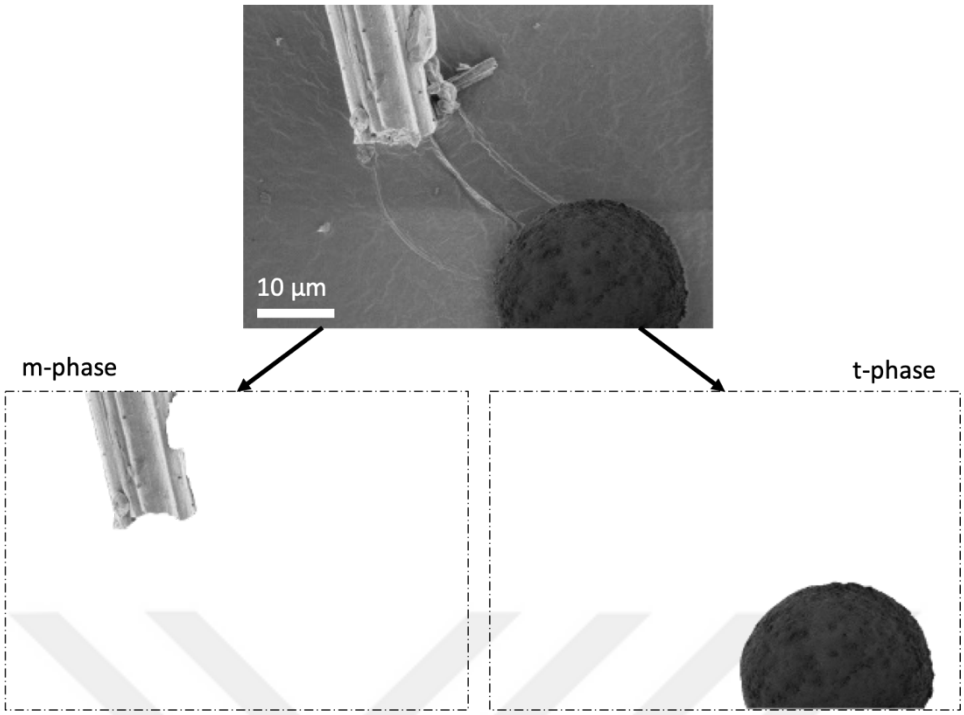


Figure 70: Manual segmentation of t-phase and m-phase from electron micrograph captured at 0.5 kV with an in-lens detector.

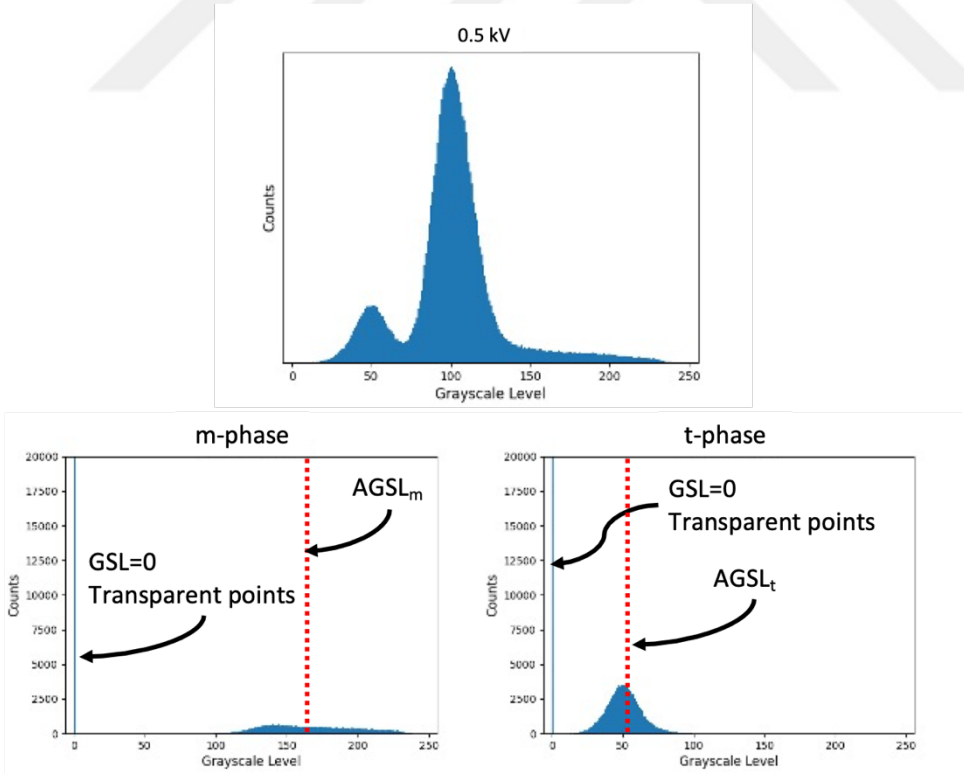


Figure 71: Histogram of grayscale levels for t-phase, m-phase and complete SEM micrograph captured with an in-lens detector at 0.5 kV.

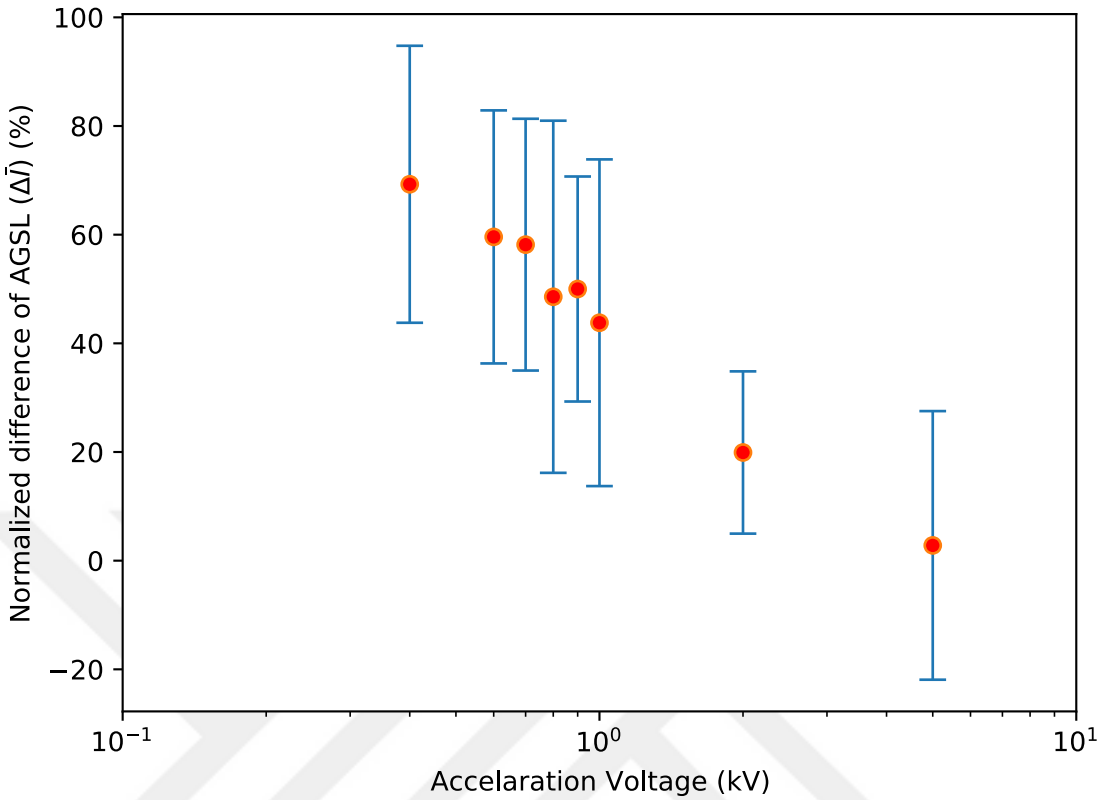


Figure 72: Standardized difference between the AGSL (right) for t-phase and m-phase in SEM micrographs captured with an in-lens detector in a range of acceleration voltages (5 - 0.4 kV).

CHAPTER 9
PHASE DIFFERENTIATION OF ZIRCONIA POLYMORPHS WITH LOW VOLTAGE SECONDARY ELECTRONS

Summary

The present study demonstrates that imaging by secondary electrons (SE) serves as a potential differential phase contrast technique in ~~scanning electron microscope (~~SEM). The mechanism of SE production is treated theoretically when primary electrons are in the low-voltage range (<5 kV). With a TTL, differences in SE yield correlate to differences in image contrast in the resulting electron micrographs. Powders of monoclinic ZrO_2 (baddeleyite) and tetragonal ZrO_2 (3 mol% Y_2O_3-doped partially stabilized) serve as challenging test samples, and the different polymorphs correlate to distinct variations in contrast level against accelerating voltage of primary electrons. The same powders are further analyzed by Raman spectroscopy to verify the results. Micro-indentation on sintered tetragonal zirconia pellets induced martensitic phase transformation into monoclinic zirconia in regions of elevated stress. The phase transformation was revealed in SE images by differences in image contrast in the regions of high stress concentration around the indent. With a Raman spectrometer-equipped SEM, the transformation zone was identified through mapping the distribution of the shift in Raman scattering that is characteristic of the two distinct polymorphic phases. The SE image contrast and Raman shift map correlated strongly, suggesting that the variation in the SE yield with accelerating voltage can be used as a phase identification method in SEM between the polymorphs.

9.1 Introduction

Differentiation between polymorphs of the same chemistry with high spatial resolution is an outstanding challenge for materials scientists. However, the different polymorphs have differences in electron affinity that can be exploited with secondary electrons of the first type in low-kV SEM. In SEMs, a beam of primary electrons (PE) is used to analyze materials. When PEs impinge on the specimen, different signals are generated, such as backscattered electrons (BSE) and secondary electrons (SE) and are used to form images [200]. While BSEs are mostly used for visualizing the atomic-number contrast in SEM images, SEs are mostly used for topographical contrast [201]. The SE signal is usually treated as a homogeneous one in conventional SEMs, but in fact it is a composite [202]. Two major components exist in an SE signal. One component comes from the SEs that are generated at the first collision of PEs with the specimen atoms at the surface (SE1). The other component comes from the SEs that are generated during multiple collisions of PEs with sub-surface atoms (SE2) [203].

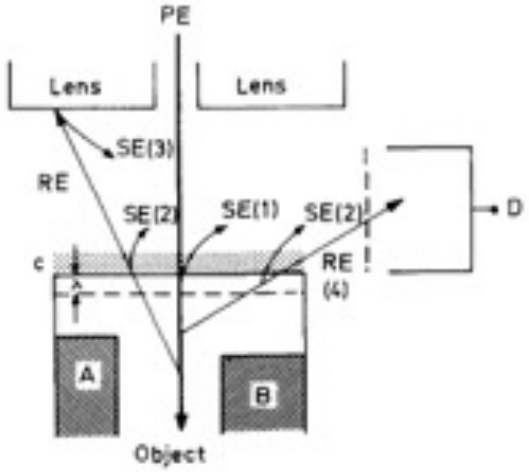


Figure 73: different signals generated when primary electrons impinge a specimen adapted from [204] with permission

Conventional SEMs usually operate with PEs with energies ranging from 5 kV to 30 kV. With such energies, PEs penetrate with an interaction volume up to 5 - 6 µm deep and 3 – 4 µm in diameter [204], [205]. This SE signal is predominantly SE2, obscuring the information contained in SE1. For this reason, Everhart-Thornley detector is unable to distinguish the SE1 from SE2. In conventional SEMs, the BSE signal could be used effectively for phase differentiation if there is a difference in stoichiometry. In the identification of polymorphs of the same stoichiometry, the contrast in BSE is low for phase identification. However, polymorphs have differences in their electron affinity

which result in differences in efficiency in SE1 generation. To obtain different image contrast from different polymorphs, the SE1 share in the total SE signal must be boosted by reducing the interaction volume [206]. In Low Voltage SEM (< 5 kV), the interaction volume becomes small, and in conjunction with the use of an in-lens detector, SE1 share predominates the total SEs collected (Figure 1) [207].

9.1.1 Secondary Electron Emission (Bethe's theory)

SEs are generated when charged particles like primary electrons hit the surface of a sample [208]–[211]. Beneath the surface, primary electrons lose their kinetic energy by interacting with the material's nuclei and/or electrons. They transfer some portion of their energy to the electrons of the material while being decelerated through their path. If the transferred energy is high enough, the generated SEs might escape from the surface of the material [204], [208]–[210], [212], [213].

9.1.2 Stopping power

For certain materials, the energy loss of PEs (stopping power) was expressed by Bethe formula [214]:

$$-\frac{dE}{ds} = 785\frac{\rho Z}{AE}\ln\left[\frac{1.166E}{J}\right] \qquad \text{Equation (1)}$$

where E is the instantaneous kinetic energy of the electron (in eV), s is the path length along the trajectory (in Å), ρ is the density (in the units of g cm^{-3}), Z is the atomic number, A is the atomic weight of the target, and J is the mean ionization potential of the material (in eV).

9.1.3 Error in low voltages

For $E \gg J$, the Bethe stopping power accurately predicts the behavior of electrons, but for $E \approx J$, the expression fails to predict the stopping power because the logarithmic term dominates Equation (1). Finally, the stopping power becomes zero for $E = J/1.166$, and switches to physically meaningless negative values for $E < J/1.166$. Therefore, the formula needed a modification so that the ionization potential becomes an energy-dependent term [215].

9.1.4 Energy-dependent mean ionization potential

The modified mean ionization potential is determined by,

$$J' = \frac{J}{1 + k\frac{J}{E}} \qquad \text{Equation (2)}$$

k is a variable whose value depends on the material examined, which is always close to, but less than, unity. J is the mean ionization potential of the material, which either can be measured experimentally or approximated as follows [216]:

$$J = \left[9.76\,Z + \frac{58.5}{Z^{0.19}}\right] \qquad Z \geq 13 \qquad \text{Equation (3)}$$

$$J = 11.15\,Z \qquad Z \leq 12 \qquad \text{Equation (4)}$$

After this modification, the Bethe formula converts to,

$$-\frac{dE}{ds} = 785\frac{\rho Z}{AE}\ln\left[\frac{1.166E}{J'}\right] \qquad \text{Equation (5)}$$

9.1.5 Stopping power and SE production

The stopping power of the material determines the number of generated SEs [217]:

$$n(z,E) = -\frac{1}{\epsilon}\frac{dE}{dz} \qquad \text{Equation (6)}$$

ϵ is an experimentally measured material constant and is defined as the average energy needed to generate one SE [218].

9.1.6 Escape probability of SEs

Once the SEs are generated, some of them move towards the surface. Only a fraction of the generated SEs can manage to overcome the surface energy barrier. The probability for an SE to surmount this energy barrier is modeled as:

$$p(z) = B\exp\left(-\frac{z}{\lambda}\right) \qquad \text{Equation (7)}$$

λ is the characteristic attenuation length. B is also a material constant, which is not usually correlated by any material's property but experimentally determined to be a constant on the order of $\frac{1}{2}$.

9.1.7 SE Yield

The number of the SEs, which manage to escape the surface, when standardized by the number of impinging primary electrons, is called SE yield, δ. It is the integrated product of SE generation and SE escape probability over the penetration depth, R [217]:

$$\delta = \int_0^R n(z,E)\,p(z)\,dz \qquad \text{Equation (8)}$$

where R is the average penetration depth of primary electrons beneath the material's surface where one primary electron loses all its energy to the material and becomes part of the sample.

Substituting $n(z, E)$ from Equation (6) and $p(z)$ from Equation (7) into the SE yield equation at Equation (8) leads to,

$$\delta = \frac{B}{\epsilon}\int_0^R \left(-\frac{dE}{ds}\right) \exp\left(-\frac{z}{\lambda}\right) dz \qquad \text{Equation (9)}$$

Secondary Electron Emission (Everhart's theory)

This theory is based on the detection of the SEs in the detector. Therefore, it takes also into the account the transmission of the SEs through the surface energy barrier. It assumes all electrons of the energy less than 50 eV as SEs. Thus, for insulator materials the SE yield is modeled by Equation (10) [219]–[223]:

$$\delta = \int_0^{50\ \text{eV}} \varphi\ \frac{1}{E_P}\left[\frac{E_k}{(E_k + \chi)^3}\right] \qquad \text{Equation (10)}$$

where φ is a constant, E_P is the primary electron energy, E_k is the SE energy, and χ is the electron affinity of the material.

9.1.8 Detector Selection

LV SEM suffers from low signal to noise ratio when applied in a conventional SEM. Classically, SEM images are generated by collecting the composite signal of BSE and SE with the help of an Everhart-Thornley detector [224]. New generation of SEMs, however, are equipped with a TTL detector, mounted above the sample and inside the electron column. This detector enables SEMs to efficiently collect signals with a low share of BSEs and more share of SEs. In this configuration, the contrast on a TTL detector arises primarily from SEs. Combination of TTL detector and LV SEM facilitates taking images with SE signal which is predominated by SE1 [225]. TTL detector combined with LV SEM enables contrasts in materials with no atomic number contrast. This contrast arises from the difference in the yield of SE1 in these materials. SE1 contrast made possible the direct imaging of the n-type and p-type heterostructure semiconductors. The p-doped regions appeared bright, and the n-doped regions appeared dark [187]. Same approach differentiated the percolated and non-percolated Ni in the composite solid oxide fuel cells of Ni and yttria stabilized zirconia [199]. The combination of TTL and LV SEM was used to differentiate the intrinsic GaN and the n-doped GaN [193].

9.1.9 Zirconia Polymorphs

Zirconia (ZrO_2) can be in three distinct crystallographic configurations (polymorph), namely monoclinic (m), tetragonal (t), and cubic (c). The m-phase is the naturally occurring thermodynamically stable polymorph (called baddeleyite) at room temperature [226]. When m-phase is heated, it transforms polymorphically to t-phase around 1100 °C. Upon further heating, it converts to the c-phase around 2400 °C. The t-phase can be stabilized at room temperature through doping with MgO [227]–[230], CeO_2 [231], [232], or Y_2O_3 [183].

The doped t-phase is metastable. Under enough stress t-phase transforms back to m-phase [233]. The transformation has been accompanied by stress absorption in ZrO_2. This mechanism has been used for ceramic toughening [228] and has effectively increased the ductility of the ceramic parts by a process known as "pseudo-ductility" [184], [231]. Although ZrO_2 polymorphs have been studied extensively, the characterization of the transformation of t-phase to m-phase remains as a technologically important challenge. Localized differentiation between transformed and non-transformed regions as the order of sub-micrometer resolution continues to pose another major hurdle.

The two phases are different in their bandgap energies (E_g). The E_g difference results from the differences in the crystal structure. The bandgap of ZrO_2 phases was measured using different methods and predicted by computational simulations.

Early experimental studies to measure the bandgap energies of t-phase and m-phase were performed by x-ray photo electron spectroscopy. Using two values of the absorption coefficient, the bandgap energies was calculated. With one coefficient, the bandgap of m-phase and t-phase was 5.83 eV and 5.73 eV, respectively. With the other coefficient, the bandgap of m-phase and t-phase was 7.09 eV and 6.62 eV, respectively. Theoretical calculations showed similar results for the bandgap of m-phase and t-phase. The band gap of m-phase and t-phase was calculated to be 4.46 eV and 4.28 eV, respectively. Overall, these results showed that the bandgap of m-phase is wider than that of the t-phase [234]. However, later studies showed a reverse trend [235], [236]. The bandgap energy for m-phase and t-phase was simulated in density-functional theory with various approaches. One configuration led to the bandgap energy of 3.58 eV and 4.07 eV, respectively, for m-phase and t-phase [235]. Another simulation showed that the bandgap energy for m-phase was 4.99 eV and 5.56 eV, respectively [235]. Yet another simulation resulted in the band gap energy of m-phase and t-phase to be 5.34 eV and 5.92 eV, respectively [235]. Latest

studies also confirmed that the bandgap energy for m-phase and t-phase was 3.631 eV and 4.043 eV, respectively [236]. Overall, it might be accepted that the bandgap of the t-phase is ~0.5 eV wider than that of the m-phase [235].

9.1.10 Characterization using X-ray Diffraction

Polymorphs of ZrO_2 can be characterized by XRD methods. Pure ZrO_2 has been studied by XRD analysis at room temperature [226], [237], [238]. The crystal structure was found to be m-phase with $a = 5.147$ Å, $b = 5.206$ Å, $c = 5.135$ Å and $\beta = 99.23°$. ZrO_2 stabilized with 3 mol% Y_2O_3 was found to be of tetragonal crystal structure with lattice parameters of $a = 5.159$ Å, $b = 5.211$ Å, $c = 5.321$ Å and $\beta = 99.19°$ [183]. Characteristic peaks were identified for both t- and m-phase for quantitative measurement of each phase in polycrystalline mixes [239]:

$$v_m = \frac{I(111)_m + I(\bar{1}11)_m}{I(111)_m + I(\bar{1}11)_m + I(111)_t} \qquad \text{Equation (11)}$$

where v_M is the concentration of m-phase in the mix and $I(hkl)$ is the intensity of X-rays diffracting off (hkl).

9.1.11 Raman analysis

Raman spectroscopy is used to validate the results of LV SEM of the differentiation of ZrO_2 polymorphs. Raman spectroscopy is sensitive to the weight of atoms/molecules and the strength of the bound between them [240]–[242]. ZrO_2 polymorphs have been characterized with this method. The monoclinic ZrO_2 showed 18 Raman-active peaks ($9A_g + 9B_g$) [243], and tetragonal ZrO2 showed 6 Raman-active peaks ($A_{1g} + 2B_{1g} + 3E_g$) [243]. Several studies [239], [244]–[250][1]–[3]. In [239], [244]–[250] showed that the most reliable characteristic peaks for m-phase are at 177 cm^{-1} and 190 cm^{-1} [251], and the most reliable characteristic peaks for t-phase are at 149 cm^{-1} and 267 cm^{-1} [251].

The intensity of these peaks was used to study the phase transformation from t-phase to m-phase [252]–[254]. In an indentation experiment on t-ZrO_2 (3.5-mol% Y_2O_3-doped ZrO_2), the transformation zone was investigated near the edges of a crack using Raman microprobe spectroscopy [252]. The transformation was traced to as far as 5 μm from the crack tip. When the same experiment was repeated in Al_2O_3/ZrO_2 composites, the zone size was measured to be ~1 grain in diameter [252]. Micro-Raman mapping of the indent area showed that that the maximum transformation does not happen in the center of the

indent, but rather in the edges and corners. Dilatation associated with the transformation gives rise to the sub-surface transformations and transformations around the indent [254]. In this study, we apply SE imaging to distinguish between two zirconia polymorphs—i.e., same chemistry, different crystal structures—based on image contrast difference arising from characteristic differences in SE generation. To induce SEs in the detected combined signal, the investigation was conducted in an SEM capable of operating with accelerating voltages in the range of 150V-30V, a technique often called LV SEM.

9.2 Materials and Methods

9.2.1 Zirconia polymorphs

Tetragonal zirconia was provided by Tosoh Corporation in a partially stabilized form: 3 mol% Yttria-stabilized Zirconia. m-ZrO_2 was synthesized from zirconyl chloride octahydrate (Fluka^{TM}, Reagent Grade, Honeywell International Inc., USA) [245] by heating with 10°C min^{-1} to 1000°C and holding at this temperature for 1 hour.

9.2.2 Phase identification

Both powders were analyzed for their crystallographic structure with an XRD (Bruker D2 Phaser). The diffractometer was equipped with Cu-K_α radiation operating at 30 kV and 10 mA. The diffracted radiation was collected in the range of 10° to 90° with 0.04° increments using a 1D Lynxeye XE-T detector (Bruker AXS GmbH). The obtained signals were analyzed by DIFFRAC.EVA to identify the present phases.

9.2.3 Coating thickness

Coating thickness of the thin deposited layer was estimated based on the atomic data and the nuclear data tables [255], the sputtering deposition in the literature [256]–[258], and the manufacturer specifications of the sputter-coating equipment. Coating was conducted according to the procedure described by the manufacturer with a few deviations to reduce the thickness of the coating and minimize the interference of the signal coming from the coating with that of the sample.

The deviations from the standard procedure were as follows:

- The target was selected to be an alloy of Au and Pd (60:40), whereas the manufacturer specifications were based on a target of Au only.
- The target-to-substrate distance was set to 70 mm, while the manufacturer specifications indicated the distance of 25 and 30 mm.
- The sputtering medium was selected to be air, whereas the standard procedure was run in argon.

To estimate the actual thickness, a few simplifications were considered:

- Sputtering of Au-Pd was assumed to be the same deposition rate of that of Au target.
- Air was considered as a mixture of 78% nitrogen and 20.9% oxygen, so its sputtering effect was assumed to be a weighted mix of each constituent
- Chemical sputtering of ambient oxygen (in the air) was neglected.

In physical vapor sputtering, the deposition rate, $\dot{h}$, is inversely proportional to the target-to-substrate distance:

$$\dot{h} = K\frac{1}{r^2} \qquad \text{Equation (12)}$$

where r is the distance from target to the substrate and K is a constant [259]. Manufacturer specifications indicated that the deposition rate for a gold target with 40 mA current under 0.04 mbar of argon pressure should be $\dot{h}_{30} = 1.35$ nm s^{-1}. Starting from the given deposition rate at 30 mm, the rate for 70 mm was calculated:

$$\frac{\dot{h}_{30}}{\dot{h}_{70}} = \frac{d_{70}^2}{d_{30}^2} \Rightarrow \dot{h}_{70} = \dot{h}_{30}\frac{d_{30}^2}{d_{70}^2} \qquad \text{Equation (13)}$$

Calculations lead to $\dot{h}_{70} = 0.28$ nm s^{-1}. After 40 s of sputtering, the overall thickness of the layer was calculated to be $h = 11.2$ nm. This value would be the coating thickness in argon medium. However, the actual sputtering was performed in air – a mixture of nitrogen and oxygen. Atomic data and nuclear data tables [255] reported the sputtering yield of Au-Pd in nitrogen as $Y_N = 0.38\ Y_{Ar}$ and in oxygen as $Y_O = 0.45\ Y_{Ar}$. Considering a linear relationship between the yield and the thickness of the deposited layer, the thickness for nitrogen and oxygen was calculated to be $h_N = 0.38h_{Ar} = 4.26$ nm and $h_o = 0.45h_{Ar} = 5.04$ nm, respectively. Finally, the thickness of the deposited layer in air, h_A, which is a mixture of 0.78 nitrogen and 0.209 oxygen by weight, was calculated as the weighted average:

$$h_A = 0.78h_N + 0.209h_O = 0.78 \times 4.26 + 0.45 \times 5.04 = 5.59 \text{ nm} \qquad \text{Equation (14)}$$

9.2.4 Electron microscopy analysis

The powders were investigated with a field emission scanning electron microscope (FE-SEM, Zeiss Leo Supra 35 VP), after being sputter-coated with an Au-Pd target (Cressington 108, United Kingdom) under 0.04 mbar pressure and with a 40-mA current for 40 s. FE-SEM imaging was performed under a vacuum level on the order of 10^{-7} mbar using a range of accelerating voltages and a lateral Everhart-Thornley detector. This SEM belongs to the Gemini family of instruments manufactured by Zeiss, in which there exists also a transistor–transistor logic (TTL) detector. The commercial name of this SE detector is in-lens detector. The combination of low voltage (<5 kV) and in-lens detector was designed specifically for high resolution imaging with sensitivity to variations in the surface energy [260], enabling correlation of electronic structure, work function, and crystal structure in materials.

9.2.5 Raman analysis

The powders were analyzed in a Renishaw inVia Reflex Raman spectrometer under excitation by a green Nd-YAG laser beam of 532 nm wavelength. The laser was operated at 1% of its maximum power. The shift spectrum was collected in the range of 100 to 1000 cm^{-1}.

9.2.6 Pellet preparation

A pellet of t-ZrO_2 powder was pressed under a uniaxial load of 600 MPa, followed by sintering in a muffle furnace at 1400°C in air for 11 hours.

9.2.7 Micro-indentation

The pellet was indented under 10 N (1 kgf) (Wolpert Wilson Tukon 2100).

Correlative Raman and Secondary Electron Imaging

The indentation area was analyzed by using a correlative Raman and SE imaging microscopy in a fully-integrated Raman Imaging and Scanning Electron Microscope (RISE; WiTec+Tescan TIMA).

9.2.8 Computer programming

Attenuation length of electrons was simulated using EAL (NIST Electron Effective-Attenuation-Length Database). Computer programs were prepared based in Python Language for the visualization of electron-matter theoretical interaction and for the analysis of electron micrographs. Some basic pre-processing steps on the electron micrographs were performed by ImageJ (details in Supplementary Information). After preliminary processing, three different areas were cropped from each micrograph,

representing m-phase, t-phase, and carbon tape support. The number of the pixels in each of them was higher than 10,000. The average intensity ($\bar{I}$) of each phase was calculated from the arithmetic mean of the pixel intensities for the relevant phase.

9.3 Results

9.3.1 X-ray Diffraction Analysis

The X-ray diffraction patterns of pure ZrO_2 (Figure 74) and 3Y-PSZ (Figure 75) powders were compared with the crystal structure data from the literature [239]. It was revealed that the pure ZrO_2 powder had a monoclinic crystal structure (PDF card no.: 96-230-0544). It had a space group of C_{2h}^5; $P2_1/c$, and the number of formula units in the unit cell was $Z = 4$ [245]. The strongest characteristic reflections of m-ZrO_2 were determined as follows: the peak at $2\theta = 28.23°$ belongs to $(\bar{1}11)$ atomic plane and the peak at $2\theta = 31.47°$ belongs to (111) atomic plane.

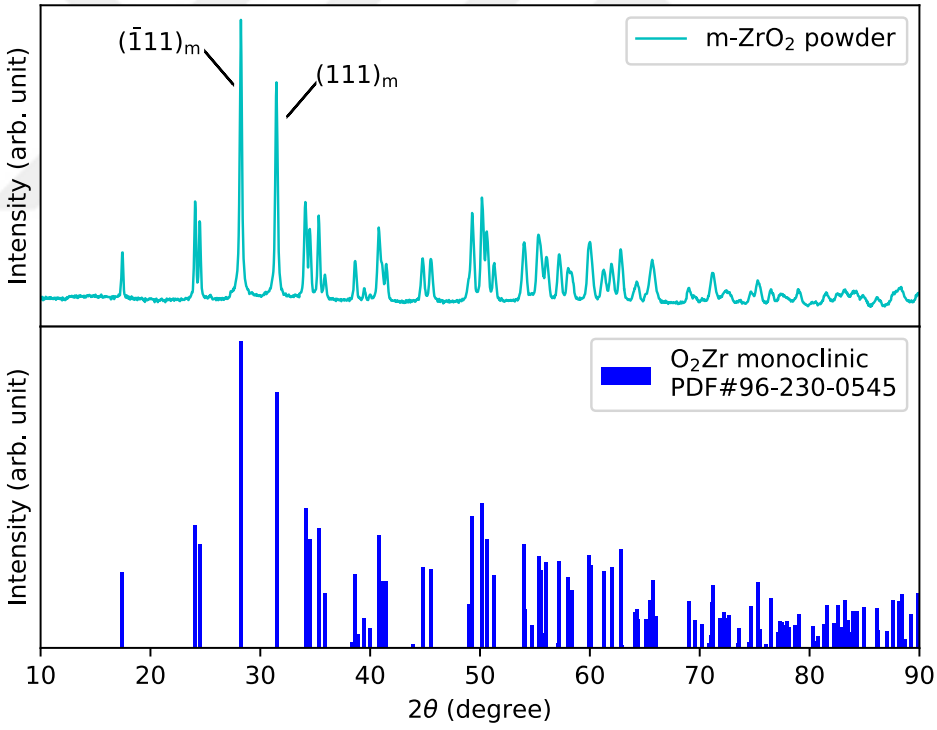


Figure 74: XRD pattern analysis of prepared ZrO_2 powder

Analysis of the XRD pattern of 3Y-PSZ revealed that the tetragonal crystal structure (PDF card no. 96-152-1475) dominates the powder. It was in the space group of D_{4h}^{15}, $P4_2/nmc$, and the number of formula units in the unit cell was $Z = 4$ [245]. The strongest characteristic peak of t-phase appeared at $2\theta = 30.18°$. It was attributed to the (111)

plane. The pattern showed that the powder was a mixture of phases. Along with the tetragonal phase, it contained some monoclinic crystals as well. The peaks at $2\theta = 28.07°$ and $2\theta = 31.27°$ were associated with $(\bar{1}11)_m$ and $(111)_m$ planes, respectively. Three peaks at $(111)_t$, $(\bar{1}11)_m$ and $(111)_m$, were used to calculate the fraction of m-phase after subtracting the background [239]. It was found that 18% of the powder was in the m-phase, therefore, 82% was in the t-phase.

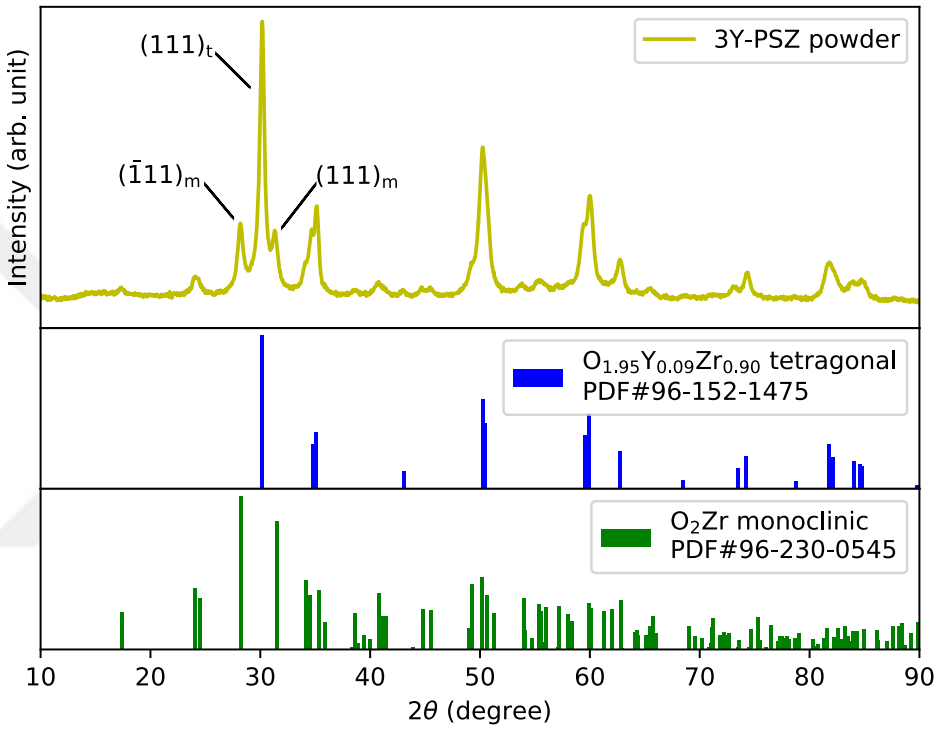


Figure 75: XRD pattern of 3Y-PSZ powder comprised mainly from tetragonal and monoclinic phases

9.3.2 Raman Spectroscopy

Raman spectroscopy was used to identify the m-ZrO_2 (Figure 76). The spectral features were consistent with the data reported in the literature, showing all 15 Raman-active bands of m-ZrO_2 out of 18 expected bands ($9A_g + 9B_g$) [239]. The bands at 178 cm^{-1} and 190 cm^{-1} were considered as the characteristic bands of m-ZrO_2 [239].

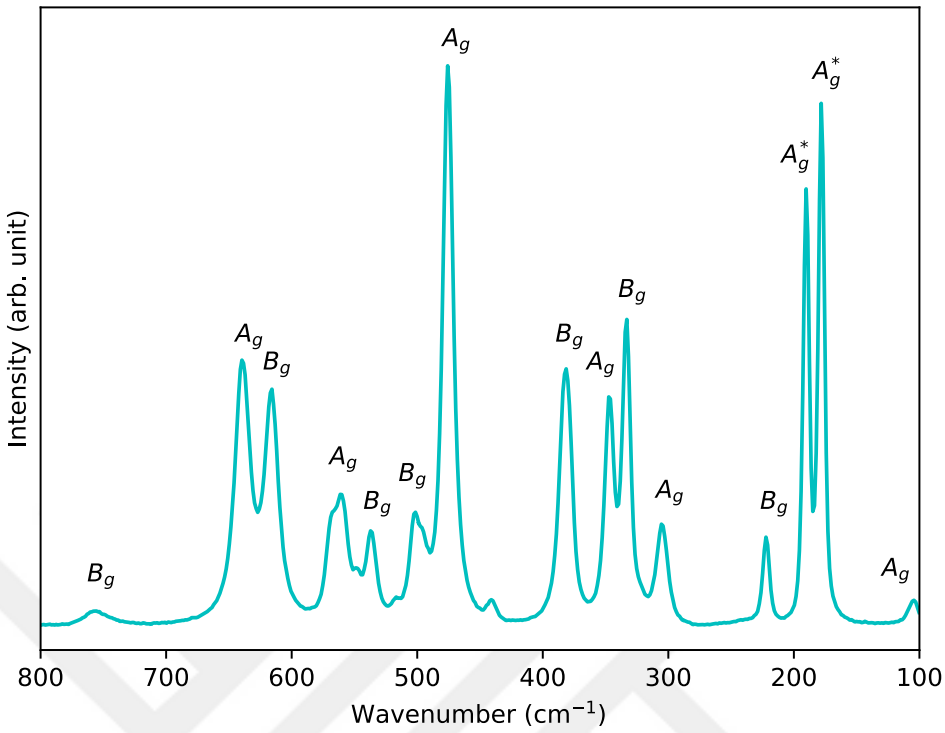


Figure 76: Raman shift spectrum of prepared monoclinic ZrO_2. Identifying characteristic peaks indicated with asterisk ($*$)

The Raman spectrum of 3Y-PSZ powder was also analyzed (Figure 77). The analysis revealed that this powder was a polycrystalline mix predominated by t-ZrO_2. It also had a trace amount of m-ZrO_2. The results from Raman spectroscopy paralleled the results observed in the XRD analysis of the same powder. Peak analysis of the spectrum in Figure 77 revealed the 6 bands of t-ZrO_2 out of 7 bands ($A_{1g} + 2B_{1g} + 3E_g + B_g$) [239]. The remaining peaks were consistent with the bands of m-ZrO_2 (indicated with (+) in Figure 77)

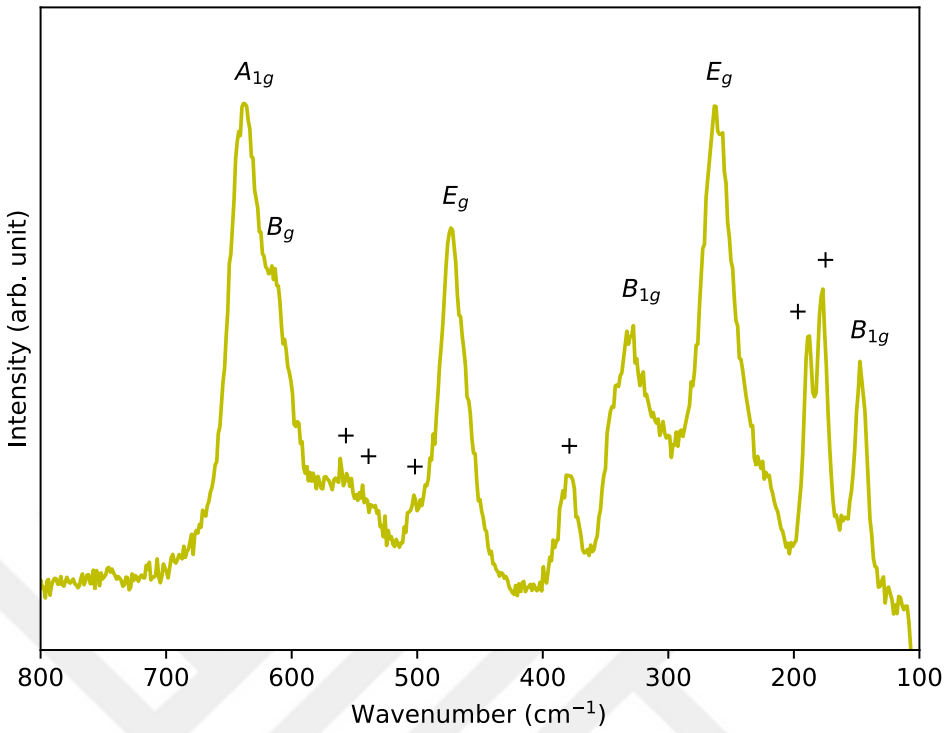


Figure 77: Raman shift spectrum of tetragonal 3Y-PSZ with peaks from monoclinic phase indicated with (+)

9.3.3 SEM analysis

To avoid chagrin of the sample, a thin Au-Pd coating was applied before SEM analysis. The thickness of Au-Pd deposition onto the sample was less than 5.59 nm (detailed calculations in Supplementary Information). This thickness was considered a minor factor, and its interference with the signal of sample was assumed to be insignificant.

9.3.4 Non-coated samples

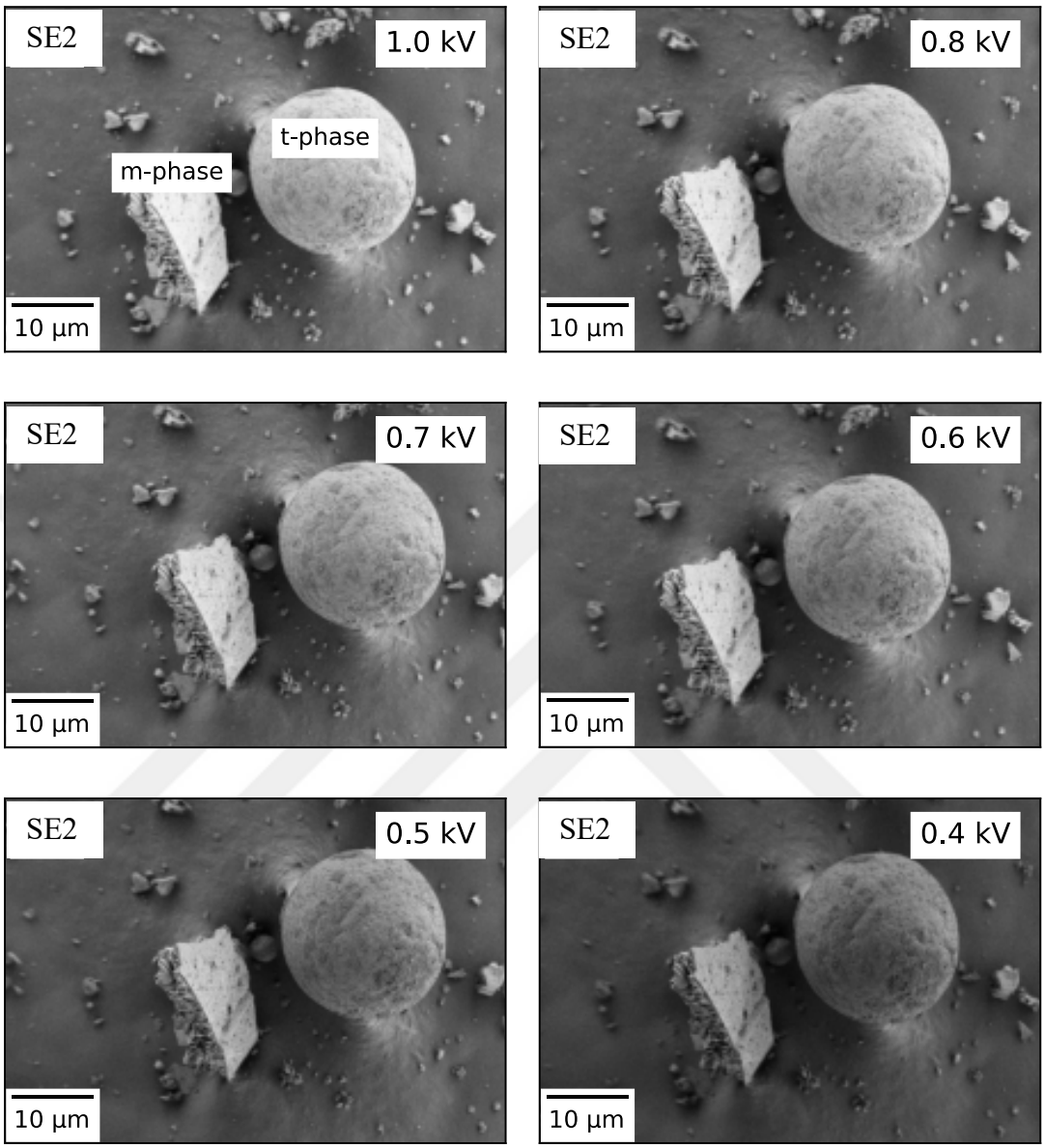


Figure 78: Micrograph of uncoated m-phase and t-phase captured on the Everhart-Thornley detector (SE2)

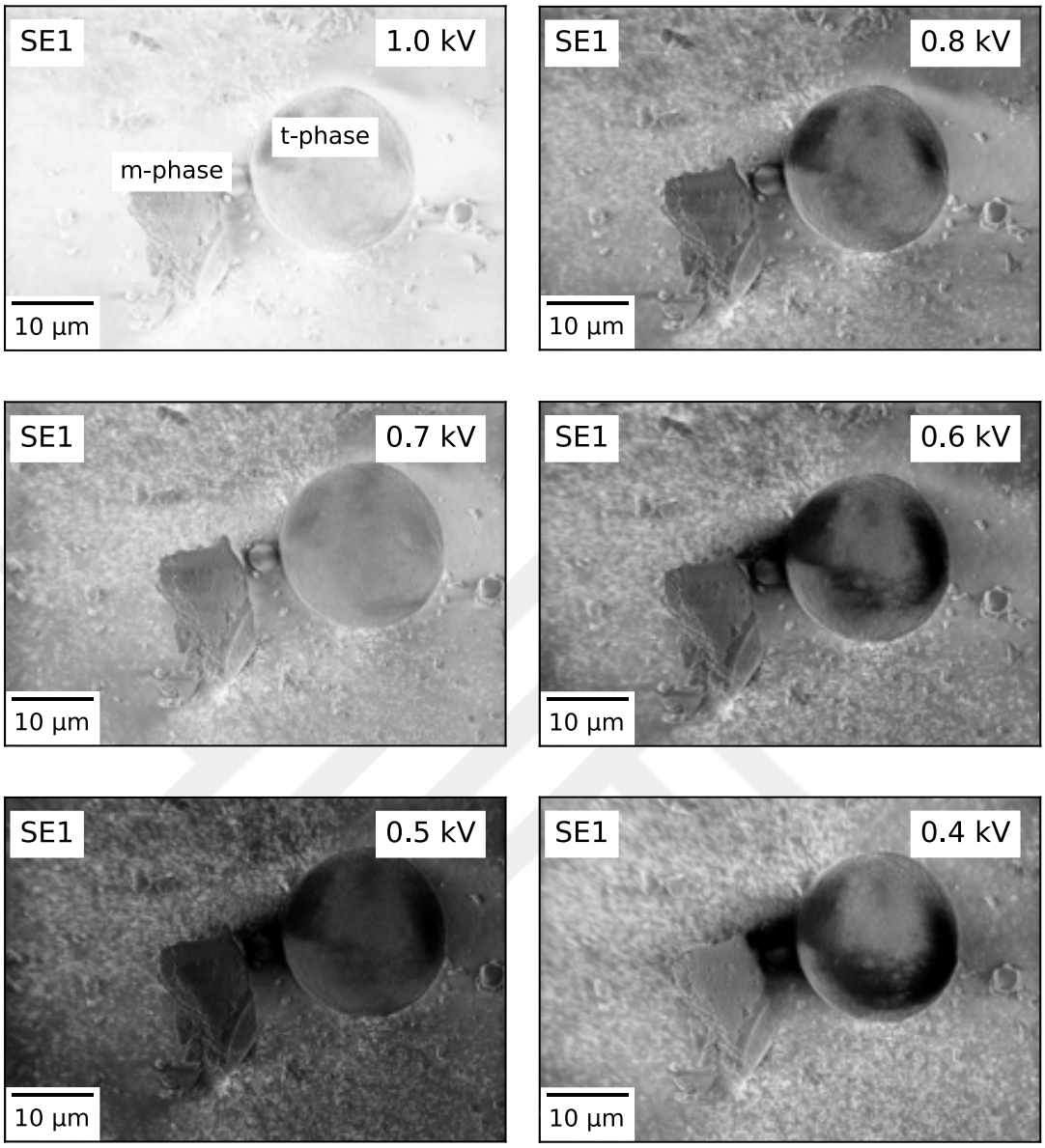


Figure 79: Micrograph of uncoated m-phase and t-phase captured on the in-lens detector (SE1)

9.3.5 Backscattered electron signal

The backscattered electron (BSE) micrographs of m-phase and t-phase are shown in Figure 80. The working distance was kept at 5.6 mm in all acceleration voltages. The micrographs were captured with the PE acceleration voltages ranging from 2.0 kV to 1.4 kV. The brightness of the images was fixed at 50%. The contrast of the images was fixed at 50%. A BSE image could not be captured in lower acceleration voltages with this working distance, the brightness, and the contrast. In the image captured at the

acceleration voltage of 2.0 kV, the m-phase and t-phase was annotated. The m-phase had a rod-like shape, and the t-phase had a spherical shape. The polymorphs showed no contrast difference, and this lack of the difference was independent of the PE acceleration voltage.

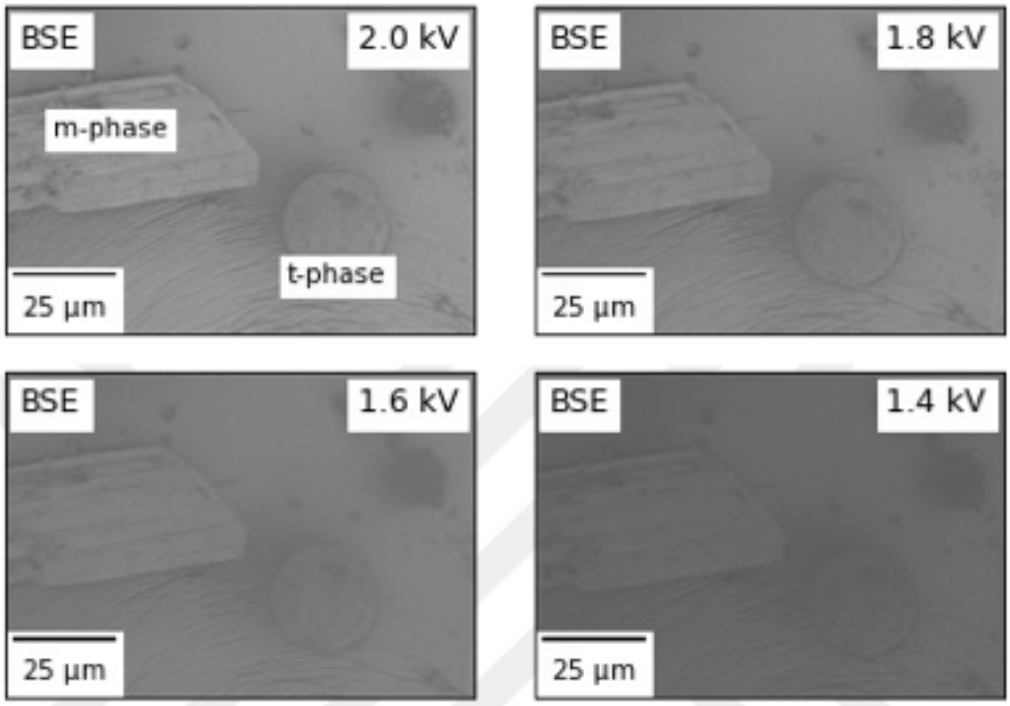


Figure 80: BSE electron micrographs of monoclinic (rod) and tetragonal (sphere) zirconia particles (Brightness 50%, Contrast 45%).

9.3.6 Secondary electron signal (SE2)

The m-phase and t-phase powders were imaged by the SEM using a conventional Everhart-Thornley detector (SE2) at different PE acceleration voltages (Figure 81). The images were captured under the fixed brightness (50%) and contrast (50%). The working distance was kept at 4.7 mm. The images, overall, became darker when the PE acceleration voltage reduced from 2.0 kV to 0.6 kV. No significant contrast was observed between m-phase and t-phase. Decrease of the acceleration voltage did not affect the lack of the differential contrast between the phases.

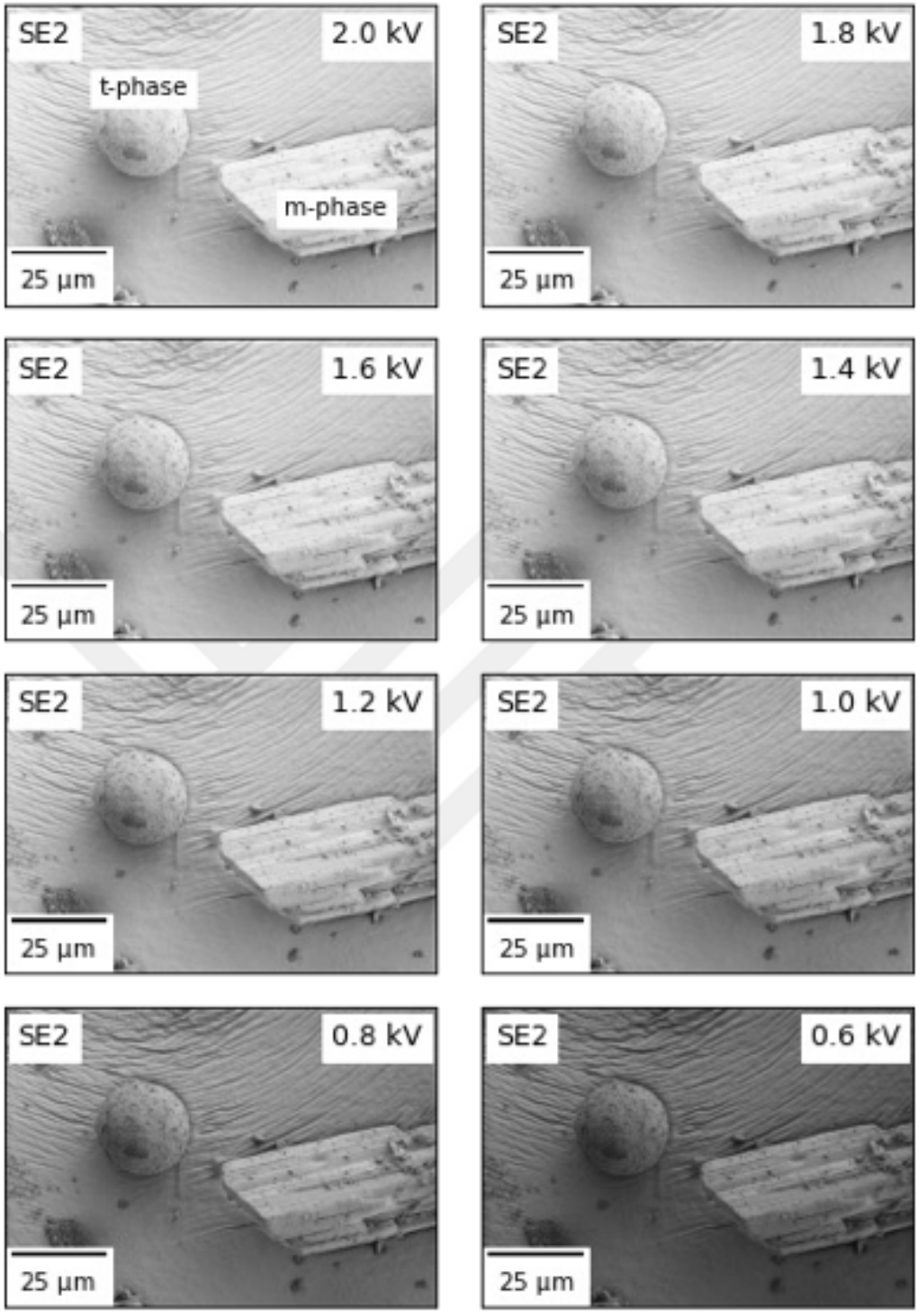


Figure 81: SE2 micrographs of monoclinic (rod) and tetragonal (sphere) zirconia particles under different accelerating voltages, collected using a conventional Everhart-Thornley detector (Brightness 50%, Contrast 50%).

9.3.7 Secondary electron signal (SE1)

The m-phase and t-phase was imaged using a TTL detector (Figure 82) while the SEM was operating in the low acceleration voltage range (<5 kV). The m-phase appeared brighter than the t-phase at 2.0 kV of PE acceleration voltage. By decreasing the PE acceleration, the brightness of the whole image appeared to be decreasing due to the reduction in the S/N. Besides, by reduction of the acceleration voltage from 2.0 kV to 0.6 kV, the difference in the contrast level of the m-phase and t-phase increased (Figure 82).

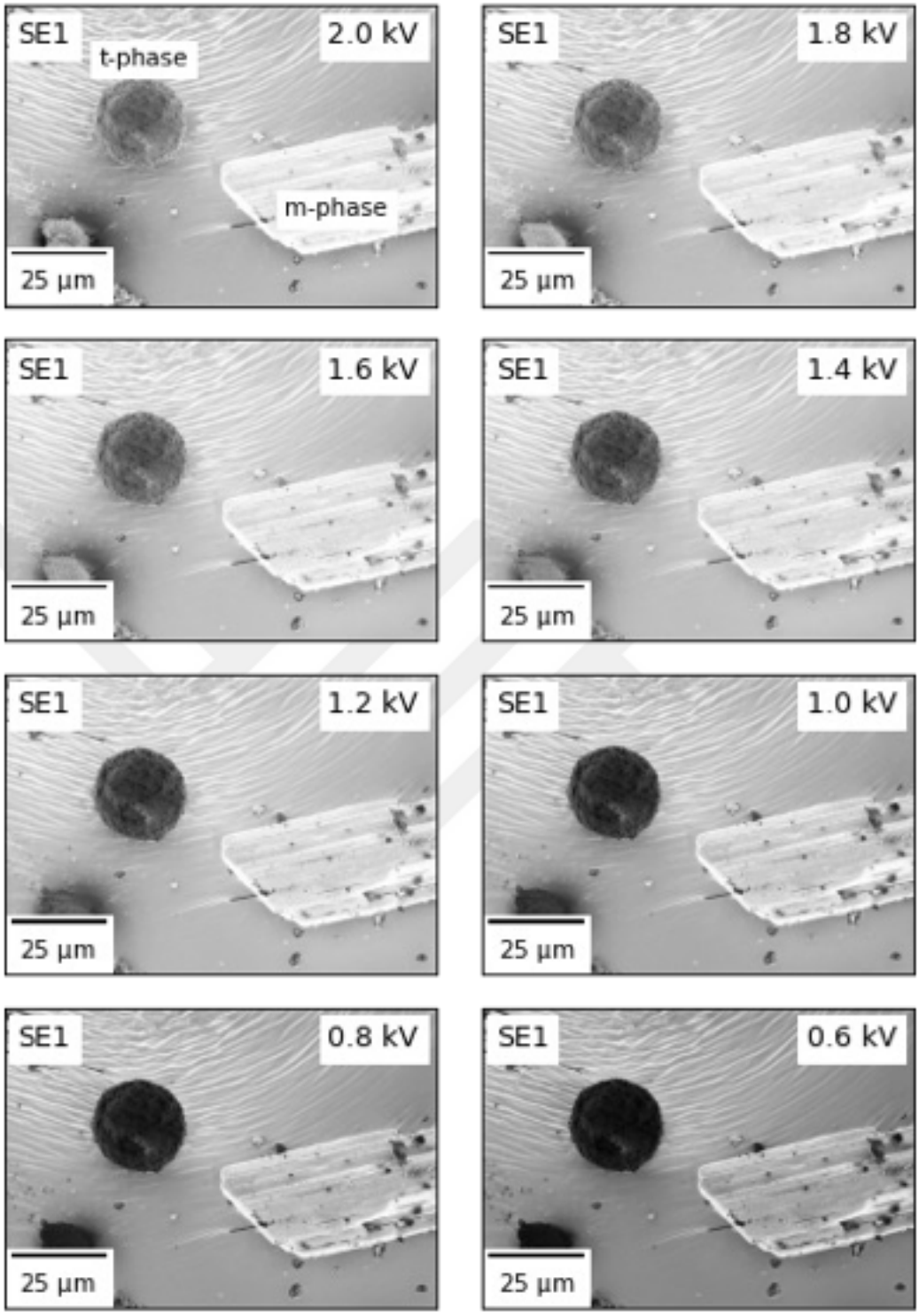


Figure 82: SE1 micrographs revealing contrasting signal intensity behavior between monoclinic (rod) and tetragonal (sphere) zirconia particles under different accelerating voltages, using a TTL detector (Brightness 50%, Contrast 32%).

9.3.8 Effect of working distance on the SE1 signal

The effect of working distance on the SE1 image of m-phase and t-phase is shown in Figure 83. The intensity of the hole image reduced by increasing the working distance. Furthermore, the difference in the intensity of the m-phase and t-phase reduced as the working distance increased.

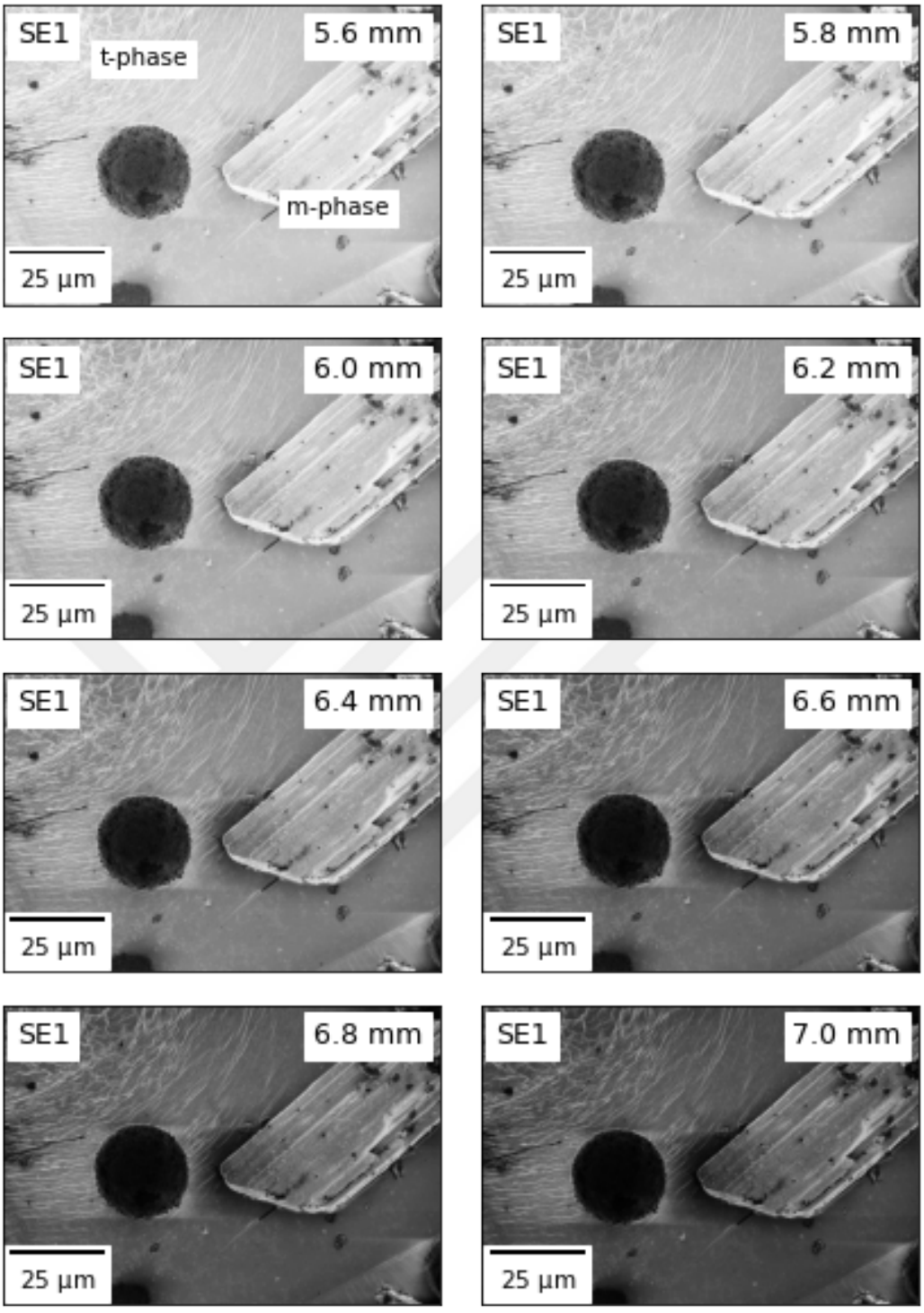


Figure 83: SE1 micrographs revealing the effect of the working distance in the intensity difference between monoclinic (rod) and tetragonal (sphere) zirconia particles under different accelerating voltages, using a TTL detector (Brightness 42.5%, Contrast 35.0%).

9.3.9 Effect of working distance on the SE2 signal

The SE2 images of m-phase and t-phase were captured in a range of working distance (Figure 84). As a hole the effect was minor. M-phase and t-phase and the support stayed almost at the same brightness levels.

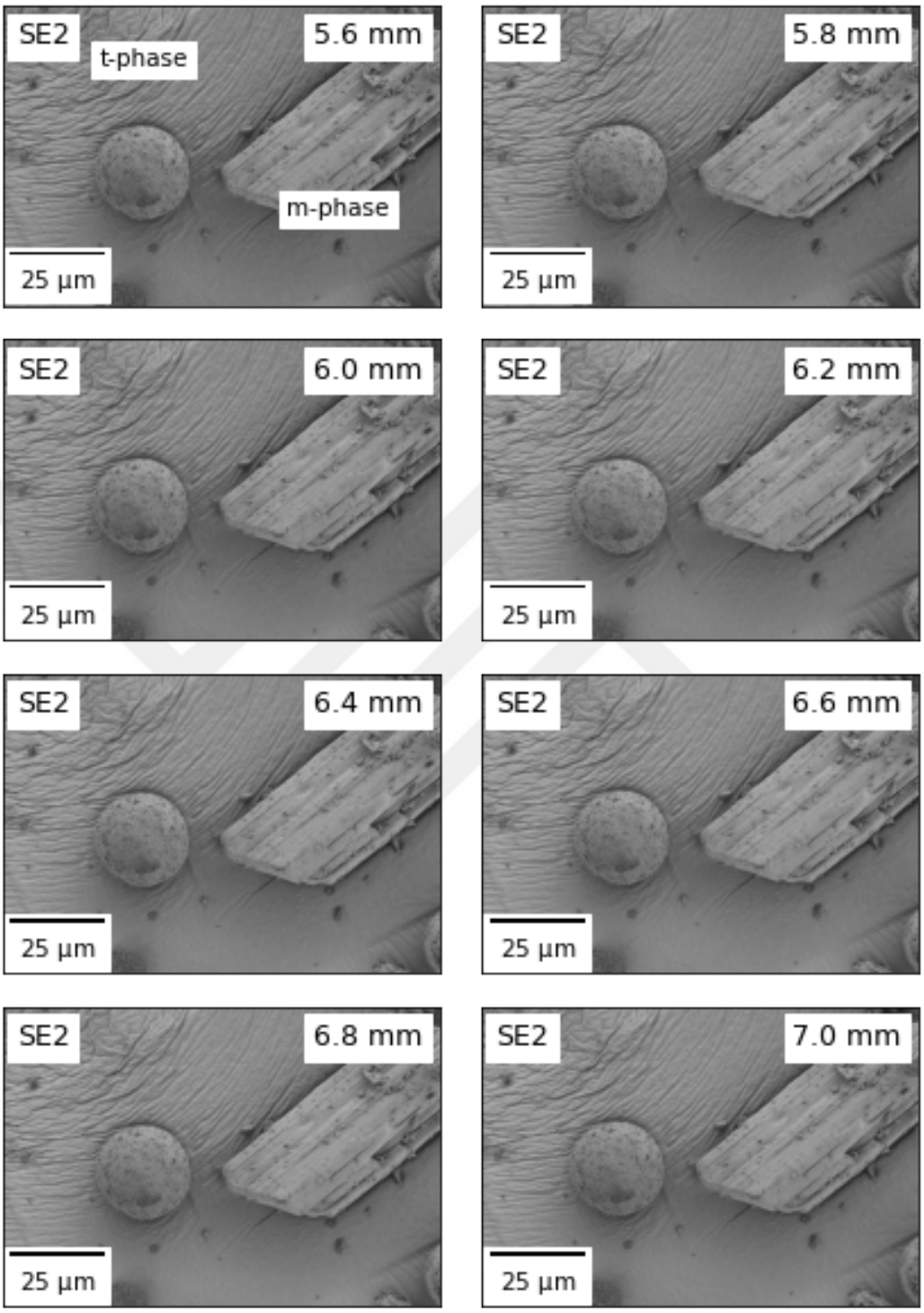


Figure 84: SE2 micrographs revealing the effect of the working distance in the intensity difference between monoclinic (rod) and tetragonal (sphere) zirconia particles under different accelerating voltages, using an ET detector (Brightness 50.0%, Contrast 50.0%).

9.3.10 Raman Shift Mapping of Micro-indented Zirconia Pellet

An indent on a pellet sintered from partially stabilized tetragonal ZrO_2 powder is shown at Figure 85a. Indentation on the pellet of t-phase created a diamond-shape indent on the surface of the pellet. The Raman spectrum of the region around the indent was analyzed. The resulted map was superposed on the SEM image of the indent (Figure 85b). Although the pellet was prepared from t-phase powder. As expected, in the region of high stress concentration martensitic phase transformation of t-phase occurred [252]. Further analysis of the Raman phase map (Figure 85c) revealed that the concentration of the m-phase was maximized on the edges and extended along the indent edges rather than its center as previously demonstrated by [254]. The transformed region stretched from the corner for about *ca.* 3 µm along the crack (Figure 85d). The smallest area from which Raman signal was collected in Figure 85d was approximately 210 nm.

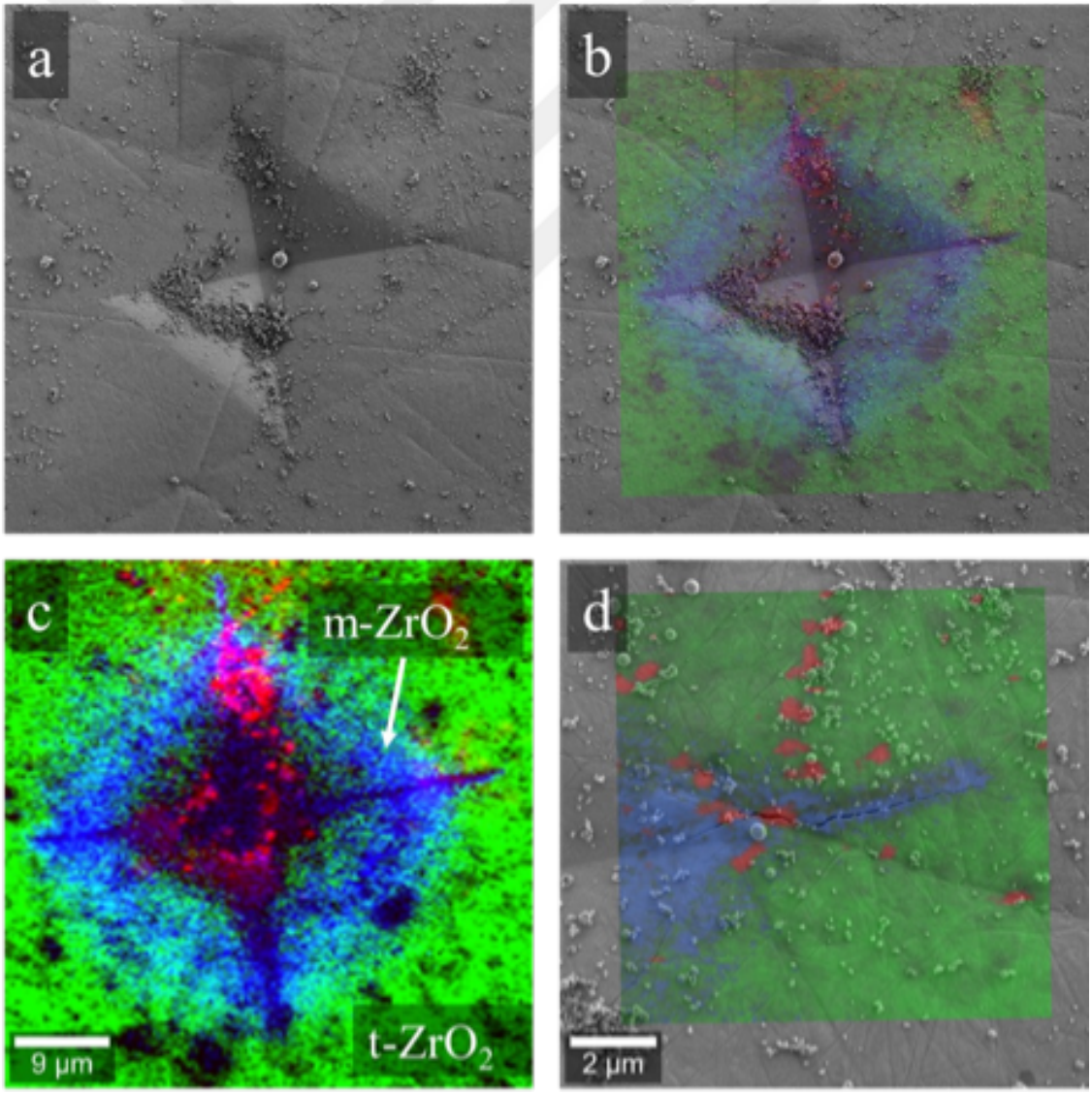


Figure 85: Identification of stress-induced phase-transformation regions in pellet sintered from partially stabilized zirconia; SEM micrograph of the micro-indented pellet (a), overlaid micrograph and Raman map (b), Raman map near a crack (c), overlaid micrograph and Raman map near crack; tetragonal matrix (green), monoclinic transformed phase (blue), carbon contaminations (red).

9.3.11 Low-kV SEM of Micro-indented Zirconia Pellet

The SE2+SE1 image of the micro-indentation on the pellet of the partially stabilized zirconia is shown in Figure 86a. The partially stabilized tetragonal matrix transformed into the monoclinic phase near the cracks initiated near the corners of the indent (blue region in Figure 85d). The TTL electron micrograph of the same crack (Figure 86c) shows the t-phase in the matrix in dark and the transformed m-phase in bright contrast. The bright region extended along the crack edges. The enhanced brightness of this region might be a mixed effect coming from two different sources: 1) the transformed phase that has a higher SE yield; and 2) the edge effect, which results in an increased SE yield. The out-of-the-surface relief along the crack edges (arrow marking in Figure 86c) suggests that the m-ZrO_2, which has a higher specific volume, exists in this region [261].

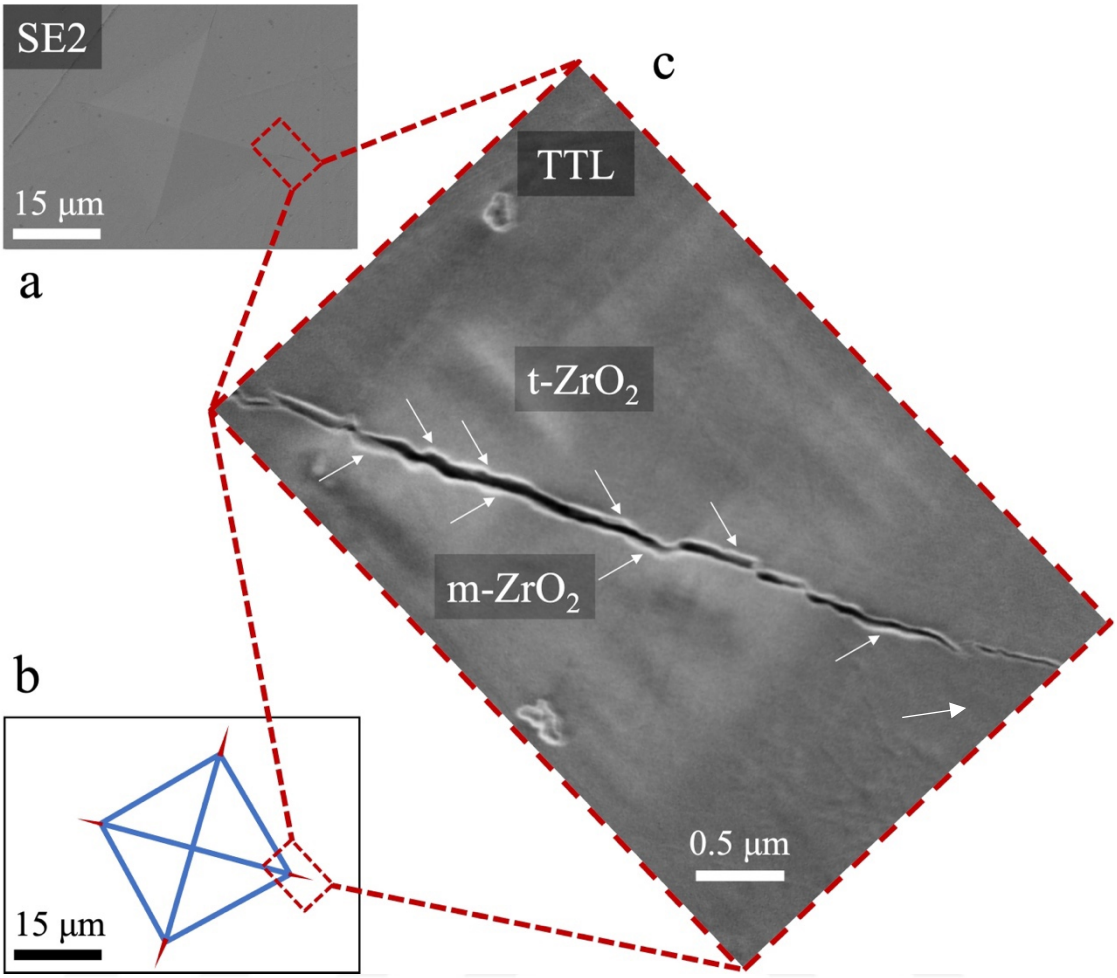


Figure 86: Contrast level difference near a crack initiated by a micro-indention on a pellet of partially stabilized zirconia; SE2 micrograph of indentation (a), schematic of indent and cracks along the corners (b), and TTL image of one of the cracks (c).

9.4 Discussion

The main goal of this study is to utilize the difference of the SE yield of materials to differentiate phases under SEM when there exists no atomic number difference. Low voltage SEM has been repeatedly used in previous studies for phase differentiation of polymorphs [188]. The results of all these studies confirmed that when the acceleration voltage of the primary electrons reduces, the effect of the electron configuration arises in the secondary electron yield of materials [219]–[222], [262]–[267]. Generated SEs in some polymorphs cannot escape the materials because their energy lays below the work function (or electron affinity in the inorganic materials) [222], [223], [262], [268]–[270]. The difference in the SE yield could be utilized for the differentiation of materials with no or low atomic number difference, yet difference in the electron configuration.

In this study, we used low voltage SEM combined with a TTL detector to differentiate two polymorphs of ZrO2. The results showed that in BSE and SE2 detection modes, both phases appeared at almost the same levels of the average intensely (Figure 80 and Figure 81). Further, the change of the acceleration voltage of primary electrons did not affect the lack of contrast between m-phase and t-phase (Table S1 and Table S2). However, when a TTL is used to collect the SE signal, m-phase always appeared with significantly higher average intensity compared to that of t-phase (Figure 82). This contrast even increased by the reduction of the acceleration voltage of PEs (Table S3). Briefly, even though there was nominally no atomic number contrast between m-phase and t-phase, these polymorphs were differentiated based on their different values of SE yield. The method was successful in the differentiation of polymorphs both in powder mode and in a transformation zone around an indent.

9.4.1 Electron Microscopy Analysis

9.4.2 Quantification of image contrast

9.4.2.1 Preprocessing steps

In every SEM like Figure 87, three segments were cropped out from the image for quantification of the average intensity: 1) homogeneous part of the carbon tape support, 2) m-phase, and 3) t-phase. It was made sure that the total number of pixels in each segment be more than 10,000.

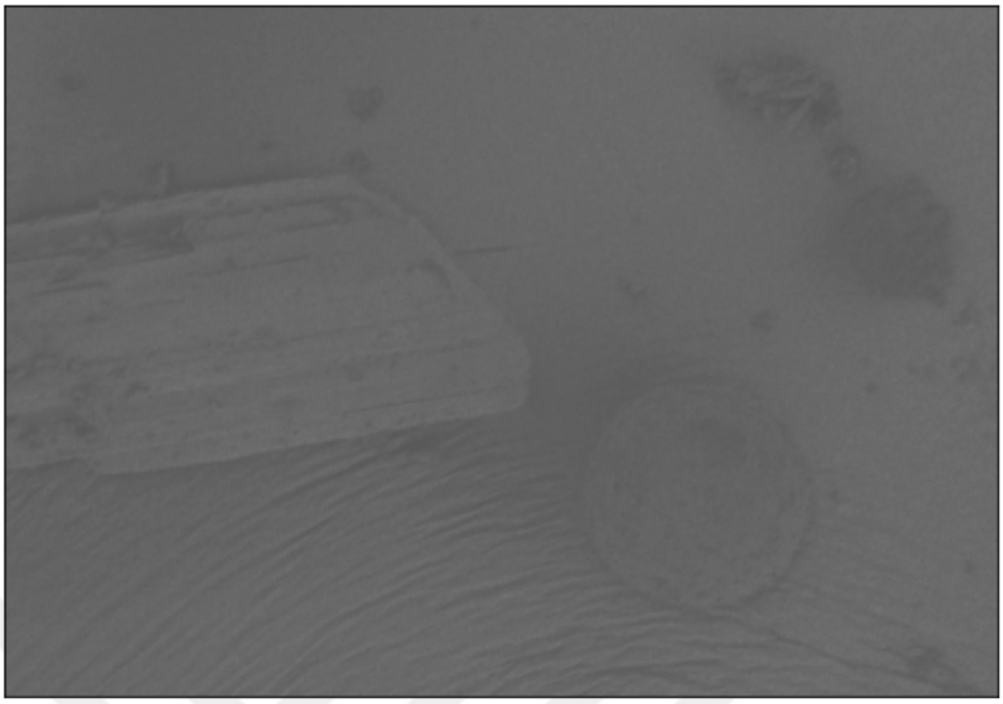


Figure 87: SEM micrograph (BSE, brightness 50%, contrast 45%).

9.4.3 Micrograph segmentation

9.4.3.1 Carbon tape support

One segment consisted of a homogenous part of carbon tape support in the image. The area of carbon tape support was selected in ImageJ. All pixels outside this area were set to the intensity value of zero. All pixel intensities in the area of the selected carbon tape support were nonzero. Therefore, the set pixel values outside the area did not interfere with the values of the pixels inside the selected area (Figure S4).



Figure 88: Cropped area of the carbon tape support from SEM micrograph (BSE, brightness 50%, contrast 45%). The intensity of the area outside the phase was set to zero.

9.4.3.2 Monoclinic phase

The m-phase was mostly the brightest part in the image. The area of m-phase might contain pixels with the maximum value (255). They did not have any pixel with the intensity equal to zero. To crop m-phase, first 1 was subtracted from all pixel intensities of the image. Then an area of m-phase was selected in ImageJ. All pixels outside this area were set to the intensity value of 255. Since already 1 was subtracted from the pixel intensities, there was no interference in the pixel values of the m-phase and that of the pixels outside m-phase.



Figure 89: Cropped area of the m-phase from SEM micrograph (BSE, brightness 50%, contrast 45%). The intensity of all pixels subtracted by one. Then, the intensity of the area outside the phase was set to 255.

9.4.3.3 Tetragonal phase

The t-phase was mostly the darkest part in the image. The area of m-phase might contain pixels with minimum intensity value (zero). They did not have any pixel with the intensity equal to 255. To crop t-phase, first 1 was added to all pixel intensities of the image. Then an area of t-phase was selected in ImageJ. All pixels outside this area were set to the intensity value of zero. Since already 1 was added to the pixel intensities, there was no interference in the pixel values of the t-phase and that of the pixels outside t-phase.



Figure 90: Cropped area of the t-phase from SEM micrograph (BSE, brightness 50%, contrast 45%). The intensity of all pixels raised by one. Then, the intensity of the area outside the phase was set to zero.

9.4.4 Histogram construction

9.4.4.1 Carbon tape support

The resulted cropped micrograph of carbon tape support was fed to a computer program in Python®. Histogram of this micrograph showed a small accumulation around 100 and a large accumulation at zero. The accumulation of zero values were related to the area outside the selected carbon tape support.

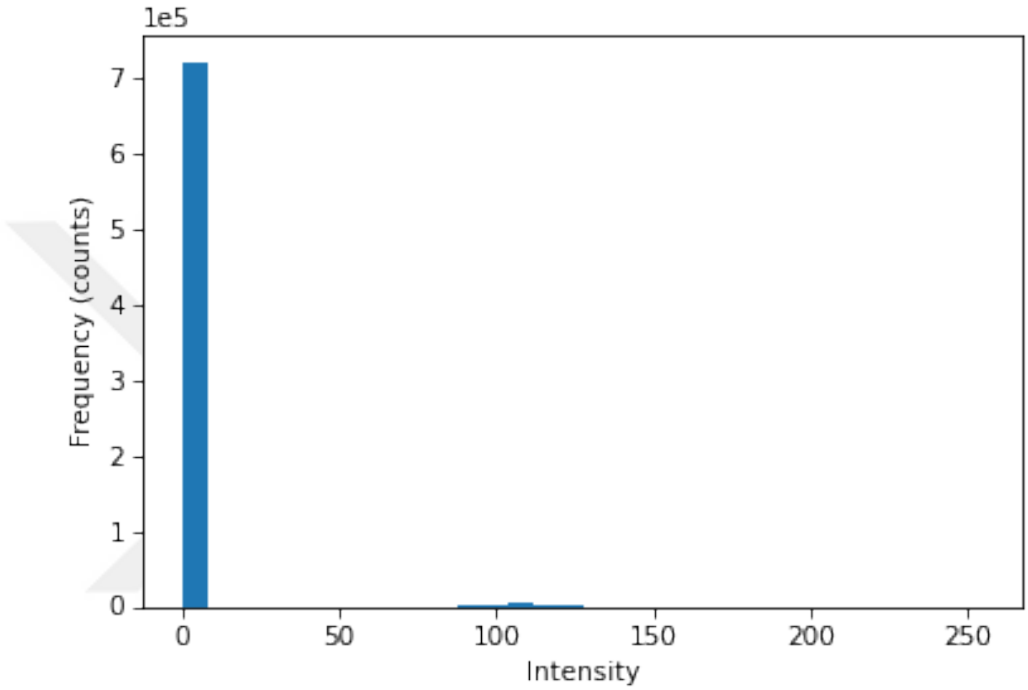


Figure 91: histogram of carbon tape support from segmented BSE image before exclusion of zero intensities (fixed brightness 50% and contrast 45%).

Pixel values equal to zero were excluded from the data. New histogram was generated based on the new data. After exclusion of pixels with the intensity of zero, the histogram emerged with the real values corresponding to the carbon tape support area. Average intensity of the pixels was calculated as the arithmetic mean of the pixel intensities. The average intensity was shown by a dashed red line in the histogram.

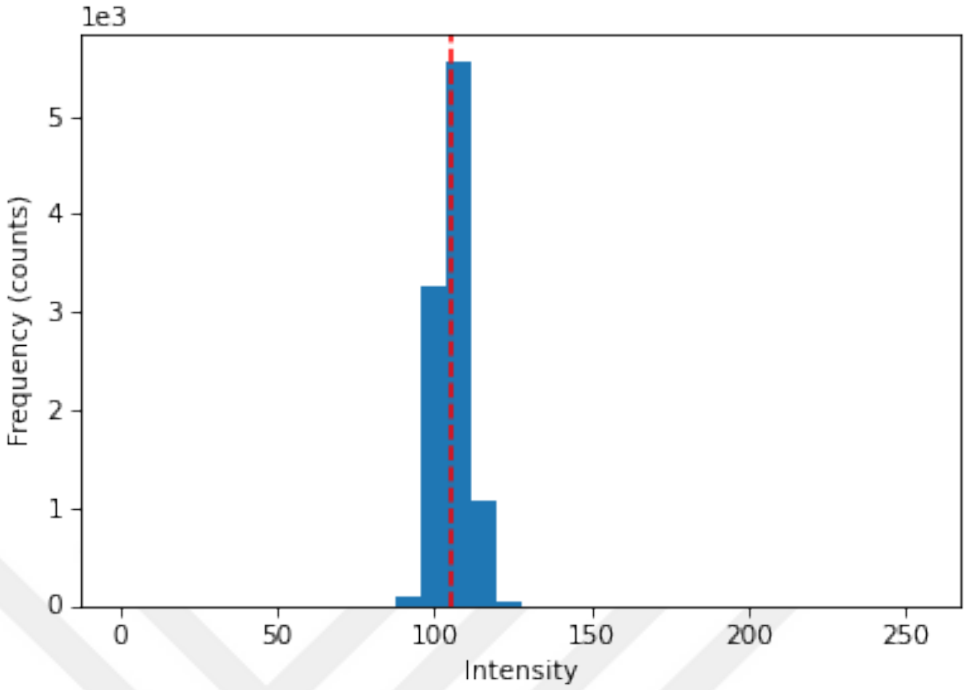


Figure 92: histogram of carbon tape support from segmented BSE image after exclusion of zero intensities (fixed brightness 50% and contrast 45%).

9.4.4.2 Monoclinic phase

The resulted cropped micrograph of m-phase was fed to a computer program in Python®. Histogram of this micrograph showed a small accumulation around 100 and a large accumulation at 255. The accumulation at 255 were related to the area outside the selected m-phase.

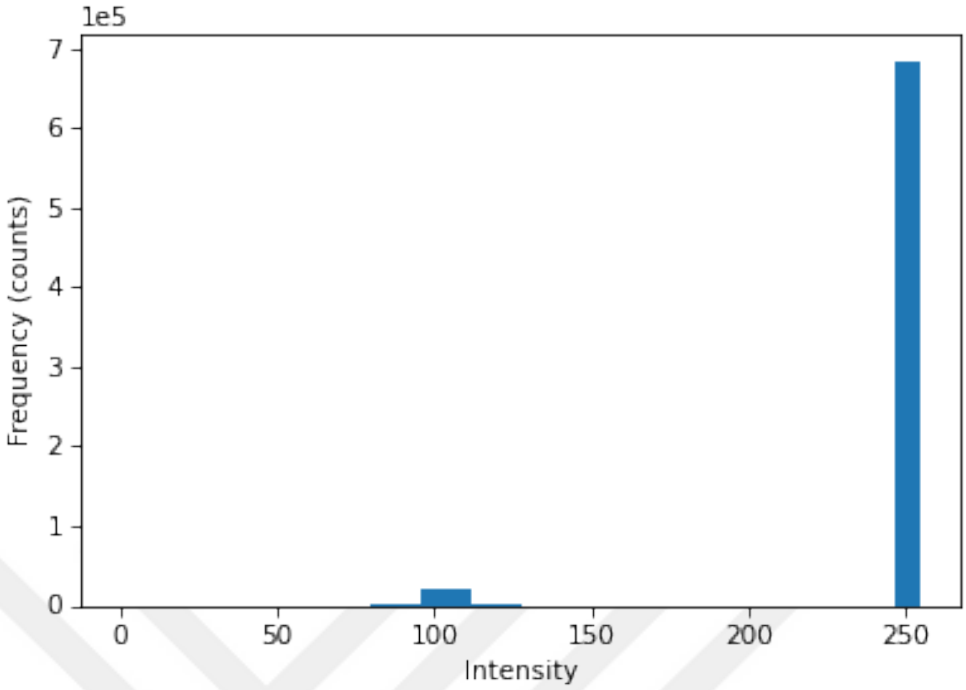


Figure 93: histogram of m-phase from segmented BSE image before the exclusion of pixels with the intensity values equal to 255 (fixed brightness 50% and contrast 45%). Pixel values equal to 255 were excluded from the data. After exclusion of pixels, 1 was added to the intensity of all remained pixel values to compensate for the previous subtraction of 1. New histogram was generated based on the new data. Average intensity of the pixels was calculated as the arithmetic mean of the pixel intensities. The average intensity was shown by a dashed red line in the histogram.

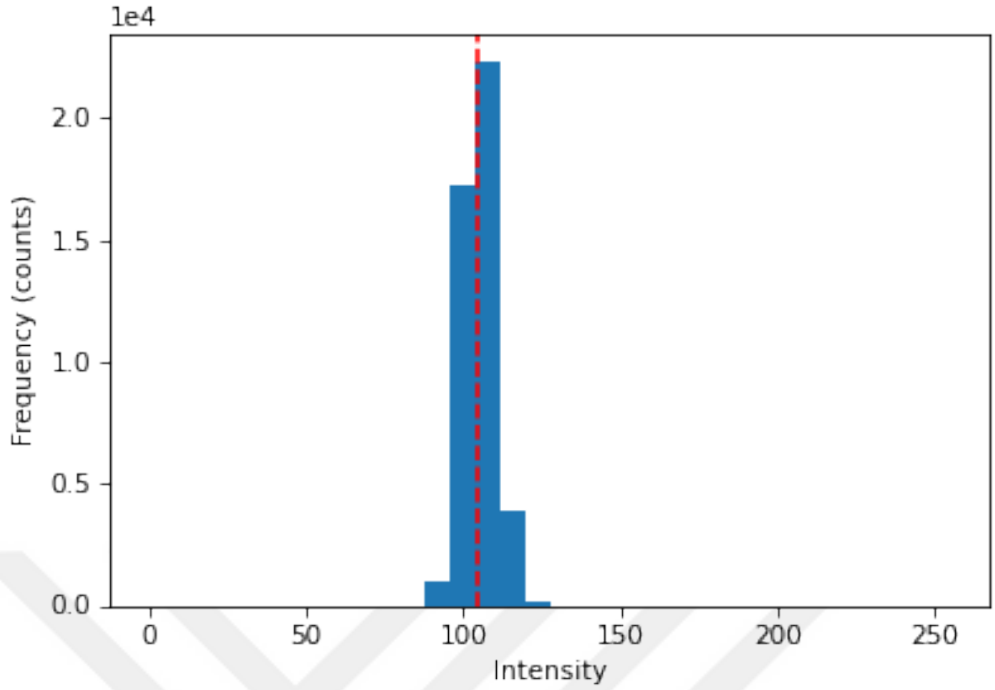


Figure 94: histogram of m-phase from segmented BSE image after the exclusion of pixels with the intensity equal to 255 and addition of 1 to all pixel intensities (fixed brightness 50% and contrast 45%).

9.4.4.3 Tetragonal phase

The resulted cropped micrograph of t-phase was fed to a computer program in Python®. Histogram of this micrograph showed a small accumulation around 100 and a large accumulation at zero. The accumulation at zero were related to the area outside the selected t-phase.

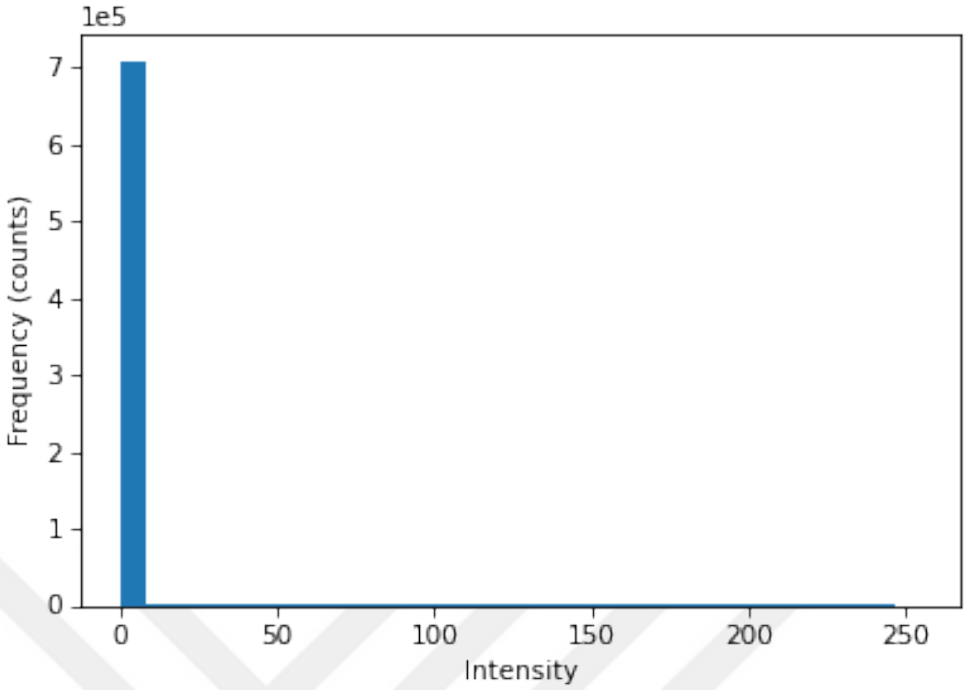


Figure 95: histogram of t-phase from segmented BSE image before the exclusion of pixels with the intensity values equal to zero (fixed brightness 50% and contrast 45%).

Pixel values equal to zero were excluded from the data. After the exclusion of pixels, 1 was subtracted from the intensity of all remained pixel to compensate for the previous addition of 1. New histogram was generated based on the new data. Average intensity of the pixels was calculated as the arithmetic mean of the pixel intensities. The average intensity was shown by a dashed red line in the histogram.

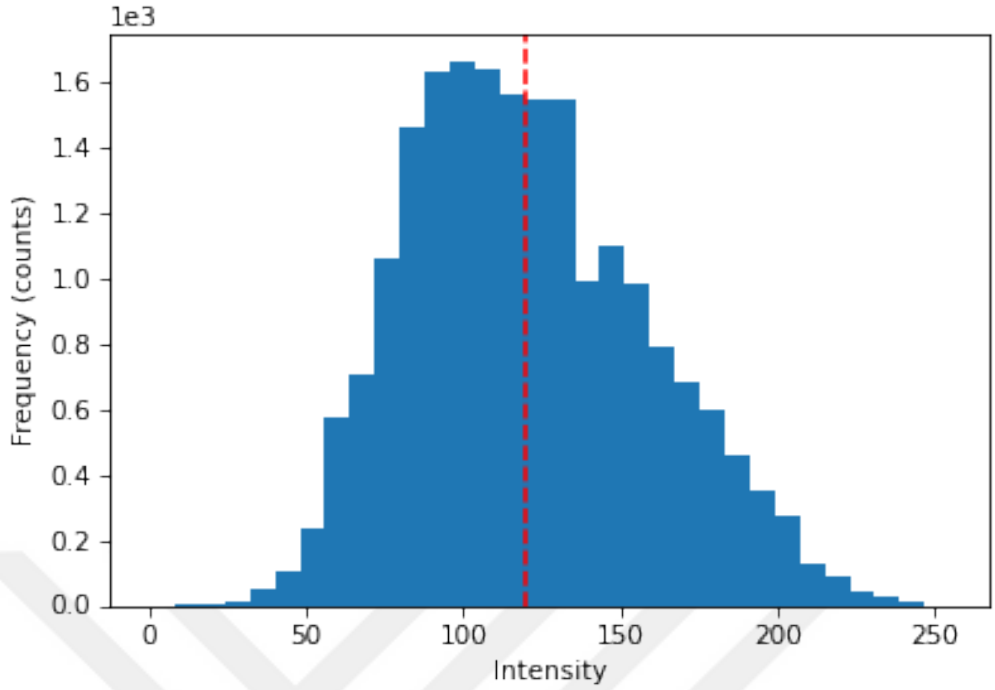


Figure 96: histogram of t-phase from segmented BSE image after the exclusion of pixels with the intensity equal to zero and subtraction of 1 from all pixel intensities (fixed brightness 50% and contrast 45%).

9.4.5 BSE signal

Quantification of BSE images captured in different acceleration voltages was performed after the preprocessing steps that was mentioned above.

9.4.5.1 Carbon tape support

Selected area of carbon tape support is shown for BSE signal at different PE acceleration voltages (Figure 97). The completely black area was the area which pixels of it were set to the intensity of zero.

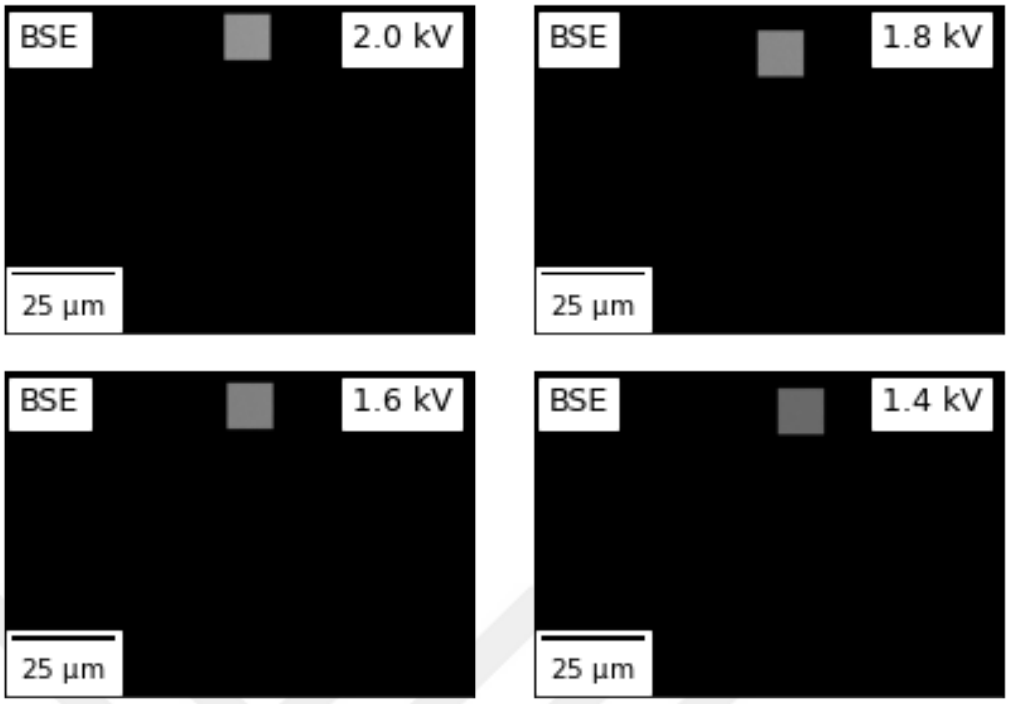


Figure 97: micrograph of carbon tape support from segmented BSE electron images (fixed brightness 50% and contrast 45%).

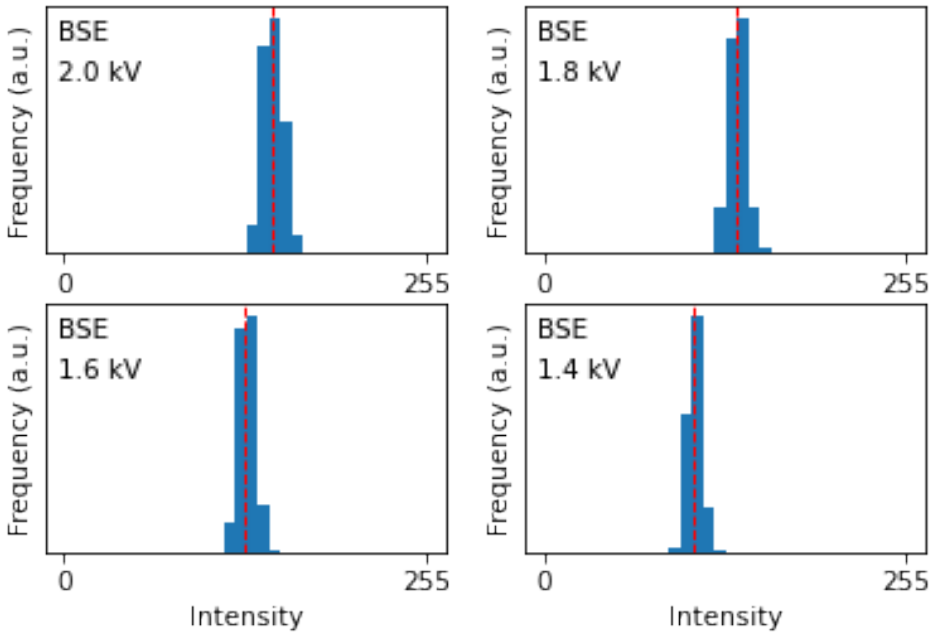


Figure 98: histogram of carbon tape support from segmented BSE electron images (fixed brightness 50% and contrast 45%).

9.4.5.2 Monoclinic phase

Selected area of m-phase is shown for BSE signal at different PE acceleration voltages (Figure 99). The completely white area was the area which pixels of it were set to the intensity of 255.

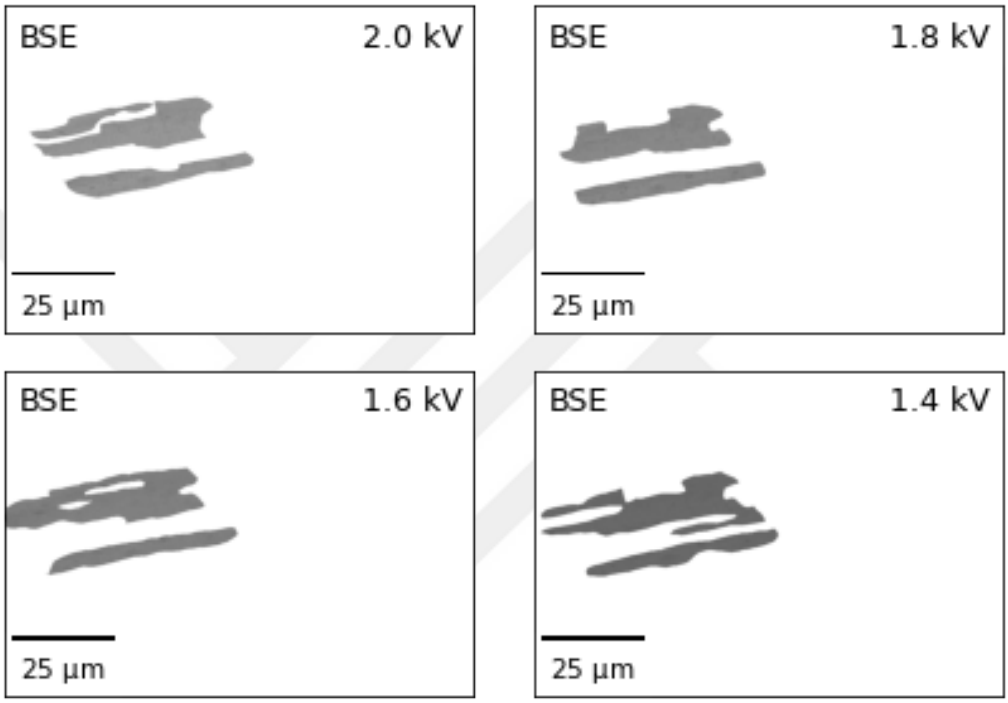


Figure 99: micrograph of m-phase from segmented BSE electron images (fixed brightness 50% and contrast 45%).

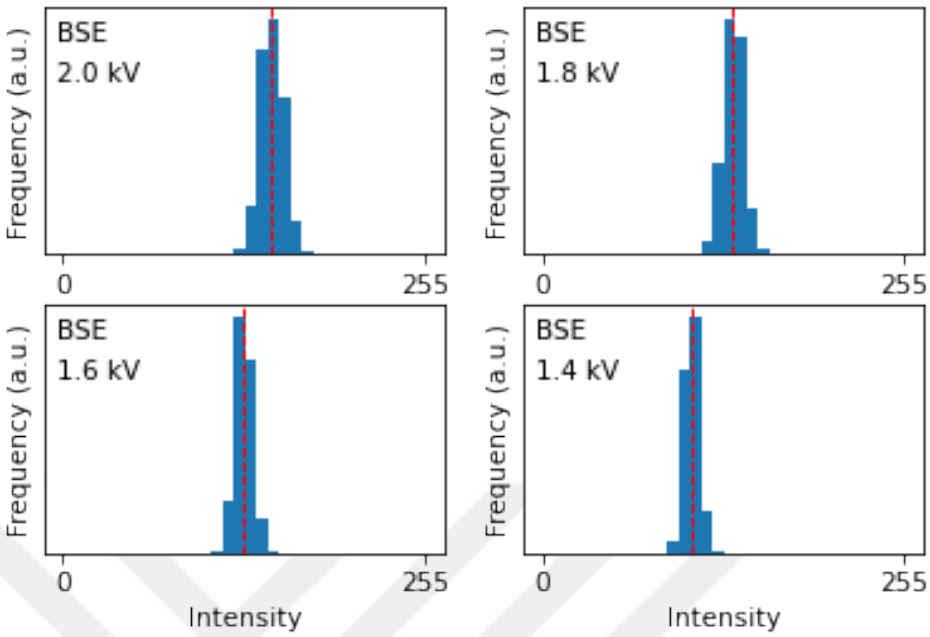


Figure 100: histogram of m-phase from segmented BSE electron images (fixed brightness 50% and contrast 45%).

9.4.5.3 Tetragonal phase

Selected area of t-phase is shown for BSE signal at different PE acceleration voltages (Figure 101). The completely black area was the area which pixels of it were set to the intensity of 0.

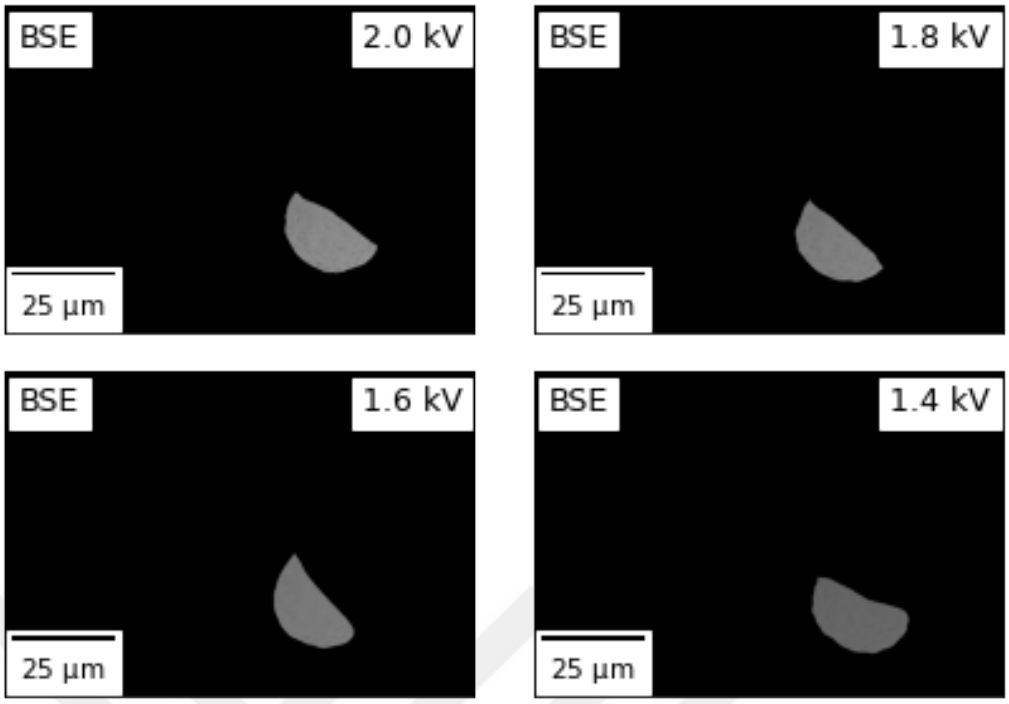


Figure 101: micrograph of t-phase from segmented BSE electron images (fixed brightness 50% and contrast 45%).

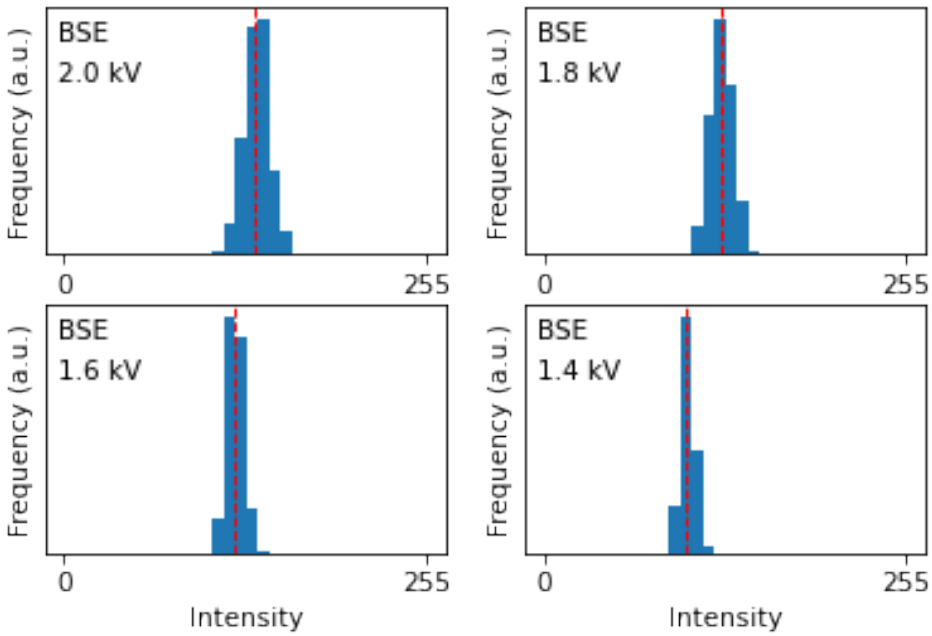


Figure 102: histogram of t-phase from segmented BSE electron images (fixed brightness 50% and contrast 45%).

The average intensity values for carbon tape support, m-phase, and t-phase were shown in Table S1.

Table 20: Average intensity for carbon tape support, m-ZrO_2, and t-ZrO_2 from SEM micrographs captured by BSE

Voltage (kV)	Average intensity of carbon tape support ($\bar{I}_s$)	Average intensity of m-phase ($\bar{I}_m$)	Average intensity of t-phase ($\bar{I}_t$)
1.4	106 ± 5	105 ± 5	101 ± 5
1.6	127 ± 5	127 ± 6	120 ± 6
1.8	136 ± 6	134 ± 7	125 ± 8
2.0	147 ± 7	147 ± 8	135 ± 9

9.4.6 SE2 signal

Quantification of SE2 images captured in different acceleration voltages was performed after the preprocessing steps that was mentioned above.

9.4.6.1 Carbon tape support

Selected area of carbon tape support is shown for SE2 signal at different PE acceleration voltages (Figure 103). The completely black area was the area which pixels of it were set to the intensity of 0.

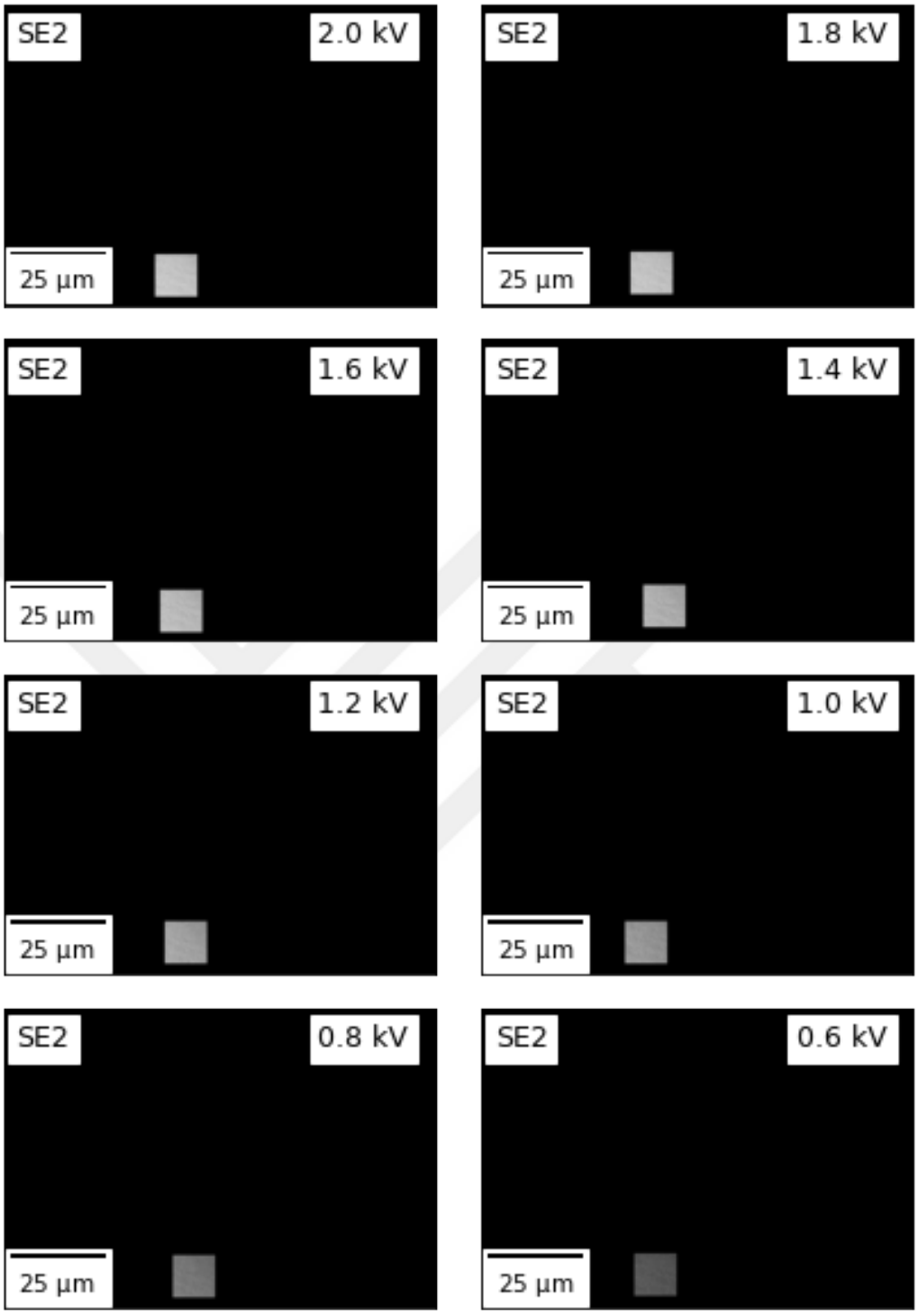


Figure 103: micrograph of carbon tape support from segmented SE2 electron images (fixed brightness 50% and contrast 50%).

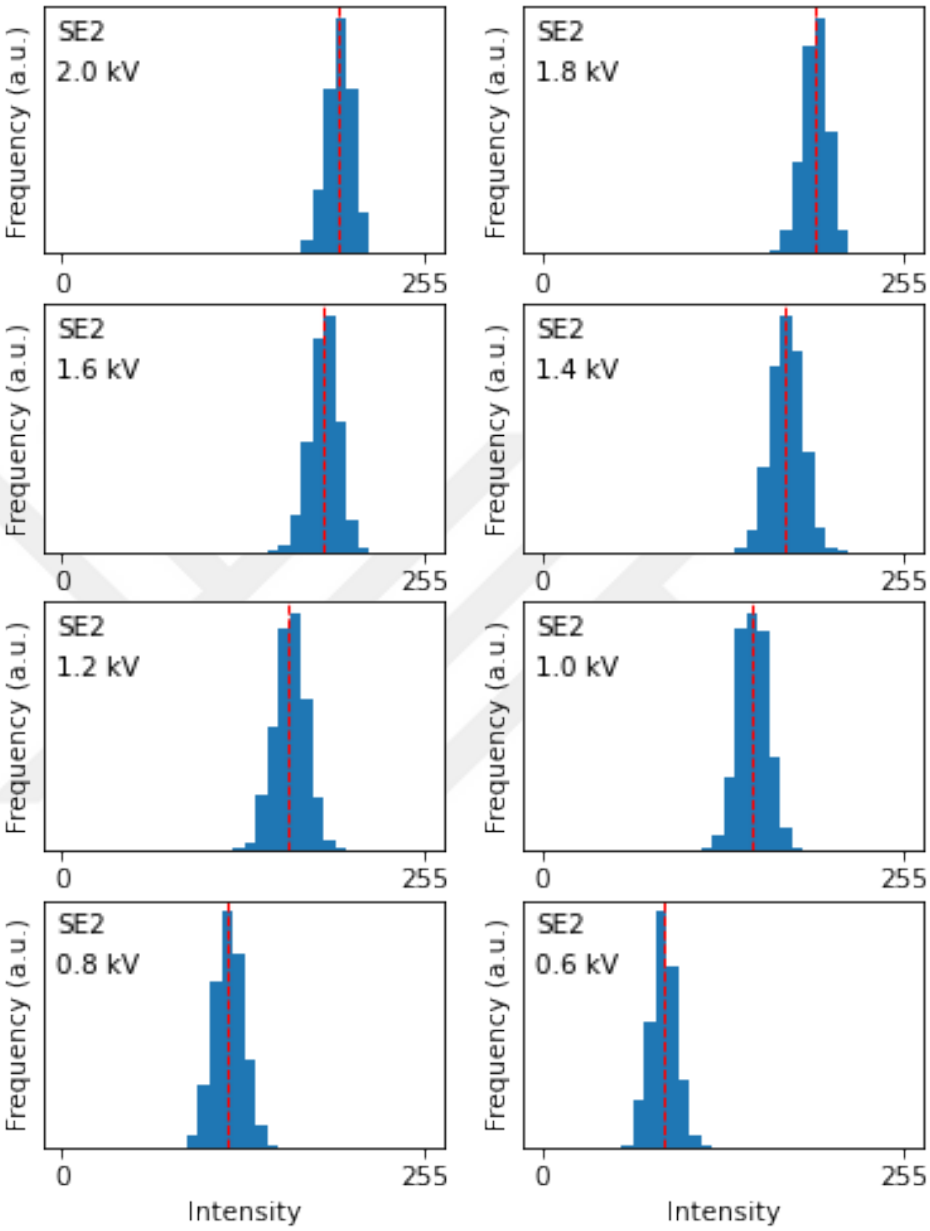


Figure 104: histogram of carbon tape support from segmented SE2 electron images (fixed brightness 50% and contrast 50%).

9.4.6.2 Monoclinic phase

Selected area of m-phase is shown for SE2 signal at different PE acceleration voltages (Figure 105). The completely white area was the area which pixels of it were set to the intensity of 255.

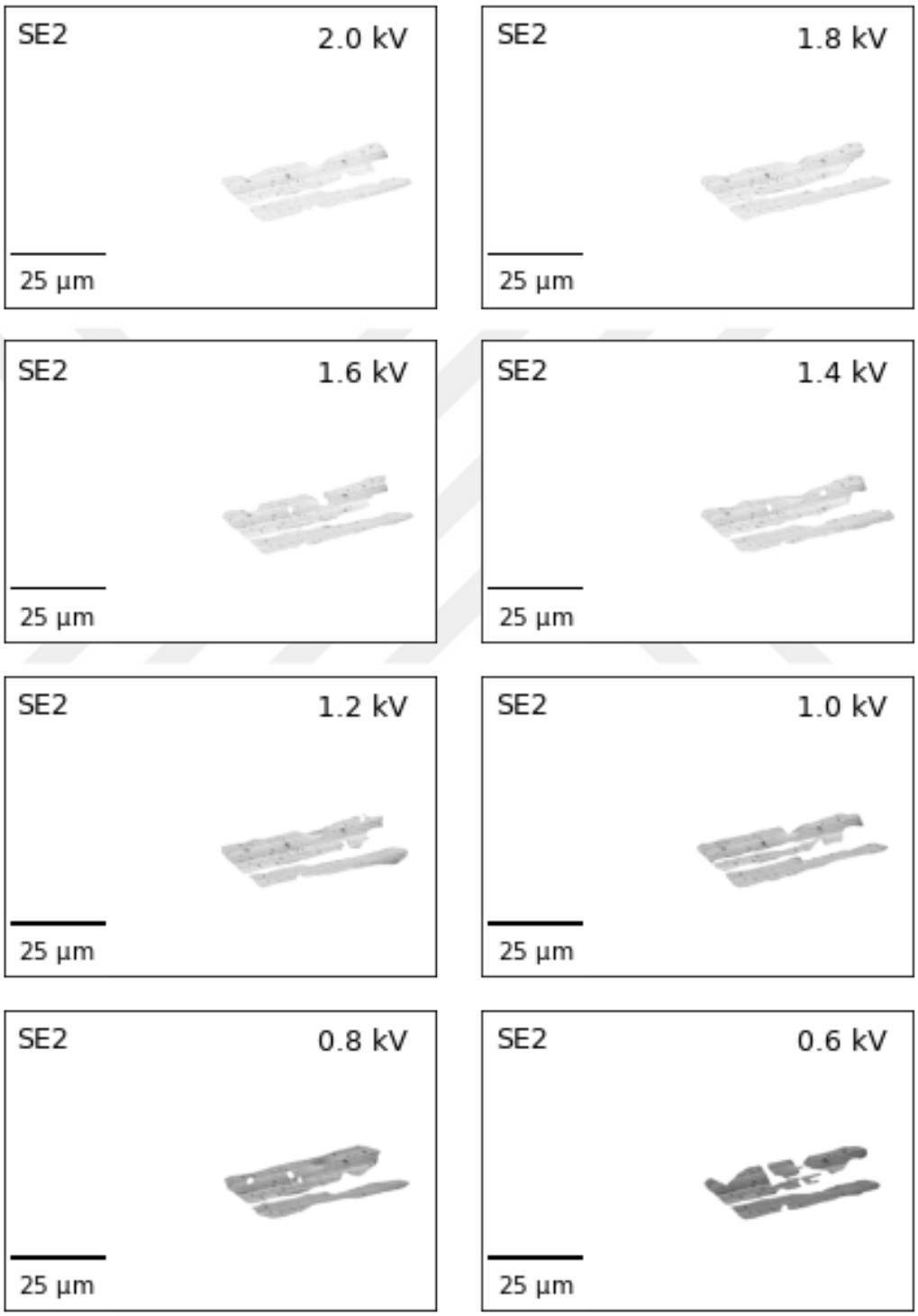


Figure 105: micrograph of m-phase from segmented SE2 electron images (fixed brightness 50% and contrast 50%).

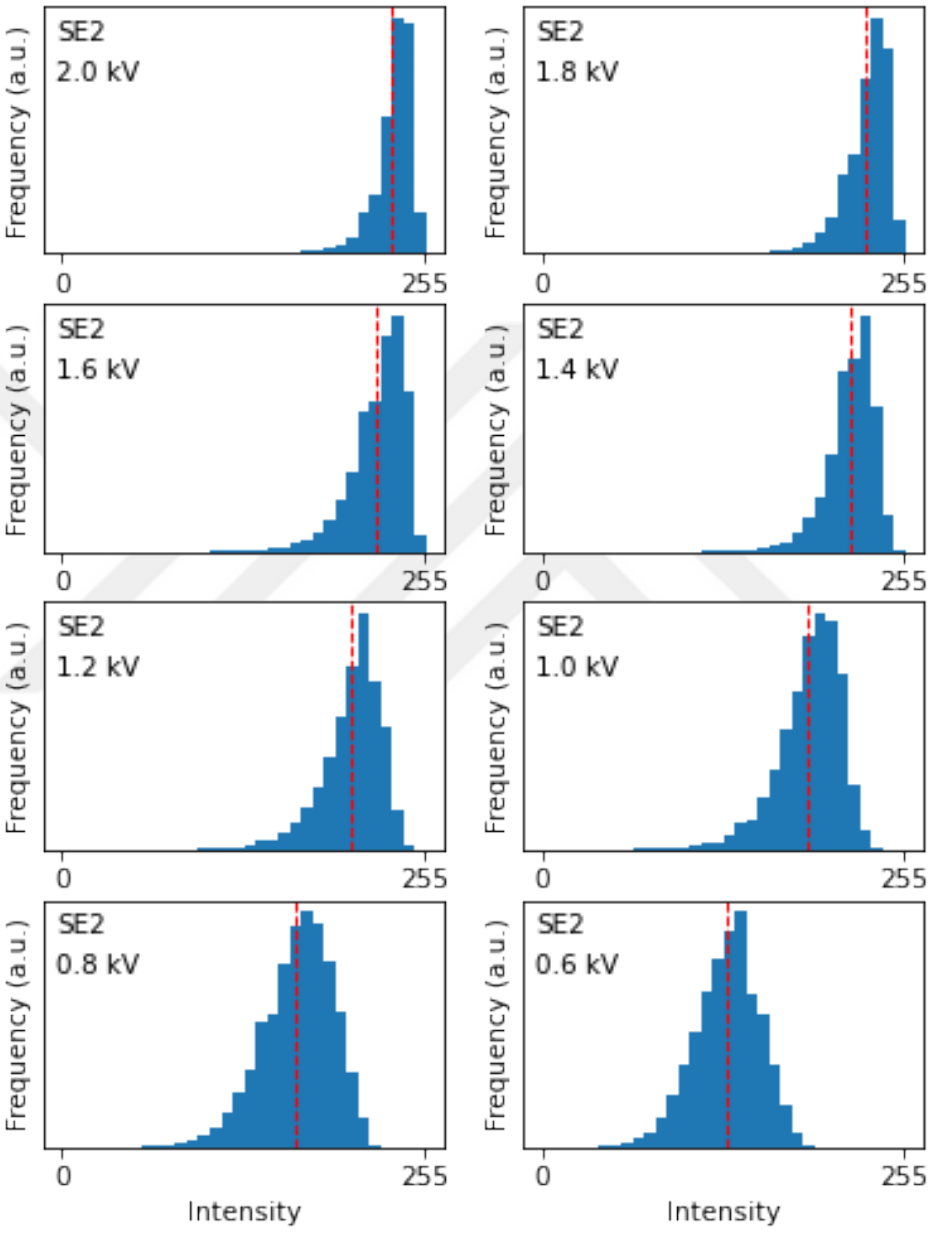


Figure 106: histogram of m-phase from segmented SE2 electron images (fixed brightness 50% and contrast 50%).

9.4.6.3 Tetragonal phase

Selected area of m-phase is shown for SE2 signal at different PE acceleration voltages (Figure 107). The completely black area was the area which pixels of it were set to the intensity of 0.

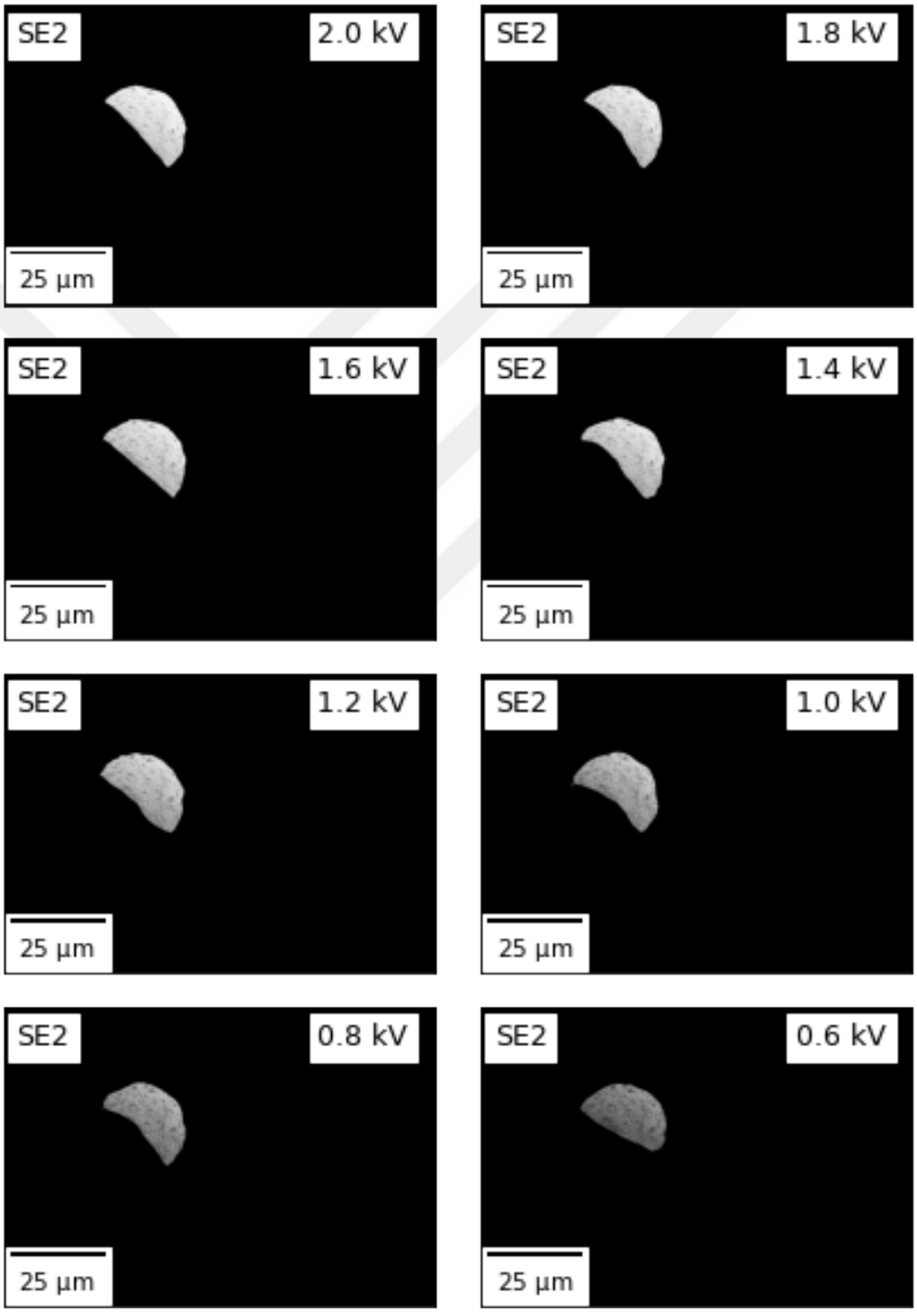


Figure 107: micrograph of t-phase from segmented BSE electron images (fixed brightness 50% and contrast 50%).

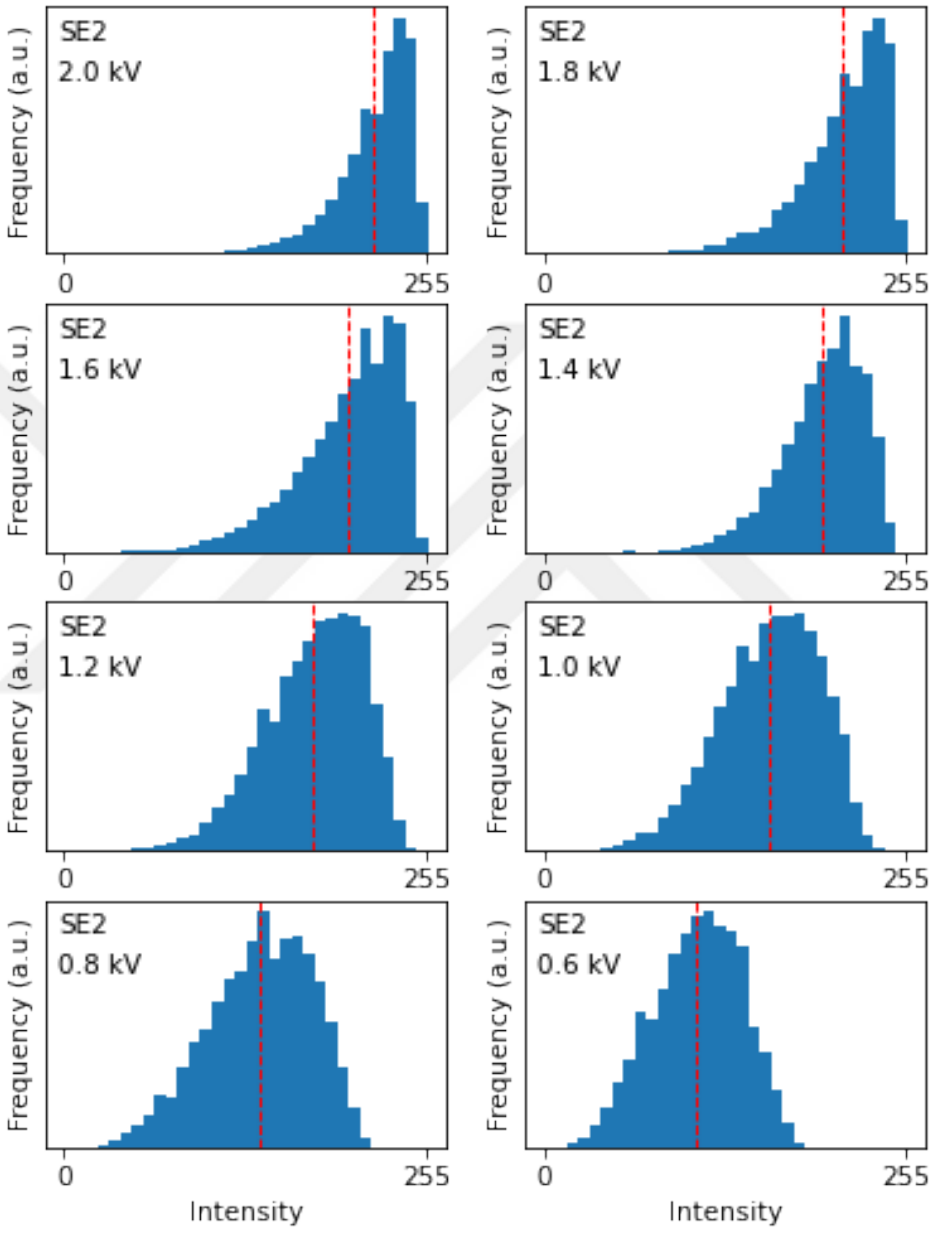


Figure 108: histogram of t-phase from segmented SE2 electron images (fixed brightness 50% and contrast 50%)

The average intensity values for carbon tape support, m-phase, and t-phase were shown in Table S1.

Table 21: average intensity for carbon tape support, m-ZrO_2, and t-ZrO_2 from SEM micrographs captured by SE2

Voltage (kV)	Average intensity of carbon tape support ($\bar{I}_s$)	Average intensity of m-phase ($\bar{I}_m$)	Average intensity of t-phase ($\bar{I}_t$)
0.6	85 ± 9	130 ± 23	108 ± 31
0.8	117 ± 10	164 ± 25	137 ± 37
1.0	148 ± 10	188 ± 23	159 ± 35
1.2	160 ± 11	203 ± 22	176 ± 34
1.4	171 ± 11	217 ± 18	196 ± 28
1.6	184 ± 10	221 ± 20	200 ± 35
1.8	191 ± 9	228 ± 18	210 ± 30
2.0	194 ± 9	232 ± 15	218 ± 26

9.4.7 SE1 signal

Quantification of SE2 images captured in different acceleration voltages was performed after the preprocessing steps that was mentioned above.

9.4.7.1 Carbon tape support

Selected area of carbon tape support is shown for SE1 signal at different PE acceleration voltages (Figure 109). The completely black area was the area which pixels of it were set to the intensity of 0.

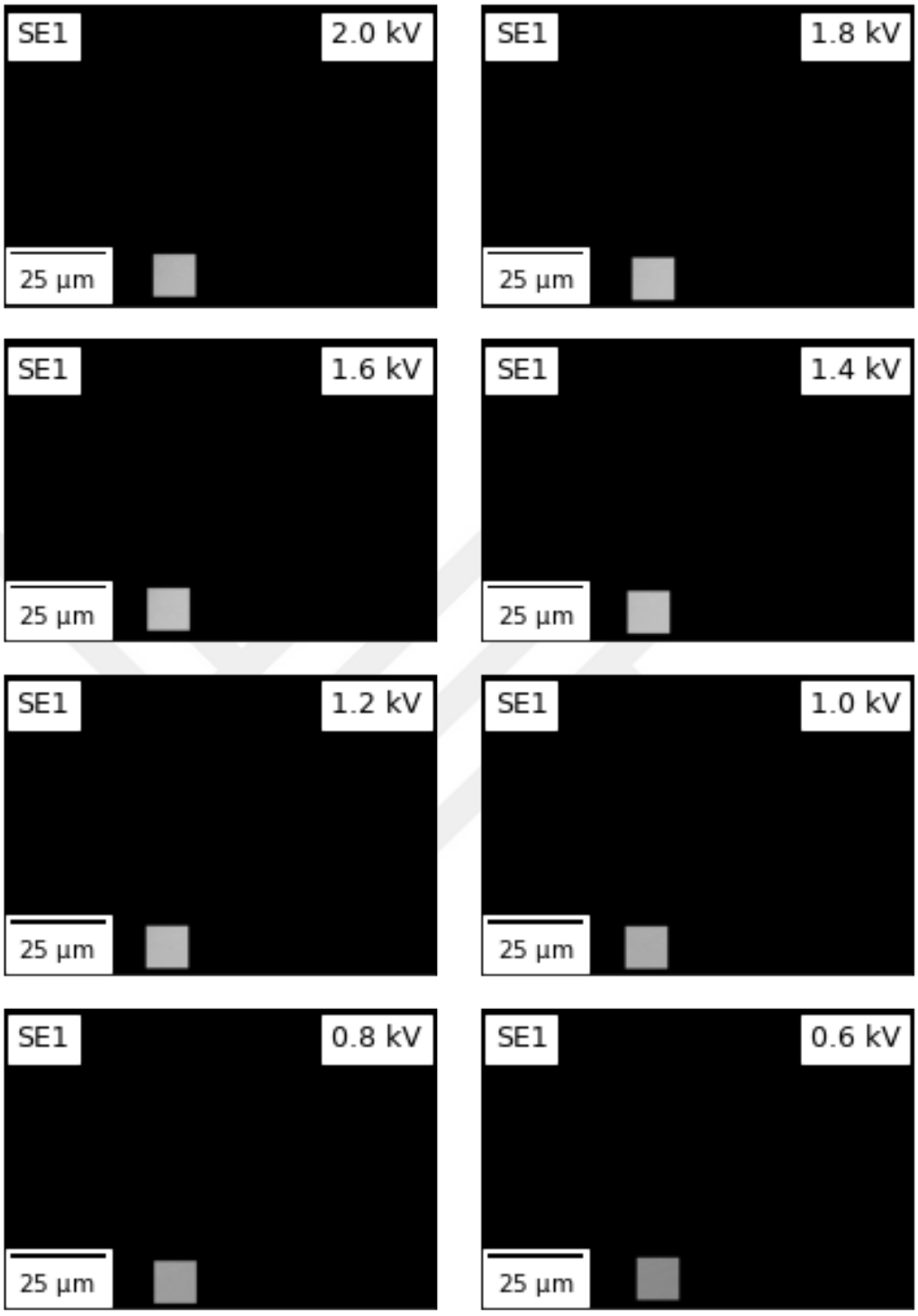


Figure 109: micrograph of carbon tape support from segmented SE1 electron images (fixed brightness 50% and contrast 32%).

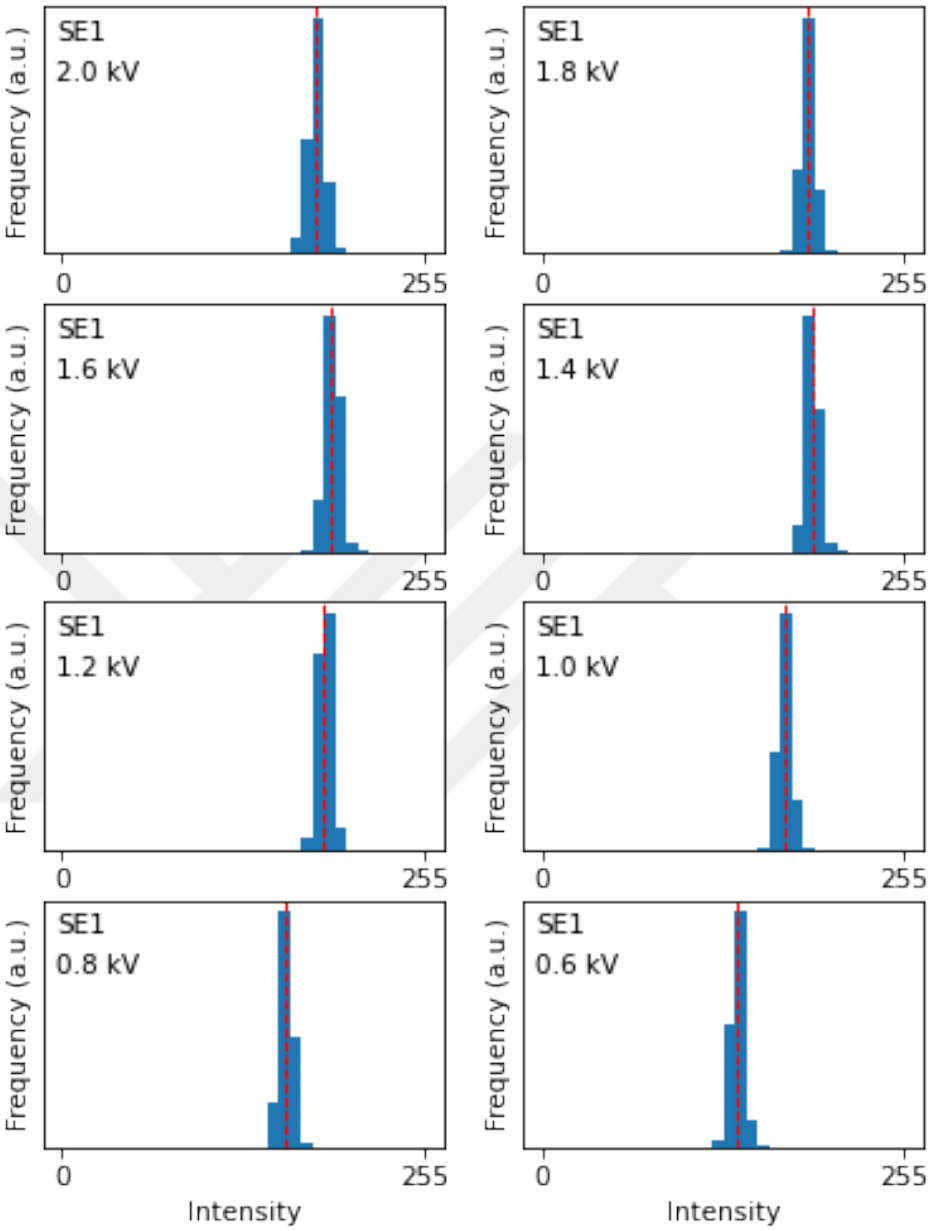


Figure 110: histogram of carbon tape support from segmented SE1 electron images (fixed brightness 50% and contrast 32%).

9.4.7.2 Monoclinic phase

Selected area of m-phase is shown for SE1 signal at different PE acceleration voltages (Figure 111). The completely white area was the area which pixels of it were set to the intensity of 0.

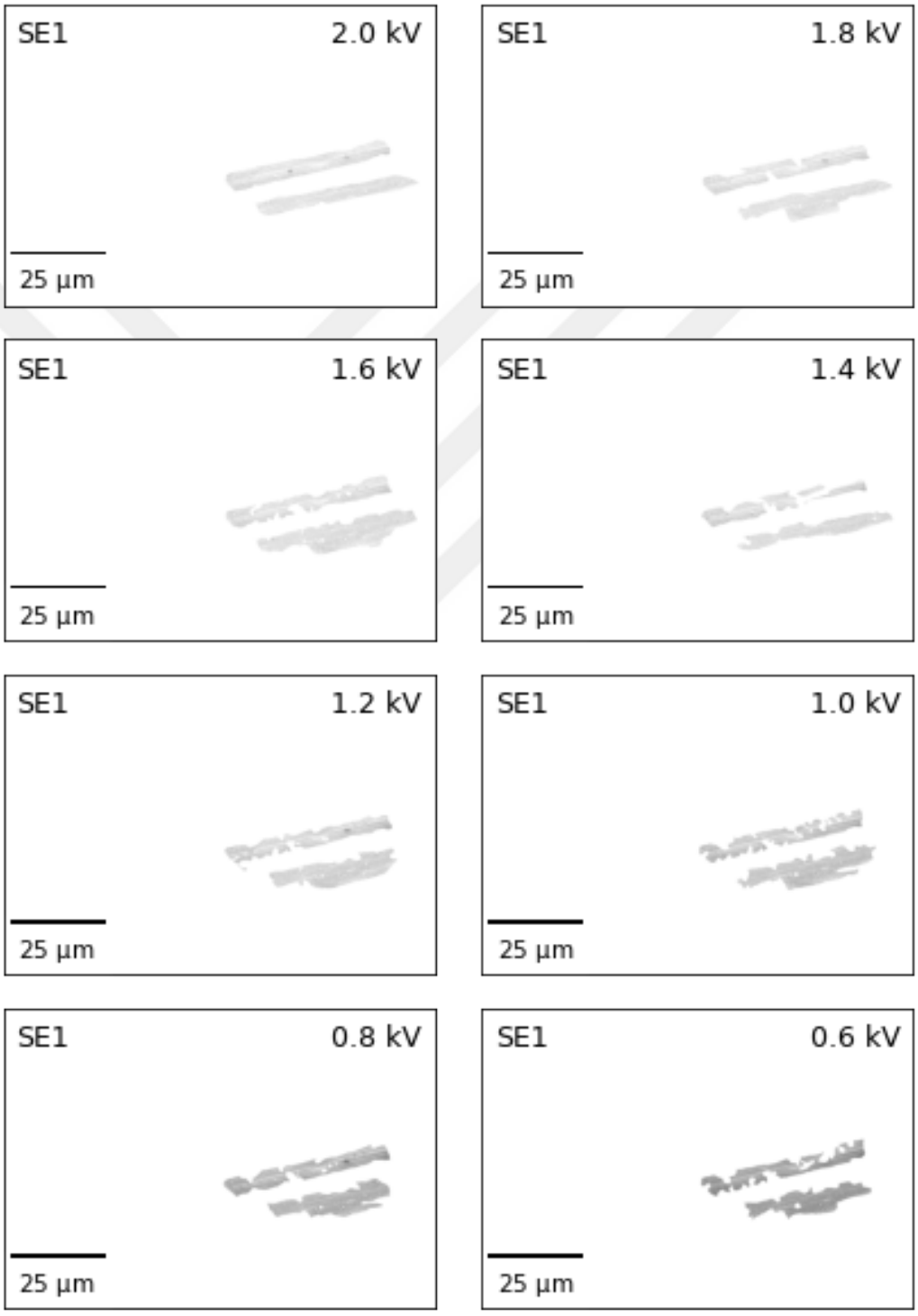


Figure 111: micrograph of m-phase from segmented SE1 electron images (fixed brightness 50% and contrast 32%).

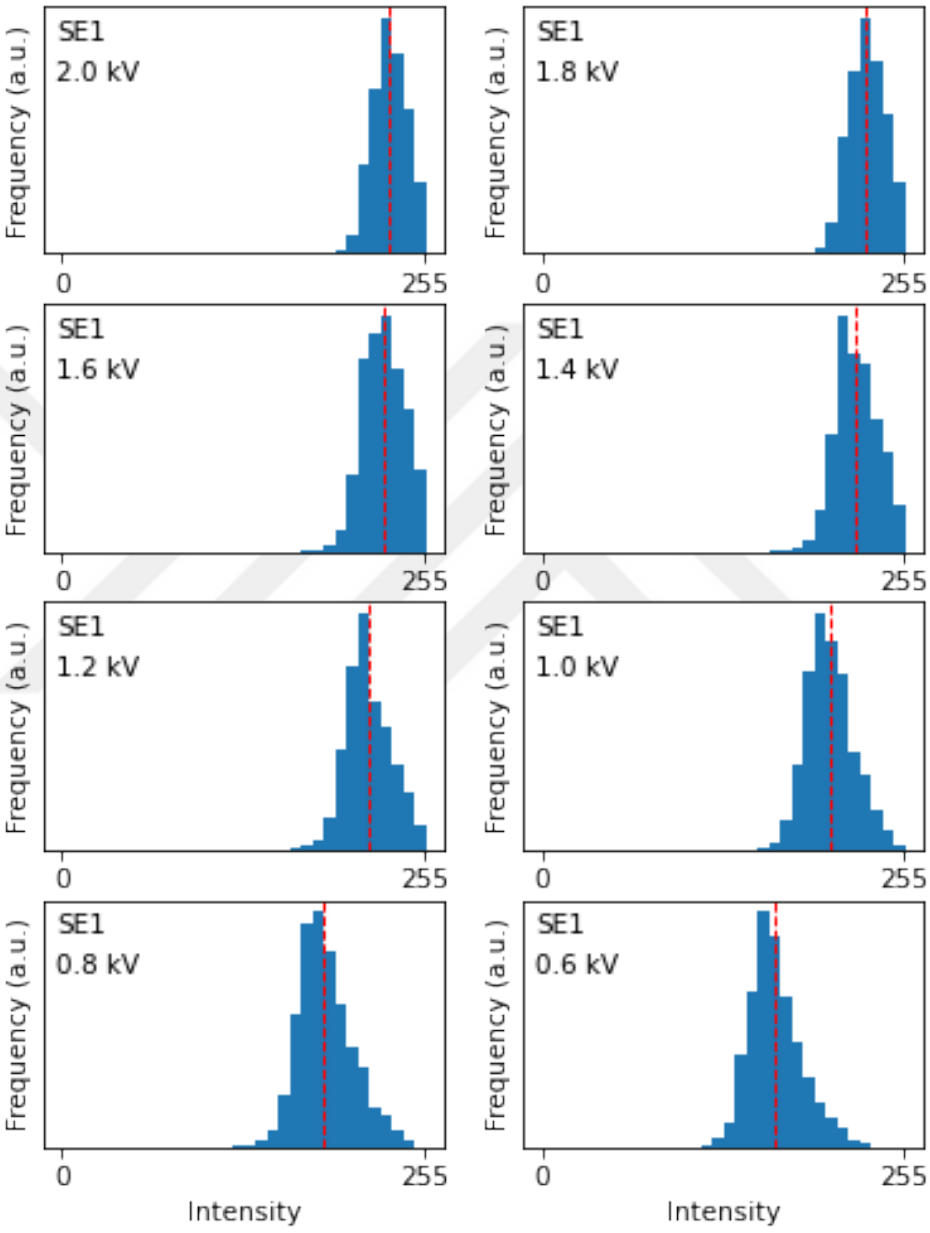


Figure 112: histogram of m-phase from segmented SE1 electron images (fixed brightness 50% and contrast 32%).

9.4.7.3 Tetragonal phase

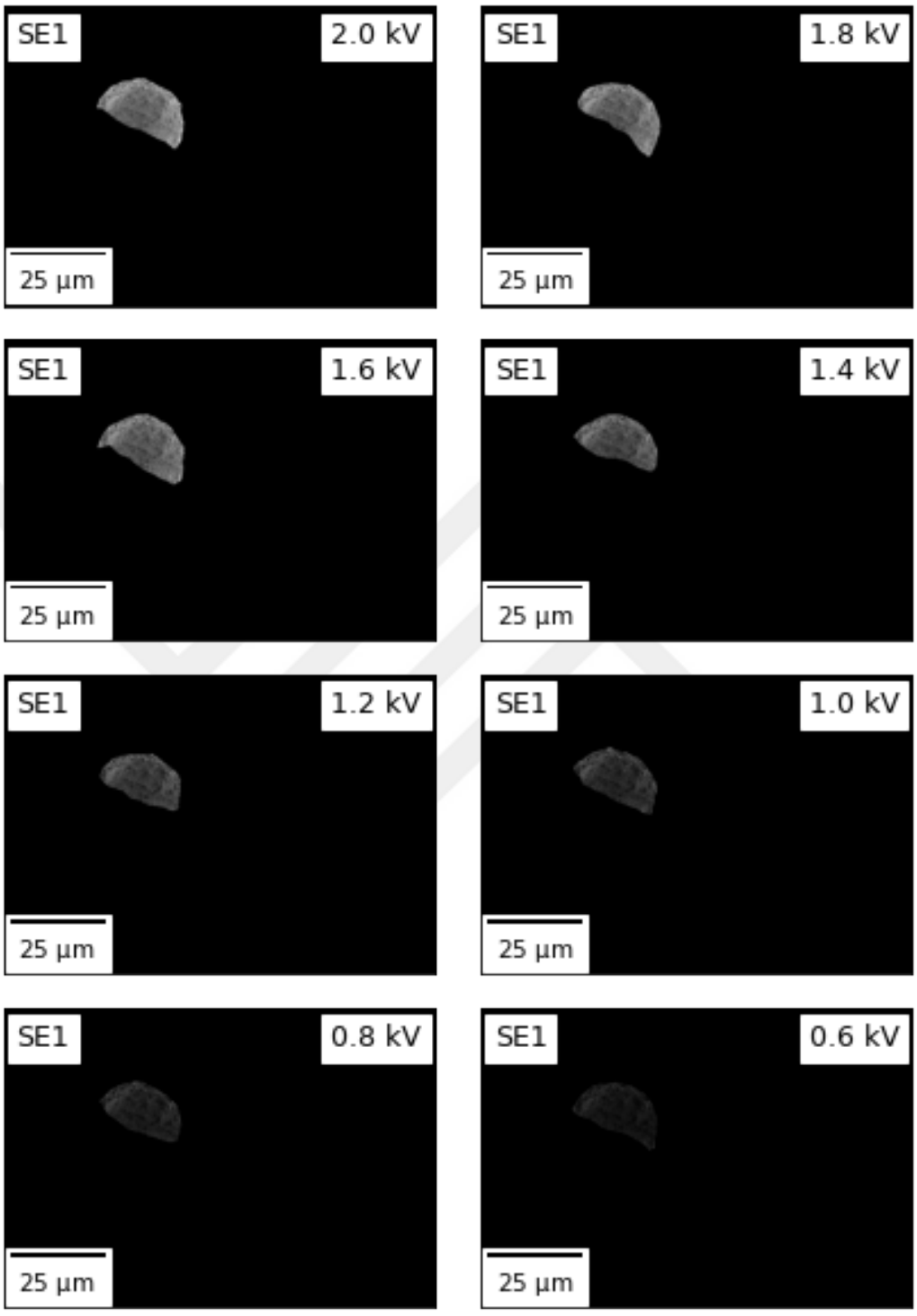


Figure 113: micrograph of t-phase from segmented SE1 electron images (fixed brightness 50% and contrast 32%).

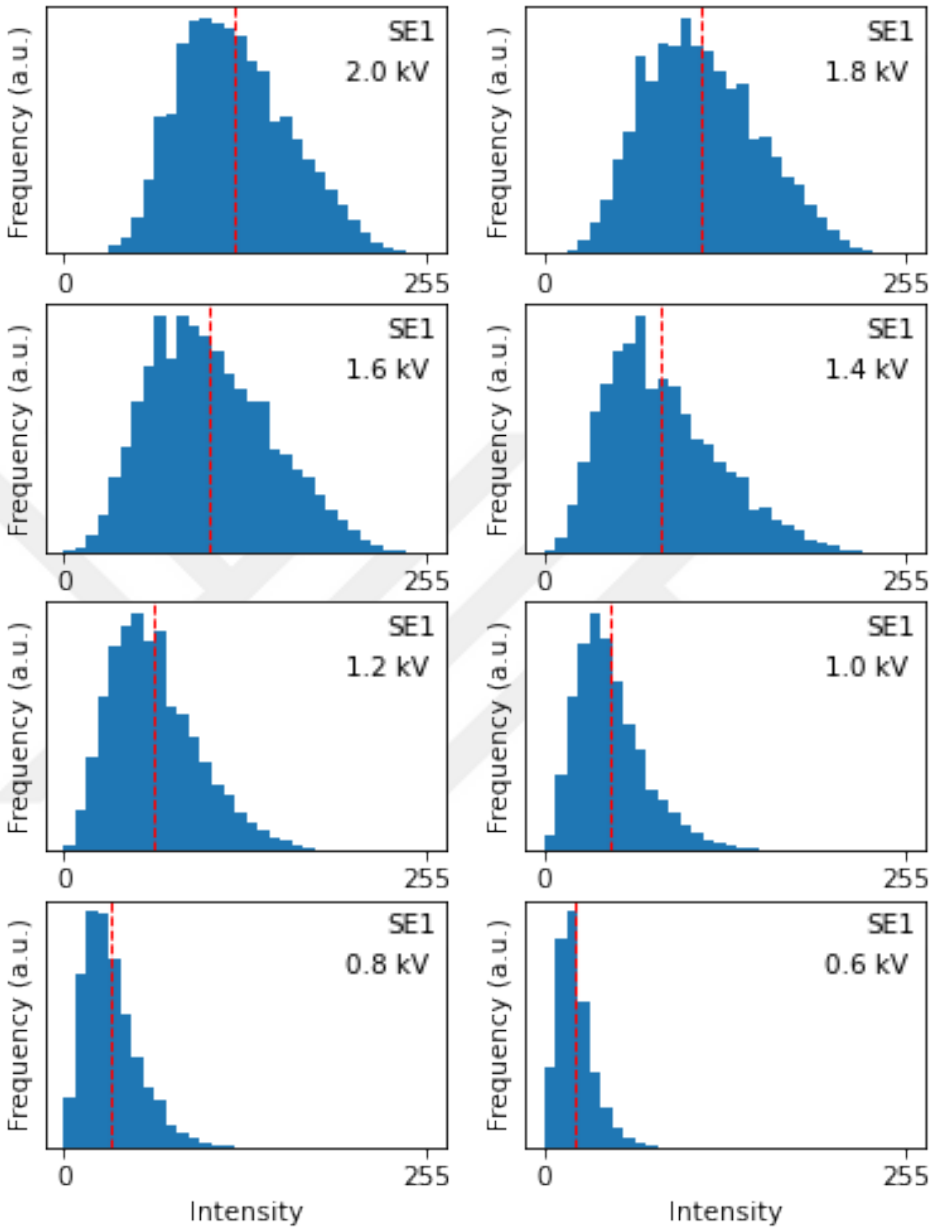


Figure 114: histogram of t-phase from segmented SE1 electron images (fixed brightness 50% and contrast 32%).

The average intensity values for carbon tape support, m-phase, and t-phase were shown in Table S1.

Table 22: average intensity for carbon tape support, m-ZrO_2, and t-ZrO_2 from SEM micrographs captured by SE1

Voltage (kV)	Average intensity of carbon tape support ($\bar{I}_s$)	Average intensity of m-phase ($\bar{I}_m$)	Average intensity of t-phase ($\bar{I}_t$)
0.6	138 ± 5	164 ± 19	22 ± 13
0.8	157 ± 5	185 ± 20	33 ± 20
1.0	170 ± 5	202 ± 16	46 ± 24
1.2	184 ± 5	215 ± 16	63 ± 31
1.4	190 ± 5	222 ± 15	83 ± 39
1.6	190 ± 5	226 ± 14	102 ± 42
1.8	187 ± 5	229 ± 13	111 ± 40
2.0	178 ± 6	230 ± 13	120 ± 38

9.4.7.4 Lack of contrast in BSE

Lack of contrast between m-phase and t-phase was observed in two main imaging modes of SEM. Backscattered Electron micrographs of the powders (Figure 80) showed insignificant difference in the SEM images that were captured in a range of acceleration voltage (2.0 kV – 1.4 kV). There was no significant difference in the average intensity of m-phase and t-phase. This was expected as there existed no atomic number difference between these phases. The BSE is sensitive to the atomic number of the material. In this situation, the SEM lost its applicability as a phase distinguishing characterization equipment. Quantified analysis of the same images (Figure S13 – Figure S18 and Table S1) revealed that the average intensity of all three segments of the image decreased by decreasing the PE acceleration voltage. The decrease in average intensity of carbon tape

support ($\bar{I}_s$), m-phase ($\bar{I}_m$) and t-phase ($\bar{I}_t$) could be associated with the decrease of the signal-to-noise ratio (S/N) (Figure 115).

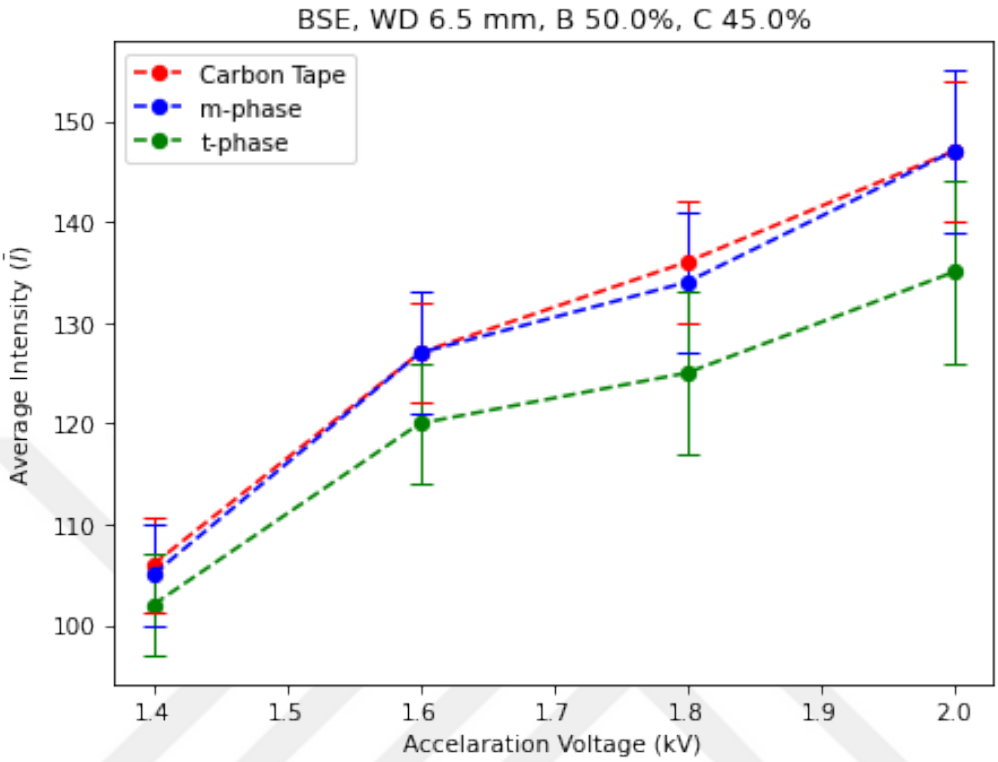


Figure 115: average intensity for carbon tape support, m-ZrO_2, and t-ZrO_2 from SEM micrographs captured by BSE detector

Relative average intensity of m-phase was calculated through dividing the average intensity of the m-phase ($\bar{I}_m$) by the average intensity of the carbon tape support ($\bar{I}_s$). Similarly, relative average intensity of t-phase was calculated through dividing the average intensity of the m-phase ($\bar{I}_t$) by the average intensity of the carbon tape support ($\bar{I}_s$). The relative average intensity of the support was always identical to unity. The difference between the average intensity of m-phase and t-phase was calculated by $(\bar{I}_m - \bar{I}_t)/\bar{I}_s$.

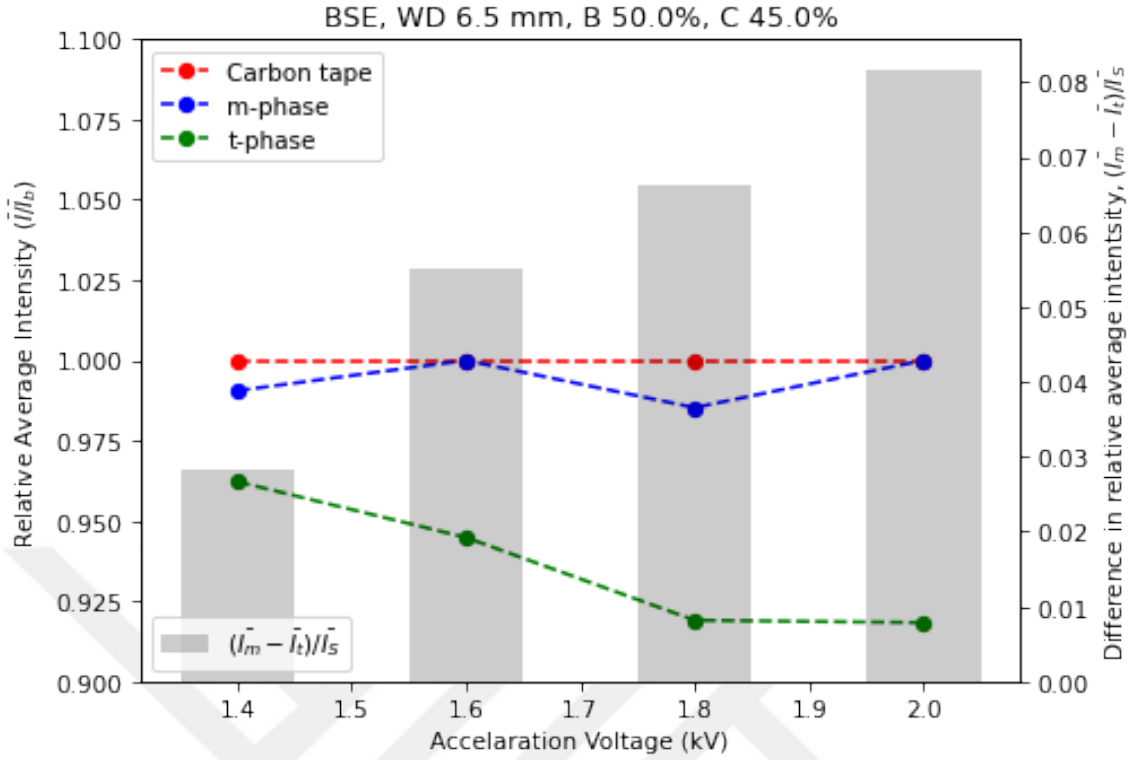


Figure 116: relative average intensity for carbon tape support, m-ZrO_2, and t-ZrO_2 from SEM micrographs captured by BSE detector

Relative average intensity was calculated for each phase at several acceleration voltage in BSE mode (Figure 116). It was found that in acceleration voltages between 2.0 kV and 1.4 kV the relative average intensity of t-phase was always lower than that of the carbon tape support and that of the t-phase. By recusing the acceleration voltage, the relative average intensity of t-phase increased while the relative average intensity of the carbon tape support and m-phase stayed still. Difference between the average intensities of t-phase and m-phase clearly reduced by the reduction of the acceleration voltage (bars in mode (Figure 116).

9.4.7.5 Lack of contrast in SE2

Similarly, no significant contrast was observed between m-phase and t-phase when the images were captures in SE2 mode in a range of acceleration voltage (2.0 kV – 1.4 kV) (Figure 81). The was no significant difference in the average intensity of m-phase and t-phase. Quantified analysis of the same images (Figure S19 – Figure S24 and Table S2) revealed that the average intensity of all three segments of the image deceased by decreasing the PE acceleration voltage. The lack of contrast did not change by reducing

the acceleration voltage of primary electrons from 2.0 kV to 0.6 kV (Table S2). Decreasing the acceleration voltage cause S/N which was observed in the parallel reduction of the average intensity of carbon tape support ($\bar{I}_s$), m-phase ($\bar{I}_m$) and t-phase ($\bar{I}_t$) (Figure 117). Briefly, it was shown in Figure 115 and Figure 117 that the lack of the contrast in BSE and SE2 modes was major shortcoming for conventional SEMs to differentiate the m-phase and t-phase.

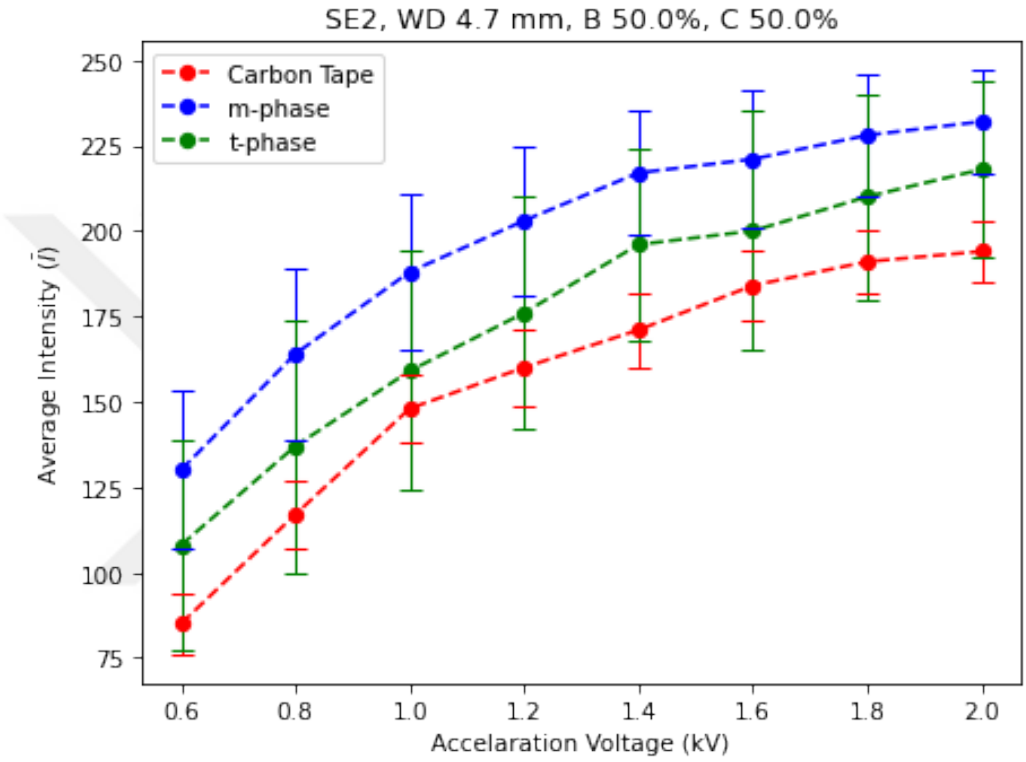


Figure 117: average intensity for carbon tape support, m-ZrO2, and t-ZrO2 from SEM micrographs captured by Everhart-Thornley detector

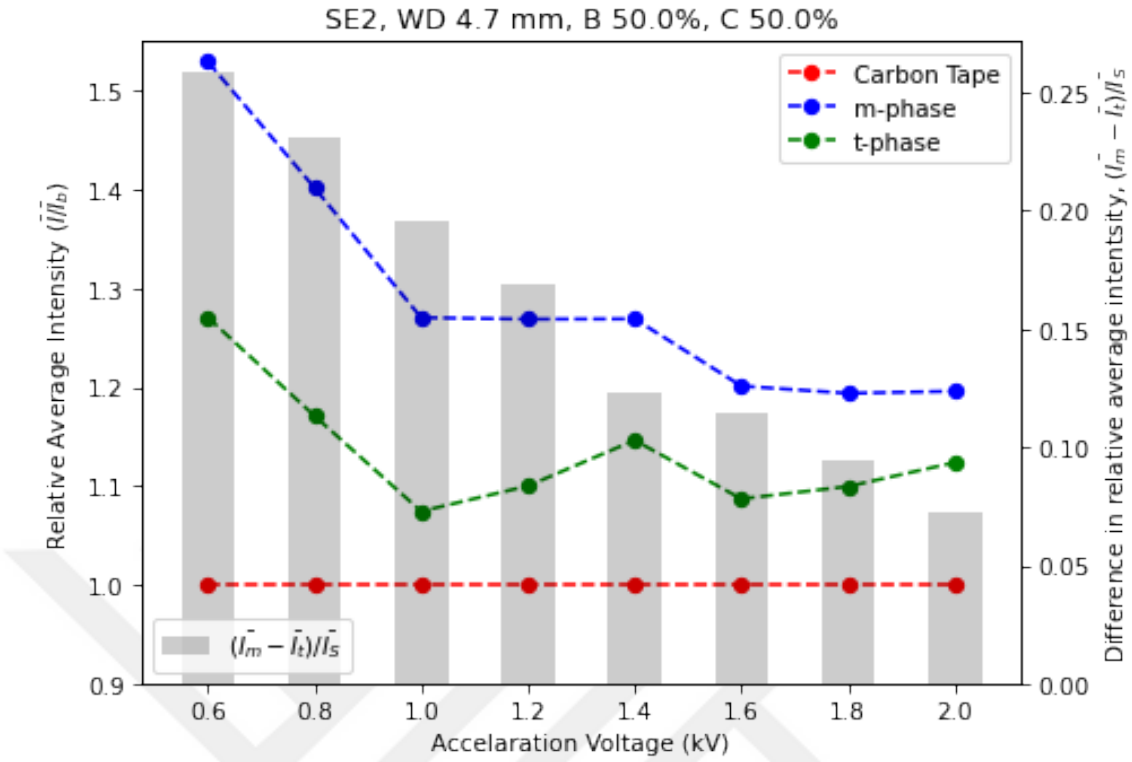


Figure 118: relative average intensity for carbon tape support, m-ZrO2, and t-ZrO2 from SEM micrographs captured by Everhart-Thornley detector

Relative average intensity was calculated for each phase at several acceleration voltage (Figure 118). It was found that in acceleration voltages between 2.0 kV and 0.6 kV the relative average intensity of t-phase was always higher than that of the carbon tape support but lower than that of the m-phase. By recusing the acceleration voltage, the relative average intensity of m-phase and t-phase increased. Difference between the average intensities of t-phase and m-phase clearly increased by the reduction of the acceleration voltage (bars in Figure 118).

9.4.7.6 Significant contrast in SE1

Unlike the other imaging modes, the m-phase and t-phase were differentiated in SE1 detection. When a combination of Low-voltage SEM was used with a collection system of TTL detector (Figure 82), m-phase and t-phase appeared in a distinct intensity level although they had nominally no atomic number difference. The contrast between the phases increased as the PE acceleration voltage reduced from 2.0 kV to 0.6 kV (Figure 82). Quantified analysis of the same images (Figure S25 – Figure S30 and Table S3) revealed that the average intensity of all three segments of the image decreased by

decreasing the PE acceleration voltage (Figure 119). The decreased in the average intensity of carbon tape support ($\bar{I}_s$), m-phase ($\bar{I}_m$) and t-phase ($\bar{I}_t$) could not be associated only with the S/N ratio anymore. The behavior of $\bar{I}_s$ did not monotonically decreased by decreasing the PE acceleration voltage. It first increased from 2.0 kV to 1.4 kV, and then decreased to 0.6 kV (Figure 119). This behavior showed was different than that of that the $\bar{I}_s$ in BSE (Figure 115) and SE1 modes (Figure 117). SE yield was reported to behave in a similar way when PE acceleration energy was in the low energy region. Similarly, the behavior of $\bar{I}_m$ and $\bar{I}_t$ was also governed by the SE yield of the polymorphs.

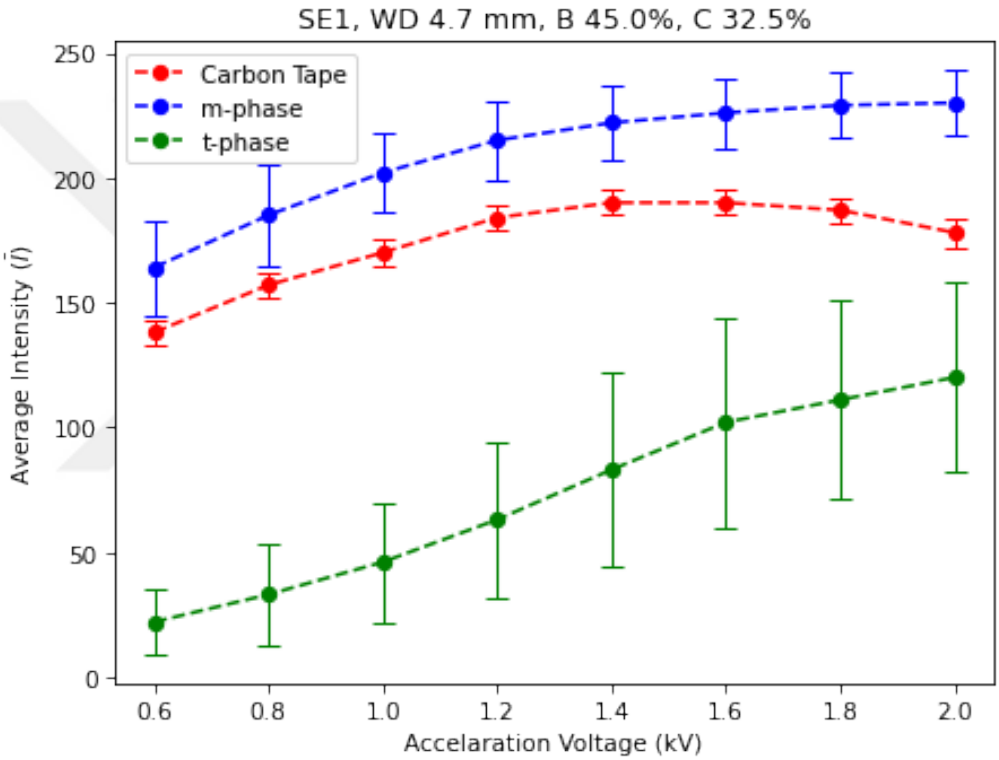


Figure 119: average intensity for carbon tape support, m-ZrO_2, and t-ZrO_2 from SEM micrographs captured by TTL detector

Relative average intensity was calculated for each phase at several acceleration voltage (Figure 120). It was found that in acceleration voltages between 2.0 kV and 0.6 kV the relative average intensity of t-phase was always lower than that of the carbon tape support and that of the m-phase. By recusing the acceleration voltage, the relative average intensity of t-phase reduces drastically. However, the relative average intensity for the carbon tape support and m-phase stays almost still. Difference between the average

intensities of t-phase and m-phase clearly increased by the reduction of the acceleration voltage (bars in Figure 120).

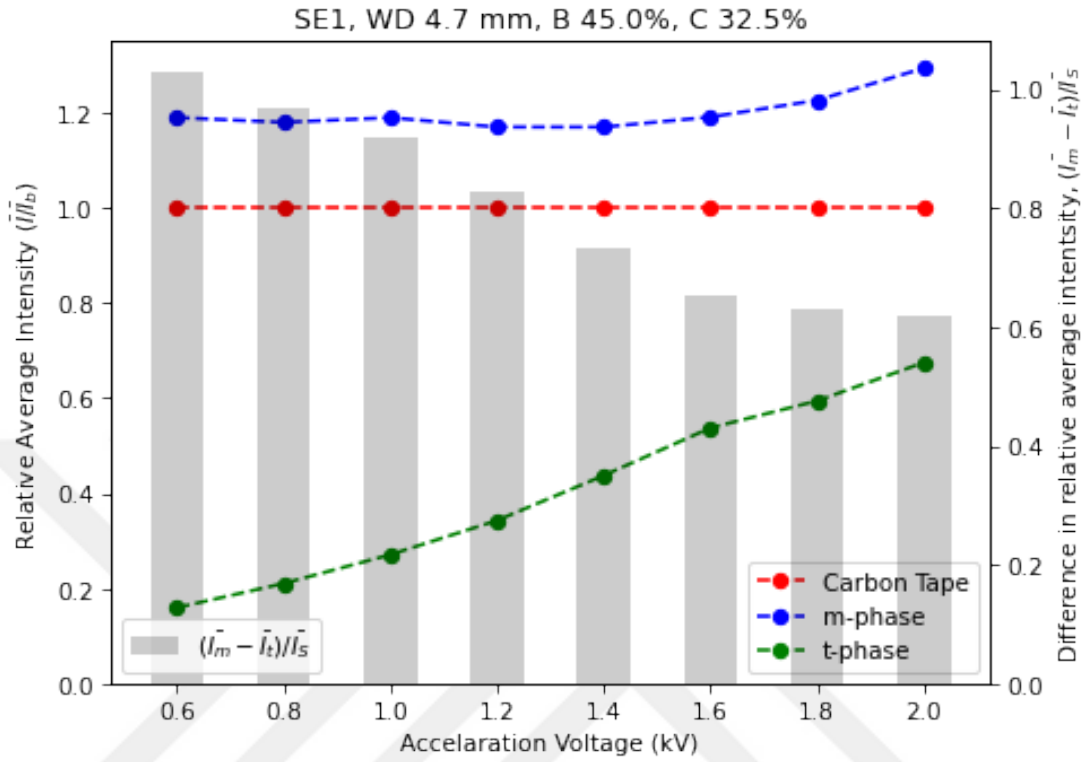


Figure 120: relative average intensity for carbon tape support, m-ZrO_2, and t-ZrO_2 from SEM micrographs captured by TTL detector

9.4.8 Theoretical analysis

The stopping power for the two polymorphs of zirconia was calculated and plotted (Figure 121) using Equation (5) in Section 2.1.3. In this equation the densities of t-ZrO_2 and m-ZrO_2 were taken as $\rho_t = 6.10$ and $\rho_m = 5.83$ g cm^{-3}, respectively. The overall atomic weight (A) of zirconia was estimated according to $A_{ZrO_2} = A_{Zr} + 2A_O = 123.2$ g mol^{-1} while the atomic number (Z) of the compound was calculated as $Z_{ZrO_2} = Z_{Zr} + 2Z_O = 96$. Two more values in Equation (5) were additionally determined: k, taken as 0.85 according to [215] and J, estimated according to Ref. [216].

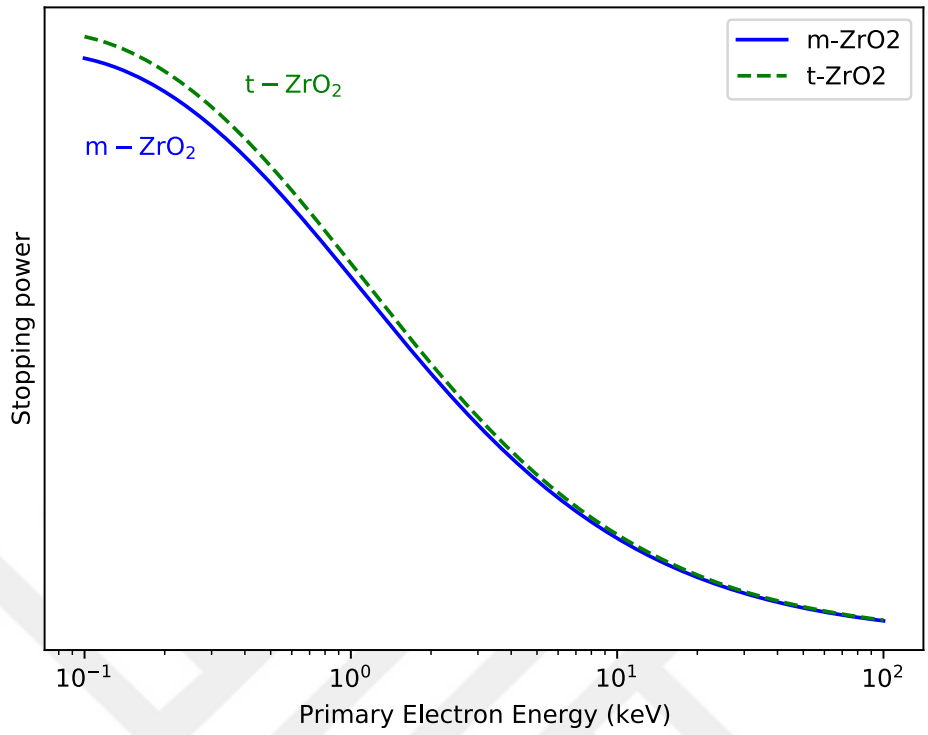


Figure 121: Stopping power of monoclinic (m-ZrO_2) and tetragonal (t-ZrO_2) phases

The results revealed that in the high-electron-energy range ($E > 10$ keV) the stopping two powers of the polymorphs were almost equal. However, they diverged as the energy of the primary electrons decreased. In particular, the divergence was significantly magnified in the low-energy region ($E < 5$ keV). In this region, the stopping power of the t-phase was found to be higher than that of the m-phase. The t-phase had a higher capacity to produce SEs, if the average energy to produce an SE, ϵ, was assumed to be the same for both polymorphs.

The other factor is the scape probability of the electrons which is governed by the electron attenuation length of the material (Equation (7)). Simulations of this parameter resulted in λ_m=2.529 Å and λ_t=2.492 Å for m-phase and t-phase, respectively [206], [271]. Using these values, the escape probability of the electrons was calculated for m-phase and t-phase in a certain depth beneath the surface (Figure 122). The escape probability of the electrons was demonstrated to be ca. 0.5 close to the surface, and it reduces to zero after 20 nm. There exists almost no difference between the escape probabilities of m-phase and t-phase.

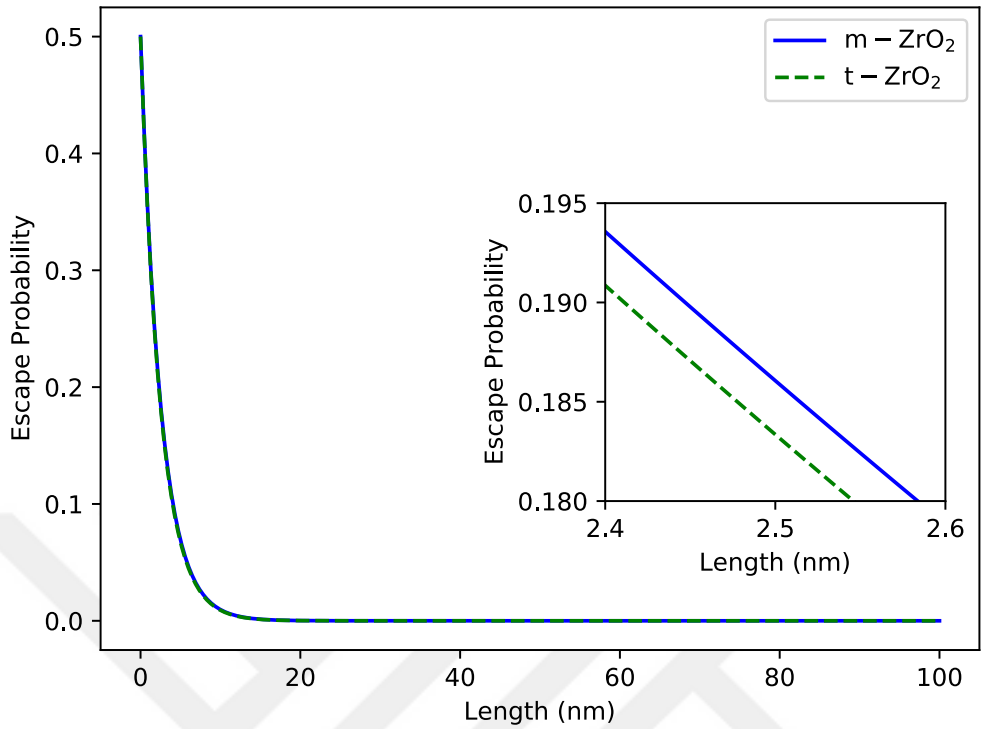


Figure 122: escape probability of electrons for m-phase and t-phase

SE yield of m-phase and t-phase was analyzed according to the Everhart's theory in Equation (10). The results for some typical values of primary electron energies shows (Figure 123) that the SE yield of m-phase is consistently higher than that of the t-phase. As the accelerating voltage decrease the difference in SE yield rises.

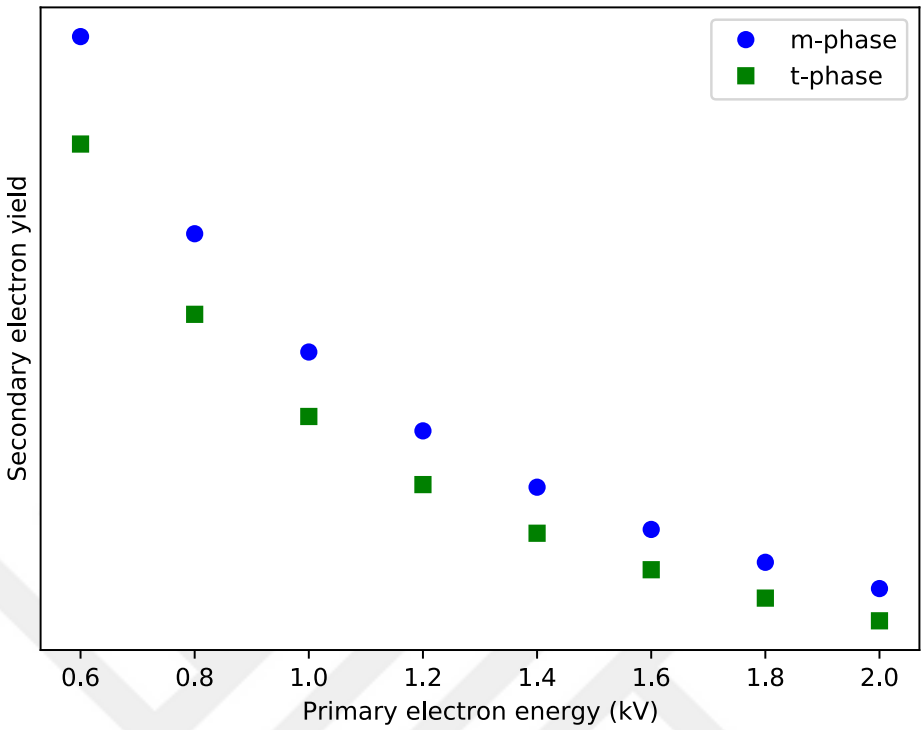


Figure 123: calculated secondary electron yield of m-phase and t-phase

Briefly, according to the theory that was formulated in Equation (9) [204], [210], [212], [213], the t-phase should have appeared brighter because it had a higher stopping power (Figure 121), given the equal escape probability of secondary electrons (Figure 122). However, this was on the contrary with the experimental results (Figure 82). On the other hand, the theory that was formulated in Equation (10) predicted that the m-phase should appear brighter and this prediction was in-line with the experimental results of Figure 82. This theory also predicted that by decreasing the primary electron energy, the difference was boosted. This prediction also was observed in Figure 82.

9.4.9 Effect of working distance on SE1

The effect of changing the working distance on the SE1 signal was quantified by segmenting the images of Figure 83. Every image was dissected into three sub-micrographs: carbon tape support, m-phase, and t-phase.

9.4.9.1 Carbon tape support

The image of the segmented carbon tape support is shown in Figure 109. The brightness of the cropped region reduced by increasing the working distance. The histogram of the cropped region was given in Figure 125. The histograms were narrow. The red dashed vertical line showed the average intensity. By increasing the working distance, the histogram gradually shifted to lower intensities.

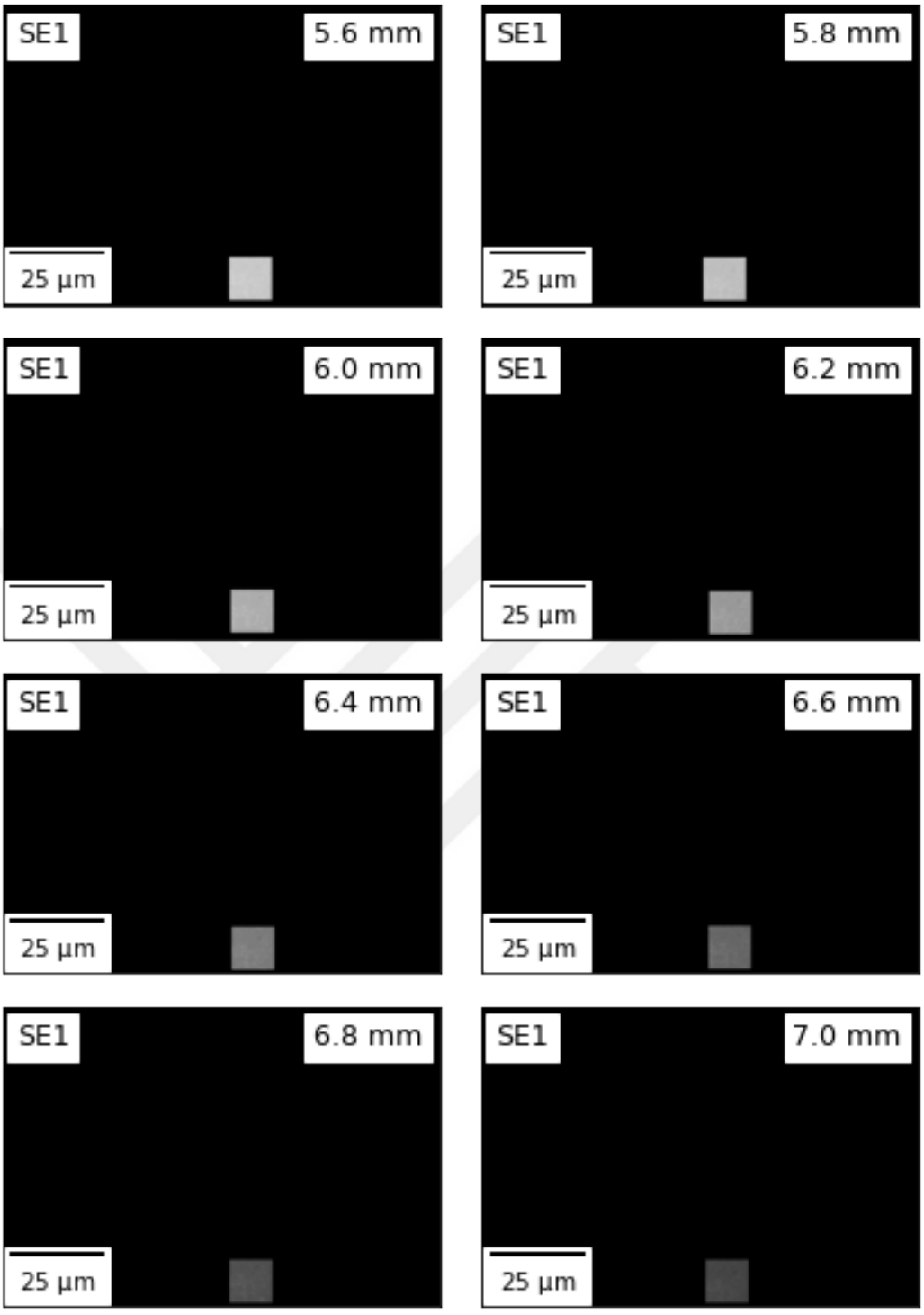


Figure 124: micrograph of carbon tape support from segmented SE1 electron images at EHT = 1 kV (fixed brightness 42.5% and contrast 35.0%).

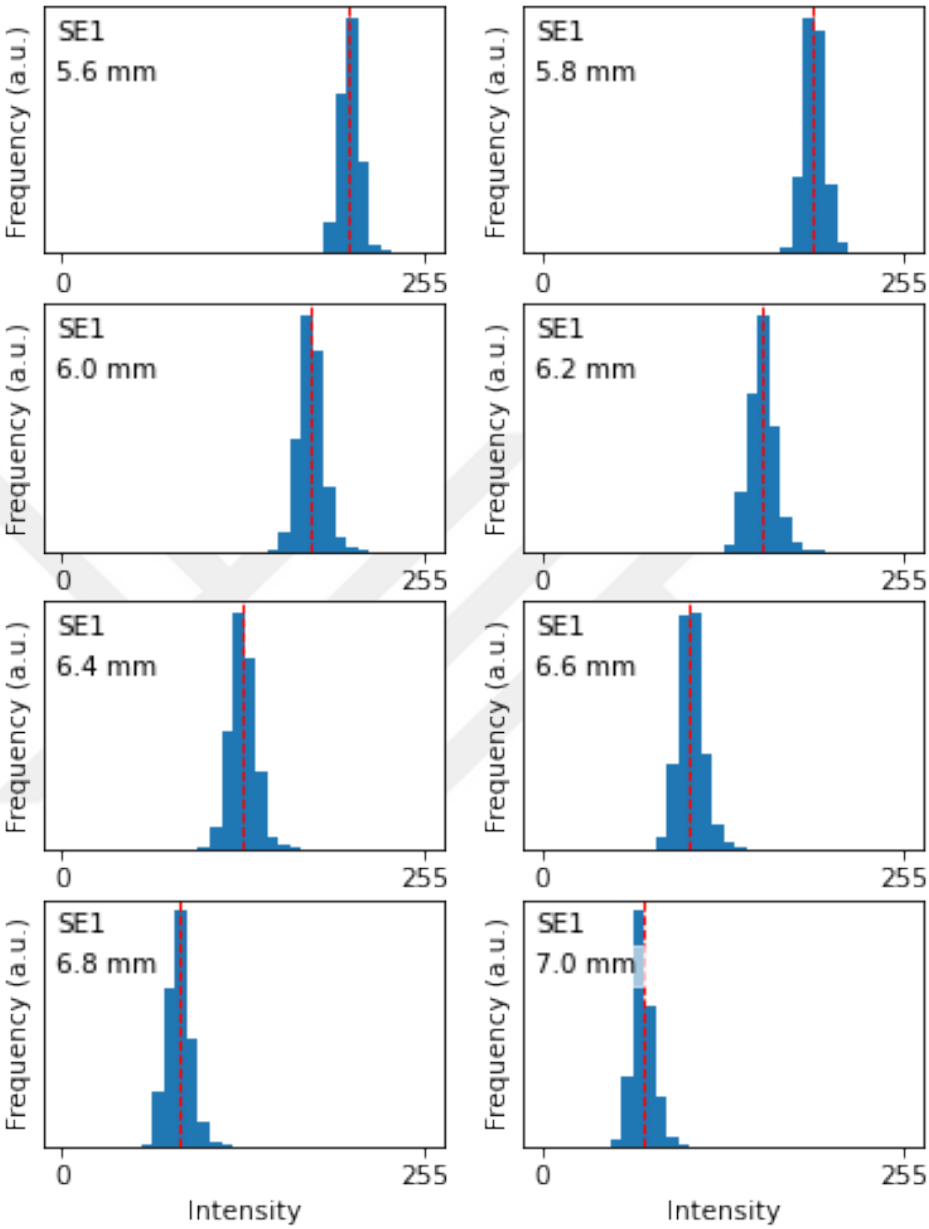


Figure 125: histogram of carbon tape support from segmented SE1 electron images at EHT = 1 kV (fixed brightness 42.5% and contrast 35.0%).

9.4.9.2 Monoclinic phase

The segmented image of the monoclinic phase was given in Figure 126. Apparently, the brightness of the phase reduced by increasing the working distance. The histogram of the same segmented images was given in Figure 127. The histograms were wide in this case. The red dashed vertical line showed the average intensity of the m-phase. By increasing the working distance, the histograms shifted to lower intensities.

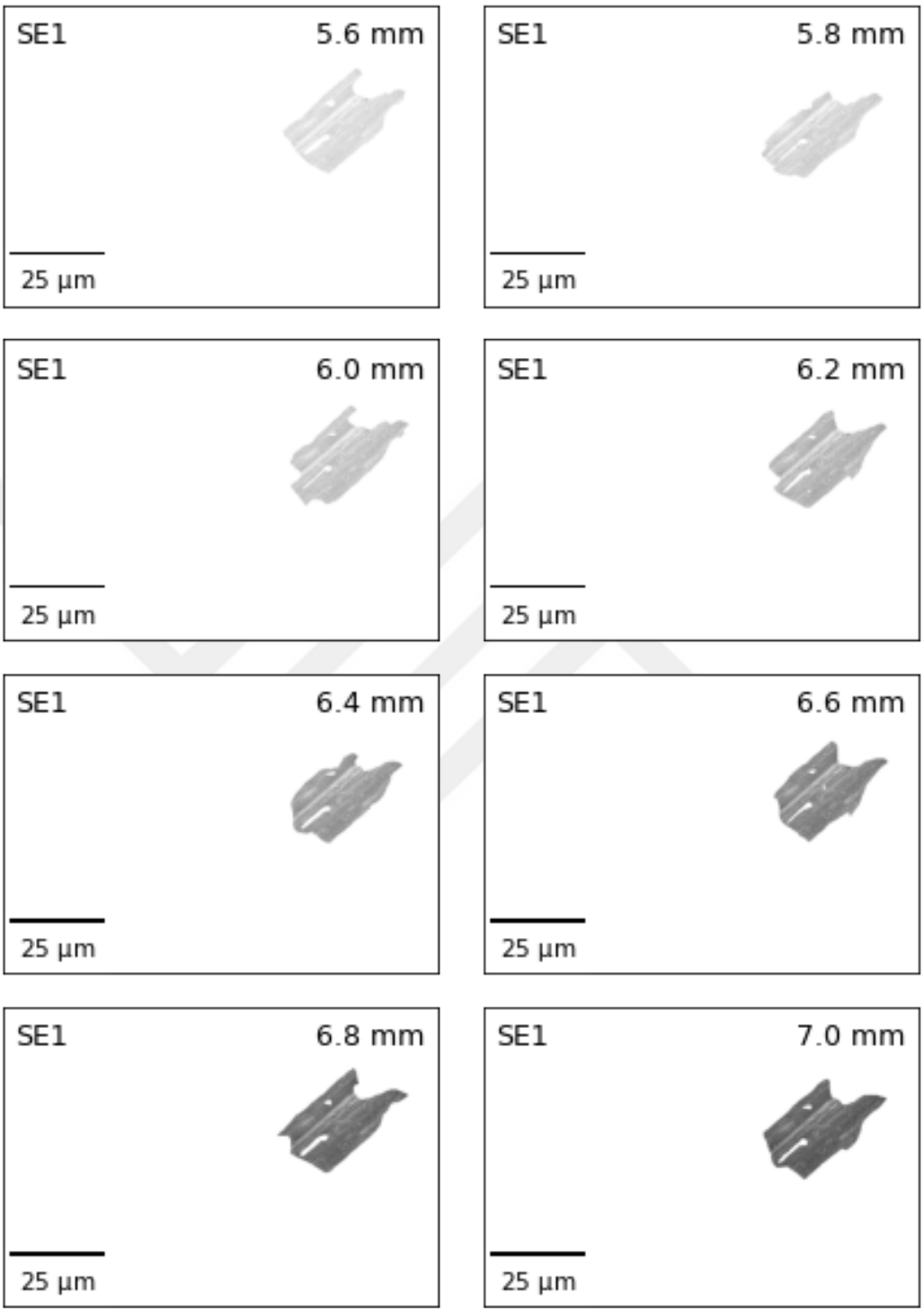


Figure 126: micrograph of m-phase from segmented SE1 electron images at EHT = 1 kV (fixed brightness 42.5% and contrast 35.0%).

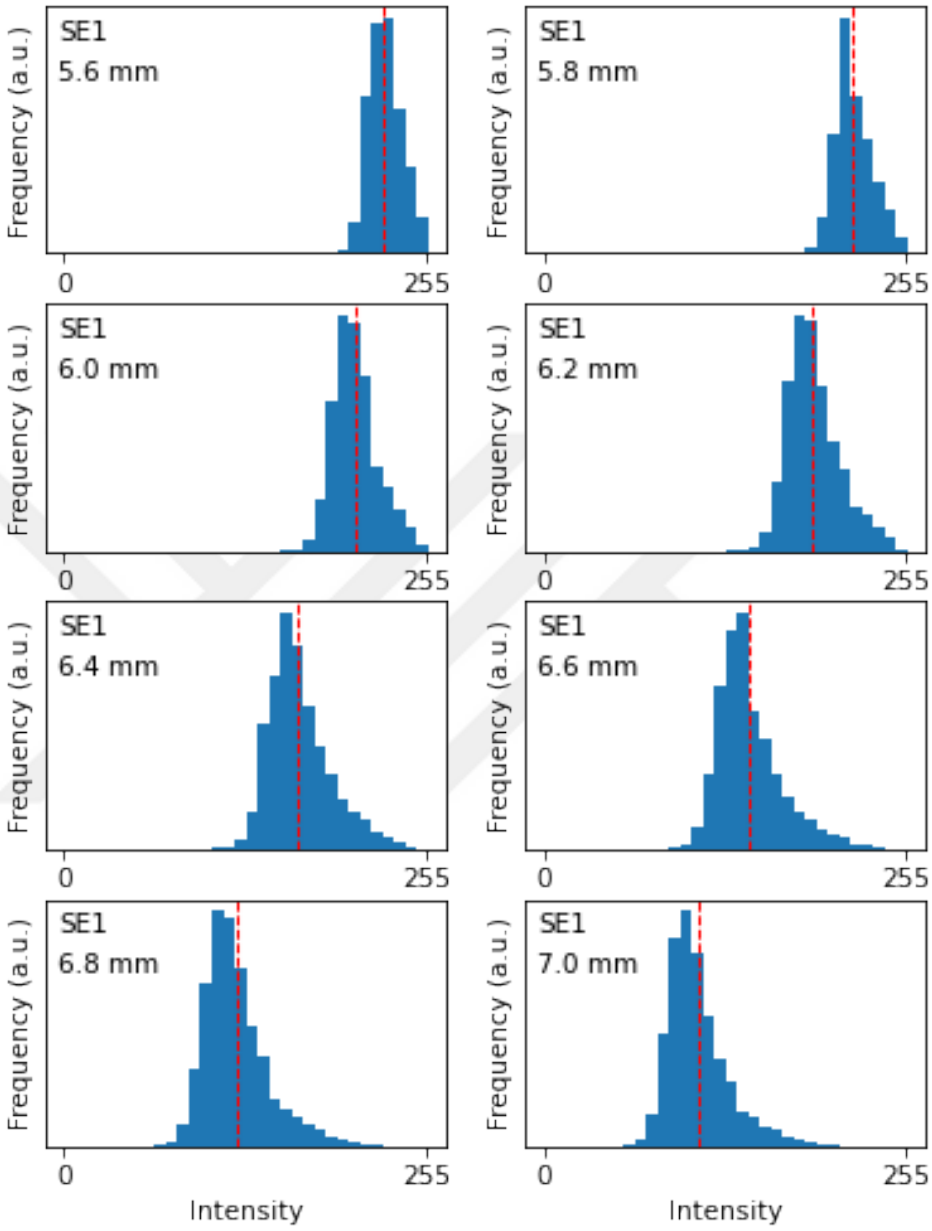


Figure 127: histogram of m-phase from segmented SE1 electron images at EHT = 1 kV (fixed brightness 42.5% and contrast 35.0%).

9.4.9.3 Tetragonal phase

The segmented micrograph of t-phase was shown in Figure 128. By increasing the working distance, the intensity of the m-phase reduced. The histogram of the same segmented sub-micrographs was given in Figure 129. The red dashed vertical line showed the average intensity of the phase. The histograms of the sub-micro graphs are wide in lower working distances. As the working distance increased the width of the histogram reduced.

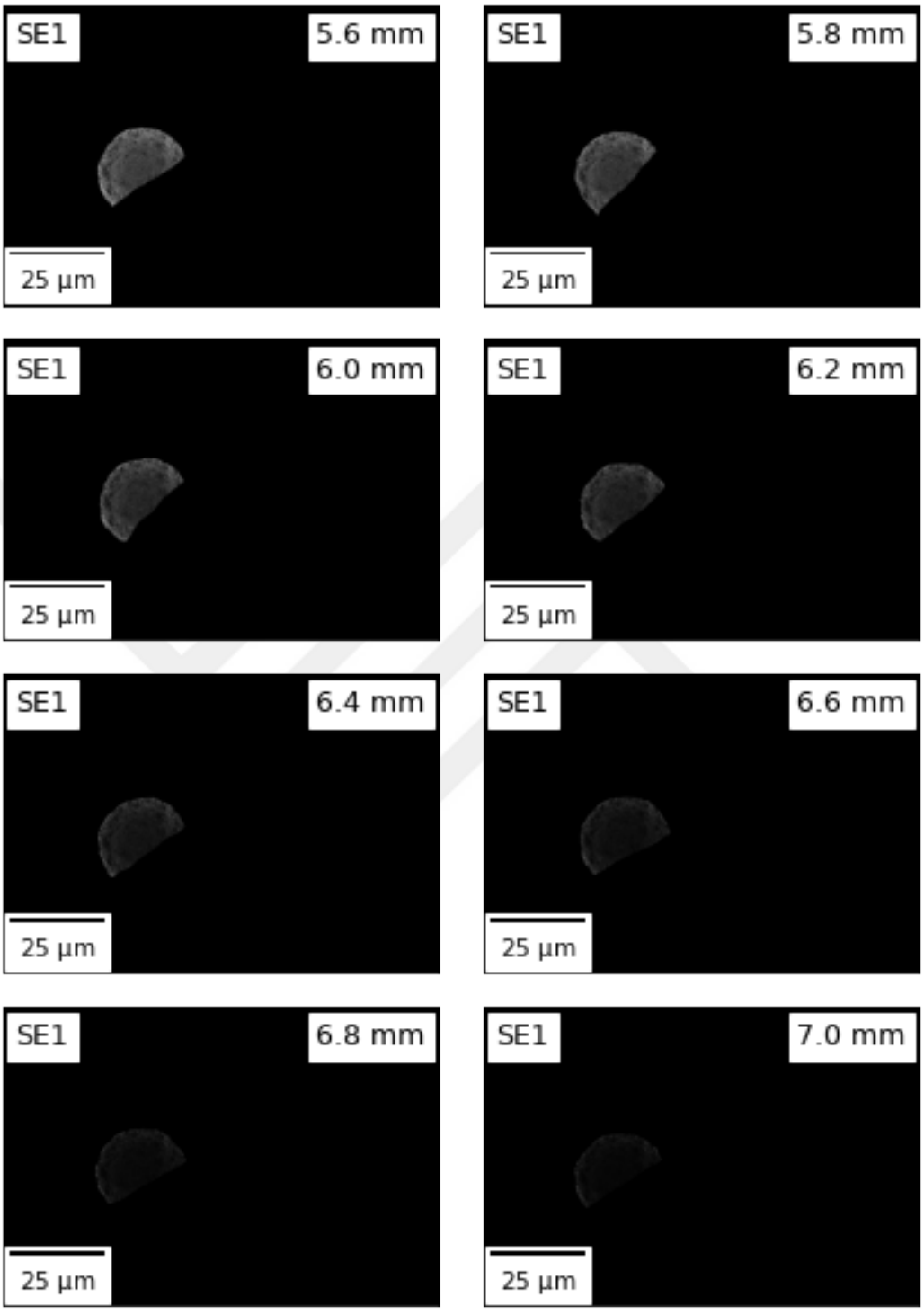


Figure 128: micrograph of t-phase from segmented SE1 electron images at EHT = 1 kV (fixed brightness 42.5% and contrast 35.0%).

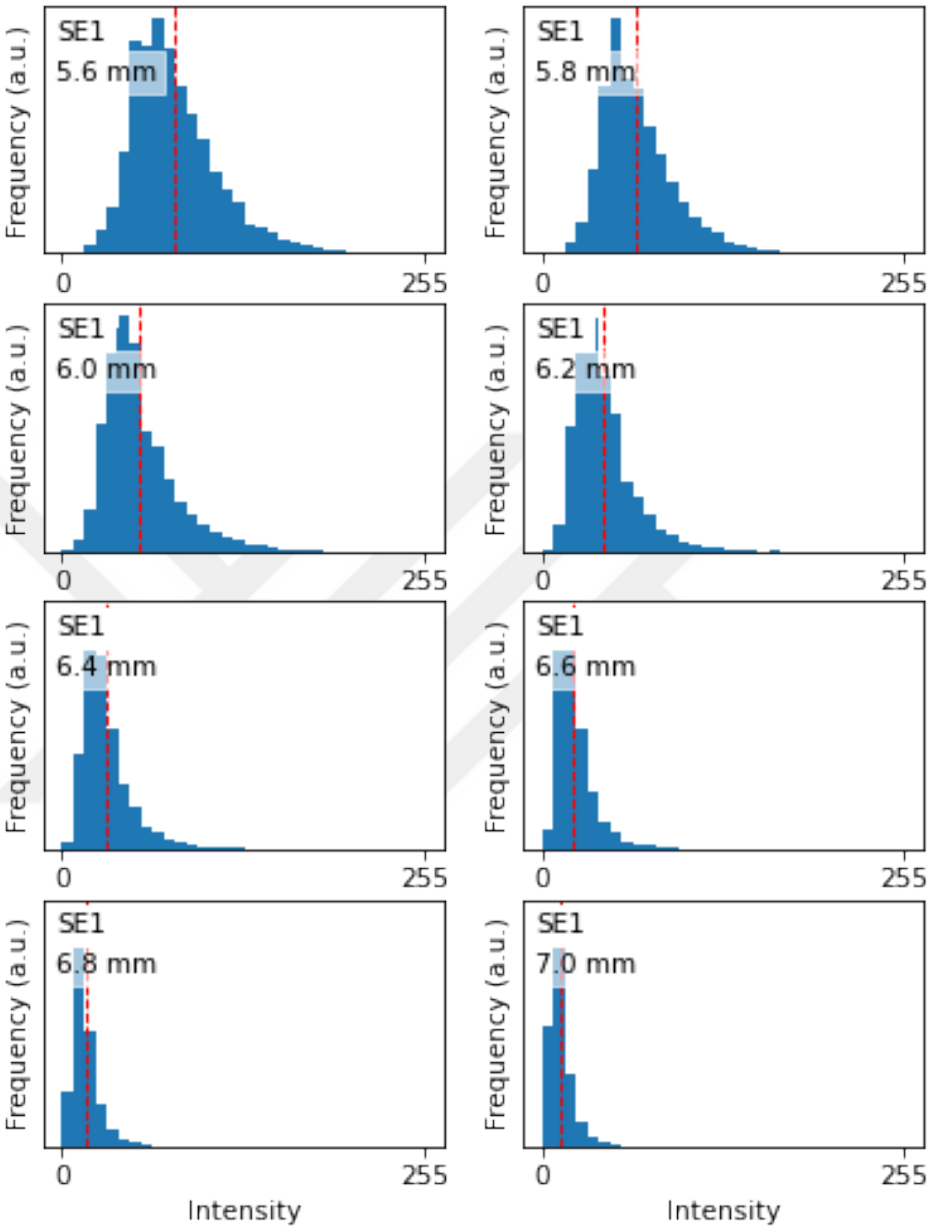


Figure 129: histogram of t-phase from segmented SE1 electron images at EHT = 1 kV (fixed brightness 42.5% and contrast 35.0%).

The average intensities for the segments of the SEM micrographs were given in Table 23 for working distance between 5.0 mm to 7.0 mm at EHT = 1 kV and a fixed brightness 42.5% and contrast 35.0%. The average intensity for the carbon tape support was 232 ± 4 at the working distance of 5.0 mm. It reduced to 71 ± 8 by increasing the working distance to 7.0 mm. The average intensity for the m-phase was 244 ± 5 at the working distance of 5.0 mm. It reduced to 108 ± 23 as the working distance increased to 7.0 mm. Similarly, the average intensity for t-phase was 123 ± 33 at 5.0 mm. It reduced to 13 ± 9 by increasing the working distance.

Table 23: average intensity for carbon tape support, m-ZrO_2, and t-ZrO_2 from SEM micrographs captured by SE1 in EHT = 1 kV (fixed brightness 42.5% and contrast 35.0%)

Working distance (mm)	Average intensity of carbon tape support ($\bar{I}_s$)	Average intensity of m-phase ($\bar{I}_m$)	Average intensity of t-phase ($\bar{I}_t$)
5.0	232 ± 4	244 ± 5	123 ± 33
5.2	226 ± 5	242 ± 7	111 ± 32
5.4	219 ± 6	235 ± 10	98 ± 31
5.6	202 ± 7	226 ± 12	79 ± 30
5.8	191 ± 8	218 ± 13	67 ± 25
6.0	174 ± 8	204 ± 16	54 ± 25
6.2	155 ± 9	190 ± 19	42 ± 20
6.4	126 ± 9	165 ± 22	31 ± 17
6.6	104 ± 9	144 ± 23	22 ± 14
6.8	82 ± 8	121 ± 24	16 ± 10
7.0	71 ± 8	108 ± 23	13 ± 9

The average intensities for the segments of the SEM micrographs were demonstrated in Figure 130 for the working distances between 5.0 mm to 7.0 mm at EHT = 1 kV and a

fixed brightness 42.5% and contrast 35.0%. In each working distance, the average intensity of m-phase was the highest. The average intensity of the carbon tape support was in the middle. The average intensity of the t-phase was the lowest. By increasing the working distance, the average intensities of the carbon tape support, m-phase, and t-phase reduced. This was indicated in the reduction of overall brightness in Figure 83. The reduction of the average intensity was almost parallel in the carbon tape support, m-phase, and t-phase. Only in the large working distances the three plots showed a tendency to converge.

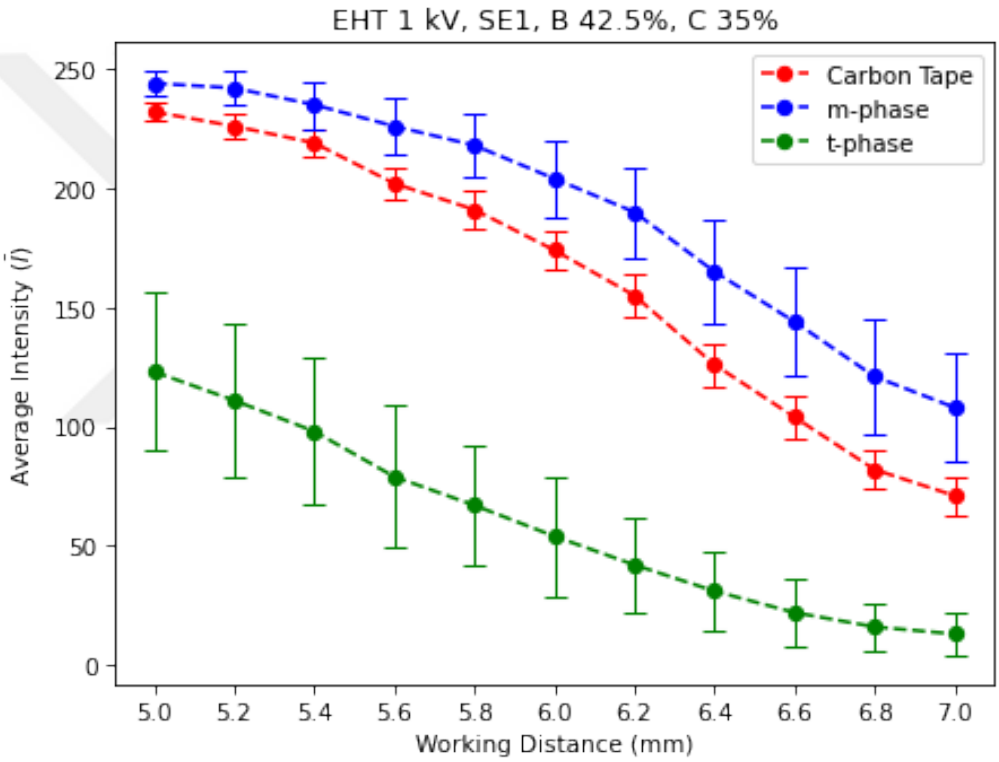


Figure 130: average intensity in different working distances for carbon tape support, m-ZrO_2, and t-ZrO_2 from SEM micrographs captured by TTL detector.

Relative average intensity is shown in Figure 131 for carbon tape support, m-phase, and t-phase in the working distances from 5.0 mm to 7.0 mm. In each working distance the relative average intensity was calculated through dividing the average intensity of that phase by that of the carbon tape support. Relative average intensity for carbon tape support was identical to unity. Relative average intensity of m-phase increased by increasing the working distance. Relative average intensity of the t-phase reduced by

increase in the working distance. increasing the working distance. The difference in the relative average intensities between m-phase and t-phase increased by increasing the working distance.

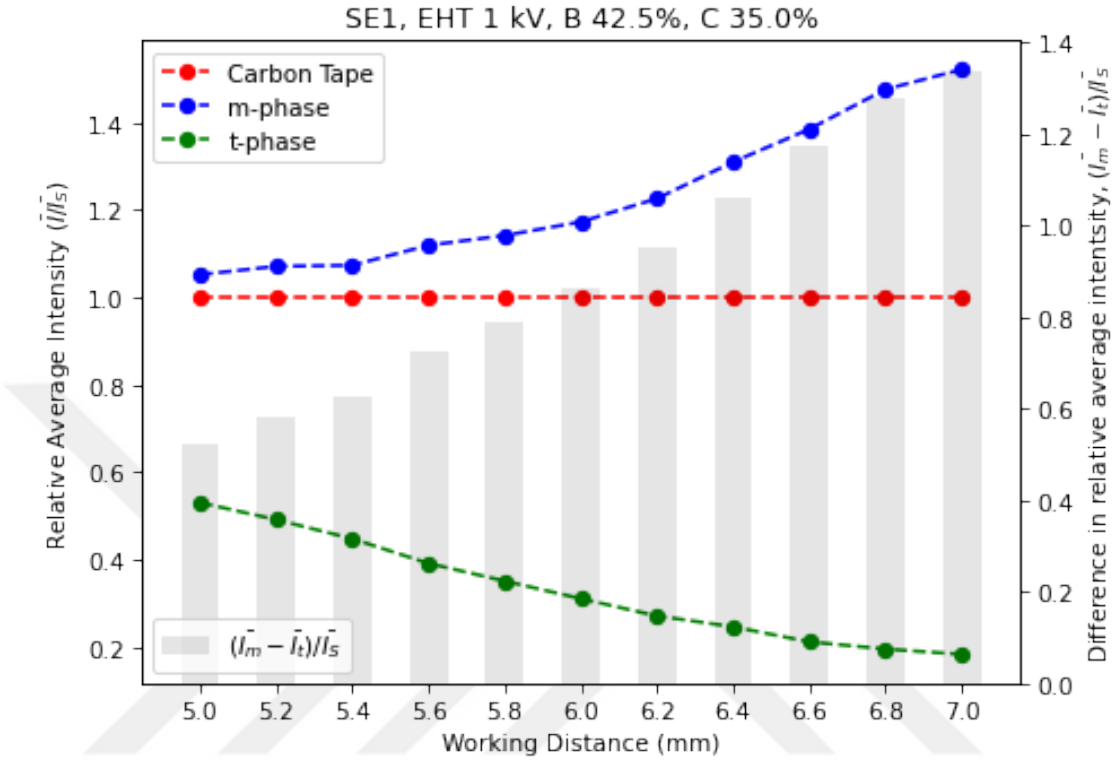


Figure 131: relative average intensity in different working distances for carbon tape support, m-ZrO_2, and t-ZrO_2 from SEM micrographs captured by TTL detector.

Working distance affects the SE1 by changing the number of SE's that can make their trajectory to the inside of the pole piece where the TTL detector (Figure 132). When the working distance is small only those SEs can make their way to the director that are generated close to the incident point of PEs with the surface. Meanwhile, many SEs are produced far from the incidence site. Those electrons cannot make their way to the detector although they are also being pulled to the detector by the electrostatic field. They hit the exterior of the pole piece and absorbed (Figure 132a). That is why the spatial resolution of SE1 signal is higher. Increasing the working distance geometrically allows the SEs generated far from the incident point to find their way into the pole piece (Figure 132b). On the other hand, increasing the working distance decreases the solid angle of detection for BSEs. When the working distance is larger the number of BSEs on the TTL detector is suppressed. The smaller the number of BSEs amplifies the role of SEs.

In the case of m-phase and t-phase, the increase in the working amplifies the already existed difference in the intensity by letting more electrons to be detected. The higher SE yield of m-phase becomes even stronger by increasing the working distance. In addition, larger working distance suppresses the BSEs and boosts the intensity difference between m-phase and t-phase.

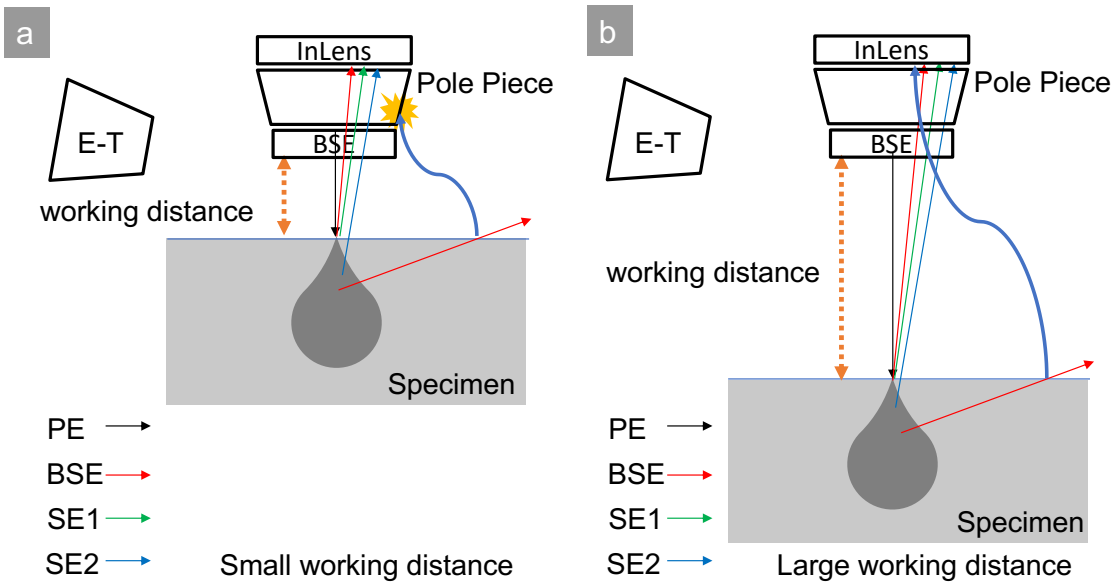


Figure 132: effect working distances for on SEM micrographs captured by TTL detector.

9.4.10 Effect of working distance on SE2 signal

The effect of changing the working distance on the SE2 signal was quantified by segmenting the images of Figure 84. Every image was dissected into three sub-micrographs: carbon tape support, m-phase, and t-phase.

9.4.10.1 Carbon tape support

The image of the segmented carbon tape support is shown in Figure 133. The brightness of the cropped region did not change noticeably by increasing the working distance. The histogram of the cropped region was given in Figure 134. The histograms were narrow. The red dashed vertical line showed the average intensity. By increasing the working distance, the histogram stayed still.

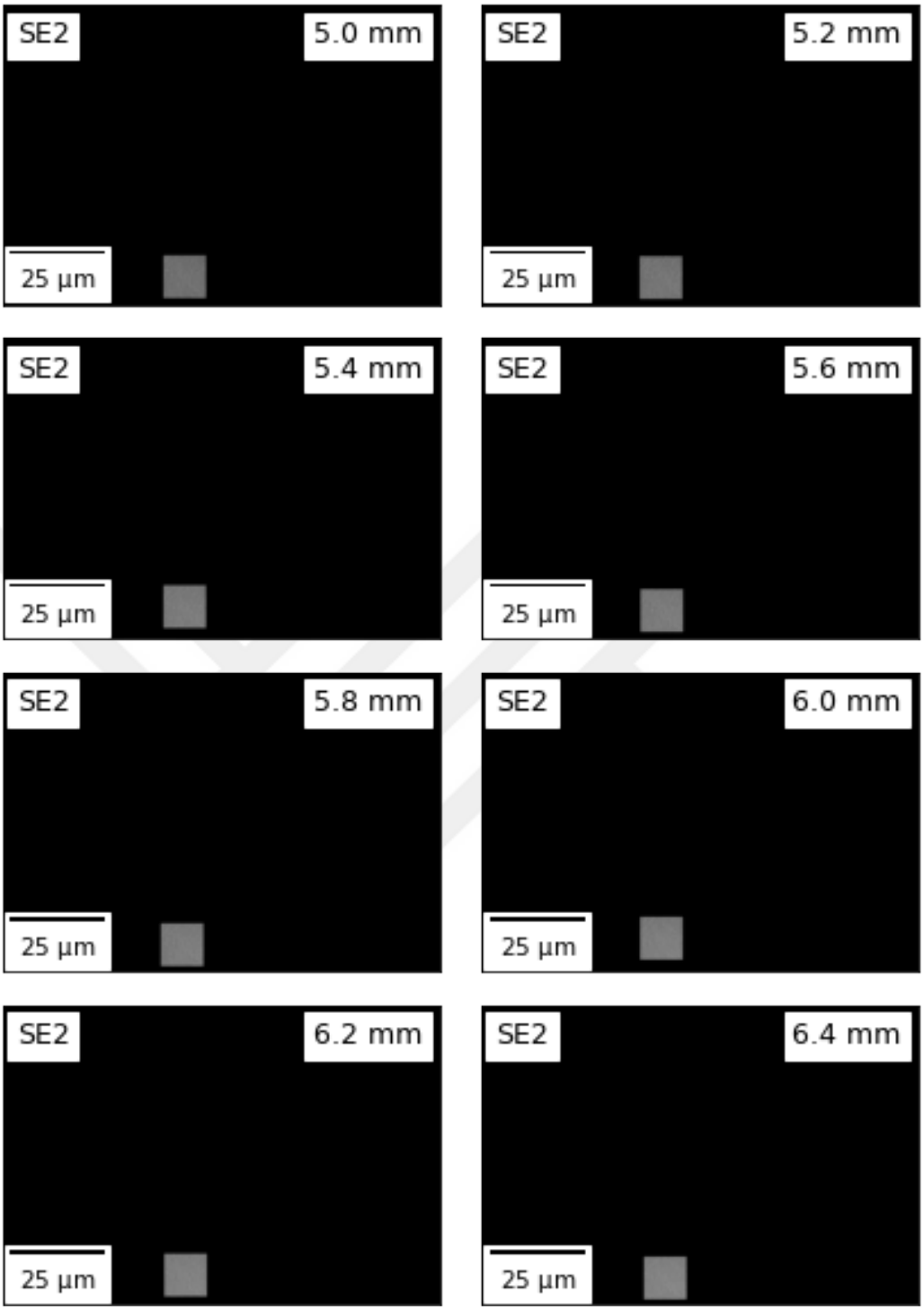


Figure 133: micrograph of carbon tape support from segmented SE2 electron images at EHT = 1 kV (fixed brightness 50.0% and contrast 50.0%).

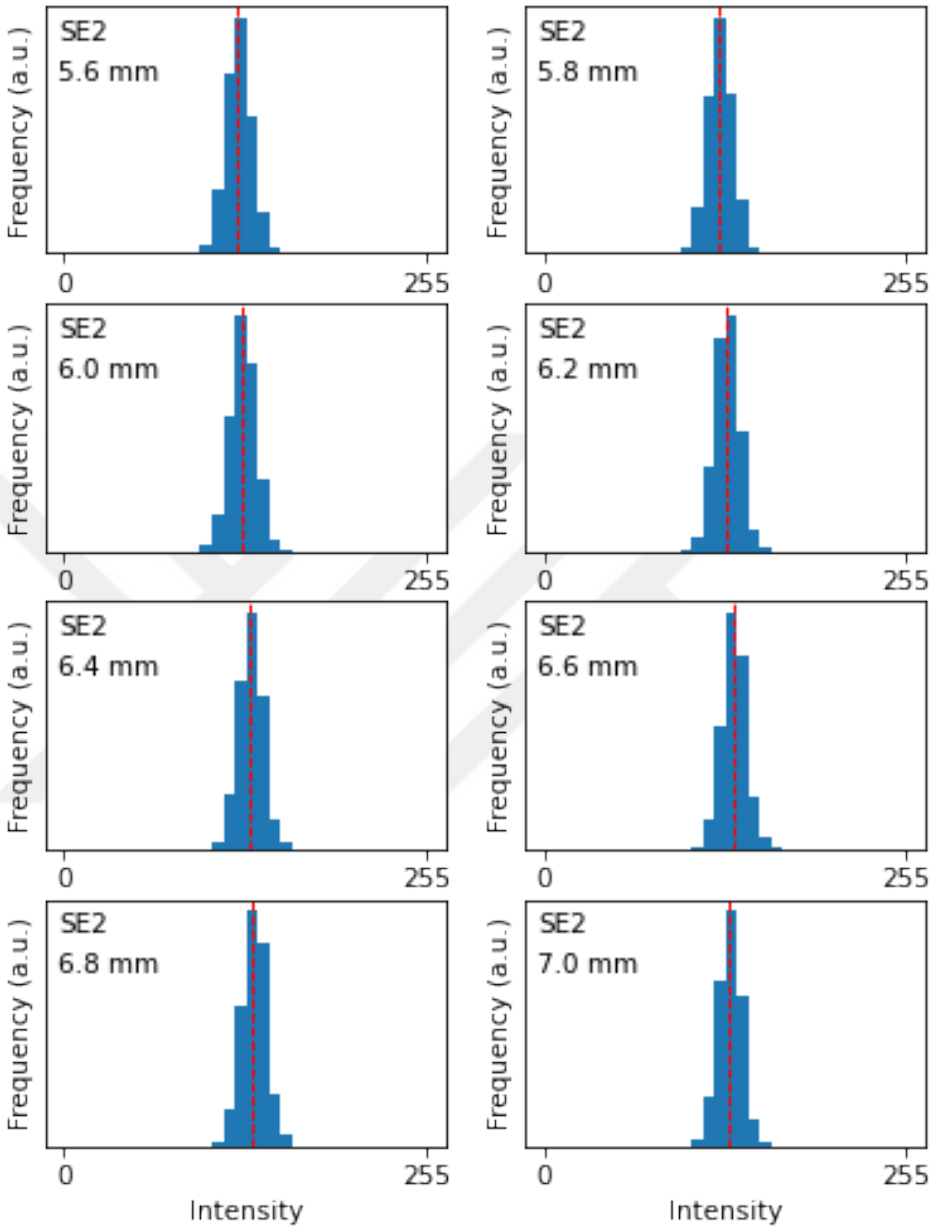


Figure 134: histogram of carbon tape support from segmented SE2 electron images at EHT = 1 kV (fixed brightness 50.0% and contrast 50.0%).

9.4.10.2 Monoclinic phase

The segmented image of the monoclinic phase was given in Figure 135 Apparently, the brightness of the phase reduced by increasing the working distance. The histogram of the same segmented images was given in Figure 136. The histograms were wide in this case. The red dashed vertical line showed the average intensity of the m-phase. By increasing the working distance, the histograms stayed invariant.

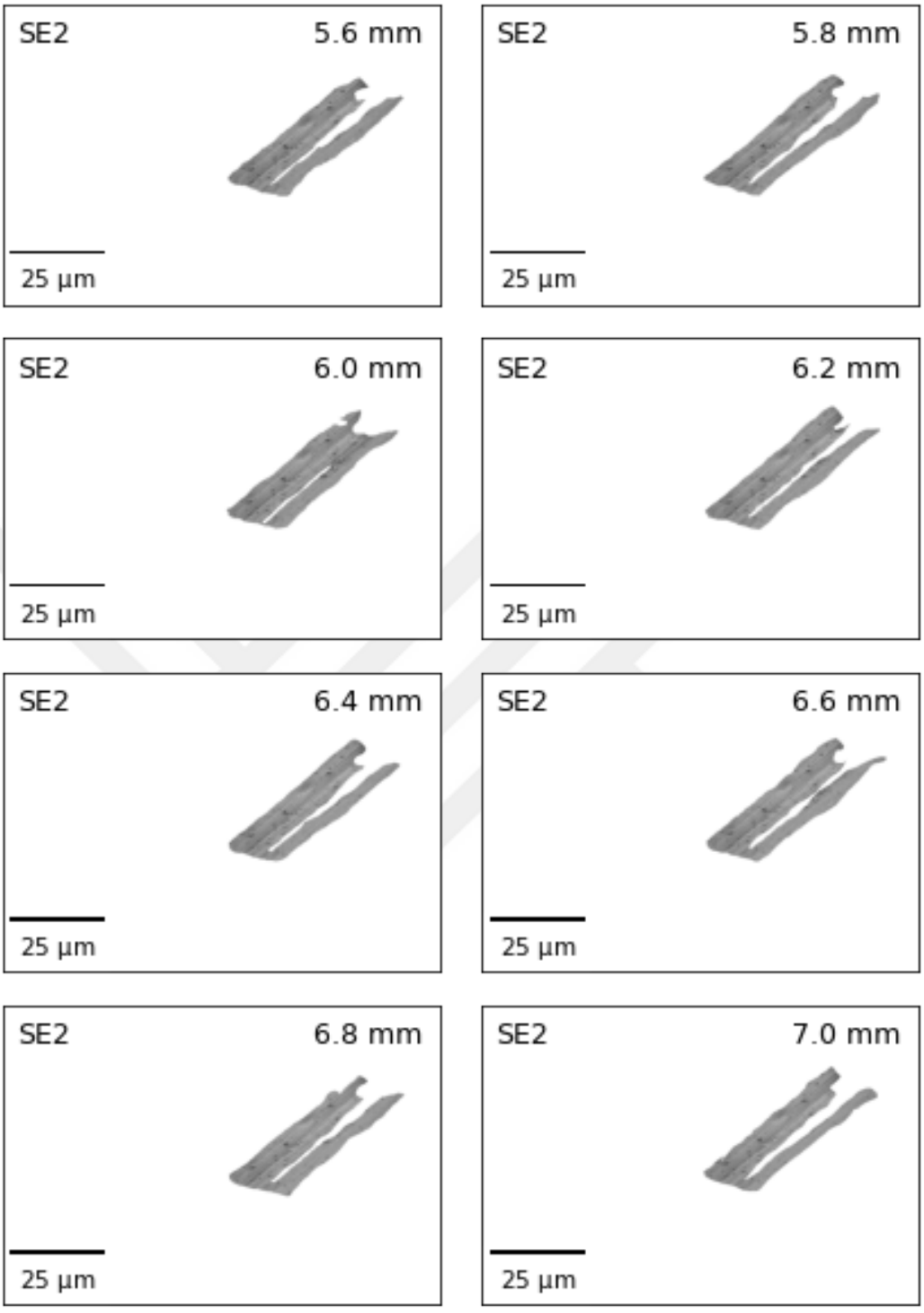


Figure 135: micrograph of m-phase from segmented SE2 electron images at EHT = 1 kV (fixed brightness 50.0% and contrast 50.0%).

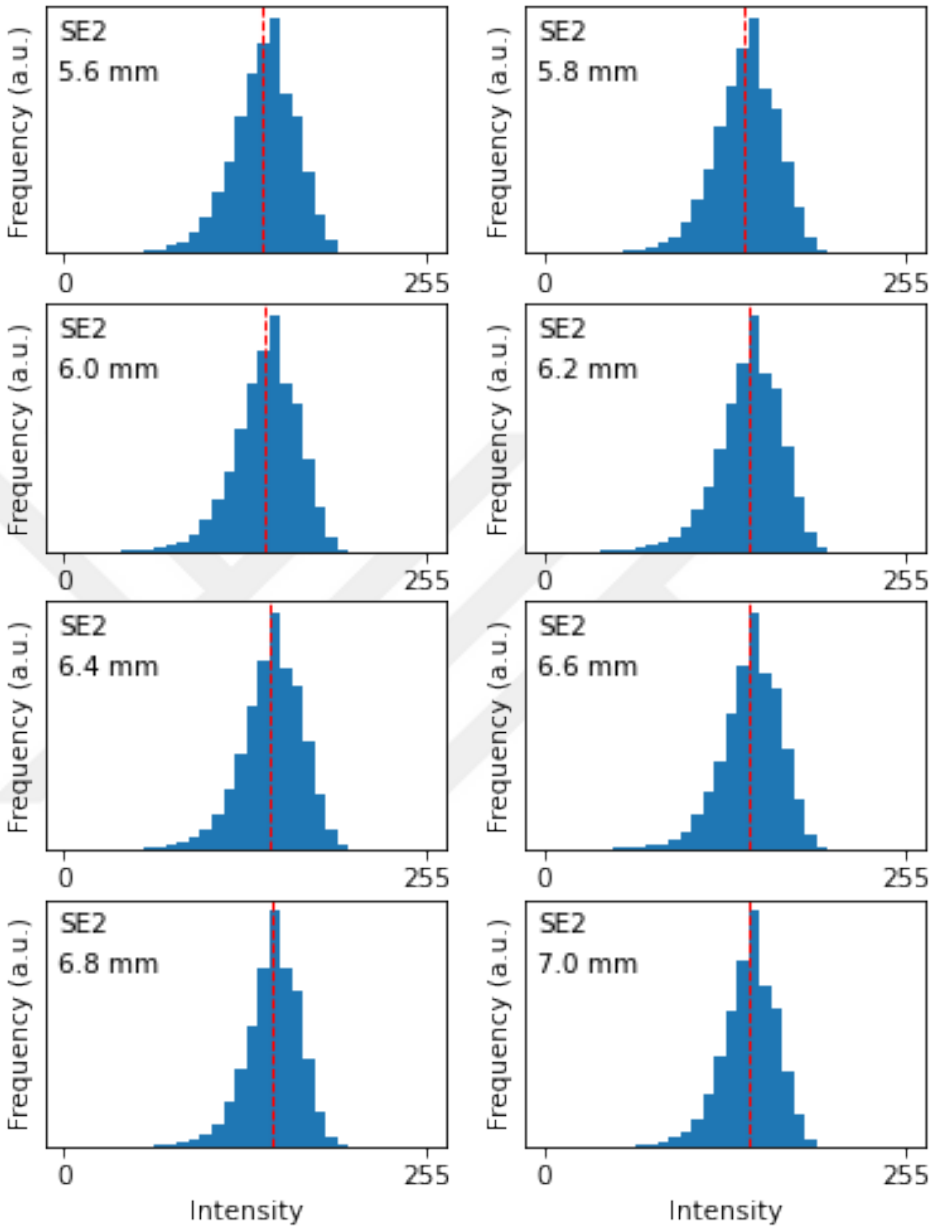


Figure 136: histogram of m-phase from segmented SE2 electron images at EHT = 1 kV (fixed brightness 50.0% and contrast 50.0%).

9.4.10.3 Tetragonal phase

The segmented micrograph of t-phase was shown in Figure 137 By increasing the working distance, the intensity of the m-phase reduced. The histogram of the same segmented sub-micrographs was given in Figure 138. The red dashed vertical line showed the average intensity of the phase. The histograms of the sub-micro graphs are wide. As the working distance increased the histogram stayed the same.

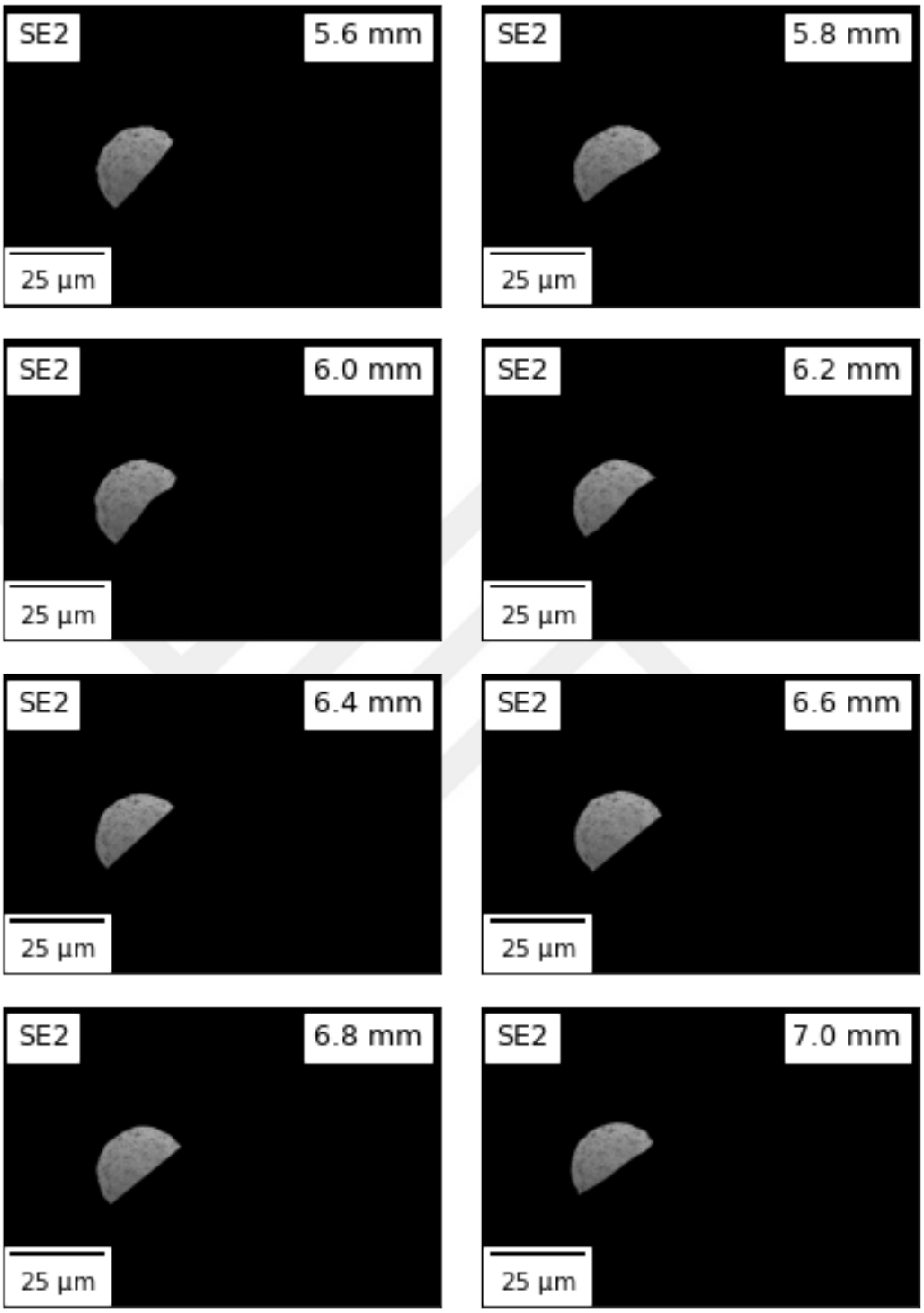


Figure 137: micrograph of t-phase from segmented SE2 electron images at EHT = 1 kV (fixed brightness 50.0% and contrast 50.0%).

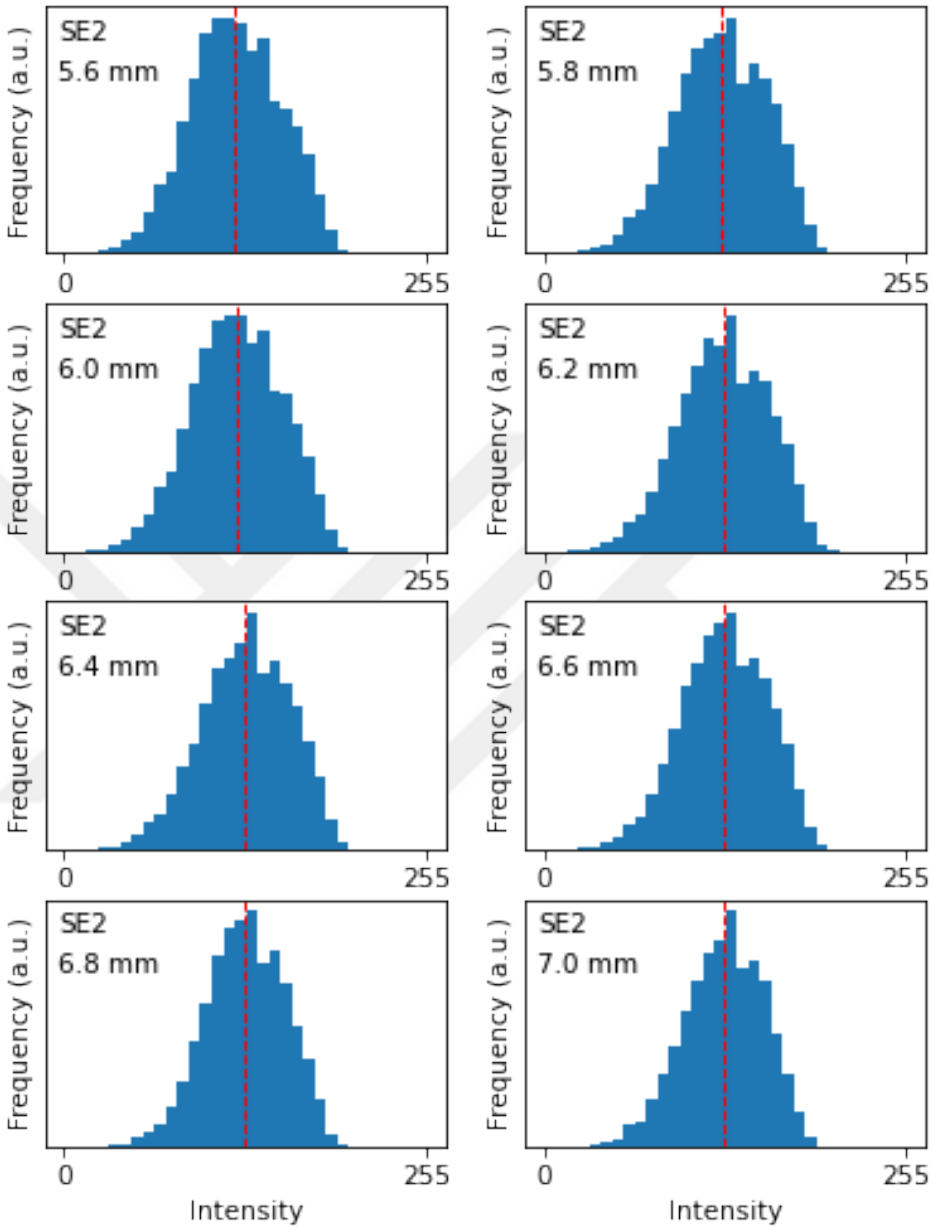


Figure 138: histogram of t-phase from segmented SE2 electron images at EHT = 1 kV (fixed brightness 50.0% and contrast 50.0%).

The average intensity the segments of the SEM micrographs were given in Table 24 for working distance between 5.0 mm to 7.0 mm at EHT = 1 kV and a fixed brightness 50.0% and contrast 50.0%. the sub-micrograph for the carbon tape support. The average intensity for the carbon tape support was 112 ± 9 at the working distance of 5.0 mm. It increased to 131 ± 9 when the working distance was increased to 7.0 mm. The average intensity for m-phase was 133 ± 25 at the working distance of 5.0 mm and increased to 144 ± 20 when the working distance increased to 7.0 mm. The average intensity for t-phase was 118 ± 34 at 5.0 mm. It increased to 128 ± 28 as the working distance increased to 7.0 mm.

Table 24: average intensity for carbon tape support, m-ZrO_2, and t-ZrO_2 from SEM micrographs captured by SE2 in EHT = 1 kV (fixed brightness 50.0% and contrast 50.0%)

Working distance (mm)	Average intensity of carbon tape support ($\bar{I}_s$)	Average intensity of m-phase ($\bar{I}_m$)	Average intensity of t-phase ($\bar{I}_t$)
5.0	112 ± 9	133 ± 25	118 ± 34
5.2	117 ± 9	136 ± 24	117 ± 33
5.4	122 ± 9	140 ± 24	121 ± 32
5.6	122 ± 10	140 ± 22	120 ± 31
5.8	124 ± 9	142 ± 22	125 ± 31
6.0	125 ± 9	142 ± 22	121 ± 31
6.2	128 ± 9	144 ± 22	126 ± 31
6.4	131 ± 9	145 ± 21	128 ± 31
6.6	133 ± 9	145 ± 21	126 ± 30
6.8	133 ± 9	146 ± 19	127 ± 28
7.0	131 ± 9	144 ± 20	128 ± 28

The average intensities for the segments of the SEM micrographs were demonstrate in Figure 139 for the working distance between 5.9 mm to 7.0 mm at EHT = 1 kV and a fixed brightness of 50.0% and contrast of 50.0%. The average. Intensity of m-phase was the highest in all working distances. The average intensity of carbon tape support was mostly in the mid-range. The average intensity of t-phase was almost always the lowest.

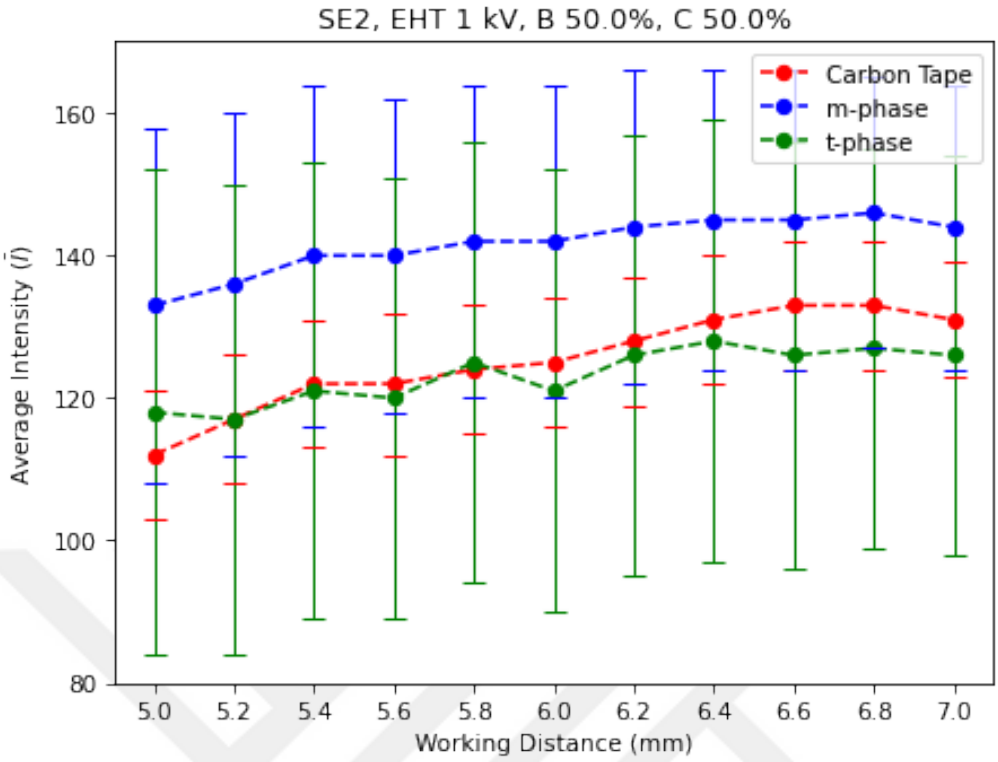


Figure 139: average intensity in different working distances for carbon tape support, m-ZrO_2, and t-ZrO_2 from SEM micrographs captured by E-T detector.

Relative average intensities for the segments of the SEM micrographs were demonstrate in Figure 140 for the working distance between 5.9 mm to 7.0 mm at EHT = 1 kV and a fixed brightness of 42.5 and contrast of 35.0%. In each working distance the relative average intensity was calculated through dividing the average intensity of that phase by that of the carbon tape support. Relative average intensity for carbon tape support was identical to unity. At small working distances the relative average intensity of m-phase t-phase quite close. By increasing the working distance, the average intensity was reduced for both phases almost in parallel. The difference in the relative average intensities of m-phase and t-phase was higher in small working distances. By increasing the working distance, the difference in the relative average intensities of m-phase and t-phase reduced.

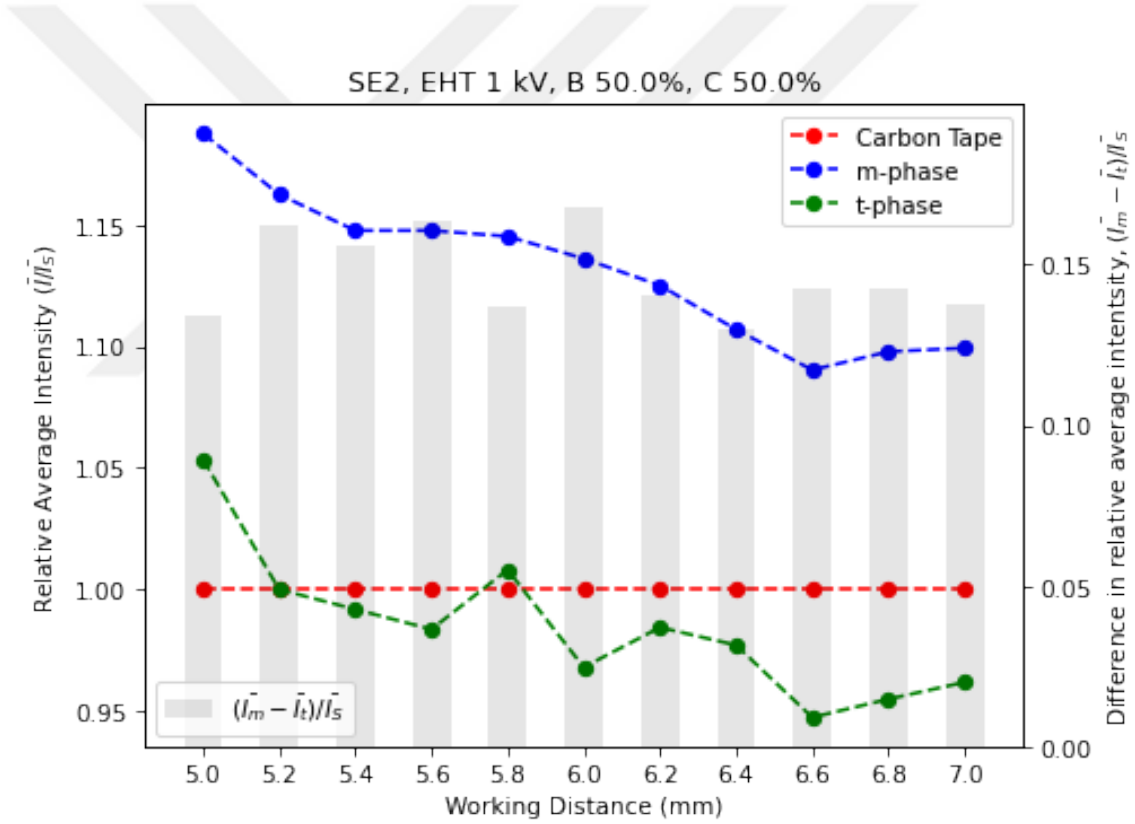


Figure 140: relative average intensity in different working distances for carbon tape support, m-ZrO_2, and t-ZrO_2 from SEM micrographs captured by E-T detector.

The signal that is collected on an E-T detector is a composite of BSE and SE2. Trend the difference of relative average intensity between m-phase and t-phase was less likely to be associated with the SE2. The SE2 electrons are always pulled to the E-T collector by a bias voltage. Only roughness can suppress SE2 electrons from reaching the E-T detector.

Trends in the difference of relative average intensity are more likely to be associated with the number of BSEs. When the working distance was low (Figure 132a), BSEs were less predominant on E-T detector. Thus, the difference in the SE yield was boosted for m-phase and t-phase. When the working distance increased, the specimen approached the optimum geometry to detect maximum number of BSEs (Figure 132b). More number of BSEs suppressed the SE yield to dominate the E-T signal. There, BSEs acted like noises which disguised the true signal.

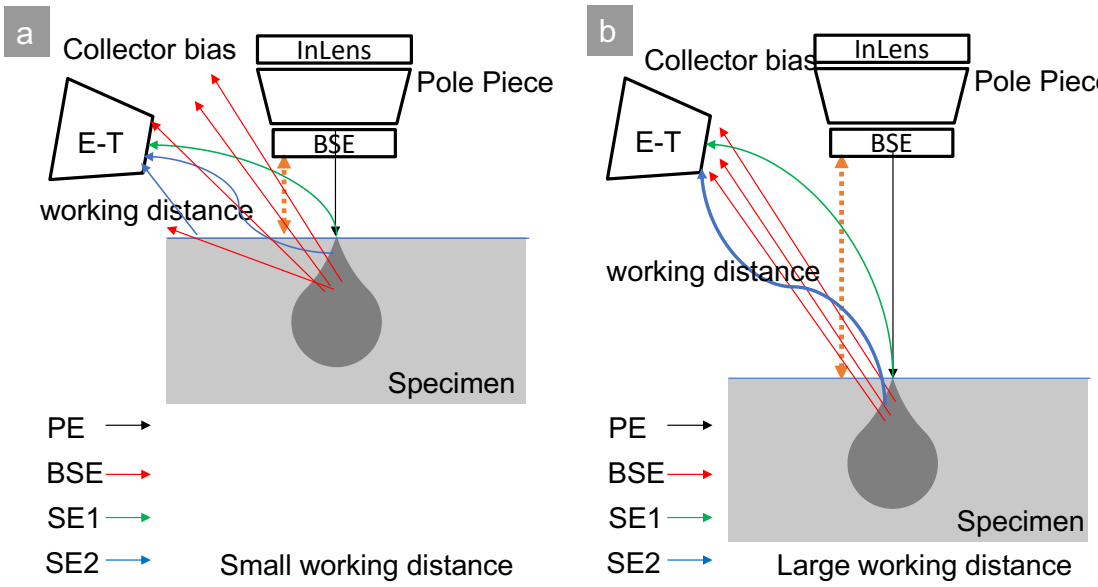


Figure 141: effect of working distances for on SEM micrographs captured by E-T detector.

9.4.11 Differentiation in the transformation zone

Pellets of t-phase transformed to m-phase under indentation (Figure 85a). Correlative Raman and electron microscopy confirmed the transformation (Figure 85c-d) in accordance with [254]. After confirmation, the same indent was analyzed using low-kV SEM technique around the created cracks (Figure 85d, Figure 86, Figure 142). The analysis revealed that the transformed regions (m-phase) appeared brighter than the original t-phase around the cracks as was shown before in the form of powders (Figure 82) and demonstrated by theoretical analysis (Relevant Result). Comparing the differentiation limit of Raman, Raman-SEM, and low-kV SEM (**Error! Reference source not found.**), the last technique is significantly more powerful than the others.

The white rectangular region on Figure 86c was segmented, rotated clockwise for 90°, and shown in Figure 142 after improving the brightness-contrast values. The image

revealed that the bright area is not symmetric around the axis of the crack. The asymmetry eliminated the possibility that the difference in the brightness came from the edge effect. Therefore, we concluded that the brightness of the edges came from the higher SE yield of the m-phase. In addition, it was found that every pixel in the Figure 142 was as small as ca. 6 nm.

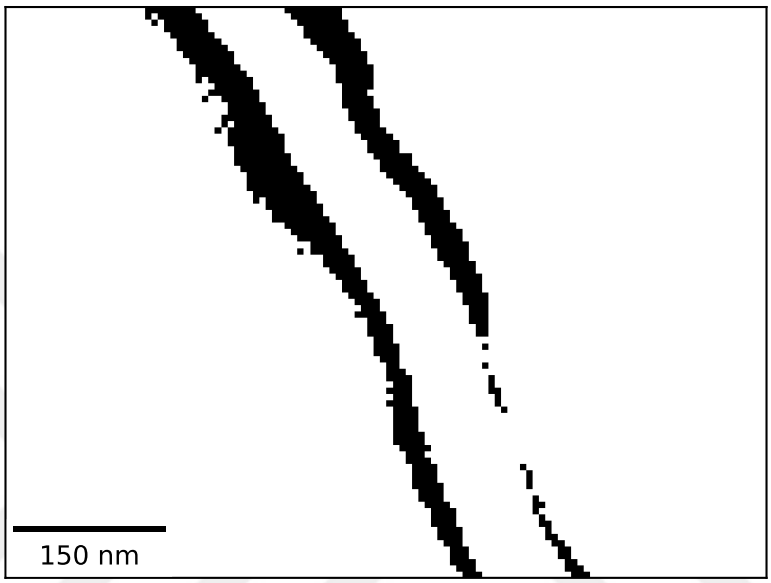


Figure 142: selected transformed region along the crack (TTL image after brightness-contrast manipulated)

The smallest detectable areas were compared for three techniques, namely Raman spectroscopy [254], Raman-SEM (Figure 85d), low-kV SEM (Figure 142). While the resolution limit of Raman spectroscopy is 5 μm, the size of the smallest detectable area in Raman-SEM were was about 10 nm. The proposed method of low-voltage SEM, however, were able to detect changes in the rother of 6 nm. It is important to state that these values are not the resolution of the methods, but only the smallest areas from which a variation in the signal can be detected. Nevertheless, this ability of LVSEM combined with the feasibility of sample preparation and test performance could outstand as a promising method for the microstructural differentiation of polymorphs.

9.5 Conclusion

Monoclinic and tetragonal zirconia phases were differentiated based on their SE yield differences in SEM operated at low PE acceleration voltages and a TTL detector. The two

polymorphs give almost no contrast in the BSE or SE2 mode because of the lack of atomic number difference. The same polymorphs, however, showed a significant contrast in the average intensity when the SEM was operated in low PE acceleration voltages, and SE1 mode of signal collection employed. The difference increased as the acceleration voltage decreased from 2.0 kV to 0.6 kV. The method was applied both for powder and pellet samples. The t-ZrO_2 pellet was indented to induce $t \rightarrow m$ phase transformation. It was demonstrated that an extra brightness appears along the crack on the indent corners under SEM with TTL detector. The brightness was suggested to be coming from the transformed phase: m-ZrO_2. Raman mapping of the indent zone also supported that the brightness was correlated with the transformed region.

References

[1] J. F. Cooley, “Apparatus for electrically dispersing fluids,” U.S. 692631, 1899

[2] W. J. Morton, “Method of dispersing fluids,” U.S. 705691, 1902

[3] J. F. Cooley, “Electrical method of dispersing fluids,” U.S. 745,276, 1903

[4] W.-E. Teo and S. Ramakrishna, “Electrospun nanofibers as a platform for multifunctional, hierarchically organized nanocomposite,” *Compos Sci Technol*, vol. 69, no. 11–12, pp. 1804–1817, Sep. 2009, doi: 10.1016/j.compscitech.2009.04.015.

[5] J. Xue, J. Xie, W. Liu, and Y. Xia, “Electrospun Nanofibers: New Concepts, Materials, and Applications,” *Acc Chem Res*, vol. 50, no. 8, pp. 1976–1987, Aug. 2017, doi: 10.1021/acs.accounts.7b00218.

[6] W. Essa, S. Yasin, I. Saeed, and G. Ali, “Nanofiber-Based Face Masks and Respirators as COVID-19 Protection: A Review,” *Membranes (Basel)*, vol. 11, no. 4, p. 250, Mar. 2021, doi: 10.3390/membranes11040250.

[7] L. A. Alshabanah *et al.*, “Elastic Nanofibrous Membranes for Medical and Personal Protection Applications: Manufacturing, Anti-COVID-19, and Anti-Colistin Resistant Bacteria Evaluation,” *Polymers (Basel)*, vol. 13, no. 22, p. 3987, Nov. 2021, doi: 10.3390/polym13223987.

[8] X. Gao, S. Han, R. Zhang, G. Liu, and J. Wu, “Progress in electrospun composite nanofibers: composition, performance and applications for tissue engineering,” *J Mater Chem B*, vol. 7, no. 45, pp. 7075–7089, 2019, doi: 10.1039/C9TB01730E.

[9] R. Palazzetti and A. Zucchelli, “Electrospun nanofibers as reinforcement for composite laminates materials – A review,” *Compos Struct*, vol. 182, pp. 711–727, Dec. 2017, doi: 10.1016/j.compstruct.2017.09.021.

[10] K. Bilge, E. Ozden-Yenigun, E. Simsek, Y. Z. Menceloglu, and M. Papila, “Structural composites hybridized with epoxy compatible polymer/MWCNT nanofibrous interlayers,” *Compos Sci Technol*, vol. 72, no. 14, pp. 1639–1645, Sep. 2012, doi: 10.1016/j.compscitech.2012.07.005.

[11] E. Ozden, A. R. Atilgan, K. Bilge, Y. Z. Menceloglu, C. Atılgan, and M. Papila, “Designed-in Molecular Interactions Lead to Superior Thermo-mechanical Properties in Nanocomposites,” *MRS Proceedings*, vol. 1304, no. 1, pp. mrsf10-1304-z09-10, Mar. 2011, doi: 10.1557/opl.2011.607.

[12] E. Özden, Y. Z. Menceloğlu, and M. Papila, “Engineering Chemistry of Electrospun Nanofibers and Interfaces in Nanocomposites for Superior Mechanical Properties,” *ACS Appl Mater Interfaces*, vol. 2, no. 7, pp. 1788–1793, Jul. 2010, doi: 10.1021/am100288r.

[13] K. Bilge, S. Venkataraman, Y. Z. Menceloglu, and M. Papila, “Global and local nanofibrous interlayer toughened composites for higher in-plane strength,” *Compos Part A Appl Sci Manuf*, vol. 58, pp. 73–76, 2014, doi: https://doi.org/10.1016/j.compositesa.2013.12.001.

[14] E. Özden-Yenigün, K. Bilge, E. Sünbüloğlu, E. Bozdağ, and M. Papila, “High strain rate response of nanofiber interlayered structural composites,” *Compos Struct*, vol. 168, pp. 47–55, May 2017, doi: 10.1016/j.compstruct.2017.02.007.

[15] L. Daelemans, S. van der Heijden, I. de Baere, H. Rahier, W. van Paepegem, and K. de Clerck, “Damage-Resistant Composites Using Electrospun Nanofibers: A Multiscale Analysis of the Toughening Mechanisms,” *ACS Appl Mater Interfaces*, vol. 8, no. 18, pp. 11806–11818, May 2016, doi: 10.1021/acsami.6b02247.

[16] L. Daelemans, W. van Paepegem, D. R. D’hooge, and K. de Clerck, “Excellent Nanofiber Adhesion for Hybrid Polymer Materials with High Toughness Based on Matrix Interdiffusion During Chemical Conversion,” *Adv Funct Mater*, p. 1807434, Dec. 2018, doi: 10.1002/adfm.201807434.

[17] T. Meireman, L. Daelemans, E. van Verre, W. van Paepegem, and K. de Clerck, “Nanofibre toughening of dissimilar interfaces in composites,” *Mater Des*, vol. 195, p. 109050, Oct. 2020, doi: 10.1016/j.matdes.2020.109050.

[18] L. Daelemans, S. van der Heijden, I. de Baere, H. Rahier, W. van Paepegem, and K. de Clerck, “Nanofibre bridging as a toughening mechanism in carbon/epoxy composite laminates interleaved with electrospun polyamide nanofibrous veils,” *Compos Sci Technol*, vol. 117, no. Complete, pp. 244–256, Sep. 2015, doi: 10.1016/j.compscitech.2015.06.021.

[19] O. İnal, M. Ç. Akbolat, C. Soutis, and K. B. Katnam, “Toughening mechanisms in cost-effective carbon-epoxy laminates with thermoplastic veils: Mode-I and in-situ SEM fracture characterisation,” *International Journal of Lightweight Materials and Manufacture*, vol. 4, no. 1, pp. 50–61, Mar. 2021, doi: 10.1016/j.ijlmm.2020.07.003.

[20] H.-Y. Liu, G.-T. Wang, Y.-W. Mai, and Y. Zeng, “On fracture toughness of nano-particle modified epoxy,” *Compos B Eng*, vol. 42, no. 8, pp. 2170–2175, Dec. 2011, doi: 10.1016/j.compositesb.2011.05.014.

[21] S. Iijima, “Helical microtubules of graphitic carbon,” *Nature*, vol. 354, no. 6348, pp. 56–58, Nov. 1991, doi: 10.1038/354056a0.

[22] S. Iijima and T. Ichihashi, “Single-shell carbon nanotubes of 1-nm diameter,” *Nature*, vol. 363, no. 6430, pp. 603–605, Jun. 1993, doi: 10.1038/363603a0.

[23] H. W. Kroto, J. R. Heath, S. C. O’Brien, R. F. Curl, and R. E. Smalley, “C60: Buckminsterfullerene,” *Nature*, vol. 318, no. 6042, pp. 162–163, Nov. 1985, doi: 10.1038/318162a0.

[24] M. M. J. Treacy, T. W. Ebbesen, and J. M. Gibson, “Exceptionally high Young’s modulus observed for individual carbon nanotubes,” *Nature*, vol. 381, no. 6584, pp. 678–680, Jun. 1996, doi: 10.1038/381678a0.

[25] E. T. Thostenson, Z. Ren, and T.-W. Chou, “Advances in the science and technology of carbon nanotubes and their composites: a review,” *Compos Sci Technol*, vol. 61, no. 13, pp. 1899–1912, Oct. 2001, doi: 10.1016/S0266-3538(01)00094-X.

[26] E. THOSTENSON, C. LI, and T. CHOU, “Nanocomposites in context,” *Compos Sci Technol*, vol. 65, no. 3–4, pp. 491–516, Mar. 2005, doi: 10.1016/j.compscitech.2004.11.003.

[27] X. Gong, J. Liu, S. Baskaran, R. D. Voise, and J. S. Young, “Surfactant-Assisted Processing of Carbon Nanotube/Polymer Composites,” *Chemistry of Materials*, vol. 12, no. 4, pp. 1049–1052, Apr. 2000, doi: 10.1021/cm9906396.

[28] D. Qian, E. C. Dickey, R. Andrews, and T. Rantell, “Load transfer and deformation mechanisms in carbon nanotube-polystyrene composites,” *Appl Phys Lett*, vol. 76, no. 20, pp. 2868–2870, May 2000, doi: 10.1063/1.126500.

[29] C.-L. Zhang and S.-H. Yu, “Nanoparticles meet electrospinning: recent advances and future prospects,” *Chem Soc Rev*, vol. 43, no. 13, p. 4423, 2014, doi: 10.1039/c3cs60426h.

[30] G. Panthi, M. Park, H.-Y. Kim, and S.-J. Park, “Electrospun polymeric nanofibers encapsulated with nanostructured materials and their applications: A review,” *Journal of Industrial and Engineering Chemistry*, vol. 24, pp. 1–13, Apr. 2015, doi: 10.1016/j.jiec.2014.09.011.

[31] S.-X. Wang, C. C. Yap, J. He, C. Chen, S. Y. Wong, and X. Li, “Electrospinning: a facile technique for fabricating functional nanofibers for environmental applications,” *Nanotechnol Rev*, vol. 5, no. 1, Jan. 2016, doi: 10.1515/ntrev-2015-0065.

[32] B.-H. Kim and K. S. Yang, “Structure and electrochemical properties of electrospun carbon fiber composites containing graphene,” *Journal of Industrial and Engineering Chemistry*, vol. 20, no. 5, pp. 3474–3479, Sep. 2014, doi: 10.1016/j.jiec.2013.12.037.

[33] B. Ding, C. K. Kim, H. Y. Kim, M. K. Seo, and S. J. Park, “Titanium dioxide nanofibers prepared by using electrospinning method,” *Fibers and Polymers*, vol. 5, no. 2, pp. 105–109, Jun. 2004, doi: 10.1007/BF02902922.

[34] Q. B. Yang *et al.*, “PREPARATION AND CHARACTERIZATION OF A PAN NANOFIBRE CONTAINING AG NANOPARTICLES VIA ELECTROSPINNING,” *Synth Met*, vol. 137, no. 1–3, pp. 973–974, Apr. 2003, doi: 10.1016/S0379-6779(02)00963-3.

[35] A. E. Deniz, A. Celebioglu, F. Kayaci, and T. Uyar, “Electrospun polymeric nanofibrous composites containing TiO2 short nanofibers,” *Mater Chem Phys*, vol. 129, no. 3, pp. 701–704, Oct. 2011, doi: 10.1016/j.matchemphys.2011.06.018.

[36] D. Zhang *et al.*, “Electrospun polyacrylonitrile nanocomposite fibers reinforced with Fe3O4 nanoparticles: Fabrication and property analysis,” *Polymer (Guildf)*, vol. 50, no. 17, pp. 4189–4198, Aug. 2009, doi: 10.1016/j.polymer.2009.06.062.

[37] I.-H. Chen, C.-C. Wang, and C.-Y. Chen, “Fabrication and characterization of magnetic cobalt ferrite/polyacrylonitrile and cobalt ferrite/carbon nanofibers by electrospinning,” *Carbon N Y*, vol. 48, no. 3, pp. 604–611, Mar. 2010, doi: 10.1016/j.carbon.2009.09.062.

[38] O. Chiscan, I. Dumitru, P. Postolache, V. Tura, and A. Stancu, “Electrospun PVC/Fe3O4 composite nanofibers for microwave absorption applications,” *Mater Lett*, vol. 68, pp. 251–254, Feb. 2012, doi: 10.1016/j.matlet.2011.10.084.

[39] J. Kong *et al.*, “Carbon/SnO 2 /carbon core/shell/shell hybrid nanofibers: tailored nanostructure for the anode of lithium ion batteries with high reversibility and rate capacity,” *Nanoscale*, vol. 4, no. 2, pp. 525–530, 2012, doi: 10.1039/C1NR10962F.

[40] J. Kong, S. Y. Wong, Y. Zhang, H. R. Tan, X. Li, and X. Lu, “One-dimensional carbon–SnO2 and SnO2 nanostructures via single-spinneret electrospinning: tunable morphology and the underlying mechanism,” *J Mater Chem*, vol. 21, no. 40, p. 15928, 2011, doi: 10.1039/c1jm12492g.

[41] D. Cho, A. Naydich, M. W. Frey, and Y. L. Joo, “Further improvement of air filtration efficiency of cellulose filters coated with nanofibers via inclusion of electrostatically active nanoparticles,” *Polymer (Guildf)*, vol. 54, no. 9, pp. 2364–2372, Apr. 2013, doi: 10.1016/j.polymer.2013.02.034.

[42] Z. Guo, Z.-H. Huang, M. Wang, and F. Kang, “Graphene/carbon composite nanofibers for NO oxidation at room temperature,” *Catal Sci Technol*, vol. 5, no. 2, pp. 827–829, 2015, doi: 10.1039/C4CY01393J.

[43] S. Lee, “Multifunctionality of layered fabric systems based on electrospun polyurethane/zinc oxide nanocomposite fibers,” *J Appl Polym Sci*, vol. 114, no. 6, pp. 3652–3658, Dec. 2009, doi: 10.1002/app.30778.

[44] K. Lee and S. Lee, “Multifunctionality of poly(vinyl alcohol) nanofiber webs containing titanium dioxide,” *J Appl Polym Sci*, vol. 124, no. 5, pp. 4038–4046, Jun. 2012, doi: 10.1002/app.34929.

[45] L. Fan, C. Luo, Z. Lv, F. Lu, and H. Qiu, “Preparation of magnetic modified chitosan and adsorption of Zn2+ from aqueous solutions,” *Colloids Surf B Biointerfaces*, vol. 88, no. 2, pp. 574–581, Dec. 2011, doi: 10.1016/j.colsurfb.2011.07.038.

[46] C.-L. Zhang, K.-P. Lv, H.-P. Cong, and S.-H. Yu, “Controlled Assemblies of Gold Nanorods in PVA Nanofiber Matrix as Flexible Free-Standing SERS Substrates by Electrospinning,” *Small*, vol. 8, no. 5, pp. 648–653, Mar. 2012, doi: 10.1002/smll.201102230.

[47] S. Maity, L. N. Downen, J. R. Bochinski, and L. I. Clarke, “Embedded metal nanoparticles as localized heat sources: An alternative processing approach for complex polymeric materials,” *Polymer (Guildf)*, vol. 52, no. 7, pp. 1674–1685, Mar. 2011, doi: 10.1016/j.polymer.2011.01.062.

[48] H.-C. Chang, C.-L. Liu, and W.-C. Chen, “Flexible Nonvolatile Transistor Memory Devices Based on One-Dimensional Electrospun P3HT:Au Hybrid Nanofibers,” *Adv Funct Mater*, vol. 23, no. 39, pp. 4960–4968, Oct. 2013, doi: 10.1002/adfm.201300283.

[49] G.-M. Kim *et al.*, "One-Dimensional Arrangement of Gold Nanoparticles by Electrospinning," *Chemistry of Materials*, vol. 17, no. 20, pp. 4949–4957, Oct. 2005, doi: 10.1021/cm0508120.

[50] D. He, B. Hu, Q.-F. Yao, K. Wang, and S.-H. Yu, "Large-Scale Synthesis of Flexible Free-Standing SERS Substrates with High Sensitivity: Electrospun PVA Nanofibers Embedded with Controlled Alignment of Silver Nanoparticles," *ACS Nano*, vol. 3, no. 12, pp. 3993–4002, Dec. 2009, doi: 10.1021/nn900812f.

[51] K. D. Behler, A. Stravato, V. Mochalin, G. Korneva, G. Yushin, and Y. Gogotsi, "Nanodiamond-Polymer Composite Fibers and Coatings," *ACS Nano*, vol. 3, no. 2, pp. 363–369, Feb. 2009, doi: 10.1021/nn800445z.

[52] L. Ji, C. Saquing, S. A. Khan, and X. Zhang, "Preparation and characterization of silica nanoparticulate–polyacrylonitrile composite and porous nanofibers," *Nanotechnology*, vol. 19, no. 8, p. 085605, Feb. 2008, doi: 10.1088/0957-4484/19/8/085605.

[53] T. Ding *et al.*, "Anisotropic oxygen plasma etching of colloidal particles in electrospun fibers," *Chem. Commun.*, vol. 47, no. 8, pp. 2429–2431, 2011, doi: 10.1039/C0CC04393A.

[54] Y. Jin, D. Yang, D. Kang, and X. Jiang, "Fabrication of Necklace-like Structures via Electrospinning," *Langmuir*, vol. 26, no. 2, pp. 1186–1190, Jan. 2010, doi: 10.1021/la902313t.

[55] C.-Y. Hsu and Y.-L. Liu, "Rhodamine B-anchored silica nanoparticles displaying white-light photoluminescence and their uses in preparations of photoluminescent polymeric films and nanofibers," *J Colloid Interface Sci*, vol. 350, no. 1, pp. 75–82, Oct. 2010, doi: 10.1016/j.jcis.2010.06.011.

[56] B. Ding, J. Lin, X. Wang, J. Yu, J. Yang, and Y. Cai, "Investigation of silica nanoparticle distribution in nanoporous polystyrene fibers," *Soft Matter*, vol. 7, no. 18, p. 8376, 2011, doi: 10.1039/c1sm05791j.

[57] S. K. Choi, S. Kim, S. K. Lim, and H. Park, "Photocatalytic Comparison of TiO 2 Nanoparticles and Electrospun TiO 2 Nanofibers: Effects of Mesoporosity and Interparticle Charge Transfer," *The Journal of Physical Chemistry C*, vol. 114, no. 39, pp. 16475–16480, Oct. 2010, doi: 10.1021/jp104317x.

[58] X. Huang *et al.*, “Mechanical endurance of polymer electrolyte membrane and PEM fuel cell durability,” *J Polym Sci B Polym Phys*, vol. 44, no. 16, pp. 2346–2357, Aug. 2006, doi: 10.1002/polb.20863.

[59] K. Friedemann, A. Turshatov, K. Landfester, and D. Crespy, “Characterization via Two-Color STED Microscopy of Nanostructured Materials Synthesized by Colloid Electrospinning,” *Langmuir*, vol. 27, no. 11, pp. 7132–7139, Jun. 2011, doi: 10.1021/la104817r.

[60] Z. Hou *et al.*, “Electrospinning Preparation and Drug-Delivery Properties of an Up-conversion Luminescent Porous NaYF4:Yb3+, Er3+@Silica Fiber Nanocomposite,” *Adv Funct Mater*, vol. 21, no. 12, pp. 2356–2365, Jun. 2011, doi: 10.1002/adfm.201100193.

[61] K. Cho, M. Kim, J. Choi, K. Kim, and S. Kim, “Synthesis and characterization of electrospun polymer nanofibers incorporated with CdTe nanoparticles,” *Synth Met*, vol. 160, no. 9–10, pp. 888–891, May 2010, doi: 10.1016/j.synthmet.2010.01.041.

[62] S. Piperno, L. A. Gheber, P. Canton, A. Pich, G. Dvorakova, and A. Biffis, “Microgel electrospinning: A novel tool for the fabrication of nanocomposite fibers,” *Polymer (Guildf)*, vol. 50, no. 26, pp. 6193–6197, Dec. 2009, doi: 10.1016/j.polymer.2009.11.004.

[63] J.-M. Lim, J. H. Moon, G.-R. Yi, C.-J. Heo, and S.-M. Yang, “Fabrication of One-Dimensional Colloidal Assemblies from Electrospun Nanofibers,” *Langmuir*, vol. 22, no. 8, pp. 3445–3449, Apr. 2006, doi: 10.1021/la053057d.

[64] A. Stoiljkovic, R. Venkatesh, E. Klimov, V. Raman, J. H. Wendorff, and A. Greiner, “Poly(styrene- co - n -butyl acrylate) Nanofibers with Excellent Stability against Water by Electrospinning from Aqueous Colloidal Dispersions,” *Macromolecules*, vol. 42, no. 16, pp. 6147–6151, Aug. 2009, doi: 10.1021/ma900354u.

[65] S. Lee *et al.*, “Preparation of macroporous carbon nanofibers with macroscopic openings in the surfaces and their applications,” *Nanotechnology*, vol. 20, no. 44, p. 445702, Nov. 2009, doi: 10.1088/0957-4484/20/44/445702.

[66] L. Buruaga, H. Sardon, L. Irusta, A. González, M. J. Fernández-Berridi, and J. J. Iruin, “Electrospinning of waterborne polyurethanes,” *J Appl Polym Sci*, vol. 115, no. 2, pp. 1176–1179, Jan. 2010, doi: 10.1002/app.31219.

[67] M. Beck-Broichsitter *et al.*, “Novel ‘Nano in Nano’ Composites for Sustained Drug Delivery: Biodegradable Nanoparticles Encapsulated into Nanofiber Non-Wovens,” *Macromol Biosci*, vol. 10, no. 12, pp. 1527–1535, Dec. 2010, doi: 10.1002/mabi.201000100.

[68] B. Dong, M. E. Smith, and G. E. Wnek, “Encapsulation of Multiple Biological Compounds Within a Single Electrospun Fiber,” *Small*, vol. 5, no. 13, pp. 1508–1512, Jul. 2009, doi: 10.1002/smll.200801750.

[69] K. Yoshimatsu, L. Ye, P. Stenlund, and I. S. Chronakis, “A simple method for preparation of molecularly imprinted nanofiber materials with signal transduction ability,” *Chemical Communications*, no. 17, p. 2022, 2008, doi: 10.1039/b719586a.

[70] K. E. Roskov *et al.*, “Long-Range Alignment of Gold Nanorods in Electrospun Polymer Nano/Microfibers,” *Langmuir*, vol. 27, no. 23, pp. 13965–13969, Dec. 2011, doi: 10.1021/la2021066.

[71] P. Wang, L. Zhang, Y. Xia, L. Tong, X. Xu, and Y. Ying, “Polymer Nanofibers Embedded with Aligned Gold Nanorods: A New Platform for Plasmonic Studies and Optical Sensing,” *Nano Lett*, vol. 12, no. 6, pp. 3145–3150, Jun. 2012, doi: 10.1021/nl301055f.

[72] C.-L. Zhang *et al.*, “Macroscopic-Scale Alignment of Ultralong Ag Nanowires in Polymer Nanofiber Mat and Their Hierarchical Structures by Magnetic-Field-Assisted Electrospinning,” *Small*, vol. 8, no. 19, pp. 2936–2940, Oct. 2012, doi: 10.1002/smll.201201353.

[73] J. Lee and Y. Deng, “Increased mechanical properties of aligned and isotropic electrospun PVA nanofiber webs by cellulose nanowhisker reinforcement,” *Macromol Res*, vol. 20, no. 1, pp. 76–83, Jan. 2012, doi: 10.1007/s13233-012-0008-3.

[74] R. Qi *et al.*, “Electrospun poly(lactic-co-glycolic acid)/halloysite nanotube composite nanofibers for drug encapsulation and sustained release,” *J Mater Chem*, vol. 20, no. 47, p. 10622, 2010, doi: 10.1039/c0jm01328e.

[75] V. v. Matrenichev *et al.*, “Properties of Film Materials Based on Composite Nanofibers from Aliphatic Copolyamide and Carbon Nanotubes for Tissue Engineering,” *Polymer Science, Series A*, vol. 60, no. 2, pp. 215–221, Mar. 2018, doi: 10.1134/S0965545X18020104.

[76] V. Obradović, D. B. Stojanović, I. Janković Častvan, V. Radojević, and P. S. Uskoković, "Processing and Characterisation of Hybrid Aramid Fabrics Reinforced with Cross-linked Electrospun PVB Composite Nanofibres," *Fibers and Polymers*, vol. 19, no. 9, pp. 1921–1929, Sep. 2018, doi: 10.1007/s12221-018-8381-y.

[77] M. B. Bazbouz and G. K. Stylios, "Novel mechanism for spinning continuous twisted composite nanofiber yarns," *Eur Polym J*, vol. 44, no. 1, pp. 1–12, Jan. 2008, doi: 10.1016/j.eurpolymj.2007.10.006.

[78] T. Gong, W. Li, H. Chen, L. Wang, S. Shao, and S. Zhou, "Remotely actuated shape memory effect of electrospun composite nanofibers," *Acta Biomater*, vol. 8, no. 3, pp. 1248–1259, Mar. 2012, doi: 10.1016/j.actbio.2011.12.006.

[79] X. Wang *et al.*, "Novel electrochemical biosensor based on functional composite nanofibers for sensitive detection of p53 tumor suppressor gene," *Anal Chim Acta*, vol. 765, pp. 63–69, Feb. 2013, doi: 10.1016/j.aca.2012.12.037.

[80] A. A. Merati, A. Mousavi Shoushtari, and J. Mirzaei, "A comparison between the UV protection of PAN/ZnO and PAN/MWNT composite nanofiber mats," *The Journal of The Textile Institute*, vol. 108, no. 12, pp. 2086–2089, Dec. 2017, doi: 10.1080/00405000.2017.1313361.

[81] W. Ahmad *et al.*, "Highly Sensitive Humidity Sensors Based on Polyethylene Oxide/CuO/Multi Walled Carbon Nanotubes Composite Nanofibers," *Materials*, vol. 14, no. 4, p. 1037, Feb. 2021, doi: 10.3390/ma14041037.

[82] E. Özden-Yenigün, Y. Z. Menceloğlu, and M. Papila, "MWCNTs/P(St- co -GMA) Composite Nanofibers of Engineered Interface Chemistry for Epoxy Matrix Nanocomposites," *ACS Appl Mater Interfaces*, vol. 4, no. 2, pp. 777–784, Feb. 2012, doi: 10.1021/am2014162.

[83] K. Bilge, A. Ürkmez, E. Şimşek, and M. Papila, "Stabilized electrospinning of heat stimuli/ in situ crosslinkable nanofibers and their self-same nanocomposites," *J Appl Polym Sci*, vol. 133, no. 43, Nov. 2016, doi: 10.1002/app.44090.

[84] K. Bilge *et al.*, "Synergistic role of in-situ crosslinkable electrospun nanofiber/epoxy nanocomposite interlayers for superior laminated composites," *Compos Sci Technol*, vol. 151, pp. 310–316, Oct. 2017, doi: 10.1016/j.compscitech.2017.08.029.

[85] C. C. Chiao and T. T. Chiao, “Aramid fibers and composites,” in *Handbook of Composites*, Springer, 1982, pp. 272–317.

[86] Jr. Harold Wayne Hill, L. Kwolek, and W. Sweeny, “Aromatic polyamides,” 1968

[87] S. L. Kwolek, P. W. Morgan, and W. R. Sorenson, “Process of making wholly aromatic polyamides,” 1962

[88] H. Blades, “Dry-jet wet spinning process,” 1973

[89] M. G. Northolt, “X-ray diffraction study of poly (p-phenylene terephthalamide) fibres,” *Eur Polym J*, vol. 10, no. 9, pp. 799–804, 1974.

[90] L. Penn and F. Larsen, “Physicochemical properties of kevlar 49 fiber,” *J Appl Polym Sci*, vol. 23, no. 1, pp. 59–73, 1979.

[91] H. Blades, “High modulus, high Tenacity poly(p-phenylene terephtalamide) fiber,” 1975

[92] A. R. Bunsell, “The tensile and fatigue behaviour of Kevlar-49 (PRD-49) fibre,” *J Mater Sci*, vol. 10, no. 8, pp. 1300–1308, 1975.

[93] T. T. Chiao and R. L. Moore, “A tensile test method for fibers,” *J Compos Mater*, vol. 4, no. 1, pp. 118–123, 1970.

[94] J. Kalantar and L. T. Drzal, “The bonding mechanism of aramid fibres to epoxy matrices,” *J Mater Sci*, vol. 25, no. 10, pp. 4186–4193, 1990, doi: 10.1007/BF00581071.

[95] P. Lee-Sullivan, K. S. Chian, C. Y. Yue, and H. C. Looi, “Effects of bromination and hydrolysis treatments on the morphology and tensile properties of Kevlar-29 fibres,” *J Mater Sci Lett*, vol. 13, no. 5, pp. 305–309, 1994.

[96] Y. Wang, J. Li, and D. Zhao, “Mechanical properties of fiber glass and Kevlar woven fabric reinforced composites,” *Composites Engineering*, vol. 5, no. 9, pp. 1159–1175, 1995, doi: https://doi.org/10.1016/0961-9526(95)00100-2.

[97] D. B. Eagles, B. F. Blumentritt, and S. L. Cooper, “Interfacial properties of kevlar-49 fiber-reinforced thermoplastics,” *J Appl Polym Sci*, vol. 20, no. 2, pp. 435–448, 1976.

[98] L. S. Penn, F. A. Bystry, and H. J. Marchionni, “Relation of interfacial adhesion in Kevlar®/epoxy systems to surface characterization and composite performance,” *Polym Compos*, vol. 4, no. 1, pp. 26–31, 1983.

[99] Y. W. Mai and F. Castino, “Fracture toughness of Kevlar-epoxy composites with controlled interfacial bonding,” *J Mater Sci*, vol. 19, no. 5, pp. 1638–1655, 1984, doi: 10.1007/BF00563062.

[100] Y. Wu and G. C. Tesoro, “Chemical modification of Kevlar fiber surfaces and of model diamides,” *J Appl Polym Sci*, vol. 31, no. 4, pp. 1041–1059, 1986.

[101] A. Mittelman and I. Roman, “Tensile properties of real unidirectional Kevlar/epoxy composites,” *Composites*, vol. 21, no. 1, pp. 63–69, 1990, doi: https://doi.org/10.1016/0010-4361(90)90099-I.

[102] J. R. Brown, P. J. C. Chappell, and Z. Mathys, “Plasma surface modification of advanced organic fibers. I: Effects on the mechanical, fracture and ballistic properties of aramid epoxy composites,” *J Mater Sci*, vol. 26, no. 15, pp. 4172–4178, 1991.

[103] M. Shaker, I. Kamel, F. Ko, and J. W. Song, “Improvement of the interfacial adhesion between Kevlar fiber and resin by using RF plasma,” *Journal of Composites, Technology and Research*, vol. 18, no. 4, pp. 249–255, 1996.

[104] C. Y. Yue and K. Padmanabhan, “Interfacial studies on surface modified Kevlar fibre/epoxy matrix composites,” *Compos B Eng*, vol. 30, no. 2, pp. 205–217, 1999.

[105] R. J. Young, D. J. Bannister, A. J. Cervenka, and I. Ahmad, “Effect of surface treatment upon the pull-out behaviour of aramid fibres from epoxy resins,” *J Mater Sci*, vol. 35, no. 8, pp. 1939–1947, 2000.

[106] D. H. Reneker and I. Chun, “Nanometre diameter fibres of polymer, produced by electrospinning,” *Nanotechnology*, vol. 7, no. 3, pp. 216–223, Sep. 1996, doi: 10.1088/0957-4484/7/3/009.

[107] Y. Dzenis, “Spinning continuous fibers for nanotechnology,” *Science (1979)*, vol. 304, no. 5679, pp. 1917–1919, 2004, doi: 10.1126/science.1099074.

[108] D. Papkov, Y. Zou, M. N. Andalib, A. Goponenko, S. Z. D. Cheng, and Y. A. Dzenis, “Simultaneously Strong and Tough Ultrafine Continuous Nanofibers,” *ACS Nano*, vol. 7, no. 4, pp. 3324–3331, 2013, doi: 10.1021/nn400028p.

[109] A. Zucchelli, M. L. Focarete, C. Gualandi, and S. Ramakrishna, “Electrospun nanofibers for enhancing structural performance of composite materials,” *Polym Adv Technol*, vol. 22, no. 3, pp. 339–349, Mar. 2011, doi: 10.1002/pat.1837.

[110] Z.-M. Huang, Y.-Z. Zhang, M. Kotaki, and S. Ramakrishna, “A review on polymer nanofibers by electrospinning and their applications in nanocomposites,” *Compos*

Sci Technol, vol. 63, no. 15, pp. 2223–2253, Nov. 2003, doi: 10.1016/S0266-3538(03)00178-7.

[111] G. Wang, D. Yu, A. D. Kelkar, and L. Zhang, "Electrospun nanofiber: Emerging reinforcing filler in polymer matrix composite materials," *Prog Polym Sci*, vol. 75, pp. 73–107, Dec. 2017, doi: 10.1016/j.progpolymsci.2017.08.002.

[112] L. Daelemans, S. van der Heijden, I. de Baere, H. Rahier, W. van Paepegem, and K. de Clerck, "Improved fatigue delamination behaviour of composite laminates with electrospun thermoplastic nanofibrous interleaves using the Central Cut-Ply method," *Compos Part A Appl Sci Manuf*, 2017, doi: 10.1016/j.compositesa.2016.12.004.

[113] B. D. Agarwal and L. J. Broutman, *Analysis and performance of fiber composites*. John Wiley & Sons, 1990.

[114] K. Bilge and M. Papila, "Interlayer toughening mechanisms of composite materials," in *Toughening Mechanisms in Composite Materials*, Q. Qin and J. Ye, Eds. Elsevier, 2015, pp. 263–294. doi: 10.1016/B978-1-78242-279-2.00010-X.

[115] K. Bilge, "Multi-scale nature of composite materials: Three case studies," MSc, Sabanci University, 2012.

[116] J. Xu, G. Lindbergh, and J. Varna, "Multiphysics modeling of mechanical and electrochemical phenomena in structural composites for energy storage: Single carbon fiber micro-battery," *Journal of Reinforced Plastics and Composites*, vol. 37, no. 10, pp. 701–715, May 2018, doi: 10.1177/0731684418760207.

[117] L. Daelemans, S. van der Heijden, I. de Baere, H. Rahier, W. van Paepegem, and K. de Clerck, "Using aligned nanofibres for identifying the toughening micromechanisms in nanofibre interleaved laminates," *Compos Sci Technol*, vol. 124, no. Complete, pp. 17–26, 2016, doi: 10.1016/j.compscitech.2015.11.021.

[118] T. Meireman, L. Daelemans, S. Rijckaert, H. Rahier, W. van Paepegem, and K. de Clerck, "Delamination resistant composites by interleaving bio-based long-chain polyamide nanofibers through optimal control of fiber diameter and fiber morphology," *Compos Sci Technol*, p. 108126, 2020, doi: https://doi.org/10.1016/j.compscitech.2020.108126.

[119] F. A. Arpatappeh, A. A. Gharehaghaji, and H. Nosraty, "Epoxy-matrix nanocomposites reinforced by electrospun polymeric nanofibrous layers: PAN,

PA-6,6, and hybrid PAN/PA-6,6," *Proc Inst Mech Eng C J Mech Eng Sci*, vol. 236, no. 7, pp. 3615–3622, Apr. 2022, doi: 10.1177/09544062211042657.

[120] F. A. Arpatappeh, M. Papila, and B. E. Aydemir, "Multiscale Reinforcing Interlayers of Self-same P(St-co-GMA) Nanofibers Loaded with MCF for Polymer Composites and Nanocomposites," in *AIAA Scitech 2019 Forum*, Jan. 2019. doi: 10.2514/6.2019-1762.

[121] Y. Li *et al.*, "Developments of Advanced Electrospinning Techniques: A Critical Review," *Adv Mater Technol*, p. 2100410, Jul. 2021, doi: 10.1002/admt.202100410.

[122] S. Sasidharan and A. Anand, "Epoxy-Based Hybrid Structural Composites with Nanofillers: A Review," *Ind Eng Chem Res*, vol. 59, no. 28, pp. 12617–12631, Jul. 2020, doi: 10.1021/acs.iecr.0c01711.

[123] K. Saravanakumar, V. Arumugam, R. Souhith, and C. Santulli, "Influence of Milled Glass Fiber Fillers on Mode I & Mode II Interlaminar Fracture Toughness of Epoxy Resin for Fabrication of Glass/Epoxy Composites," *Fibers*, vol. 8, no. 6, p. 36, Jun. 2020, doi: 10.3390/fib8060036.

[124] G. Marsh, "Reclaiming value from post-use carbon composite," *Reinforced Plastics*, vol. 52, no. 7, pp. 36–39, 2008, doi: https://doi.org/10.1016/S0034-3617(08)70242-X.

[125] A. C. Garg, "Delamination—a damage mode in composite structures," *Eng Fract Mech*, vol. 29, no. 5, pp. 557–584, 1988, doi: http://dx.doi.org/10.1016/0013-7944(88)90181-6.

[126] T. K. Tsotsis, "Interlayer toughening of composite materials," *Polym Compos*, vol. 30, no. 1, pp. 70–86, Jan. 2009, doi: 10.1002/pc.20535.

[127] C. Wu, P. Feng, Y. Bai, and Y. Lu, "Epoxy Enhanced by Recycled Milled Carbon Fibres in Adhesively-Bonded CFRP for Structural Strengthening," *Polymers (Basel)*, vol. 6, no. 1, pp. 76–92, Dec. 2013, doi: 10.3390/polym6010076.

[128] S. T. Cholake *et al.*, "Physico-chemical characterization of novel epoxy matrix system reinforced with recycled short milled carbon fibre," *Journal of Minerals and Materials Characterization and Engineering*, vol. 3, no. 05, p. 373, 2015, doi: 10.4236/jmmce.2015.35040.

[129] S. T. Cholake *et al.*, "Improved fracture toughened epoxy matrix system reinforced with recycled milled carbon fibre," *Ann. Mater. Sci. Eng*, vol. 2, no. 2, 2015.

[130] S. T. Cholake *et al.*, “Improved Mode I fracture resistance of CFRP composites by reinforcing epoxy matrix with recycled short milled carbon fibre,” *Constr Build Mater*, vol. 111, pp. 399–407, May 2016, doi: 10.1016/j.conbuildmat.2016.02.039.

[131] O. Zabihi, M. Ahmadi, S. Shafei, S. M. Seraji, A. Oroumei, and M. Naebe, “One-step amino-functionalization of milled carbon fibre for enhancement of thermo-physical properties of epoxy composites,” *Compos Part A Appl Sci Manuf*, vol. 88, pp. 243–252, 2016, doi: https://doi.org/10.1016/j.compositesa.2016.06.005.

[132] S. Karimi and S. Javadpour, “Comparison of the role of milled glass and carbon fibers on mechanical properties of (bisphenol A)-based epoxy composites,” *Journal of Vinyl & Additive Technology*, vol. 24, no. 2, pp. 130–138, 2018, doi: 10.1002/vnl.21536.

[133] S.-Y. Fu, X.-Q. Feng, B. Lauke, and Y.-W. Mai, “Effects of particle size, particle/matrix interface adhesion and particle loading on mechanical properties of particulate–polymer composites,” *Compos B Eng*, vol. 39, no. 6, pp. 933–961, Sep. 2008, doi: 10.1016/j.compositesb.2008.01.002.

[134] M. Y. Zakaria, A. B. Sulong, J. Sahari, and H. Suherman, “Effect of the addition of milled carbon fiber as a secondary filler on the electrical conductivity of graphite/epoxy composites for electrical conductive material,” *Compos B Eng*, vol. 83, pp. 75–80, 2015, doi: https://doi.org/10.1016/j.compositesb.2015.08.034.

[135] M. Papila, A. ÜRKMEZ, K. BILGE, E. Simsek, Y. Z. Menceloglu, and E. Özden-YENIGUN, “Stable electrospinning composition for stable Nano-/submicrostructure production and preparation method thereof,” U.S. 10422053B2, 2015

[136] O. S. Yördem, M. Papila, and Y. Z. Menceloğlu, “Effects of electrospinning parameters on polyacrylonitrile nanofiber diameter: An investigation by response surface methodology,” *Mater Des*, vol. 29, no. 1, pp. 34–44, Jan. 2008, doi: 10.1016/j.matdes.2006.12.013.

[137] S. A. Hosseini Ravandi, M. Sadrjahani, A. Valipouri, F. Dabirian, and F. K. Ko, “Recently developed electrospinning methods: a review,” *Textile Research Journal*, p. 004051752110698, Jan. 2022, doi: 10.1177/00405175211069880.

[138] A. L. Yarin, S. Koombhongse, and D. H. Reneker, “Taylor cone and jetting from liquid droplets in electrospinning of nanofibers,” *J Appl Phys*, vol. 90, no. 9, pp. 4836–4846, Nov. 2001, doi: 10.1063/1.1408260.

[139] J. Lin, B. Ding, J. Yang, J. Yu, and G. Sun, “Subtle regulation of the micro- and nanostructures of electrospun polystyrene fibers and their application in oil absorption,” *Nanoscale*, vol. 4, no. 1, pp. 176–182, 2012, doi: 10.1039/C1NR10895F.

[140] D. Lubasova and L. Martinova, “Controlled morphology of porous polyvinyl butyral nanofibers,” *J Nanomater*, 2011, doi: 10.1155/2011/292516.

[141] N. Sabetzadeh, A. A. Gharehaghaji, and M. Javanbakht, “Porous PAN micro/nanofiber membranes with potential application as Lithium-ion battery separators: physical, morphological and thermal properties,” *Journal of Polymer Research*, vol. 26, no. 1, p. 9, 2019, doi: 10.1007/s10965-018-1678-0.

[142] H. Fong, I. Chun, and D. H. Reneker, “Beaded nanofibers formed during electrospinning,” *Polymer (Guildf)*, vol. 40, no. 16, pp. 4585–4592, Jul. 1999, doi: 10.1016/S0032-3861(99)00068-3.

[143] V. Khrenov, F. Schwager, M. Klapper, M. Koch, and K. Müllen, “Compatibilization of inorganic particles for polymeric nanocomposites. Optimization of the size and the compatibility of ZnO particles,” *Polymer Bulletin*, vol. 58, no. 5–6, pp. 799–807, May 2007, doi: 10.1007/s00289-006-0721-1.

[144] M. Qu, J. S. Meth, G. S. Blackman, G. M. Cohen, K. G. Sharp, and K. J. van Vliet, “Tailoring and probing particle–polymer interactions in PMMA/silica nanocomposites,” *Soft Matter*, vol. 7, no. 18, p. 8401, 2011, doi: 10.1039/c1sm05668a.

[145] B. Jung, C. K. Ober, and M. O. Thompson, “Controlled roughness reduction of patterned resist polymers using laser-induced sub-millisecond heating,” *J. Mater. Chem. C*, vol. 2, no. 43, pp. 9115–9121, 2014, doi: 10.1039/C4TC01548G.

[146] L. E. Asp, M. Johansson, G. Lindbergh, J. Xu, and D. Zenkert, “Structural battery composites: a review,” *Functional Composites and Structures*, vol. 1, no. 4, p. 042001, Nov. 2019, doi: 10.1088/2631-6331/ab5571.

[147] A. Bachinger, J. Rössler, and L. E. Asp, “Electrocoating of carbon fibres at ambient conditions,” *Compos B Eng*, vol. 91, pp. 94–102, Apr. 2016, doi: 10.1016/j.compositesb.2016.01.027.

[148] A. Buchman, H. Dodiuk-Kenig, A. Dotan, R. Tenne, and S. Kenig, “Toughening of epoxy adhesives by nanoparticles,” *J Adhes Sci Technol*, vol. 23, no. 5, pp. 753–768, 2009.

[149] W. M. Speri and C. F. Jenkins, “Effect of fiber-matrix adhesion on the properties of short fiber reinforced ABS,” *Polym Eng Sci*, vol. 13, no. 6, pp. 409–414, 1973.

[150] A. C. Garg and Y.-W. Mai, “Failure prediction in toughened epoxy resins,” *Compos Sci Technol*, vol. 31, no. 3, pp. 225–242, 1988, doi: https://doi.org/10.1016/0266-3538(88)90010-3.

[151] J. Chen, G.-T. Wang, Z.-Z. Yu, Z. Huang, and Y.-W. Mai, “Critical particle size for interfacial debonding in polymer/nanoparticle composites,” *Compos Sci Technol*, vol. 70, no. 5, pp. 861–872, 2010.

[152] A. H. Ribeiro Junior *et al.*, “Statistical and numerical approaches of particulate reinforced polymers and their effect on the interlocking effect of hybrid composite joints,” *J Compos Mater*, vol. 56, no. 8, pp. 1267–1285, Apr. 2022, doi: 10.1177/00219983211073511.

[153] A. C. Garg and Y.-W. Mai, “Failure mechanisms in toughened epoxy resins—A review,” *Compos Sci Technol*, vol. 31, no. 3, pp. 179–223, 1988, doi: https://doi.org/10.1016/0266-3538(88)90009-7.

[154] H. Saghafi, R. Palazzetti, A. Zucchelli, and G. Minak, “Influence of electrospun nanofibers on the interlaminar properties of unidirectional epoxy resin/glass fiber composite laminates,” *Journal of Reinforced Plastics and Composites*, vol. 34, no. 11, pp. 907–914, Jun. 2015, doi: 10.1177/0731684415584635.

[155] H. Saghafi, G. Minak, A. Zucchelli, T. M. Brugo, and H. Heidary, “Comparing various toughening mechanisms occurred in nanomodified laminates under impact loading,” *Compos B Eng*, p. 106964, May 2019, doi: 10.1016/J.COMPOSITESB.2019.106964.

[156] M. S. Islam and P. Prabhakar, “Interlaminar strengthening of multidirectional laminates using polymer additive manufacturing,” *Mater Des*, vol. 133, pp. 332–339, Nov. 2017, doi: 10.1016/j.matdes.2017.07.038.

[157] F. Cataldo, “Study on the reinforcing effect of milled carbon fibers in a natural rubber based composite,” *Journal of Macromolecular Science, Part B: Physics*, vol. 47, no. 4, pp. 818–828, 2008, doi: 10.1080/00222340802122798.

[158] S. Ivaturi, H. Baske, and P. Ghosal, “Distribution of milled carbon fibers as a function of their length on S-glass fabric and its effect on the electromagnetic properties of S-glass epoxy composites,” *J Compos Mater*, vol. 53, no. 20, pp. 2891–2899, Aug. 2019, doi: 10.1177/0021998318819738.

[159] B. Yu, X.-M. Zhao, X.-N. Jiao, and D.-Y. Qi, “Composite Nanofiber Membrane for Lithium-Ion Batteries Prepared by Electrostatic Spun/Spray Deposition,” *Journal of Electrochemical Energy Conversion and Storage*, vol. 13, no. 1, Feb. 2016, doi: 10.1115/1.4034030.

[160] Y. M. Im *et al.*, “Preparation of poly(vinyl alcohol)/ZrO2 composite nanofibers via co-axial electrospinning with higher ZrO2 particle content,” *Fibers and Polymers*, vol. 15, no. 10, pp. 2066–2071, Oct. 2014, doi: 10.1007/s12221-014-2066-y.

[161] V. G. Thakare, P. A. Joshi, R. R. Godse, V. B. Bhatkar, P. A. Wadegaokar, and S. K. Omanwar, “Fabrication of polycaprolactone/zirconia nanofiber scaffolds using electrospinning technique,” *Journal of Polymer Research*, vol. 24, no. 12, p. 232, Dec. 2017, doi: 10.1007/s10965-017-1388-z.

[162] F. Asghari Arpatappeh, E. Manga, K. Bilge, B. E. Aydemir, M. A. Gülgün, and M. Papila, “Morphology evolution of self-same nanocomposites hybridized with jumbo-sized particles,” *J Appl Polym Sci*, vol. 139, no. 48, Dec. 2022, doi: 10.1002/app.53073.

[163] R. Stone and K. Krishnamurthy, “A neural network thrust force controller to minimize delamination during drilling of graphite-epoxy laminates,” *Int J Mach Tools Manuf*, vol. 36, no. 9, pp. 985–1003, 1996, doi: 10.1016/0890-6955(96)00013-2.

[164] L. Sorrentino, S. Turchetta, and C. Bellini, “A new method to reduce delaminations during drilling of FRP laminates by feed rate control,” *Compos Struct*, vol. 186, pp. 154–164, 2018, doi: 10.1016/j.compstruct.2017.12.005.

[165] V. Schulze, C. Becke, K. Weidenmann, and S. Dietrich, “Machining strategies for hole making in composites with minimal workpiece damage by directing the process forces inwards,” *J Mater Process Technol*, vol. 211, no. 3, pp. 329–338, Mar. 2011, doi: 10.1016/j.jmatprotec.2010.10.004.

[166] H. Qian, E. S. Greenhalgh, M. S. P. Shaffer, and A. Bismarck, “Carbon nanotube-based hierarchical composites: a review,” *J Mater Chem*, vol. 20, no. 23, pp. 4751–4762, 2010.

[167] Y. Nakamura, K. Nagata, Y. Tobita, N. Yokouchi, H. Nigo, and T. Iida, “Surface structure of silane-treated glass beads and its influence on the mechanical

properties of filled composites," *J Adhes Sci Technol*, vol. 16, no. 5, pp. 523–542, 2002, doi: 10.1163/156856102760070358.

[168] J.-L. Tsai, B.-H. Huang, and Y.-L. Cheng, "Enhancing fracture toughness of glass/epoxy composites by using rubber particles together with silica nanoparticles," *J Compos Mater*, vol. 43, no. 25, pp. 3107–3123, 2009.

[169] X. Jia, G. Li, B. Liu, Y. Luo, G. Yang, and X. Yang, "Multiscale reinforcement and interfacial strengthening on epoxy-based composites by silica nanoparticle-multiwalled carbon nanotube complex," *Compos Part A Appl Sci Manuf*, vol. 48, pp. 101–109, 2013.

[170] M. Omastová, K. Boukerma, M. M. Chehimi, and M. Trchová, "Novel silicon carbide/polypyrrole composites; preparation and physicochemical properties," *Mater Res Bull*, vol. 40, no. 5, pp. 749–765, 2005.

[171] W. Nhuapeng, W. Thamjaree, S. Kumfu, P. Singjai, and T. Tunkasiri, "Fabrication and mechanical properties of silicon carbide nanowires/epoxy resin composites," *Current Applied Physics*, vol. 8, no. 3, pp. 295–299, 2008, doi: http://dx.doi.org/10.1016/j.cap.2007.10.074.

[172] M. Derradji *et al.*, "Mechanical and thermal properties of phthalonitrile resin reinforced with silicon carbide particles," *Mater Des*, vol. 71, pp. 48–55, 2015.

[173] Z. Guo, T. Y. Kim, K. Lei, T. Pereira, J. G. Sugar, and H. T. Hahn, "Strengthening and thermal stabilization of polyurethane nanocomposites with silicon carbide nanoparticles by a surface-initiated-polymerization approach," *Compos Sci Technol*, vol. 68, no. 1, pp. 164–170, 2008.

[174] D. Liu, Y. Tang, and W. L. Cong, "A review of mechanical drilling for composite laminates," *Compos Struct*, vol. 94, no. 4, pp. 1265–1279, 2012, doi: https://doi.org/10.1016/j.compstruct.2011.11.024.

[175] Z. Spitalsky, D. Tasis, K. Papagelis, and C. Galiotis, "Carbon nanotube–polymer composites: Chemistry, processing, mechanical and electrical properties," *Prog Polym Sci*, vol. 35, no. 3, pp. 357–401, 2010, doi: http://dx.doi.org/10.1016/j.progpolymsci.2009.09.003.

[176] J. N. Coleman, U. Khan, W. J. Blau, and Y. K. Gun'ko, "Small but strong: A review of the mechanical properties of carbon nanotube-polymer composites," *Carbon N Y*, vol. 44, no. 9, pp. 1624–1652, 2006, doi: 10.1016/j.carbon.2006.02.038.

[177] K. Kumar and R. K. Verma, “Measurement and evaluation of delamination factors and thrust force generation during drilling of multiwall carbon nanotube (MWCNT) modified polymer laminates,” *Archive of Mechanical Engineering*, vol. 69, no. 2, pp. 269–300, 2022.

[178] N. Li, Y. Li, J. Zhou, Y. He, and X. Hao, “Drilling delamination and thermal damage of carbon nanotube/carbon fiber reinforced epoxy composites processed by microwave curing,” *Int J Mach Tools Manuf*, vol. 97, pp. 11–17, 2015, doi: 10.1016/j.ijmachtools.2015.06.005.

[179] Y. Song, N. Zheng, X. Dong, and J. Gao, “Flexible Carboxylated CNT/PA66 Nanofibrous Mat Interleaved Carbon Fiber/Epoxy Laminates with Improved Interlaminar Fracture Toughness and Flexural Properties,” *Ind Eng Chem Res*, vol. 59, no. 3, pp. 1151–1158, Jan. 2020, doi: 10.1021/acs.iecr.9b05854.

[180] G. W. Beckermann and K. L. Pickering, “Mode I and Mode II interlaminar fracture toughness of composite laminates interleaved with electrospun nanofibre veils,” *Compos Part A Appl Sci Manuf*, vol. 72, pp. 11–21, May 2015, doi: 10.1016/j.compositesa.2015.01.028.

[181] I. Touaiher, M. Saâdaoui, J. Chevalier, L. Preiss, and H. Reveron, “Fracture behavior of Ce-TZP/alumina/aluminate composites with different amounts of transformation toughening. Influence of the testing methods,” *J Eur Ceram Soc*, vol. 38, no. 4, pp. 1778–1789, 2018, doi: 10.1016/j.jeurceramsoc.2017.09.052.

[182] J. Chevalier *et al.*, “Forty years after the promise of «ceramic steel?»: Zirconia-based composites with a metal-like mechanical behavior,” *Journal of the American Ceramic Society*, vol. 103, no. 3, pp. 1482–1513, Mar. 2020, doi: 10.1111/jace.16903.

[183] H. G. Scott, “Phase relationships in the zirconia-yttria system,” *J Mater Sci*, vol. 10, no. 9, pp. 1527–1535, Sep. 1975, doi: 10.1007/BF01031853.

[184] R. C. GARVIE, R. H. HANNINK, and R. T. PASCOE, “Ceramic steel?,” *Nature*, vol. 258, no. 5537, pp. 703–704, Dec. 1975, doi: 10.1038/258703a0.

[185] R. H. J. Hannink, P. M. Kelly, and B. C. Muddle, “Transformation Toughening in Zirconia-Containing Ceramics,” *Journal of the American Ceramic Society*, vol. 83, no. 3, pp. 461–487, 2000, doi: 10.1111/j.1151-2916.2000.tb01221.x.

[186] I. M. Low, “ZrO2 transformation toughening criteria,” *J Mater Sci Lett*, vol. 7, no. 3, pp. 297–299, Mar. 1988, doi: 10.1007/BF01730204.

[187] D. D. Perovic, M. R. Castell, A. Howie, C. Lavoie, T. Tiedje, and J. S. W. Cole, “Field-emission SEM imaging of compositional and doping layer semiconductor superlattices,” *Ultramicroscopy*, vol. 58, no. 1, pp. 104–113, 1995, doi: https://doi.org/10.1016/0304-3991(94)00183-N.

[188] M. R. Castell, D. D. Perovic, and H. Lafontaine, “Electronic contribution to secondary electron compositional contrast in the scanning electron microscope,” *Ultramicroscopy*, vol. 69, no. 4, pp. 279–287, 1997, doi: https://doi.org/10.1016/S0304-3991(97)00051-X.

[189] M. R. Castell, T. W. Simpson, I. v Mitchell, D. D. Perovic, and J.-M. Baribeau, “Deactivation and diffusion of boron in ion-implanted silicon studied by secondary electron imaging,” *Appl Phys Lett*, vol. 74, no. 16, pp. 2304–2306, Apr. 1999, doi: 10.1063/1.123832.

[190] I. Jóźwik, J. Jagielski, E. Dumiszewska, M. Kamiński, and U. Kentsch, “Resistivity contrast imaging in semiconductor structures using ultra-low energy scanning electron microscopy,” *Ultramicroscopy*, vol. 228, p. 113333, Sep. 2021, doi: 10.1016/j.ultramic.2021.113333.

[191] I. Jóźwik, J. Jagielski, P. Caban, M. Kamiński, and U. Kentsch, “Direct visualization of highly resistive areas in GaN by means of low-voltage scanning electron microscopy,” *Mater Sci Semicond Process*, vol. 138, p. 106293, Feb. 2022, doi: 10.1016/j.mssp.2021.106293.

[192] R. Turan, D. D. Perovic, and D. C. Houghton, “Mapping electrically active dopant profiles by field-emission scanning electron microscopy,” *Appl Phys Lett*, vol. 69, no. 11, pp. 1593–1595, 1996, doi: 10.1063/1.117041.

[193] C. Schönjahn, C. J. Humphreys, and M. Glick, “Energy-filtered imaging in a field-emission scanning electron microscope for dopant mapping in semiconductors,” *J Appl Phys*, vol. 92, no. 12, pp. 7667–7671, Dec. 2002, doi: 10.1063/1.1525862.

[194] S. L. Elliott, R. F. Broom, and C. J. Humphreys, “Dopant profiling with the scanning electron microscope—A study of Si,” *J Appl Phys*, vol. 91, no. 11, pp. 9116–9122, Jun. 2002, doi: 10.1063/1.1476968.

[195] E. Najafi, T. D. Scarborough, J. Tang, and A. Zewail, “Four-dimensional imaging of carrier interface dynamics in p-n junctions,” *Science (1979)*, vol. 347, no. 6218, pp. 164–167, Jan. 2015, doi: 10.1126/science.aaa0217.

[196] T. Nakamura, K. Sato, M. Nagoshi, K. Ogata, Y. Kitahara, and T. Sakurada, "Identification and Visualization of Fine Precipitates in a Cr–Mo Steel Based on SEM Contrast," *Mater Trans*, vol. 60, no. 8, pp. 1591–1597, 2019, doi: 10.2320/matertrans.M2019078.

[197] K. W. Kim and H. Jaksch, "Compositional contrast of uncoated fungal spores and stained section-face by low-loss backscattered electron imaging," *Micron*, vol. 40, no. 7, pp. 724–729, 2009, doi: http://dx.doi.org/10.1016/j.micron.2009.05.001.

[198] K. Sempf, M. Boese, P. Gnauck, S. Höhn, and M. Herrmann, "Determination of local resistivity in ceramic composites by electron microscopy," *J Eur Ceram Soc*, vol. 36, no. 14, pp. 3531–3537, 2016, doi: https://doi.org/10.1016/j.jeurceramsoc.2016.05.034.

[199] K. Thydén, Y. L. Liu, and J. B. Bilde-Sørensen, "Microstructural characterization of SOFC Ni–YSZ anode composites by low-voltage scanning electron microscopy," *Solid State Ion*, vol. 178, no. 39, pp. 1984–1989, 2008, doi: http://dx.doi.org/10.1016/j.ssi.2007.12.075.

[200] J. I. Goldstein *et al.*, *Scanning electron microscopy and x-ray microanalysis*, 3rd ed. New York: Kluwer Academic/Plenum Publishers, 2003.

[201] L. Reimer, *Scanning electron microscopy : physics of image formation and microanalysis*. Berlin ; New York: Springer-Verlag, 1985. [Online]. Available: https://lccn.loc.gov/85012627

[202] S. Mil'shteinand and D. C. Joy, "Microanalysis using secondary electrons in scanning electron microscopy," *Scanning*, vol. 23, no. 5, pp. 295–297, Dec. 2006, doi: 10.1002/sca.4950230501.

[203] P. Echlin, *Handbook of Sample Preparation for Scanning Electron Microscopy and X-Ray Microanalysis*. Boston, MA: Springer US, 2009. doi: 10.1007/978-0-387-85731-2.

[204] H. Seiler, "Secondary electron emission in the scanning electron microscope," *J Appl Phys*, vol. 54, no. 11, pp. R1–R18, Nov. 1983, doi: 10.1063/1.332840.

[205] T. E. Everhart, "2.4A Contrast Formation in the Scanning Electron Microscope," 2004, pp. 137–145. doi: 10.1016/S1076-5670(04)33008-9.

[206] C. J. Powell, "Attenuation lengths of low-energy electrons in solids," *Surf Sci*, vol. 44, no. 1, pp. 29–46, Jul. 1974, doi: 10.1016/0039-6028(74)90091-0.

[207] L. Reimer, *Image formation in low-voltage scanning electron microscopy*. Bellingham, Wash: SPIE Optical Engineering Press, 1993. [Online]. Available: https://lccn.loc.gov/92043451

[208] H. Bruining and J. H. de Boer, “Secondary electron emission: Part i. secondary electron emission of metals,” *Physica*, vol. 5, no. 1, pp. 17–30, 1938.

[209] H. Bruining and J. H. de Boer, “Secondary electron emission Part V. The mechanism of secondary electron emission,” *Physica*, vol. 6, no. 7–12, pp. 834–839, 1939, doi: 10.1016/S0031-8914(39)90086-8.

[210] H. Bruining, *Physics and applications of secondary electron emission*. London: Pergamon Press, 1954. [Online]. Available: https://lccn.loc.gov/56003326

[211] L. Austin and H. Starke, “Ueber die Reflexion der Kathodenstrahlen und eine damit verbundene neue Erscheinung secundärer Emission,” *Ann Phys*, vol. 314, no. 10, pp. 271–292, 1902, doi: 10.1002/andp.19023141003.

[212] A. J. Dekker, “Secondary Electron Emission,” in *Solid State Physics*, vol. 6, 1958, pp. 251–311. doi: 10.1016/S0081-1947(08)60728-6.

[213] K. G. McKay, “Secondary electron emission,” in *Advances in Electronics and Electron Physics*, vol. 1, Elsevier, 1948, pp. 65–130.

[214] H. Bethe, “Zur Theorie des Durchgangs schneller Korpuskularstrahlen durch Materie,” *Ann Phys*, vol. 397, no. 3, pp. 325–400, 1930, doi: doi:10.1002/andp.19303970303.

[215] D. C. Joy and S. Luo, “An empirical stopping power relationship for low-energy electrons,” *Scanning*, vol. 11, no. 4, pp. 176–180, 1989, doi: 10.1002/sca.4950110404.

[216] M. Berger and S. Seltzer, “10. Tables of energy-losses and ranges of electrons and positrons,” in *Studies in penetration of charged particles in matter*, no. 39, 1964, p. 205.

[217] D. C. Joy, “A model for calculating secondary and backscattered electron yields,” *J Microsc*, vol. 147, no. 1, pp. 51–64, Jul. 1987, doi: 10.1111/j.1365-2818.1987.tb02817.x.

[218] D. Joy, “Image simulation for secondary electron micrographs in the scanning electron microscope,” *Scanning Microsc*, vol. 2, pp. 57–64, 1988.

[219] J. Cazaux, “On some contrast reversals in SEM: Application to metal/insulator systems,” *Ultramicroscopy*, vol. 108, no. 12, pp. 1645–1652, 2008, doi: https://doi.org/10.1016/j.ultramic.2008.06.005.

[220] J. Cazaux, “Material contrast in SEM: Fermi energy and work function effects,” *Ultramicroscopy*, vol. 110, no. 3, pp. 242–253, Feb. 2010, doi: 10.1016/j.ultramic.2009.12.002.

[221] J. Cazaux, “Calculated influence of work function on SE escape probability and Secondary Electron Emission yield,” *Appl Surf Sci*, vol. 257, no. 3, pp. 1002–1009, 2010, doi: http://dx.doi.org/10.1016/j.apsusc.2010.08.007.

[222] J. Cazaux, “Secondary electron emission and charging mechanisms in Auger Electron Spectroscopy and related e-beam techniques,” *J Electron Spectros Relat Phenomena*, vol. 176, no. 1–3, pp. 58–79, Jan. 2010, doi: 10.1016/j.elspec.2009.06.004.

[223] J. Cazaux, “Electron Probe Microanalysis of Insulating Materials: Quantification Problems and Some Possible Solutions,” *X-Ray Spectrometry*, vol. 25, no. 6, pp. 265–280, Nov. 1996, doi: 10.1002/(SICI)1097-4539(199611)25:6<265::AID-XRS172>3.0.CO;2-3.

[224] T. E. Everhart and R. F. M. Thornley, “2.4B Wide-Band Detector for Micro-microampere Low-Energy Electron Currents,” 2004, pp. 147–152. doi: 10.1016/S1076-5670(04)33009-0.

[225] H. Jaksch, “Field emission SEM for true surface imaging and analysis,” *Materials world*, vol. 4, no. 10, pp. 583–584, 1996.

[226] G. L. Clark and D. H. Reynolds, “Chemistry of Zirconium Dioxide X-Ray Diffraction Studies,” *Ind Eng Chem*, vol. 29, no. 6, pp. 711–715, Jun. 1937, doi: 10.1021/ie50330a027.

[227] D. L. PORTER and A. H. HEUER, “Microstructural Development in MgO-Partially Stabilized Zirconia (Mg-PSZ),” *Journal of the American Ceramic Society*, vol. 62, no. 5–6, pp. 298–305, May 1979, doi: 10.1111/j.1151-2916.1979.tb09484.x.

[228] D. L. Porter, A. G. Evans, and A. H. Heuer, “Transformation-toughening in partially-stabilized zirconia (PSZ),” *Acta Metallurgica*, vol. 27, no. 10, pp. 1649–1654, 1979.

[229] S. J. Deteresa, R. J. Farris, and R. S. Porter, “Behavior of an aramid fiber under uniform compression,” *Polym Compos*, vol. 3, no. 2, pp. 57–58, 1982.

[230] D. L. Porter and A. H. Heuer, “Mechanisms of toughening partially stabilized zirconia (PSZ),” *Journal of the American Ceramic Society*, vol. 60, no. 3–4, pp. 183–184, 1977.

[231] P. E. REYES-MOREL, J.-S. CHERNG, and I.-W. CHEN, “Transformation Plasticity of CeO2-Stabilized Tetragonal Zirconia Polycrystals: II, Pseudoelasticity and Shape Memory Effect,” *Journal of the American Ceramic Society*, vol. 71, no. 8, pp. 648–657, Aug. 1988, doi: 10.1111/j.1151-2916.1988.tb06383.x.

[232] P. E. REYES-MOREL and I.-W. CHEN, “Transformation Plasticity of CeO2-Stabilized Tetragonal Zirconia Polycrystals: I, Stress Assistance and Autocatalysis,” *Journal of the American Ceramic Society*, vol. 71, no. 5, pp. 343–353, May 1988, doi: 10.1111/j.1151-2916.1988.tb05052.x.

[233] P. Duwez, F. H. Brown, and F. Odell, “The Zirconia-Yttria System,” *J Electrochem Soc*, vol. 98, no. 9, p. 356, 1951, doi: 10.1149/1.2778219.

[234] R. H. French, S. J. Glass, F. S. Ohuchi, Y.-N. Xu, and W. Y. Ching, “Experimental and theoretical determination of the electronic structure and optical properties of three phases of <math display="inline"> <mrow> <msub> <mrow> <mi mathvariant="normal">ZrO</mi> </mrow> <mrow> <mn>2</mn> </mrow> </msub> </mrow> </math>,” *Phys Rev B*, vol. 49, no. 8, pp. 5133–5142, Feb. 1994, doi: 10.1103/PhysRevB.49.5133.

[235] H. Jiang, R. I. Gomez-Abal, P. Rinke, and M. Scheffler, “Electronic band structure of zirconia and hafnia polymorphs from the GW perspective,” *Phys Rev B*, vol. 81, no. 8, p. 85119, 2010, doi: 10.1103/PhysRevB.81.085119.

[236] M. Delarmelina, M. G. Quesne, and C. R. A. Catlow, “Modelling the bulk properties of ambient pressure polymorphs of zirconia,” *Physical Chemistry Chemical Physics*, vol. 22, no. 12, pp. 6660–6676, 2020, doi: 10.1039/d0cp00032a.

[237] K. Yardley, “The structure of baddeleyite and of prepared zirconia,” *Mineralogical Magazine and Journal of the Mineralogical Society*, vol. 21, no. 115, pp. 169–175, Dec. 1926, doi: 10.1180/minmag.1926.021.115.05.

[238] J. D. McCullough and K. N. Trueblood, “The crystal structure of baddeleyite (monoclinic ZrO2),” *Acta Crystallogr*, vol. 12, no. 7, pp. 507–511, Jul. 1959, doi: 10.1107/S0365110X59001530.

[239] T. Hirata, E. Asari, and M. Kitajima, “Infrared and Raman Spectroscopic Studies of ZrO2 Polymorphs Doped with Y2O3 or CeO2,” *J Solid State Chem*, vol. 110, no. 2, pp. 201–207, Jun. 1994, doi: 10.1006/jssc.1994.1160.

[240] J. Ferraro, K. Nakamoto, and C. W. Brown, *Introductory Raman Spectroscopy*, 2nd ed. Amsterdam ; Boston: Academic Press, 2003.

[241] G. Teufer, “The crystal structure of tetragonal ZrO2,” *Acta Crystallogr*, vol. 15, no. 11, p. 1187, 1962, doi: 10.1107/S0365110X62003114.

[242] C. R. Brundle, C. A. Jr. Evans, S. Wilson, and L. E. Fitzpatrick, Eds., *Encyclopedia of materials characterization : surfaces, interfaces, thin films*. Boston, 1992.

[243] A. J. Perry, K. Phillips, and E. de Lamotte, “The mechanical properties of carbon fibres,” *Fibre Science and Technology*, vol. 3, no. 4, pp. 317–319, 1971.

[244] C. M. PHILLIPPI and K. S. MAZDIYASNI, “Infrared and Raman Spectra of Zirconia Polymorphs,” *Journal of the American Ceramic Society*, vol. 54, no. 5, pp. 254–258, May 1971, doi: 10.1111/j.1151-2916.1971.tb12283.x.

[245] V. G. KERAMIDAS and W. B. WHITE, “Raman Scattering Study of the Crystallization and Phase Transformations of ZrO2,” *Journal of the American Ceramic Society*, vol. 57, no. 1, pp. 22–24, Jan. 1974, doi: 10.1111/j.1151-2916.1974.tb11355.x.

[246] A. Feinberg and C. H. Perry, “Structural disorder and phase transitions in ZrO2-Y2O3 system,” *Journal of Physics and Chemistry of Solids*, vol. 42, no. 6, pp. 513–518, Jan. 1981, doi: 10.1016/0022-3697(81)90032-9.

[247] D. W. Liu, C. H. Perry, and R. P. Ingel, “Infrared spectra in nonstoichiometric yttria-stabilized zirconia mixed crystals at elevated temperatures,” *J Appl Phys*, vol. 64, no. 3, pp. 1413–1417, 1988, doi: 10.1063/1.341839.

[248] C. H. PERRY, D.-W. LIU, and R. P. INGEL, “Phase Characterization of Partially Stabilized Zirconia by Raman Spectroscopy,” *Journal of the American Ceramic Society*, vol. 68, no. 8, pp. C-184-C–187, Aug. 1985, doi: 10.1111/j.1151-2916.1985.tb10176.x.

[249] T. Hirata, “Raman-active modes and the tetragonal-monoclinic phase transition in ZrO2 doped with 12mol% CeO2,” *Journal of Physics and Chemistry of Solids*, vol. 56, no. 7, pp. 951–957, 1995, doi: https://doi.org/10.1016/0022-3697(95)00027-5.

[250] T. Hirata, H. Zhu, T. Furubayashi, and I. Nakatani, “Low-Temperature Structural Phase Transition in ZrO2-12 mol% CeO2 Studied by Infrared Spectroscopy and X-ray Diffractometry,” *Journal of the American Ceramic Society*, vol. 76, no. 5, pp. 1361–1364, May 1993, doi: 10.1111/j.1151-2916.1993.tb03767.x.

[251] P. Barberis, T. Merle-Méjean, and P. Quintard, “On Raman spectroscopy of zirconium oxide films,” *Journal of Nuclear Materials*, vol. 246, no. 2–3, pp. 232–243, Aug. 1997, doi: 10.1016/S0022-3115(97)00038-X.

[252] D. R. CLARKE and F. ADAR, “Measurement of the Crystallographically Transformed Zone Produced by Fracture in Ceramics Containing Tetragonal Zirconia,” *Journal of the American Ceramic Society*, vol. 65, no. 6, pp. 284–288, Jun. 1982, doi: 10.1111/j.1151-2916.1982.tb10445.x.

[253] C. S. Lim, T. R. Finlayson, F. Ninio, and J. R. Griffiths, “In-Situ Measurement of the Stress-Induced Phase Transformations in Magnesia-Partially-Stabilized Zirconia Using Raman Spectroscopy,” *Journal of the American Ceramic Society*, vol. 75, no. 6, pp. 1570–1573, Jun. 1992, doi: 10.1111/j.1151-2916.1992.tb04227.x.

[254] A. Paul, B. Vaidhyanathan, and J. Binner, “Micro-Raman spectroscopy of indentation induced phase transformation in nanozirconia ceramics,” *Advances in Applied Ceramics*, vol. 110, no. 2, pp. 114–119, Feb. 2011, doi: 10.1179/1743676110Y.0000000016.

[255] N. Matsunami *et al.*, “Energy dependence of the ion-induced sputtering yields of monatomic solids,” *At Data Nucl Data Tables*, vol. 31, no. 1, pp. 1–80, Jul. 1984, doi: 10.1016/0092-640X(84)90016-0.

[256] D. M. Mattox, “Physical Sputtering and Sputter Deposition (Sputtering),” in *Handbook of Physical Vapor Deposition (PVD) Processing*, Second., Elsevier, 2010. [Online]. Available: https://app.knovel.com/hotlink/pdf/id:kt00B4U252/handbook-physical-vapor/physical-s-introduction

[257] J. A. Thornton, “Influence of apparatus geometry and deposition conditions on the structure and topography of thick sputtered coatings,” *Journal of Vacuum Science and Technology*, vol. 11, no. 4, pp. 666–670, Jul. 1974, doi: 10.1116/1.1312732.

[258] D. Depla, S. Mahieu, and J. E. Greene, “Sputter Deposition Processes,” in *Handbook of Deposition Technologies for Films and Coatings (Third Edition)*, P. M. Martin, Ed. Boston: William Andrew Publishing, 2010, pp. 253–296. doi: https://doi.org/10.1016/B978-0-8155-2031-3.00005-3.

[259] B. Wang *et al.*, “Simulation and Optimization of Film Thickness Uniformity in Physical Vapor Deposition,” *Coatings*, vol. 8, no. 9, p. 27, 2018, doi: 10.3390/coatings8090325.

[260] CarlZeissMicroscopyGmbH, “ZEISS GeminiSEM – Field Emission Scanning Electron Microscope.” https://www.zeiss.com/microscopy/int/products/scanning-electron-microscopes/geminisem.html#gemini-basics (accessed Oct. 09, 2019).

[261] S. Deville and J. Chevalier, “Martensitic Relief Observation by Atomic Force Microscopy in Yttria-Stabilized Zirconia,” *Journal of the American Ceramic Society*, vol. 86, no. 12, pp. 2225–2227, Dec. 2003, doi: 10.1111/j.1151-2916.2003.tb03639.x.

[262] J. Cazaux, “Calculated effects of work function changes on the dispersion of secondary electron emission data: Application for Al and Si and related elements,” *J Appl Phys*, vol. 110, no. 2, p. 024906, Jul. 2011, doi: 10.1063/1.3608046.

[263] J. Cazaux, “About the role of the various types of secondary electrons (SE1; SE2; SE3) on the performance of LVSEM,” *J Microsc*, vol. 214, no. 3, pp. 341–347, 2004.

[264] J. Cazaux, “About the mechanisms of charging in EPMA, SEM, and ESEM with their time evolution,” *Microscopy and Microanalysis*, vol. 10, no. 6, pp. 670–684, 2004.

[265] J. Cazaux, “From the physics of secondary electron emission to image contrasts in scanning electron microscopy†,” *J Electron Microsc (Tokyo)*, vol. 61, no. 5, pp. 261–284, 2012, doi: 10.1093/jmicro/dfs048.

[266] J. Cazaux, “e-Induced secondary electron emission yield of insulators and charging effects,” *Nuclear Instruments & Methods in Physics Research Section B-Beam Interactions with Materials and Atoms*, vol. 244, no. 2, pp. 307–322, 2006, doi: 10.1016/j.nimb.2005.10.006.

[267] J. Cazaux and P. Lehuede, “Some physical descriptions of the charging effects of insulators under incident particle bombardment,” *J Electron Spectros Relat Phenomena*, vol. 59, no. 1, pp. 49–71, Jun. 1992, doi: 10.1016/0368-2048(92)85011-U.

[268] J. Cazaux, “Some considerations on the secondary electron emission, δ, from e− irradiated insulators,” *J Appl Phys*, vol. 85, no. 2, pp. 1137–1147, Jan. 1999, doi: 10.1063/1.369239.

[269] J. Cazaux, “Secondary electron emission and charging mechanisms in Auger Electron Spectroscopy and related e-beam techniques,” *J Electron Spectros Relat Phenomena*, vol. 176, no. 1–3, pp. 58–79, Jan. 2010, doi: 10.1016/j.elspec.2009.06.004.

[270] J. Cazaux, “Charging in scanning electron microscopy ‘from inside and outside,’” *Scanning*, vol. 26, no. 4, pp. 181–203, Dec. 2006, doi: 10.1002/sca.4950260406.

[271] C. J. Powell and A. Jablonski, “The NIST electron effective-attenuation-length database,” *Journal of Surface Analysis*, vol. 9, no. 3, pp. 322–325, 2002.